
Non-LTE diagnostics of the infrared observations of the planetary atmosphere

Oleg Goussev



München 2002

Non-LTE diagnostics of the infrared observations of the planetary atmosphere

Oleg Goussev

Dissertation
an der Fakultät für Physik
der Ludwig-Maximilians-Universität
München

vorgelegt von
Oleg Goussev
aus St. Petersburg

München, den 16.12.2002

Erstgutachter: Prof. Dr. A. W. A. Pauldrach

Zweitgutachter: Prof. Dr. H. Lesch, Prof. Dr. K.-U. Großmann

Tag der mündlichen Prüfung: 03.06.2003

Table of contents

1	Introduction	1
2	The non-LTE problem for molecular gas in the planetary atmosphere	3
2.1	Formulation of the problem	3
2.2	Complete thermodynamic equilibrium (CTE)	5
2.3	Local thermodynamic equilibrium (LTE)	5
2.4	Partial LTE	7
2.4.1	Rotational LTE	7
2.4.2	Vibrational LTE in groups of levels	9
2.5	Ro-vibrational non-LTE	10
3	Methods of solution of the non-LTE problem (current status)	11
3.1	Lambda iteration	11
3.2	Matrix method	11
3.3	Comparison of lambda iteration and matrix method	13
3.4	Accelerated lambda iteration	14
3.5	Treating the nonlinearity arising from collisions	15
3.5.1	Straightforward iteration and “decoupling”	15
3.5.2	Newton–Raphson method	16
4	Comparison of methods used to solve non-LTE problem in atmospheric science	19
4.1	Comparison of the ALI and lambda iteration techniques	19
4.2	Comparison of ALI algorithms utilising various radiative transfer techniques	23
4.3	ALI–ARMS, MCM and ARC codes	27
5	Applications of ALI-ARMS: non-LTE retrievals of the atmospheric parameters from CRISTA-1 and CRISTA-2 radiance data	29
5.1	CRISTA-1 and -2 spectral channels with non-LTE emissions	30
5.2	Method of retrieval	33
5.3	Non-LTE retrieval of CO ₂ densities	35
5.4	Non-LTE retrieval of O ₃ densities	36
5.5	Non-LTE retrieval of temperature	37
6	Applications of ALI-ARMS: analysis of the TES/MGS observations of the Martian atmosphere	49

7 Applications of ALI-ARMS: vibration-rotational non-LTE in CO₂ in the Earth atmosphere	53
8 Conclusions	57
9 Appendixes	59
A Using spectral line databases for non-LTE studies	61
A.1 Using HITRAN for non-LTE applications	61
A.1.1 Line profiles and frequency quadrature scheme	64
A.2 Definitions of vibrational temperature	67
B Electronic-vibrational-rotational levels and bands of molecules used in this study	71
B.1 H ₂ O	71
B.2 CO ₂	72
B.3 O ₃	73
B.4 N ₂ O	75
B.5 CO	75
B.6 O ₂	76
B.7 N ₂	77
C Collisional rates	83
C.1 <i>R – T</i> collisional processes	83
C.1.1 Rate coefficients for the CO ₂ <i>R – T</i> energy exchange	83
C.2 <i>V – T</i> collisional processes	83
C.2.1 <i>V – T</i> collisional transitions in H ₂ O	83
C.2.2 <i>V – T</i> collisional transitions in CO ₂	84
C.2.3 <i>V – T</i> collisional transitions in O ₃	86
C.2.3.1 Kinetic model of Manuilova	87
C.2.3.2 Kinetic models of Mlynczak	88
C.2.3.3 Kinetic model of Koutoulaki	88
C.2.4 <i>V – T</i> collisional transitions in N ₂ O	89
C.2.5 <i>V – T</i> collisional transitions in CO	90
C.2.6 <i>V – T</i> collisional transitions in N ₂	90
C.2.7 <i>V – T</i> collisional transitions in O ₂	90
C.3 <i>V – V</i> collisional processes	91
C.4 <i>C – V</i> processes	95
C.4.1 Production of ozone: recombination reaction	95
C.4.2 Chemical deactivation of ozone by O(³ P _f)	96

C.4.3	Destruction of ozone by reactions with other minor chemical species	97
C.4.4	Chemical excitation of O ₂	97
D	Solution of the radiative transfer equation (RTE)	99
D.1	Optical depth	100
D.2	Lambda and psi operators	100
D.3	Integral methods	101
D.3.1	Method of long characteristics (MLC)	101
D.3.2	Method of short characteristics (MSC)	101
D.4	Differential methods	102
D.4.1	Feautrier method	102
D.4.2	Discontinuous finite element (DFE) method	103
D.5	Treating laser bands	104
D.6	Comparison of the methods	105
E	Numerical acceleration techniques	107
E.1	Ng acceleration	107
E.2	Orthomin acceleration	108
F	Atmospheric models used in this study	109
F.1	Earth atmosphere	109
F.1.1	Pressure and temperature	109
F.1.2	Volume mixing ratios	110
F.2	Mars atmosphere	111
F.2.1	Mars and Earth atmospheres: the comparison	113
G	Current status of the code package ALI-ARMS (technical details)	115
G.1	General features of the code	115
G.2	Possible future extensions	116
G.3	Implemented models	116
H	The non-LTE problems for various molecules in the Earth atmosphere solved by ALI-ARMS	119
H.1	Vibrational non-LTE in CO ₂	119
H.2	Vibrational non-LTE in O ₃	120
H.3	Vibrational non-LTE in H ₂ O	123
H.4	Vibrational non-LTE in N ₂ O	124
H.5	Vibrational non-LTE in CO	126
H.6	Vibrational non-LTE in O ₂	127

H.7 Vibrational non-LTE in N ₂	128
Acknowledgements	131
Lebenslauf	133
Bibliography	134

Abbildungsverzeichnis

4.1	Convergence plots for the 9-level CO ₂ model of a spring equinox atmosphere at night. Logarithms of the maximum absolute relative change (MARC) are presented for the 00011 CO ₂ level. Labels on the curves refer to various iteration schemes (LI, LI+V, etc); use of Ng's acceleration method indicated by (+NG).	20
4.2	Convergence plots for the 9-level CO ₂ model of a spring equinox atmosphere at night. Logarithms of MARC are presented for the 00011 and 01101 CO ₂ levels (thick solid and dashed curves)	22
4.3	Convergence plots for a 64-level CO ₂ model of a spring equinox atmosphere for night and for day conditions (at solar zenith angle 0°).	23
4.4	Convergence plots for the CO ₂ problem in the Martian atmosphere for day and night conditions. Labels on the curves refer to various iteration schemes (see text for details).	25
4.5	Convergence plots for the CO ₂ problem in the Earth's atmosphere for day and night conditions. Labels on the curves refer to various iteration schemes (see text for details).	26
5.1	The geometry of limb scanning (CRISTA flight parameters used)	29
5.2	The measured limb spectra in the SCL2 CRISTA channel	31
5.3	The simulated spectra in the SCL2 CRISTA channel at different tangent heights	32
5.4	The simulated spectra in the SCS8 CRISTA channel at different tangent heights (daytime)	33
5.5	The simulated spectra in the SCS8 CRISTA channel at different tangent heights (nighttime)	34
5.6	The measured daytime limb spectra in the SCS2 CRISTA channel at different tangent heights	39
5.7	The simulated spectra in the SCS2 CRISTA channel at different tangent heights (daytime)	40
5.8	The simulated spectra in the SCS2 CRISTA channel at different tangent heights (nighttime)	40
5.9	The measured limb spectra in the SCS3 CRISTA channel (day/night)	41
5.10	The simulated spectra in the SCS3 CRISTA channel at different tangent heights (nighttime)	42
5.11	The simulated spectra in the SCS3 CRISTA channel at different tangent heights (daytime)	42
5.12	CO ₂ volume mixing ratios.	43
5.13	Integrated limb radiances in the SCS2 channel for selected CO ₂ profiles	43
5.14	Retrieved CO ₂ VMR for selected CRISTA-1 profiles.	44
5.15	Effects of the reduction of temperature in the mesosphere and different kinetic models used for the ozone number density retrieval	45

5.16	The profiles of retrieved non-LTE O ₃ VMR, the LTE retrieved O ₃ VMR and the MAS measurement	45
5.17	Zonal averages of the temperature (top: CRISTA-1, bottom: CRISTA-2 extended scans). The latitude binning is 10° in both cases.	46
5.18	The zonal temperature cross-section (bottom: CRISTA-1, top: CRISTA-2).	47
6.1	The vibrational temperatures for CO ₂ (626) levels (daytime).	49
6.2	The vibrational temperatures for CO ₂ (626) levels (nighttime).	49
6.3	The temperatures in Mars atmosphere and on its surface, measured by MGS/TES.	50
6.4	Global distribution of the emissions in CO ₂ 10 μm laser band: modelled (contour lines) and measured by MGS/TES. The figure is taken from <i>Maguire et al.</i> (126).	51
7.1	The rotational distribution functions for the vibrational level 00011 of CO ₂ (626) at different altitudes	55
7.2	The nighttime limb radiances for the CO ₂ (626) 00011 → 00001 band at different tangent heights. Effects of the rotational LTE breakdown.	56
A.1	Dependence of Einstein coefficient of spontaneous emission for the vibrational band on temperature (in case of rotational LTE).	63
A.2	The populations of the ground vibrational state	67
B.1	The vibrational levels and most important 6.3 μm (solid lines) and 2.7 μm (dashed lines) bands of H ₂ O	72
B.2	Energies of H ₂ O vibrational levels, cm ⁻¹	72
B.10	The vibrational levels and bands of CO	75
B.11	Energies of CO vibrational levels, cm ⁻¹	75
B.3	The vibrational levels of CO ₂ (extended model).	78
B.4	Vibrational bands of CO ₂ : black - 15μm , red - 10μm , blue - 4.3 μm , magenta - 2.0 μm	79
B.5	The vibrational levels of O ₃ (taken from <i>Koutoulaki</i> (92)).	80
B.6	The vibrational levels of O ₃ included in the model of <i>Manuilova et al.</i> (132).	80
B.7	Most important 4.8 μm (left) and 9.6 μm (right) bands of O ₃	81
B.8	The vibrational levels and bands of N ₂ O	81
B.9	Energies of N ₂ O vibrational levels	81
C.1	Most important V – V processes.	91
C.2	Rate constants for O ₂ (v)+O ₂ (0) process.	95
C.3	V – V rate constants for O ₂ (v)+N ₂ (0) process.	95
C.4	Chemical production rate constant of O ₂ (³ Σ, v) from O ₃	98
D.1	Line opacity and source function for laser line from CO ₂ (626) 00011 → 10002 10.4 μm band	106

F.1	Altitude profiles of pressure and temperature, used for the Earth atmosphere modeling.	109
F.2	Altitude profiles of molecular VMRs used for the Earth atmosphere modeling. . .	110
F.3	Altitude profiles of molecular VMRs used for the Earth atmosphere modeling (cont.)	111
F.4	Altitude profiles of pressure and temperature, used for the modeling of Mars atmosphere.	112
F.5	Volume mixing ratio of CO ₂ in Mars atmosphere	112
F.6	Volume mixing ratio of N ₂ in Mars atmosphere.	112
F.7	Volume mixing ratio of CO in Mars atmosphere	112
F.8	Volume mixing ratio of O(³ P _J) in Mars atmosphere.	112
F.9	Altitude profiles of pressure and temperature, used for the Earth and Mars atmospheres	113
F.10	Altitude profiles of CO ₂ number density in the Earth and Mars atmospheres	113
H.1	The vibrational temperatures for CO ₂ (626) levels (daytime).	119
H.2	The vibrational temperatures for CO ₂ (626) levels (nighttime).	119
H.3	The convolved limb radiances of CO ₂ 15, 12.6, 9.4, 4.3 μm bands (only daytime profiles are shown)	120
H.4	The cooling rates for CO ₂ (626) molecule	121
H.5	The cooling rates for CO ₂ (636) molecule	121
H.6	The vibrational temperatures for O ₃ (666) levels (daytime).	121
H.7	The vibrational temperatures for O ₃ (666) levels (nighttime).	121
H.8	The convolved limb radiances of O ₃ 9.6 μm bands (daytime)	122
H.9	The convolved limb radiances of O ₃ 9.6 μm bands (nighttime)	122
H.10	The convolved limb radiances of O ₃ 4.8 μm bands (nighttime)	122
H.11	The cooling rate for O ₃ molecule	123
H.12	The vibrational temperatures for H ₂ O (161) levels (daytime).	123
H.13	The vibrational temperatures for H ₂ O (161) levels (nighttime).	123
H.14	Daytime convolved limb radiances of 6.3 μm H ₂ O bands.	124
H.15	Nighttime convolved limb radiances of 6.3 μm H ₂ O bands.	124
H.16	The cooling rate for H ₂ O molecule	125
H.17	The vibrational temperatures for N ₂ O (446) levels (daytime).	125
H.18	The vibrational temperatures for N ₂ O (446) levels (nighttime).	125
H.19	The vibrational temperatures for CO (26) levels (daytime).	127
H.20	The vibrational temperatures for CO (26) levels (nighttime).	127
H.21	The convolved limb radiances of CO ₂ 4.7 μm bands	127
H.22	The cooling rate for CO molecule	128
H.23	The vibrational temperatures for O ₂ (66) levels (daytime).	128

H.24 The vibrational temperatures for O ₂ (66) levels (nighttime).	128
H.25 The vibrational temperatures for N ₂ (44) levels (daytime).	129
H.26 The vibrational temperatures for N ₂ (44) levels (nighttime).	129

Tabellenverzeichnis

5.1	Spectral channels of CRISTA-1 and -2. The /E denotes the CRISTA-2 extended channels.	30
5.2	CRISTA-1 and -2 spectral channels with the non-LTE emissions.	31
A.1	Molecular parameters (source - HITRAN-2000)	69
B.1	Energies of O ₃ vibrational levels	74
B.2	Energies of O ₂ electronic states. The values are in cm ⁻¹	76
B.3	Constants used for the calculation of vibrational energies of O ₂ . The values are taken from <i>Lafer and Gilmore</i> (105) and <i>Herzberg</i> (77).	76
B.4	Constants used for calculation of rotational energies of O ₂ . The values are taken from <i>Herzberg</i> (77) in cm ⁻¹	77
B.5	Constants used for the calculation of vibrational energies of N ₂ . The energies are in cm ⁻¹	77
B.6	Constants used for calculation of rotational energies of N ₂ . The values are in cm ⁻¹	77
C.1	$V - T$ rate constants for H ₂ O ν_2 transitions.	84
C.2	$V - T$ rate constants for H ₂ O $\nu_1 \leftrightarrow \nu_3$ exchange.	84
C.3	$V - T$ rate constants for H ₂ O $\nu_1, \nu_3 \leftrightarrow 2\nu_2$ exchange.	84
C.4	Rate constants for the $V - T$ processes, which lead to splitting of the ν_3 quantum of CO ₂ molecules.	85
C.5	$V - T$ rate constants for CO ₂ ν_2 quenching.	85
C.6	$V - T$ rate constants for CO ₂ transitions inside the n -family.	86
C.7	Branching ratios ϵ_{nl} for CO ₂ ν_3 splitting.	86
C.8	$V - T$ rate constants for O ₃ $\nu_1 \leftrightarrow \nu_3$ transitions.	87
C.9	$V - T$ rate constants for O ₃ $\nu_1 \leftrightarrow \nu_2$ and $\nu_3 \leftrightarrow \nu_2$ transitions.	87
C.10	$V - T$ rate constants for O ₃ ν_2 transitions.	87
C.11	$V - T$ rate constants for O ₃ O(³ P _J) quenching.	88
C.12	Parameters A and B used by <i>Koutoulaki</i> (92).	88
C.13	Averaged collisional rates used by <i>Koutoulaki</i> (92)	89
C.14	$V - T$ processes for N ₂ O ν_2 bending mode.	89
C.15	$V - T$ rate constants for O ₂ (³ Σ, v) quenching.	90
C.16	Rate constants for N ₂ (v)+N ₂ (0) process	95
C.17	Rate constants of O ₃ chemical production	96
D.1	Time (in ms) required to find the integrated line intensity $\bar{J}_{ll'}$	106

Zusammenfassung

Für die Analyse der Infrarotmessungen von mehreren Weltraumexperimenten benötigt man die Berechnung der molekularen Infrarotstrahlung unter Berücksichtigung des nichtlokalen thermodynamischen Gleichgewichts (non-LTE). In dieser Dissertation wird die allgemeine Formulierung des non-LTE-Problems für die Mischung molekularer Gase in einer Planetenatmosphäre gegeben. Die hier vorgeschlagene Methode für die Lösung dieses Problems verwendet die "Accelerated Lambda Iteration (ALI)", die in der Astrophysik für die non-LTE Modellierung der Sternatmosphären entwickelt worden ist. Diese für die Atmosphärenforschung neue Technik ist frei von den Beschränkungen der Matrix- und Lambda-Iterationsmethoden, mit denen man traditionell die non-LTE Probleme in den Planetenatmosphären behandelt. Mit der Lösung des CO₂ - non-LTE Problems in der Erd- und Marsatmosphäre wird demonstriert, dass die ALI-Methode den anderen Algorithmen in Rechenzeit und Arbeitsspeicherverbrauch weit überlegen ist. Während sich die Atmosphärengruppen auf die Lösung einiger ausgewählter non-LTE-Probleme beschränkten, erlaubt das im Rahmen dieser Studie entwickelte Computerprogramm ALI-ARMS (für "Accelerated Lambda Iteration for Atmospheric Radiation and Molecular Spectra") die non-LTE-Modellierung einer beliebigen Anzahl von Molekülen, die durch den Stoß- und Strahlungsaustausch von Energie gekoppelt sind. ALI-ARMS wurde angewandt für die Datenauswertung der Infrarotspektren, die von dem "CRYogene Infrarot-Spektrometer und Teleskope für die Atmosphäre (CRISTA)"-Experiment an Bord des deutschen ASTRO-SPAS-Satelliten gemessen wurden, und für die Analyse der 10 μm Laser Banden, die von dem Thermal Emission Spectrometer (TES) an Bord von Mars Global Surveyor (MGS) aufgenommen wurden. Im Fall der Erdatmosphäre wurden die ersten detaillierten Karten der Temperatur sowie der Spurengaskonzentrationen in der oberen Mesosphäre und untereren Thermosphäre erzeugt. Die Ergebnisse dieser Arbeit sind ein wesentlicher Beitrag zu Studien der Mesosphäre, die heute als Indikator der globalen Klimaveränderungen betrachtet wird.

Abstract

The analysis of the infrared measurements of a number of sophisticated space experiments requires modeling of molecular infrared radiation with accounting for the nonlocal thermodynamic equilibrium (non-LTE). In this dissertation a general formulation is given of the multilevel vibrational-rotational non-LTE problem for a mixture of radiating molecular gases in a planetary atmosphere. The approach for the solution of this problem suggested here utilizes the Accelerated Lambda Iteration (ALI) technique developed in stellar astrophysics for spectrum formation calculations and for the computation of non-LTE model stellar atmospheres. This new for atmospheric science technique is not subject to the limitations of the traditional matrix and conventional lambda iteration methods which dominate the studies dealing with non-LTE in planetary atmospheres. In the case of the CO₂ non-LTE problems in the atmospheres of Earth and Mars it is demonstrated that ALI approach is far superior to the other algorithms in minimizing computer time and storage and in converging much more rapidly. While "atmospheric" groups concentrated on the development of codes suitable for treatment of limited number of selected non-LTE problems the computer code package ALI-ARMS (for "Accelerated Lambda Iteration for Atmospheric Radiation and Molecular Spectra") compiled in framework of this study allows non-LTE treatment of arbitrary number of molecules interacting by collisionally induced exchange of energy and by the band overlaps. It was applied to the analysis of large amount of the infrared limb radiance data obtained both in the CRYogenic Infrared Spectrometers and Telescopes for the Atmosphere (CRISTA) experiments on board of the german ASTRO-SPAS satellite and by the Thermal Emission Spectrometer (TES) instrument orbiting Mars on board of the NASA Mars Global Surveyor (MGS) satellite. In case of the Earth's atmosphere first detailed distributions of temperature and trace gas concentrations in the upper mesosphere and lower thermosphere were obtained. The retrieved temperature data confirmed the "two-level" structure of the Earth's mesopause which was recently discovered in the lidar and rocket experiments. These results contribute to the studies of the mesosphere, which is considered today to be the tracer of the global climate changes.

1. Introduction

Adequate interpretation of the infrared space observations of the Earth's and planetary atmospheres plays an important role in the comparative analysis of the planetary atmospheres which is aimed at understanding of possible evolution ways of the Earth's ecosystem.

In recent years the observations of infrared molecular emissions from the middle and upper layers of the Earth's atmosphere have attracted particular attention since trends in this altitude region are significant for understanding of global changes of the atmosphere. Simultaneously a number of sophisticated ground based and space infrared experiments provided unique data about the upper planetary atmospheres. However, an essential problem here is that in many cases the interpretation of these data requires accounting for deviations from the local thermodynamic equilibrium (non-LTE). The non-LTE effects are crucial in the middle and upper Earth's atmosphere for the majority of infrared molecular bands and influence strongly the radiation emerging from these layers. In some cases the observations of these emissions from space are influenced by the non-LTE effects down to the lower stratosphere.

The non-LTE problems for the infrared ro-vibrational molecular bands are studied in atmospheric science since 1950s. Any of these problems has two primary constituents: (1) the statistical equilibrium equations (SEE), which express the equality of the total population and de-population rates for each molecular level; (2) the radiative transfer equation (RTE), which relates the radiation field at a given height to the level populations at *all altitudes* in the atmosphere. Hence the system of equations for the level populations is *nonlocal* (and nonlinear).

The most obvious way of dealing with this situation is to iterate between the SEE and RTE (see *Wintersteiner et al.*(219), *López-Puertas and Taylor* (121)). This process, traditionally called "lambda iteration", has been investigated in detail in the astronomical context in the 1920's (c.f. Unsöld(206)). It involves matrices no larger than $L \times L$, where L is the total number of molecular levels, but in some cases (if the optical depths are large) it converges very slowly.

An alternative way of dealing with this non-LTE problem is the simultaneous treatment of the SEE and RTE, in which the RTE is discretized with respect to the optical depth or pressure grid to get a matrix representation of the radiative terms in the SEE. This requires the inversion of a matrix of dimension $(L \times D) \times (L \times D)$, where D is the number of altitude (or pressure) points in the atmospheric model. This approach is known in atmospheric science as the Curtis-matrix technique (see Curtis and Goody(34), Goody(63)). It has been employed in a series of papers beginning with *López-Puertas et al.*(109) (see also *López-Puertas and Taylor* (121)).

However, in order to construct adequate models, one must consider a large number of excited levels of different molecular species coupled by a variety of collisional energy exchange processes and by band overlapping, together with a detailed model of atmospheric stratification; thus both L and D can become large. The dimensions of the primary matrices were consequently reduced by introducing approximations; these, however, need careful investigation, since in many cases they lead to unrealistic results. Typical of these are: 1) the assumption of rotational LTE for rotational substructures of vibrational levels, which reduces L to the number of vibrational levels; 2) the assumption of vibrational LTE for groups of vibrational levels closely spaced in energy and interacting by intensive inter- or intra-molecular collisional V-V energy exchange; 3) the neglect of certain vibrational levels or exclusion from the model of certain molecules. Moreover, in many cases a large number of weak bands are omitted or treated approximately, the total number of molecules is not conserved, etc.

The importance of treating IR band radiation accurately by non-LTE techniques for a variety of applications in atmospheric modeling has motivated the search for a new method of solving these transfer problems which is not subject to the limitations of the traditional matrix or conventional lambda iteration methods. While in atmospheric science these methods since 1950s continue dominating studies dealing with non-LTE *López-Puertas and Taylor* (121)) stellar astrophysicists have

developed (see *Hubený et al.*(80)) a family of powerful techniques, which utilize iteration with an approximate (or accelerated) lambda operator; these are now the standard techniques for spectrum formation calculations and for the computation of non-LTE model stellar atmospheres. In these so-called ALI techniques (for Accelerated Lambda Iteration) the lambda operator, which express the radiation intensity at a point in terms of the level populations at all points, is approximated by a local (or nearly local) operator and the *difference* is treated iteratively. Again, the largest matrix has dimension $L \times L$, but the convergence is now rapid.

The Chapter 2 of this dissertation gives general formulation of the multilevel vibrational-rotational non-LTE problem for a mixture of radiating molecular gases in a planetary atmosphere. Chapter 3 contains description and comparative analysis of conventional lambda iteration-, matrix- and ALI techniques. The ALI-ARMS (for “Accelerated Lambda Iteration for Atmospheric Radiation and Molecular Spectra”) code developed in framework of this study utilizes newest results of the ALI techniques obtained in the stellar astrophysics. Chapter 4 gives the convergence rates and timing of various computational schemes based on accelerated lambda iteration which are incorporated in the code, as well as compares the code with other codes currently used in atmospheric non-LTE studies. In the last three Chapters the application of ALI-ARMS are discussed. Chapter 5 outlines results of the non-LTE diagnostics of the limb radiance data obtained in the CRYogenic Infrared Spectrometers and Telescopes for the Atmosphere (CRISTA) experiments on board of the german ASTRO-SPAS satellite. Chapter 6 deals with the analysis of the limb radiance data of the Thermal Emission Spectrometer (TES) instrument orbiting Mars on board of the NASA Mars Global Surveyor (MGS) satellite. Chapter 7 presents analysis of the rovibrational non-LTE in CO₂ in the Earth’s middle atmosphere. In the conclusion the main results and implications of the dissertation are summarized. Appendices A-H contain spectroscopic and collisional rate data, mathematical algorithms and atmospheric models used in this study, as well as reference non-LTE results for a number of molecules and technical details of the CRISTA experiments which support the discussion presented in the main body of the dissertation.

2. The non-LTE problem for molecular gas in the planetary atmosphere

2.1 Formulation of the problem

Let us consider a Maxwellian gas mixture in a planetary atmosphere consisting of molecular and atomic gases whose energy levels are enumerated by the index l throughout the entire mixture. Each energy level is characterized by its statistical weight g_l and energy E_l .

We consider only the *steady state* of this gas mixture, in which its temperature and the degree of excitation do not change with time. The statistical equilibrium (or steady-state) equation (SEE) which expresses the balance between various elementary processes can be written as

$$n_l \left(\sum_{l'} R_{ll'} + C_l^- \right) = \sum_{l'} n_{l'} R_{l'l} + C_l^+ + Y_l. \quad (2.1)$$

Here n_l are the populations of electronic–vibration–rotational (EVR) levels of the molecules or the electronic (E) levels of atoms, $R_{ll'}$ are the radiative rate coefficients for transitions from level l to l' , $n_l C_l^-$ and C_l^+ are the total rates of de-population and population of level l , respectively, due to the variety of energy exchange processes by atomic and molecular collisions. Y_l in Eq. 2.1, (p.3) is a source term prescribing the net production rate of level l through processes other than collisions and absorption of radiation emitted within the atmosphere, such as the absorption of radiation from external sources (“sun” and/or “ground”), production of excited constituents in various chemical reactions, etc.

For the sake of simplicity we confine ourselves to the case of a plane-parallel atmosphere for which the transfer equation is

$$\mu \frac{dI_{\mu\nu}}{dz} = -\chi_{\mu}(\nu) I_{\mu\nu} + \eta_{\mu}(\nu), \quad (2.2)$$

where $I_{\mu\nu}$ is the specific intensity of atmospheric radiation, and $\chi_{\mu}(\nu)$ and $\eta_{\mu}(\nu)$ are the total opacity and emissivity, respectively, at frequency ν and direction cosine μ .

The radiative properties of the gas being considered are completely characterized by the emissivity $\eta_{ll'}$ and the opacity $\chi_{ll'}$ for each pair of levels connected by a line transition¹. If the macroscopic velocity field can be neglected, which is obviously a good approximation for any molecular radiative transfer problem in planetary atmospheres, these quantities do not depend on μ . Abbreviating the energy relations $E_l < E_{l'}$ and $E_l > E_{l'}$ by $l < l'$ and $l > l'$, respectively, we obtain for $l > l'$

$$\begin{aligned} \eta_{ll'}(\nu) &= \frac{h\nu_{ll'}}{4\pi} n_l A_{ll'} \varphi_{ll'}(\nu), \\ \chi_{ll'}(\nu) &= \frac{h\nu_{ll'}}{4\pi} (n_{l'} B_{l'l} - n_l B_{ll'}) \varphi_{ll'}(\nu), \end{aligned} \quad (2.3)$$

where $\nu_{ll'}$ is the line center frequency, $A_{ll'}$, $B_{ll'}$ and $B_{l'l}$ are the Einstein coefficients and $\varphi_{ll'}(\nu)$ is the line profile function normalized such that $\int d\nu \varphi_{ll'}(\nu) = 1$. The line source function for the transition is defined by

$$S_{ll'} = \frac{\eta_{ll'}(\nu)}{\chi_{ll'}(\nu)} = \frac{n_l A_{ll'}}{n_{l'} B_{l'l} - n_l B_{ll'}}. \quad (2.4)$$

It is frequency and angle independent as a result of assuming in Eq.2.3, (p.3) the equality of emission and absorption profiles (the assumption of complete frequency redistribution within

¹This is not true in case of line mixing which will not be discussed here

a line) and isotropic scattering. Generalizations to include angle and frequency variations are available, but will not be considered here.

The total emissivity and opacity are given in terms of above line quantities by

$$\begin{aligned}\eta(\nu) &= \sum_{l>l'} \eta_{ll'}(\nu) + \eta_c(\nu), \\ \chi(\nu) &= \sum_{l>l'} \chi_{ll'}(\nu) + \chi_c(\nu),\end{aligned}\tag{2.5}$$

where $\eta_c(\nu)$ and $\chi_c(\nu)$ are the emissivity and opacity of the background continuum which is slowly varying across the line; these quantities are assumed to be prescribed and do not change from iteration to iteration. In writing Eq. 2.3, (p. 3) we ignored the processes of monochromatic scattering of photons such as Rayleigh scattering or scattering due to aerosol particles which can be important for certain atomic transitions and some molecular near-infrared bands in planetary atmospheres. Finally, the total source function is then

$$S_\nu = \frac{\eta(\nu)}{\chi(\nu)}.\tag{2.6}$$

The radiative rate coefficients in SEE Eq. 2.1, (p. 3) are given by

$$R_{ll'} = A_{ll'} + B_{ll'} \bar{J}_{ll'}\tag{2.7}$$

for both $l > l'$ and $l < l'$ (since in latter case $A_{ll'} \equiv 0$), where $\bar{J}_{ll'} (= \bar{J}_{l'l})$ is the integrated mean intensity, defined by

$$\bar{J}_{ll'} = \frac{1}{4\pi} \int d\Omega \int d\nu \varphi_{ll'}(\nu) I_{\mu\nu}.\tag{2.8}$$

C_l^- in Eq. 2.1, (p. 3) describes the total loss rate for the level l (per its unit population) due to collisionally induced energy transfer processes. It is written as

$$C_l^- = \sum_{l'} C_{ll'} + \sum_{l', \ell, \ell'} n_\ell C_{ll', \ell \ell'}.\tag{2.9}$$

The first term here defines the rate of electronic–vibration–rotational energy transfer to the translational energy (EVR–T). In it

$$C_{ll'} = \sum_{\beta} n^\beta k_{ll'}^\beta,\tag{2.10}$$

where $k_{ll'}^\beta$ are rate constants for EVR–T transition $l \rightarrow l'$ by the collisions with molecules or atoms of β -constituent of gas mixture with total density n^β .

The second term in Eq. 2.9, (p. 4) describes the loss rate of level l via the processes of EVR–EVR energy exchange. There $C_{ll', \ell \ell'}$ are rate coefficients for the transitions $l \rightarrow l'$ in one and the transitions $\ell \rightarrow \ell'$ in another of two colliding molecules and/or atoms.

Accounting for Eq. 2.9, (p. 4), we can write the term C_l^- in the right-hand side of Eq. 2.1, (p. 3) as

$$C_l^- = \sum_{l'} n_{l'} C_{l'l} + \sum_{l', \ell, \ell'} n_{l'} n_{\ell'} C_{l'l, \ell \ell'}.\tag{2.11}$$

The collisional rate coefficients in Eq. 2.9, (p. 4)-Eq. 2.11, (p. 4) are related by the obvious detailed balance expressions

$$n_l^* C_{ll'} = n_{l'}^* C_{l'l} \quad \text{and} \quad n_l^* n_{\ell'}^* C_{ll', \ell \ell'} = n_{l'}^* n_{\ell}^* C_{l'l, \ell \ell'},\tag{2.12}$$

where n_i^* are the LTE populations.

Since the RTE Eq. 2.2, (p. 3) relates the radiation field at a given height to the level populations at *all altitudes* in the atmosphere, the SEE system Eq. 2.1, (p. 3) for the level populations is *nonlocal* (and nonlinear). While the total densities n^β of all constituents are assumed to be known, the

coefficients Eq. 2.10, (p. 4) do not introduce non-linearity in SEE. However, the additional (local) non-linearity enters SEE through the second terms in C_l^+ and C_l^- which deal with the processes of EVR-EVR energy exchange.

The non-LTE problem for the gas in the planetary atmosphere formulated above is aimed at utmost detailed description of molecular bands. In the majority of applications those are infra-red or near-infrared bands related to vibrational levels of electronic ground states of molecules. Also some electronically excited atoms produced in the photo-chemical reaction are usually involved due to the importance of collisional transfer of electronic energy to molecular vibrations. The number of these atomic states is limited. However, the total number of levels in the problem can be very large (up to a few thousands) because of the large number of rotational sublevels of vibrational levels required to be accounted for the adequate description of bands.

Now let us look in more detail at several special steady states of the gas. We will follow here the discussions by *Ivanov* (84) and *Mihalas* (139) of similar situations for an atomic gas in the astrophysical context.

2.2 Complete thermodynamic equilibrium (CTE)

In this state the velocity distribution of molecules is Maxwellian, the level populations obey the Boltzmann law

$$\frac{n_{l'}}{n_l} = \frac{g_{l'}}{g_l} \exp\left(-\frac{E_{l'} - E_l}{kT}\right) \quad (2.13)$$

and the radiation intensity is isotropic, unpolarised, homogenous and is given by the Planck function. Only one parameter - the temperature T - completely determines this state. Moreover, in CTE all processes obey the principle of detailed balance: each process is exactly compensated by its inverse. In particular, the number of radiative transitions from an upper level l to a lower level l' then is equal to the number of $l' \rightarrow l$ radiative excitations

$$n_l(A_{ll'} + B_{l,l'}\bar{J}_{ll'}) = n_{l'}B_{l'l}\bar{J}_{ll'}. \quad (2.14)$$

Here $\bar{J}_{ll'}$ is the radiative mean intensity at the line center frequency $\nu_{ll'}$

$$h\nu_{ll'} = E_{l'} - E_l. \quad (2.15)$$

It follows from Eq. 2.13, (p. 5) and Eq. 2.14, (p. 5) that

$$\bar{J}_{ll'} = B_{\nu_{ll'}}(T) = 2hc\nu_{ll'}^3 \left[\exp\left(\frac{h\nu_{ll'}}{kT}\right) - 1 \right]^{-1} \quad (2.16)$$

is also the Planck function.

For collisional transitions the detailed balance relation has the form

$$n_{l'}C_{l'l} = n_lC_{ll'}, \quad (2.17)$$

or with the accounting for Eq. 2.13, (p. 5)

$$C_{l'l} = C_{ll'} \frac{g_l}{g_{l'}} \exp\left(-\frac{E_l - E_{l'}}{kT}\right). \quad (2.18)$$

2.3 Local thermodynamic equilibrium (LTE)

We now assume the gas considered consists of molecules and will limit our discussion to only rotational and vibrational excitation. The generalization to electronic excitation as well as to other types of molecules is straightforward.

We now assume that the index l corresponds to the pair of indices vj , which specify the ro-vibrational state of molecule; here v and j are the indices of a vibrational level and its rotational sub-level, respectively. For a triatomic linear molecule, for instance, v represents the combination of four indices $v_1v_2v_3$ specifying the vibrational state, therefore the sums over this index in our treatment imply summation over all available combinations of these four indices.

LTE is the state of the gas in which the velocity distribution of molecules is Maxwellian, populations follow the Boltzmann distribution, while the radiation intensity is not, in general, given by Planck function. Such a state can exist when both radiative and external source terms in the SEE are small in comparison to the collisional terms. If the velocity distribution of all molecules is Maxwellian then the detailed balance relations Eq. 2.17, (p. 5) are still valid. If one now neglects all radiative terms as well as the source terms in the SEE, these equations reduce to the Boltzmann law. Since these equations are linear in the quantities n_{vj} , the equilibrium populations are in fact the only solution. The temperature in the Boltzmann relation may now change from point to point. A Maxwellian gas is also in LTE in those layers where the external source terms in the SEE are small compared to collisional terms and the radiative terms dominate the collisional terms but cancel each other according to the relations (Eq. 2.14, (p. 5)). This occurs, for instance, for optically thick transitions in deep atmospheric layers.

Let us now introduce the population probability W_{vj} of a ro-vibrational level vj of a specific molecular specie α , such that

$$W_{vj} = \frac{n_{vj}}{n^\alpha}, \quad (2.19)$$

where n^α is the number density of specie in question. All the LTE values later on will be marked with the star symbol (*). Accounting for the Boltzmann relation (Eq. 2.13, (p. 5)) one can easily derive that

$$W_{vj}^* = \frac{g_{vj}}{Q^*(T)} \exp\left(-\frac{E_{vj}}{kT}\right), \quad (2.20)$$

where

$$Q^*(T) = \sum_{vj} g_{vj} \exp\left(-\frac{E_{vj}}{kT}\right) \quad (2.21)$$

is the total ro-vibrational internal sum, so that

$$\sum_{vj} W_{vj}^* = 1. \quad (2.22)$$

One can also introduce the probability W_v that the molecule is in the vibrational state v

$$n_v = \sum_j n_{vj} = n^\alpha W_v, \quad (2.23)$$

where n_v is the population of vibrational level v . Deriving the expression for W_v two facts should be considered

1. the energy of the ro-vibrational level may be expressed as the sum

$$E_{vj} = E_v + E_{j,v} \quad (2.24)$$

of the vibrational energy E_v of state v and the rotational energy $E_{j,v}$,

2. the statistical weight of the ro-vibrational level is the product

$$g_{vj} = g_v g_v(j) \quad (2.25)$$

of the statistical weight g_v of vibrational level v and the degeneracy $g_v(j)$ of its rotational sublevel j .

Accounting for Eq. 2.20, (p. 6), Eq. 2.21, (p. 6), Eq. 2.24, (p. 6) and Eq. 2.25, (p. 6) one can derive that

$$W_v^* = g_v \frac{Q_v^*(T)}{Q^*(T)} \exp\left(-\frac{E_v}{kT}\right), \quad (2.26)$$

where

$$Q_v^*(T) = \sum_j g_v(j) \exp\left(-\frac{E_{j,v}}{kT}\right) \quad (2.27)$$

is the rotational partition sum for the vibrational level v . Finally, introducing the population probability

$$W_v^*(j) = \frac{g_v(j)}{Q_v^*(T)} \exp\left(-\frac{E_{j,v}}{kT}\right) \quad (2.28)$$

of the rotational sublevel j of level v , one may rewrite Eq. 2.20, (p. 6) as

$$W_{vj}^* = W_v^* W_v^*(j). \quad (2.29)$$

It follows from Eq. 2.23, (p. 6) and Eq. 2.26, (p. 7) that the LTE populations of two vibrational levels v and v' are related as

$$\frac{n_{v'}^*}{n_v^*} = \frac{W_{v'}^*}{W_v^*} = \frac{g_{v'}}{g_v} \exp\left(-\frac{E_{v'} - E_v}{kT}\right) \frac{Q_{v'}^*(T)}{Q_v^*(T)}. \quad (2.30)$$

2.4 Partial LTE

The gas is said to be in a non-LTE state when the level populations do deviate from the Boltzmann law while the molecular velocity distribution remains Maxwellian. One may describe this state with the same probability formalism as was used above for the case of LTE by introducing at each point a set of excitation temperatures instead of the one parameter T .

The complete LTE or non-LTE are hardly ever encountered in planetary atmospheres. In reality the gas is mainly in a state that might be called *partial LTE* in which the velocity distribution of molecules is Maxwellian but only some groups of levels obey the Boltzmann relation (Eq. 2.13, (p. 5)). If one considers a certain volume of gas and traces its state as the density decreases, then generally one will observe a series of the partial LTE states, in which ever fewer levels follow the Boltzmann relation. Two such states are discussed, which are of special importance.

2.4.1 Rotational LTE

If the gas density is relatively high, the collisional processes dominate the excitation of molecules and the level populations are in LTE. As the density decreases the most highly excited vibrational levels are the first to depart from the Boltzmann law. This occurs since $V - T$ and $V - V$ collisional processes are no longer able to maintain the coupling of these levels with the thermalized levels against the influence of non-Planckian radiative transitions. As the density decreases further, departures occur for ever lower vibrational levels. However, within a wide range of densities the collisional processes between the rotational levels ($R - T$) can still keep the rotational substructure of all vibrational levels thermalized. This state of the gas may be described by means of probabilities as follows

$$W_{vj} = W_v W_v^*(j). \quad (2.31)$$

Here $W_v^*(j)$ is still given by Eq. 2.28, (p. 7), while W_v has now the form

$$W_v = g_v \frac{Q_v^*(T)}{Q} \exp\left(-\frac{E_v}{kT_v}\right) \quad (2.32)$$

with $T_v = T$ for vibrational levels which remain in the equilibrium and with $T_v \neq T$ for those which do not. Q , which replaces Q^* in Eq. 2.32, (p. 7), is the total internal sum

$$Q = \sum_v g_v \exp\left(-\frac{E_v}{kT_v}\right) Q_v^*(T) \quad (2.33)$$

and is no longer a function of a single parameter T .

The state of the gas described above is a typical example of a partial LTE state and is usually called vibrational non-LTE with an assumption that the rotational substructure of all vibrational levels is thermalized, i.e. is in rotational LTE. Since the $W_v^*(j)$ are known for each vibrational level v , then only the populations n_v are to be found, thus reducing greatly the number of unknown variables. The corresponding SEE is the sum over j of the Eq. 2.1, (p. 3). Since transitions between the sublevels j of vibrational level v can not change the total population of this level n_v , the sums of corresponding terms in Eq. 2.1, (p. 3) cancel. Then, accounting for Eq. 2.31, (p. 7), instead of the system Eq. 2.1, (p. 3), one obtains

$$n_v \left(\sum_{v'} R_{vv'} + C_v^- \right) = \sum_{v'} n_{v'} R_{v'v} + C_v^- + Y_v. \quad (2.34)$$

Here

$$R_{vv'} = \sum_{j,j'} W_v^*(j) R_{vj,v'j'} = A_{vv'}(T) + B_{vv'}(T) \bar{J}_{vv'}, \quad (2.35)$$

$$A_{vv'}(T) = \sum_{j,j'} W_v^*(j) A_{vj,v'j'} \quad (2.36)$$

is the de-excitation rate per molecule in the vibrational state v for spontaneous emission in the ro-vibrational band $v \rightarrow v'$ (for $v < v'$ $A_{vv'} \equiv 0$); $B_{vv'}(T)$ and $B_{v'v}(T)$ are related to $A_{vv'}(T)$ by expressions

$$A_{vv'} = 2hc\nu_{vv'}^3 B_{vv'}, \quad g_v B_{vv'} = g_{v'} B_{v'v}; \quad (2.37)$$

where $\nu_{vv'}$, defined as

$$h\nu_{vv'} = E_v - E_{v'} \quad (2.38)$$

is the frequency of vibrational transition; $B_{vv'} \bar{J}_{vv'}$ is the de-excitation (stimulated emission) or excitation (absorption) rate for the ro-vibrational band $v \rightarrow v'$ per molecule in state v ; the terms C_v^- and $C_{v'}^-$ have the same structure as the corresponding terms in Eq. 2.1, (p. 3), however involve vibrational populations and collisional rate coefficients for V-T transitions between vibrational levels

$$C_{vv'}(T) = \sum_{j,j'} W_v^*(j) C_{vj,v'j'} \quad (2.39)$$

and rates of V-V transitions (see detailed discussion of these terms in Section 3.5 (p. 15))

$\bar{J}_{vv'}$ in Eq. 2.35, (p. 8) has the form

$$\bar{J}_{vv'} = \frac{1}{B_{vv'}} \sum_{j,j'} W_v^*(j) B_{vj,v'j'} \bar{J}_{vj,v'j'}. \quad (2.40)$$

It replaces $\bar{J}_{ll'}$ in similar expression (Eq. 2.7, (p. 4)) for the radiative rate coefficients for a single line and has, therefore, the meaning of the integrated mean intensity in the ro-vibrational band.

Note that Eq. 2.34, (p. 8) for vibrational level populations have the same form as Eq. 2.1, (p. 3) for the ro-vibrational populations in which the integrated mean intensities for single lines $\bar{J}_{ll'}$, Eq. 2.8, (p. 4) are replaced by $\bar{J}_{vv'}$ for bands and where $A_{vv'}(T)$ and $B_{vv'}(T)$ enter as the effective (temperature dependent) Einstein coefficients for vibrational transitions. This temperature dependence results from summation the temperature independent coefficients $A_{vj,v'j'}$ for ro-vibrational transitions with the temperature dependent weighting function $W_v^*(j)$, Eq. 2.28, (p. 7).

The detailed balance relation for $C_{vv'}$ is now

$$\frac{C_{vv'}}{C_{v'v}} = \frac{g_{v'}}{g_v} \exp\left(-\frac{E_{v'} - E_v}{kT}\right) \frac{Q_{v'}^*(T)}{Q_v^*(T)}, \quad (2.41)$$

which one obtains by summing the detailed balance relation Eq. 2.12, (p. 4) for ro-vibrational transitions and accounting for Eq. 2.29, (p. 7).

Rotational LTE for vibrational levels of a ro-vibrational band is rather similar to the case of complete frequency redistribution in a single line. In the latter case the frequency of the emitted photon is not correlated with that of the absorbed photon. As a result, the line absorption and emission profiles coincide. Similarly, in the case of rotational LTE, the molecule “forgets” the rotational level to which it was excited, so there is no correlation between the lines in which the photon was absorbed and subsequently emitted. This “forgetting” is caused by collisions which the molecule undergoes during its radiative lifetime; in rotational LTE these are frequent enough to keep the rotational structure of the vibrational levels thermalized. In other words, rotational LTE provides an efficient additional large scale (compared to redistribution in a single line) frequency redistribution mechanism, in which photons absorbed in optically thick lines in the cores of band branches may be emitted in weak lines in the band wings.

It is worth noticing here that assumption of rotational LTE is the standard one in the majority of applications since rotation–translational (R–T) collisional processes keep the rotational substructure of all vibrational levels thermalized within a wide range of densities in the planetary atmospheres. Moreover, the temperature dependences of $A_{vv'}$ (T) and $g_l(T)/g_{l'}$ (T), which are rather weak for the atmospheric temperature range, are usually ignored. Nevertheless, the Einstein coefficients of ro-vibrational lines, energies of ro-vibrational levels, etc, required for an exact treatment are available (see, for instance HITRAN and other databases). This is not true for collisional rate coefficients. The majority of the data available from experimental and theoretical studies are rate coefficients for transitions between vibrational levels or vibrational and electronic levels which were obtained neglecting the initial and final rotational states. Therefore, only a few publications dealt with the rotational non-LTE at selected vibrational levels of certain molecules (see, for instance the paper by *Kutepov et al.*(99)).

2.4.2 Vibrational LTE in groups of levels

Another typical state of partial LTE occurs when vibrational levels are closely spaced in energy and, although out of equilibrium ensemble, are however in equilibrium with each other. It happens since the rate coefficients of the intramolecular $V - V$ energy exchange between these levels are usually a few orders of magnitude larger than those for $V - T$ exchange, so even if the density is low, collisional processes are able to keep these levels in equilibrium at the local temperature. For a pair of such levels one may write a Boltzmann ratio

$$\begin{aligned} \frac{n_{v'}}{n_v} &= \frac{W_{v'}}{W_v} = \frac{g_{v'}}{g_v} \exp \left[- \left(\frac{E_{v'}}{kT_{v'}} - \frac{E_v}{kT_v} \right) \right] \frac{Q_{v'}^*(T)}{Q_v^*(T)} \\ &= \frac{g_{v'}}{g_v} \exp \left[- \left(\frac{E_{v'} - E_v}{kT} \right) \right] \frac{Q_{v'}^*(T)}{Q_v^*(T)} \end{aligned} \quad (2.42)$$

which also establishes a relation between T_v , $T_{v'}$ and T .

One can proceed further and describe a group of such levels in the framework of a probability formalism as a complex vibrational level V having a few sublevels s . One can assign to this complex level some value of vibrational energy E_V (for instance, equal to the energy of the lower vibrational level or to some average value) and some statistical weight g_V . Each vibrational level v in this group now acquires a pair of indices Vs . As in our consideration of the rotational substructure of a single vibrational level one can express within this complex vibrational level the vibrational energy E_{Vs} and the statistical weight g_{Vs} of each sublevel as

$$E_{Vs} = E_V + E_{s,V}; \quad g_{Vs} = g_V g_V(s) \quad (2.43)$$

Then the probability $W(V)$ of vibrational population for such a complex level will be still given by Eq. 2.32, (p. 7),

$$W(V) = g_V \frac{Q_V^*(T)}{Q} \exp \left(- \frac{E_V}{kT_V} \right) \quad (2.44)$$

with $Q_v^*(T)$ replaced by the ro-vibrational partition function

$$Q_V^*(T) = \sum_s g_V(s) \exp\left(-\frac{E_{s,V}}{kT}\right) Q_{V_s}^*(T) \quad (2.45)$$

for the complex level V , where $Q_{V_s}^*(T)$ are the rotational partition functions (Eq. 2.27, (p. 7)) for the vibrational sublevels. T_V in Eq. 2.44, (p. 9) is now the vibrational temperature associated with the complex level V . It will coincide with T if all sublevels of the complex level belong to the equilibrium ensemble of vibrational levels and will differ from it if some (at least one) of sublevels are out of this ensemble. Subsequently the probability $W_V^*(s)$ of population of the vibrational sublevel s is expressed by

$$W_V^*(s) = \frac{g_V(s)}{Q_V^*} \exp\left(-\frac{E_{s,V}}{kT}\right). \quad (2.46)$$

Consequently the population probability of the ro-vibrational level vj , where v denotes the vibrational level which is considered as a sublevel s of a complex thermalized vibrational level V , (i.e. Vs is equivalent to v), could be expressed as

$$W_{vj} = W_v W_v^*(j) = W(V) W_V^*(s) W_{V_s}^*(j). \quad (2.47)$$

Because $W_v^*(j) = W_{V_s}^*(j)$, the relation between T_v , T_V and T follows from equating W_v to $W_V W_V^*(v)$. Since for each of these LTE groups of vibrational levels one needs to find only its total population

$$n_V = \sum_s n_{V_s}, \quad (2.48)$$

the dimension of the SEE system (Eq. 2.34, (p. 8)) may be reduced once more as in the case of rotational LTE by summing equations (Eq. 2.34, (p. 8)) over v within each group. Again, as radiative and collisional transitions between levels of the group do not effect its total population, the corresponding terms cancel. The new system of equations for the populations of level groups (the group may obviously consist of a single level as well) will look identical to the system (Eq. 2.34, (p. 8)). However its dimension $L' = L - M + G$ is smaller : here L is the total number of vibrational levels considered, M is the number of vibrational levels in the LTE groups and G is the number of these groups.

2.5 Ro-vibrational non-LTE

At still lower densities rotational LTE breaks down. This occurs first for the higher vibrational levels whose radiative lifetimes are too short for collisions to thermalize their rotational structure. Rotational LTE for a given vibrational level fails first for rotational sublevels with large j since they become easily uncoupled from the ensemble of thermalized sublevels. As the density decreases further, more and more sublevels down to small values of j and more and more vibrational levels down to lower vibrational energies depart from equilibrium. The gas is approaching a state which may be called total ro-vibrational non-LTE. In order to describe it one may use the relation (Eq. 2.31, (p. 7)), where $W_v^*(j)$ is replaced by

$$w_v(j) = \frac{g_v(j)}{Q_v} \exp\left(-\frac{E_{j,v}}{kT_{j,v}}\right). \quad (2.49)$$

Here $T_{j,v}$ is the rotational temperature of the rotational sublevel j of vibrational level v ; $T_{j,v}$ is equal to T for thermalized sublevels and differs from T for those which are out of the thermalized ensemble. The rotational partition function Q_v in Eq. 2.49, (p. 10) is given now by the sum

$$Q_v = \sum_j g_v(j) \exp\left(-\frac{E_{j,v}}{kT_{j,v}}\right) \quad (2.50)$$

which no longer depends on the single parameter T .

3. Methods of solution of the non-LTE problem (current status)

The radiative rate coefficients in the SEE (Eq. 2.1, (p. 3)) or (Eq. 2.34, (p. 8)) make them not only nonlinear but also nonlocal, as the integrated mean intensities $\bar{J}_{ll'}$ are determined by the level populations at all altitudes in the atmosphere. In addition, molecular collisions introduce a local nonlinearity as their rates often depend on certain level populations. These features appear to demand an iterative solution.

In this section we will consider in detail three approaches which handle the nonlocality and nonlinearity arising from the radiative rate coefficients, namely lambda iteration, the matrix technique and accelerated (or approximate) lambda iteration. Later we will discuss ways of treating the local nonlinearity coming from the collisional and chemical rate coefficients. The techniques described below avoid linearizing the problem in small variations of populations and iterating.

3.1 Lambda iteration

The most obvious way of solving the problem specified by Eq. 2.1, (p. 3) or Eq. 2.34, (p. 8) is to iterate between the SEE and the RTE. This process is traditionally called “lambda iteration”.

The integrated mean intensity (Eq. 2.8, (p. 4)) is defined with the help of lambda operator as

$$\bar{J}_{ll'} = \int_{\Omega} d\Omega \int_0^{+\infty} \Lambda_{\mu\nu} S_{\nu} \varphi_{ll'}(\nu) d\nu. \quad (3.1)$$

In “lambda iteration” the new populations are found from the solution of the SEE

$$n_l \sum_{l'} (R_{ll'}^{\dagger} + C_{ll'}) = \sum_{l'} n_{l'} (R_{l'l}^{\dagger} + C_{l'l}) + Y_l, \quad (3.2)$$

in which the radiative rate coefficients are evaluated from the populations given by the previous iteration,

$$R_{ll'}^{\dagger} = A_{ll'} + B_{ll'} \bar{J}_{ll'}^{\dagger} \quad (3.3)$$

where

$$\bar{J}_{ll'}^{\dagger} = \int_{\Omega} d\Omega \int_0^{+\infty} \Lambda_{\mu\nu}^{\dagger} S_{\nu}^{\dagger} \varphi_{ll'}(\nu) d\nu. \quad (3.4)$$

In these expressions a dagger (\dagger) denotes quantities evaluated using “old” variables, from the previous iteration. We assume for the time being that the collisional rate coefficients and source terms do not vary in the course of iteration. In this way the nonlinearity from the collisional rate coefficients is avoided.

“Lambda iteration” has been investigated in detail in the astronomical context since the 1920’s (see *Unsöld* (206)). It is attractive as it involves matrices no larger than $L \times L$, where L is the total number of molecular levels, and is actually a numerical simulation of the process of multiple scattering of photons in lines and bands. Unfortunately, if for some transitions the atmosphere is optically thick, the photons can be effectively trapped in cores of optically thick lines. Thus the number of scattering and correspondingly the number of iterations before the final state is reached may be very large. Convergence rate can be so slow that false solutions appear to be stable, or the accumulation of numerical errors will cause the process to diverge.

3.2 Matrix method

An alternative way of solving non-LTE problems is to treat the SEE and RTE simultaneously, discretizing the RTE with respect to an optical depth or pressure grid to get a matrix representation of

the radiative terms in the SEE. Here, we consider only the case in which the lines do not overlap. A generalization including line overlap will be outlined below.

If a single line does not overlap other lines or continua the RTE is

$$\mu \frac{dI_{\mu\nu}}{dz} = -\chi_{l'l'}(\nu)I_{\mu\nu} + \eta_{l'l'}(\nu) = -\chi_{l'l'}(\nu)(I_{\mu\nu} - S_{l'l'}), \quad (3.5)$$

where η , χ and S are defined by Eq. 2.3, (p. 3) and Eq. 2.4, (p. 3), respectively. The formal solution of this equation takes the form

$$I_{\mu\nu} = \Lambda_{\mu\nu}[S_{l'l'}], \quad (3.6)$$

and the integrated mean intensity may be written as

$$\bar{J}_{l'l} = \Lambda_{l'l}[S_{l'l'}] = \Lambda_{l'l} \left[\frac{n_l A_{l'l'}}{n_{l'} B_{l'l} - n_l B_{l'l'}} \right] = \tilde{\Lambda}_{l'l}[n_l], \quad (3.7)$$

where $\Lambda_{l'l}$ is obtained from $\Lambda_{\mu\nu}$ by the operator $\int d\Omega \int d\nu \varphi_{l'l'}(\nu) \dots$. The relation between $\Lambda_{l'l}$ and $\tilde{\Lambda}_{l'l}$ is obvious.

In lambda iteration the non-local radiative terms at each iteration step are calculated using the populations obtained in previous step. This makes the equations at each step linear, so the non-local problem is solved as a sequence of local linear problems for each altitude point in the atmosphere. From this point of view matrix methods utilize the opposite strategy: the non-local radiative terms are considered as unknown and expressed in terms of populations. The problem is then solved *iteratively* as a sequence of non-local linear problems.

In any matrix method the integral operators $\Lambda_{l'l}$ or $\tilde{\Lambda}_{l'l}$ are discretized on some depth or pressure grid and replaced by matrices using one or another standard technique. For instance, S or n in the integrals (Eq. 3.7, (p. 12)) are replaced by a step-functions for some set of layers in the atmosphere. The integrals are replaced by the matrix expressions $\bar{\mathbf{J}}_{l'l} = \tilde{\Lambda}_{l'l} \mathbf{n}_l$, where \mathbf{n}_l is a vector of dimension D and $\tilde{\Lambda}_{l'l}$ is a matrix of dimension $D \times D$. In order to make the SEE (Eq. 2.1, (p. 3)) linear at each iteration step, the terms $n_l \bar{J}_{l'l}$ which represent stimulated emission are replaced by $n_l \bar{J}_{l'l}^\dagger$, whereas the absorption terms are replaced by $\mathbf{n}_l^\dagger \tilde{\Lambda}_{l'l}^\dagger \mathbf{n}_l$. In the latter case \mathbf{n}_l^\dagger is a diagonal matrix acting on the vector $\bar{\mathbf{J}}_{l'l}$. Instead of D systems of equations (Eq. 2.1, (p. 3)) of dimension $L \times L$ we now obtain a large system of equations of dimension $(L \times D) \times (L \times D)$

$$\sum_{l'} \tilde{\mathbf{R}}_{l'l}^\dagger \mathbf{n}_{l'} = \mathbf{Y}_l, \quad (3.8)$$

where

$$\tilde{\mathbf{R}}_{l'l}^\dagger = \begin{cases} -(\mathbf{R}_{l'l}^\dagger + \mathbf{C}_{l'l}) + B_{l'l} \mathbf{n}_l^\dagger \tilde{\Lambda}_{l'l}^\dagger & l' > l \\ -\mathbf{C}_{l'l} & l' < l \end{cases} \quad (3.9)$$

$$\tilde{\mathbf{R}}_{l'l}^\dagger = -(\sum_{l' \neq l} \tilde{\mathbf{R}}_{l'l}^\dagger).$$

In these expressions $\mathbf{R}_{l'l}^\dagger$ are the diagonal matrices with elements $R_{l'l}^\dagger = A_{l'l} + B_{l'l} \bar{J}_{l'l}^\dagger$, $\mathbf{C}_{l'l}$ are the diagonal matrices of collisional rate coefficients, \mathbf{P}_l is the vector of sources and a dagger as usual denotes quantities evaluated using variables from the previous iteration.

In the matrix algorithm outlined here the level populations are the unknown variables. In order to construct the system matrix we used a discrete matrix representation of the lambda operators $\Lambda_{l'l}$ (or $\tilde{\Lambda}_{l'l}$). In the so called Curtis-matrix method (see *Goody* (63)), the lambda matrices are replaced by the Curtis-matrices which relate the radiative flux divergences $\mathcal{H}_{l'l}$ in lines or bands to the source functions. The relation between the Curtis and lambda matrices is found by writing $\mathcal{H}_{l'l}$ in terms of both $\Lambda_{l'l}$ and $\mathcal{C}_{l'l}$

$$\begin{aligned} \mathcal{H}_{l'l} &= \int_{\Omega} d\Omega \int \mu \frac{dI_{\mu\nu}}{dz} d\nu = \\ &= \bar{\chi}_{l'l}(\bar{J}_{l'l} - S_{l'l}) = \bar{\chi}_{l'l}(\Lambda_{l'l}[S_{l'l}] - S_{l'l}) = \mathcal{C}_{l'l}[S_{l'l}], \end{aligned} \quad (3.10)$$

where

$$\bar{\chi}_{l'l'} = \frac{h\nu_{l'l'}}{4\pi} (n_{l'} B_{l'l} - n_l B_{l'l'}) \quad (3.11)$$

is the frequency integrated opacity $\chi_{l'l'}(\nu)$, Eq. 2.3, (p. 3). Therefore, the SEE (Eq. 3.8, (p. 12)) may be rewritten in terms of Curtis matrices $\mathcal{C}_{l'l'}$.

The matrix approach described here for non-overlapping lines can be easily generalized to include overlapping. It is only necessary to write the total source function S_ν , Eq. 2.6, (p. 4) as

$$S_\nu = \sum_{l>l'} \frac{\vartheta_{l'l'}(\nu)}{\chi(\nu)} n_l + S_c(\nu), \quad (3.12)$$

where the sum includes all combinations $l < l'$ which are active at frequency ν . Here

$$\vartheta_{l'l'}(\nu) = \frac{h\nu_{l'l'} A_{l'l'} \varphi_{l'l'}(\nu)}{4\pi \chi_{l'l'}(\nu)}$$

and $S_c(\nu) = \eta_c(\nu)/\chi(\nu)$ is the continuum source function. It follows from Eq. 3.1, (p. 11) that

$$\bar{J}_{l'l'} = \sum_{\ell>\ell'} \tilde{\Lambda}_{l'l',\ell\ell'} [n_\ell] + \bar{J}_{l'l',c}, \quad (3.13)$$

where $\Lambda_{l'l',\ell\ell'}$ are obtained from $\Lambda_{\mu\nu}$ by the operator $\int d\Omega \int d\nu \varphi_{l'l'}(\nu) \dots \vartheta_{\ell\ell'}(\nu)$ and $\bar{J}_{l'l',c}$ is the contribution of the continuum emission to the total integrated mean intensity. The latter is obtained by replacing in Eq. 3.1, (p. 11) the total source function S_ν by the continuum source function $S_{\nu,c}$. If one now replaces the absorption terms $\mathbf{n}_l \bar{J}_{l'l'}$ in the SEE (Eq. 2.1, (p. 3)) by the sums

$$\sum_{\ell>\ell'} \tilde{\Lambda}_{l'l',\ell\ell'}^\dagger \mathbf{n}_\ell + \bar{J}_{l'l',c}^\dagger \quad (3.14)$$

one again obtains the system (Eq. 3.8, (p. 12)), where the matrices (Eq. 3.9, (p. 12)) now have a somewhat different structure.

3.3 Comparison of lambda iteration and matrix method

Let us now compare lambda iteration with an iterative process which utilizes the matrix equation (Eq. 3.8, (p. 12)). In the first case the iteration proceed as following:

1. The initial populations n_l^\dagger are chosen, for instance, LTE populations.
2. The RTE is solved, the mean intensities $\bar{J}_{l'l'}^\dagger$ at all D altitude grid points are calculated and the radiative rate coefficients $R_{l'l'}$ are determined.
3. The sequence of D system of equations (Eq. 3.2, (p. 11)) is solved and new populations n_l at all grid points are obtained. As each iteration requires inversion of D matrices with dimension $L \times L$, the number of operations, and consequently the computer time are proportional to DL^2 .

In the case of iteration using the matrix equations (Eq. 3.8, (p. 12)) steps (1) and (2) remain the same while step (3) is different. At this step a matrix of dimension $(L \times D) \times (L \times D)$ must be inverted, which requires time $\sim D^2 L^2$, i.e. a factor D larger than in the previous case. Therefore, from the point of view of time required, one "matrix iteration" is equivalent to about D lambda iterations. The advantage of the matrix method lies in the simultaneous determination of all populations at all altitudes instead of the sequential evaluation of the populations at using the radiative field from the previous iteration. Therefore, as a rule, "matrix iteration" converges very rapidly. However, if both L and D are large, each iteration is very expensive in computer time and memory; the same result is more quickly achieved with lambda iteration using significantly less storage. Nevertheless, for optically thick transitions lambda iteration may converge so slowly that the solution requires significantly more time than "matrix iteration". This difficulty is overcome in the accelerated lambda iteration techniques.

3.4 Accelerated lambda iteration

The family of accelerated lambda iteration (ALI) methods utilize iteration with an approximate (or accelerated) lambda operators (see for more details *Rybicki and Hummer (181; 182)*).

ALI methods are based on operator splitting of the form

$$\Lambda = \Lambda^* + (\Lambda - \Lambda^*), \quad (3.15)$$

where the choice of the approximate lambda operator Λ^* is discussed below. This approach leads to the iteration scheme

$$I_{\mu\nu} = \Lambda_{\mu\nu}^{*\dagger}[S_\nu] + (\Lambda_{\mu\nu}^\dagger - \Lambda_{\mu\nu}^{*\dagger})[S_\mu^\dagger] = \Lambda_{\mu\nu}^{*\dagger}[S_\nu] + I_{\mu\nu}^{\text{eff}\dagger}, \quad (3.16)$$

where

$$I_{\mu\nu}^{\text{eff}\dagger} = (\Lambda_{\mu\nu}^\dagger - \Lambda_{\mu\nu}^{*\dagger})[S_\nu^\dagger]. \quad (3.17)$$

Although this equation is only approximate at each stage of the iteration, it becomes exact for the converged solution, where $S_\nu^\dagger = S_\nu$, $\Lambda_{\mu\nu}^{*\dagger} = \Lambda_{\mu\nu}^*$ and $\Lambda_{\mu\nu}^\dagger = \Lambda_{\mu\nu}$.

The Eq. 3.16, (p. 14) describes a whole class of methods, each specified by the choice of a particular approximate lambda operator. One of the simplest choices is to use the diagonal part of the matrix representation of exact lambda operator. The principal advantage of the diagonal approximation is that SEE remain completely local, whereas more sophisticated approximations, such as the tridiagonal, make the equations non-local, which become harder to solve and may be more unstable. Nevertheless, tridiagonal operators may offer much faster convergence, and have been used successfully in a number of applications.

Eq. 3.16, (p. 14) gives $I_{\mu\nu}$ in terms of populations. It is important to note that S_ν^\dagger as well as the operators $\Lambda_{\mu\nu}^{*\dagger}$ and $\Lambda_{\mu\nu}^\dagger$ are constructed from the ‘‘old’’ populations. However the ‘‘new’’ populations are still present here through the source function S_ν . The direct implementation of this expression for the intensity in the radiative rate coefficients of the SEE will cause these equations to become nonlinear. The distinguishing feature of the ALI approach is that the linearity of the SEE is easily restored by ‘‘preconditioning’’. *Rybicki and Hummer (181; 182)* described several strategies for this procedure. For instance, ‘‘preconditioning within the same transition only’’, is designed to handle the case when lines do not overlap or the overlap is ‘‘weak’’ i.e. the cores of a few lines overlap, while for the remainder at most only wing overlap occurs. This leaves the form of the SEE (Eq. 2.1, (p. 3)) unchanged, while the radiative rate coefficients $R_{ll'}$ are replaced by

$$R_{ll'}^{\text{eff}} = A_{ll'}(1 - \bar{\Lambda}_{ll'}^{*\dagger}) + B_{ll'}\bar{J}_{ll'}^{\text{eff}\dagger}. \quad (3.18)$$

Here $\bar{\Lambda}_{ll'}^{*\dagger}$ and $\bar{J}_{ll'}^{\text{eff}\dagger}$ are obtained from $\Lambda_{\mu\nu}^{*\dagger}$ and $I_{\mu\nu}^{\text{eff}\dagger}$ by the operator $\text{int}d\Omega \int d\nu \varphi_{ll'}(\nu) \dots$. The conditioning of the SEE is improved because much of the transfer in the ‘‘core’’ of the line (described by the local part of the lambda operator) is canceled analytically. These preconditioned equations are still linear in the populations, notwithstanding the presence of stimulated emission terms. These modified equations automatically guarantee non-negative solutions for the new populations (see *Rybicki and Hummer (181; 182)* for details) and thus a stable iteration process.

It is worth noticing here that the SEE are linearly dependent. Therefore to solve the system (Eq. 2.1, (p. 3)) one of its equations for each specie replaced by the particle conservation equation. Thus the conservation law is built into the method and is enforced at every iteration.

This formalism has been presented as a method of solution for the general non-LTE problem, in which the system of equation (Eq. 2.1, (p. 3)) is solved for all molecular level populations. If only ro-vibrational excitation is involved, populations of all ro-vibrational levels are found. Additionally, if rotational LTE is valid, the radiative rate coefficients $R_{vv'}$ in the SEE (Eq. 2.34, (p. 8)) will be replaced by $R_{vv'}^{\text{eff}}$. These are obtained by summing $R_{vj,v'j'}^{\text{eff}}$, Eq. 3.18, (p. 14) over j and j' , as was done in deriving $R_{vv'}$, Eq. 2.35, (p. 8).

3.5 Treating the nonlinearity arising from collisions

Here we consider the nonlinearity due to $V - V$ energy transfer, limiting our attention to the case of rotational LTE, which corresponds to the SEE (Eq. 2.34, (p. 8)).

In the SEE (Eq. 2.34, (p. 8)) n_v are the vibrational level populations of one of the gases in the mixture. In a mixture consisting of several vibrationally excited molecular constituents coupled by $V - V$ energy exchange, the SEE (Eq. 2.34, (p. 8)) should have the form

$$n_v^\alpha \sum_{v'} \left(R_{vv'}^\alpha + C_{vv'}^{\alpha(V-T)} + \sum_{\beta, v'_\alpha, v'_\beta} n_v^\beta C_{v_\alpha v'_\alpha, v_\beta v'_\beta}^{\alpha, \beta(V-V)} + \sum_{\beta, v'_\alpha, v'_\beta} n_v^\beta C_{v_\alpha v'_\alpha, v_\beta v'_\beta}^{\alpha, \beta(C-V)} + \right) = \sum_{v'} n_{v'}^\alpha \left(R_{v'v}^\alpha + C_{v'v}^{\alpha(V-T)} + \sum_{\beta, v'_\alpha, v'_\beta} n_{v'}^\beta C_{v'_\alpha v_\alpha, v'_\beta v_\beta}^{\alpha, \beta(V-V)} + \sum_{\beta, v'_\alpha, v'_\beta} n_{v'}^\beta C_{v'_\alpha v_\alpha, v'_\beta v_\beta}^{\alpha, \beta(C-V)} + \right) + Y_{v'}^\alpha, \quad (3.19)$$

where the greek letters denote molecular species. Here $C_{v_\alpha v'_\alpha}^{\alpha(V-T)}$ are the total collisional rate coefficients for $V - T$ energy transfer for α -molecules

$$C_{v_\alpha v'_\alpha}^{\alpha(V-T)} = \sum_{\beta} n^\beta k_{v_\alpha v'_\alpha}^{\alpha, \beta}, \quad (3.20)$$

where $k_{v_\alpha v'_\alpha}^{\alpha, \beta}$ are rate constants for $V - T$ transition $v_\alpha \rightarrow v'_\alpha$ in the α -molecule by the collisions with β -molecules and n^β is total number density of β -molecules.

Since here the total number densities of all molecules is assumed to be known, the terms (Eq. 3.20, (p. 15)) do not cause nonlinearity, which enters only through the third terms on the left and right sides of Eq. 3.19, (p. 15) representing $V - V$ energy exchange. In these terms $C_{v_\alpha v'_\alpha, v_\beta v'_\beta}^{\alpha, \beta(V-V)}$ are the rate coefficients for the transitions $v_\alpha \rightarrow v'_\alpha$ in the α -molecules and the transitions $v_\beta \rightarrow v'_\beta$ in the β -molecules. These coefficients are related by the detailed balance expressions

$$W_{v_\alpha}^{*\alpha} W_{v_\beta}^{*\beta} C_{v_\alpha v'_\alpha, v_\beta v'_\beta}^{\alpha, \beta(V-V)} = W_{v'_\alpha}^{*\alpha} W_{v'_\beta}^{*\beta} C_{v'_\alpha v_\alpha, v'_\beta v_\beta}^{\alpha, \beta(V-V)} \quad (3.21)$$

or

$$\frac{C_{v_\alpha v'_\alpha, v_\beta v'_\beta}^{\alpha, \beta(V-V)}}{C_{v'_\alpha v_\alpha, v'_\beta v_\beta}^{\alpha, \beta(V-V)}} = \frac{g_{v'_\alpha} g_{v'_\beta} Q_{v'_\alpha}^*(T) Q_{v'_\beta}^*(T)}{g_{v_\alpha} g_{v_\beta} Q_{v_\alpha}^*(T) Q_{v_\beta}^*(T)} \times \exp\left(-\frac{E_{v'_\alpha} - E_{v_\alpha}}{kT}\right) \times \exp\left(-\frac{E_{v'_\beta} - E_{v_\beta}}{kT}\right).$$

The dimension $L \times L$ of the system (Eq. 3.19, (p. 15)), where $L = \sum_{\alpha} L^{\alpha}$ is now the total number of vibrational levels of M molecules considered, may be very large.

3.5.1 Straightforward iteration and "decoupling"

The first idea which usually comes to mind in attempting to solve the SEE Eq. 3.19, (p. 15) is that of iterating between different molecules. At each iteration one will solve for each molecule the SEE in which the $V - V$ collisional terms are estimated using the previous values of the vibrational level populations of all other molecules. By considering at each step a single molecular species one needs to invert only matrices of dimension $L^{\alpha} \times L^{\alpha}$ (instead of dimension $L \times L$). However, further thought shows that this strategy is ineffective, especially if quasi-resonant $V - V$ energy exchange occurs. This is easily seen in the simple case of two two-level molecules. In this case the SEE for α -molecule at the current iteration step has the form

$$n_2^\alpha (R_{21}^{\alpha\dagger} + C_{21}^{\alpha(V-T)}) + n_1^{\beta\dagger} C_{21,12}^{\alpha, \beta(V-V)} = n_1^\alpha (R_{12}^{\alpha\dagger} + C_{12}^{\alpha(V-T)}) + n_2^{\beta\dagger} C_{12,21}^{\alpha, \beta(V-V)} \quad (3.22)$$

or

$$S^\alpha = \frac{R_{12}^{\alpha\dagger} + C_{12}^{\alpha(V-T)} + n_1^{\beta\dagger} S^{\beta\dagger} C_{12,21}^{\alpha, \beta(V-V)}}{R_{21}^{\alpha\dagger} + C_{21}^{\alpha(V-T)} + n_1^{\beta\dagger} C_{21,12}^{\alpha, \beta(V-V)}}. \quad (3.23)$$

In the latter equation we have introduced $S^\alpha = n_2^\alpha/n_1^\alpha$ and $S^\beta = n_2^\beta/n_1^\beta$ and dropped for simplicity the source terms. The corresponding equations for the β -molecule are obtained by interchanging $\alpha \rightleftharpoons \beta$.

In the case of quasi-resonant $V - V$ energy exchange $C_{21,12}^{\alpha,\beta(V-V)}, C_{12,21}^{\alpha,\beta(V-V)} \gg 1$. We may assume that $C_{21,12}^{\alpha,\beta(V-V)} \approx C_{12,21}^{\alpha,\beta(V-V)}$, which follows from the balance relation (Eq. 3.22, (p. 15)) if $E_2^\alpha - E_1^\alpha \approx E_2^\beta - E_1^\beta$ (quasi-resonance) and $g_{v'_\alpha} g_{v'_\beta} Q_{v'_\alpha}^* Q_{v'_\beta}^* / g_{v_\alpha} g_{v_\beta} Q_{v_\alpha}^* Q_{v_\beta}^* \approx 1$. Since the corresponding terms dominate both the numerator and denominator of Eq. 3.23, (p. 15) and its analog for the β -molecule, both equations reduce to

$$S^\alpha \approx S^{\beta\dagger}, \quad S^\beta \approx S^{\alpha\dagger}. \quad (3.24)$$

As a result iteration between the α - and β -molecules often diverge or is instable. If convergence is still possible its rate will be extremely low.

The expression $S^\alpha \approx S^\beta$ which follows from Eq. 3.23, (p. 15) describes the case of source function equality for two bands whose levels are strongly collisionally coupled. A similar case of source function equality in atomic line doublets was investigated by *Avrett* (10). An efficient way to overcome the convergence problem outlined above is obvious: the populations n_2^α and n_2^β (or source functions S^α and S^β) should be found simultaneously. In doing this one assumes in both equations (Eq. 3.22, (p. 15)) that n_1^α and n_1^β are known from the previous iteration and solve this system for n_2^α and n_2^β . Both equations remain linear, however one may easily check that the loop (Eq. 3.24, (p. 16)) causing the transfer of errors from one iteration to another is broken. Although at each iteration one needs to solve the system of two equations, convergence is significantly improved.

This way of dealing with two two-level molecules remains valid for the problem (Eq. 3.19, (p. 15)) with an arbitrary number of multilevel molecules. Rather than iterating between molecules one should solve the entire system of equations for all molecules simultaneously: in the case of lambda iteration or the ALI approach, the system will have dimension $L \times L$ and must be solved at each depth grid level in the atmosphere. In the matrix method the complete system of equations for all altitude points having the very large dimension $(L \times D) \times (L \times D)$ must be solved. In both cases, the following recommendation for treating the nonlinear terms $\sim n_{v_\alpha}^\alpha n_{v_\beta}^\beta$ (α may also be equal to β) arising from $V - V$ coupling is suggested:

1. For the first iteration the population is taken as known of the level with smaller vibrational excitation.
2. For subsequent iterations the population which varied least rapidly during previous iterations should be selected.

In this case the matrix A^\dagger of the SEE to be solved

$$A^\dagger \mathbf{n} = \mathbf{Y} \quad (3.25)$$

is no longer the block-diagonal and, therefore, populations of all species need to be found simultaneously. However, the convergence is significantly improved and the total time required to solve the problem is reduced.

3.5.2 Newton-Raphson method

Another way of dealing with the local non-linearity of collisional terms tested was the standard Newton-Raphson method for the solution of system of non-linear equations.

In our case when non-linear terms of SEE include only products of two populations the Jacobi matrix A_J^\dagger is formed easily. We applied this method both at each iteration and allowing a few inner

iterations for populations to adjust to the radiative field. In both cases, however, this approach gives no convergence advantage compared to the “decoupling”: the convergence curves for it nearly overlap with those for “decoupling” algorithm except of a few first iterations.

We found the following explanation of this behavior of the Newton–Raphson algorithm. It solves SEE iteratively as

$$A_J^\dagger(\mathbf{n} - \mathbf{n}^\dagger) + A^\dagger \mathbf{n}^\dagger = Y \quad (3.26)$$

or

$$(A^\dagger + R^\dagger)\mathbf{n} = Y + R^\dagger \mathbf{n}^\dagger, \quad (3.27)$$

where the matrix $R = A_J - A$.

One can easily check that components of vectors $R\mathbf{n}$ in Eq. 3.27, (p. 17) are the differences

$$n_I n_\ell C_{I\ell', \ell\ell'} - n_{I'} n_{\ell'} C_{I'1, \ell'\ell}. \quad (3.28)$$

These differences are obviously small for lower altitudes where the situation is close to LTE (see detailed balances Eq. 2.12, (p. 4)). However, they remain small also for higher altitudes where the LTE is broken: due to the exponential decrease of density with the altitude collisional terms vanish compared to radiative terms. Taking this into account one may see that equations Eq. 3.25, (p. 16) and Eq. 3.27, (p. 17) are nearly identical, which results in the equal convergence rates of both iterative processes.

4. Comparison of methods used to solve non-LTE problem in atmospheric science

4.1 Comparison of the ALI and lambda iteration techniques

We investigated the convergence of a number of these schemes in solving the vibrational non-LTE problem for CO₂ in the Earth atmosphere for a few atmospheric models under both day and night conditions. For nighttime we confined ourselves mostly to a model in which CO₂ was represented with 9 vibrational levels and N₂ and O₂ each had two levels. The problem included therefore 13 vibrational levels of 3 molecules and 16 ro-vibrational bands. For the daytime we used a model similar to those applied by *López-Puertas et al.*(110; 112) and *Nebel et al.*(153). This model included $NL = 64$ vibrational levels of 5 CO₂ isotopes, two levels for each of N₂ and O₂ and 144 ro-vibrational bands. The absorption of solar radiation by the CO₂ bands in the 1–15 μm spectral region was taken into account. Rotational LTE was assumed. The spectroscopic parameters were taken from the HITRAN-96 database. The system of collisional reactions as well as the volume mixing ratio profile of CO₂ are those of *Shved et al.*(188). We used $D=61$ grid points with a constant step in the logarithm of the CO₂ column density, with the first point located at 180 km and the last one at the surface level (0 km). For the lower boundary a black body with the planet surface temperature was assumed. We used $NA = 4$ and $NF = 32$ points for integration over angle and frequency within a line, respectively.

The following iteration schemes were investigated:

1. Lambda iteration but without removing (as described in Section 3.5 (p. 15)) the local non-linearity caused by the $V - V$ exchange. This case is denoted as LI.
2. Lambda iteration including the local non-linearity due to the $V - V$ exchange but with an inner iteration loop to allow the populations to adjust to the radiative rates at a given iteration. We denote this case as LI+V (see *Vollmann* (210)). This scheme works as following:
 - (a) for given populations the radiative mean intensities are calculated and rate coefficients in the SEE (Eq. 3.2, (p. 11)) are determined and held fixed throughout the inner iteration cycle;
 - (b) at each pressure point the inner iteration proceeds as following:
 - i. for each molecule the collisional rate coefficients for $V - V$ exchange with other molecules (or with other levels of the same molecule) are fixed by setting all populations required equal to those from previous outside iteration
 - ii. the SEE are solved for one molecule after another and a new set of populations is obtained
 - iii. the collisional $V - V$ coefficients are updated using populations from step b and the SEE are solved again: the process is repeated to convergence
 - (c) a new outer iteration begins: populations obtained at all pressure points are used to update the radiative rate coefficients and so on.
3. Lambda iteration with the $V - V$ non-linearity treated according to Section 3.5 (p. 15). This case is denoted as LI+K, see *Kutepov et al.*(99) who suggested this treatment of the non-linearity.
4. As in case LI+V but replacing lambda iteration by the ALI approach. Now a rather different algorithm for the inner iteration is used to handle the local $V - V$ non-linearity, in that it uses R_{ij}^{eff} rather than R_{ij} . We denote this case as ALI+O, see *Ogibalov et al.*(160), who used this approach.

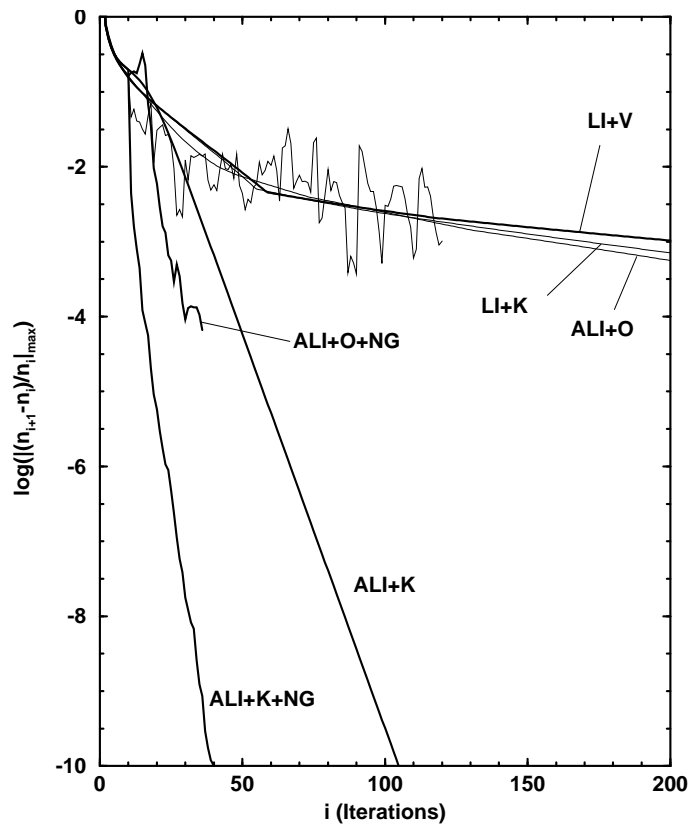


Fig. 4.1 Convergence plots for the 9-level CO_2 model of a spring equinox atmosphere at night. Logarithms of the maximum absolute relative change (MARC) are presented for the 00011 CO_2 level. Labels on the curves refer to various iteration schemes (LI, LI+V, etc); use of Ng's acceleration method indicated by (+NG).

5. ALI with the $V - V$ non-linearity treated according to Section 3.5 (p. 15). This case is denoted as ALI+K.
6. As in the previous case but using the convergence accelerating technique suggested by Ng (154) in a version described in Section E.1 (p. 107). We denote this case as ALI+K+NG.
7. As in case ALI+O but using Ng-acceleration for the outer iteration. The case is denoted as ALI+O+NG.

In Fig. 4.1 (p. 20) the logarithms of the maximum absolute relative change (MARC) in the CO_2 populations at all altitudes for successive iterations are plotted for the 9-level CO_2 model at night, for each iteration scheme considered. The spring equinox model of the atmosphere at latitude 40° generated by the MSISE-90 model was used. In all cases LTE populations were taken as the initial populations.

It is clear that both the LI and LI+V processes converge very slowly; in both cases at the 200th step a relative error of only about 10^{-3} is reached. There are two reasons for this slow convergence, namely trapping of photons in cores of the optically thick lines which is not eliminated in the ordinary LI algorithm and the strong local non-linearity due to $V - V$ coupling, which causes the errors to be propagated. Analyzing these cases we found that the maximum relative change in populations was always that for level 00011, which is the upper level of the most optically thick $4.3 \mu\text{m}$ fundamental transition and which simultaneously is efficiently coupled with the N_2 (1)-level by the near-resonant $V - V$ energy exchange (see Section 3.5 (p. 15)). We note that as a result of this coupling the corresponding population change for N_2 (1) had approximately the same value as that for 00011 at all iterations.

One might hope to accelerate convergence by removing the transfer in the line cores when LI is replaced by ALI or by breaking the error transfer loop caused by the collisional coupling as described in Section 3.5 (p. 15). Surprisingly, the “decoupling” alone gives nearly no improvement (see the curve LI+K). On the other hand replacing LI by ALI without “decoupling” significantly destabilizes the iteration process (ALI). Allowing the populations to adjust to the radiative field by means of inner iterations restores smooth convergence (ALI+O) and also slightly improves it, but at the cost of the required time for the inner iterations. We observed about that 300 to 400 inner iterations (for the criteria 10^{-4}) were required between radiative iterations for both the LI+V and ALI+O processes. Although for the 9-level model the inner iterations did not significantly increase the total time, for 60 levels of CO₂ the inner iterations increase the time required to obtain a relative error of about 10^{-3} by a factor of 3.

However the real “breakthrough” in the convergence appears when ALI and “decoupling” are introduced simultaneously. The curve ALI+K demonstrates this dramatic acceleration of convergence in comparison with previous approaches. A relative error of 10^{-3} is now obtained after about 40 iterations in comparison with 200 iterations for the ALI process.

We applied the Ng acceleration algorithm (see Section E.1 (p. 107)) to all cases (except the unstable ALI case) discussed above and found that for both the LI and LI+K schemes the Ng procedure fails and causes both calculations to collapse. This failure is independent of the iteration step at which acceleration is first applied: we tested it beginning at steps from 10 to 30 with the same negative effect. Nevertheless, despite the appreciable initial jump in the relative change, Ng-acceleration gives good results in the ALI+O case when applied to the outer radiative iterations: see the curve ALI+O+NG in Fig. 4.1 (p. 20), where the Ng-procedure is first applied at the 10th radiative iteration and 3 previous iterations are used. However it appears to be the most effective for the ALI+K scheme (see the curve ALI+K+NG), doubling the convergence rate. This is not surprising: the fast and stable convergence of the ALI iterations provides optimal conditions for applying Ng-acceleration.

As was already mentioned, the maximum relative change between the results of successive iterations presented in Fig. 4.1 (p. 20) occurs for the level 00011 of CO₂. It is always observed at altitudes around 100 km where the temperature profile has its minimum and where therefore the collisional excitation of 00011 level is least effective. As a result, the population of levels 00011 in this layer is very sensitive to radiation in the 4.3 μm band coming from the other layers of the atmosphere and absorbed by ground state CO₂.

We recorded each iteration the relative population changes for all levels included in the model. For the CO₂ vibrational levels other than level 00011 the maximum relative changes decrease when the optical thickness of the transitions from these levels are reduced. For instance, the population of the 01101 level, which gives rise to the 15 μm fundamental transition, converges much faster than that of level 00011. We display the results for this level in Fig. 4.2 (p. 22) (dash-dotted curves) in comparison with those for 00011 level (thick solid curves) both for LI and ALI+K+NG schemes. This figure shows that a relative change 10^{-3} in population is reached for the 01101 level in 15 and 7 steps for the LI and ALI+K+NG algorithms, respectively.

The results of our convergence study for the 64-level CO₂ model during day and night for the spring equinox atmospheric model appear in Fig. 4.3 (p. 23). The convergence rates of the various iteration schemes for night conditions were similar to those found for the 9-level CO₂ model (compare the thick solid curves in Fig. 4.3 (p. 23) with those in Fig. 4.3 (p. 23)). However the absorption of solar radiation had different effects on LI and ALI+K(+NG) algorithms. We found that the LI scheme converged much more slowly, requiring about 50 more iterations before the same MARC is reached. In contrast, the ALI+K and ALI+K+NG algorithms reacted to the solar pumping by converging still more rapidly: the numbers of iterations decreased by 20 and 5–10 for ALI+K and ALI+K+NG algorithms, respectively.

It should be noted that the solution using the ALI+K+NG algorithm of an extended non-LTE model in CO₂ in the Earth’s atmosphere (see *Shved et al.*(188)), which includes 328 vibrational levels of 7 CO₂ isotopic species and about 800 bands with a total of about 105000 ro-vibrational lines, converged in the same way as the calculations just reported.

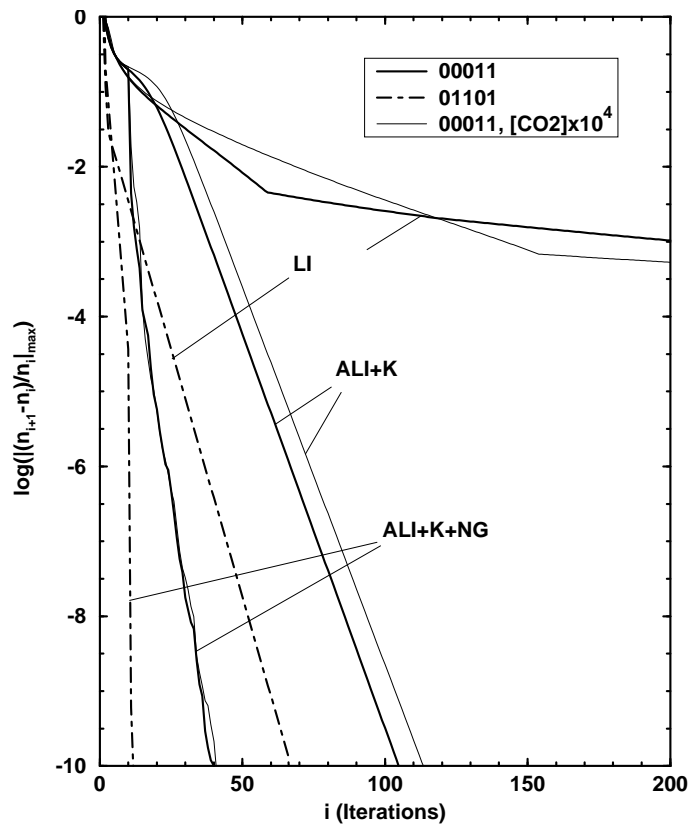


Fig. 4.2 Convergence plots for the 9-level CO₂ model of a spring equinox atmosphere at night. Logarithms of MARC are presented for the 00011 and 01101 CO₂ levels (thick solid and dashed curves)

An additional sensitivity study was performed for the ALI+K+NG scheme, which showed that its convergence is uniquely insensitive to changes of the input parameters. As it was mentioned above, this algorithm converges at the same rate for CO₂ models with 9, 60 or 328 vibrational levels. We have also increased the number of the angle-frequency quadrature grid points and find that successive doublings of $D = 61$ (up to 481) had no influence on the convergence of the ALI+K+NG scheme. The atmospheric models used had also very little influence: the number of iterations required to get a MARC of 10^{-4} for various models altered by not more than 5. This algorithm is only very slightly sensitive to the starting values of the populations. If the starting values are close to the final solution (for instance, the populations from a previous incomplete calculation or a similar model), the number of iterations can be strongly reduced. In our sensitivity study we chose initial populations which always differed significantly from the final ones. Thus, we used instead of the LTE values for a given model temperature profile those for profiles very different from the one being considered (e.g. constant temperatures or temperature profiles from another atmospheric model): again the number of iterations changed by only 3 to 5.

Rybicki and Hummer (181) performed a convergence study similar to that presented here for the ALI-algorithm they developed, using two non-LTE atomic line formation problems. Their convergence patterns are very similar to ours, both with and without the Ng procedure. In addition to MARC these authors also calculated the “true” relative error at each iteration using the converged solution from a previous calculation. They found that the MARC closely followed the “true” relative error, but was, in general, somewhat smaller.

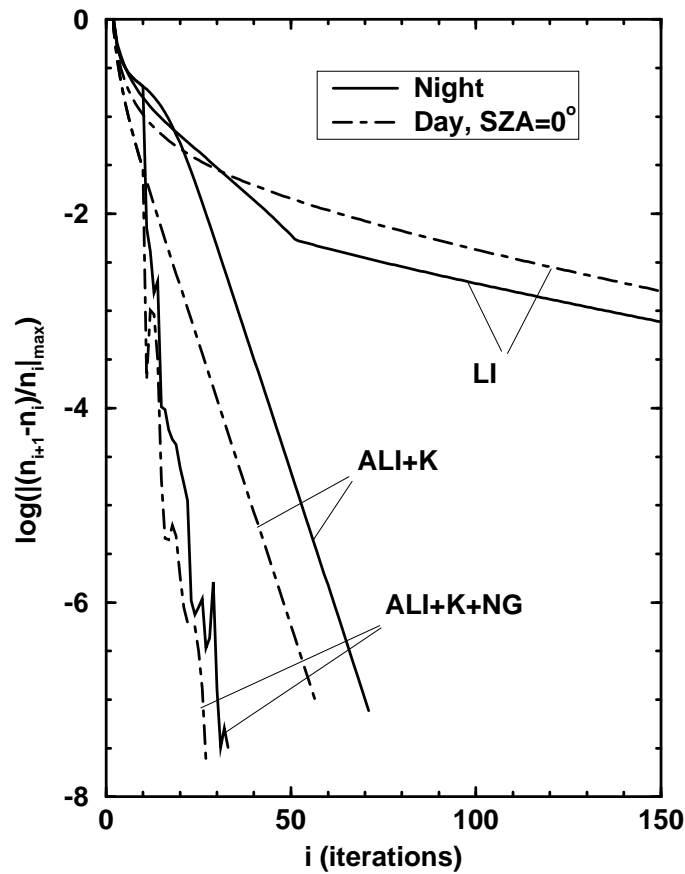


Fig. 4.3 Convergence plots for a 64-level CO₂ model of a spring equinox atmosphere for night and for day conditions (at solar zenith angle 0°).

4.2 Comparison of ALI algorithms utilising various radiative transfer techniques

In the previous section the convergence of a number of iteration schemes based both on lambda iteration and ALI in solving the non-LTE problem for CO₂ in the Earth's atmosphere for day and night conditions was investigated. Only the Feautrier algorithm in its modification described by *Rybicki and Hummer* (181) was applied to the solution of RTE. The acceleration procedure of Ng as described by *Rybicki and Hummer* (182), was applied for predicting populations of all species at each altitude and at each iteration beginning with the specified iteration step. These schemes were applied to the standard CO₂ non-LTE problem in the Earth's atmosphere and to that in which the CO₂ volume mixing ratio was increased by a factor of 10⁴. This artificial problem was extremely optically thick providing a severe challenge for iterative techniques.

It was demonstrated that ALI+Ng+“decoupling” provided the fastest convergence for both day and night for various atmospheric models and starting populations. The convergence for both normal and optically thick problem was nearly identical. In later application of the code to the optically thick CO₂ problem in the Martian atmosphere we observed, however, substantially slower convergence than that for the artificial optically thick case described above. There are two obvious reasons for this difference:

- the low pressure in the Martian atmosphere (the surface value is about 6 mb compared to 1000 mb at the Earth's surface) and, consequently, low frequency of collisions and
- very large optical depth of Martian atmosphere (about 500 times larger than that for the

Earth's).

The case of CO₂ in the Martian atmosphere was selected as a core one for the convergence study presented here, however we discuss also the case of Earth's atmosphere for the sake of comparison. Both day and night conditions were tested. Only vibrational non-LTE was considered assuming rotational LTE for all vibrational levels. Both the "decoupling" and the Newton–Raphson algorithms (see Section 3.5 (p. 15) for the solution of SEE) were tested. Since convergence curves for these two algorithms nearly completely overlap only those for "decoupling" are displayed below. Various radiative transfer algorithms were utilized.

The molecular model used included 56 vibrational levels of 5 CO₂ isotopes and 149 ro-vibrational bands. For the Earth's atmosphere N₂ and O₂ molecules were added with two levels for each. The spectroscopic parameters were taken from the HITRAN–2000 database. The absorption of solar radiation by the CO₂ bands in the 1–15 μm spectral region was taken into account. The system of collisional reactions and corresponding rate coefficients for the Earth's are those of *Shved et al.*(188). For the Martian atmosphere we applied the system of reactions as described by *López-Valverde et al.*(207; 208). Corresponding rate coefficients were generated using data of these authors for the lowest vibrational transitions and scaling them to higher ones by means of the first-order perturbation rules suggested by *Shved et al.*(188). 1km–step altitude grids starting from the ground with $D=200$ points for Martian- and 180 point for Earth's atmospheres, respectively, were applied.

For the lower boundary a black body at the surface atmospheric temperature was assumed.

The input atmospheric models are those used for non-LTE diagnostics of the CRISTA/ASTRO-SPAS (Earth) and TES/MGS (Mars) infra-red limb radiance data.

In the discussion below we use the following abbreviations: Long– and Short–0 and 1 – for the long and short characteristic radiative transfer algorithms (see Appendix D (p. 99)), respectively of zero- and first order (in the case of zero order the source function for a layer is equal to the mean of its values at layer boundaries); MF – for modified Feautrier algorithm; DFE – for discontinuous finite element algorithm; NG – for Ng subroutine. Together with Ng acceleration we tested also simple linear prediction of populations for n steps ahead which we abbreviate as LE.

In Fig. 4.2 (p. 25) the maximum absolute relative change (MARC) in the CO₂ populations at all altitudes for successive iterations are plotted for night and day condition in the Martian atmosphere for each iteration scheme considered.

One can see in Fig. 4.2 (p. 25) that processes when Long–0 and Short–0 are used (convergence curves overlap and marked in figure as "Short–0") have slowest convergence rate. The application of Long/Short–1 slightly (curve "Short–1" for both) improves convergence, however the significant acceleration is reached only when MF and DFE algorithms are utilized. Further acceleration can be reached by applying LE. The "DFE+LE" curves in Fig. 4.2 (p. 25) correspond to the case when LE was "switched on" at 20th step extrapolating in 3 steps after two successive radiative iterations (extrapolation in a number of steps more than 3 led to de-stabilization of process).

However the most efficient acceleration is provided by NG (curves "DFE+ NG"). Being activated at 20th step it reduces the number of iterations compared to the non-accelerated process by factors of 3 and 4 for MARC 10^{-3} and 10^{-7} , respectively .

As it was mentioned in the previous section MARC displayed in Fig. 4.2 (p. 25) occurs nearly exclusively for the level 00011 of the main isotope C¹²O₂¹⁶ which is the upper level of the most optically thick 4.3 μm fundamental transition¹. It is always observed at altitudes where the temperature profiles have their minima and, therefore, the collisional excitation of 00011 level is least effective. The maximum relative change decreases when the optical thickness of transitions from the level is reduced. For instance, the population of the 01101 level of C¹²O₂¹⁶, which gives rise to the main 15 μm fundamental transition (whose optical depth is about 3 times smaller than that of the 4.3 μm band), converges much rapidly than that of level 00011: for the "DFE+NG" algorithm

¹The optical depth in the center of strongest line of this band is about 3×10^8 for entire Martian atmosphere and about 3×10^6 for the non-LTE layer.

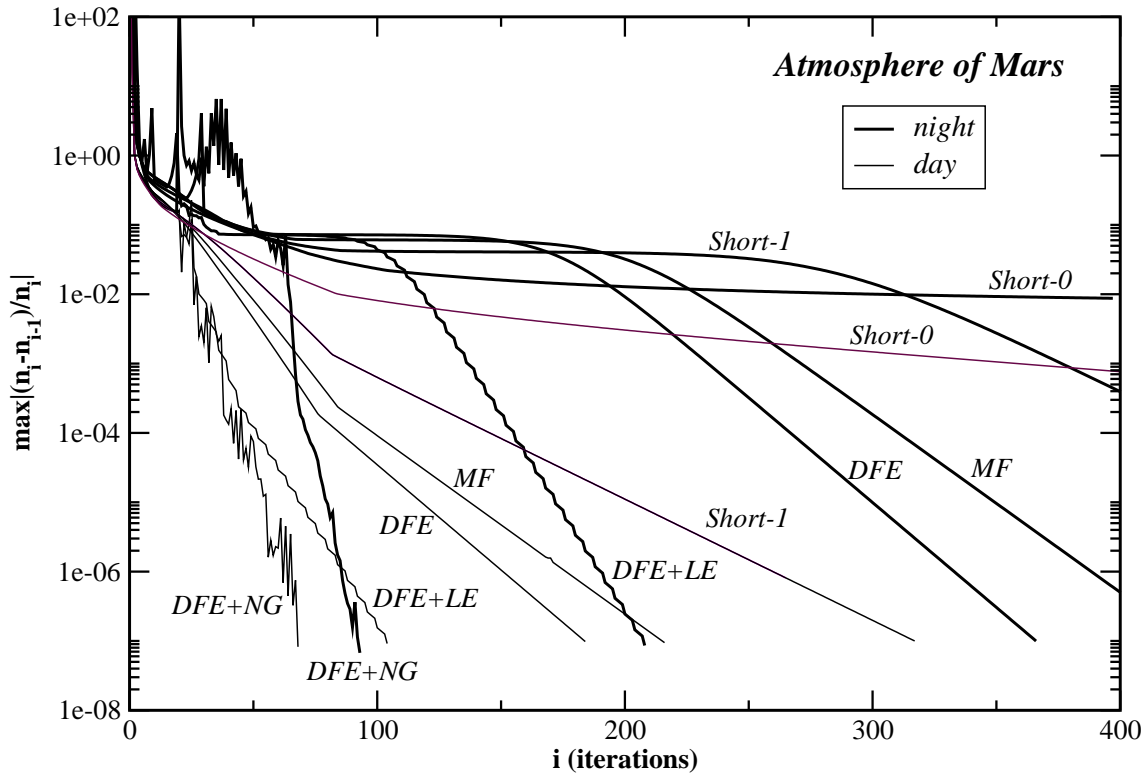


Fig. 4.4 Convergence plots for the CO₂ problem in the Martian atmosphere for day and night conditions. Labels on the curves refer to various iteration schemes (see text for details).

the relative change 10^{-7} in population is reached for the 01101 level in about 37 and 23 steps for night and day, respectively.

Fig. 4.2 (p. 26) illustrates for the Earth's atmosphere the performance of the same algorithms which were discussed above for the Martian atmosphere. Two reasons for difference between convergence rates for the atmospheres of Mars and Earth's were given at the beginning of this section. Again, as in the case of the Martian atmosphere the "DFE+NG" algorithm provides the most rapid convergence for both day and night conditions.

We also compared the time performance of different RTE solving methods. The results appeared to be dependent on the hardware configuration, especially on the mathematical co-processor involvement. However, for a number of computers with Intel processors of different generations (Intel Pentium-II, III and IV) used in the test the following inequality is true:

$$T_{Short}^{RTE} \leq T_{DFE}^{RTE} < T_{Feautrier}^{RTE} < T_{Long}^{RTE} \quad (4.1)$$

This relation is defined mainly by the number and the type of exponent calculations. It is worth noticing here that all standard soft- and hardware subroutines for exponential evaluations in the computers tested fail in case of small arguments. This causes wrong formal solution for frequency grid points where opacities are low. In order to avoid this problem we replaced these exponentials by series which are also evaluated extremely rapidly. Since in the problems we solve the majority of optical depths increments are small this provides a substantial time reduction when the short characteristic method (SCM) is used, since it involves the evaluation of many exponentials. SCM appeared to be even more efficient than the DFE and Feautrier methods which do not use exponential calculations at all, but involve more iteration cycles than the SCM. Finally, the long characteristic method (LCM) requires calculation of exponentials of large arguments which makes this method the slowest of all.

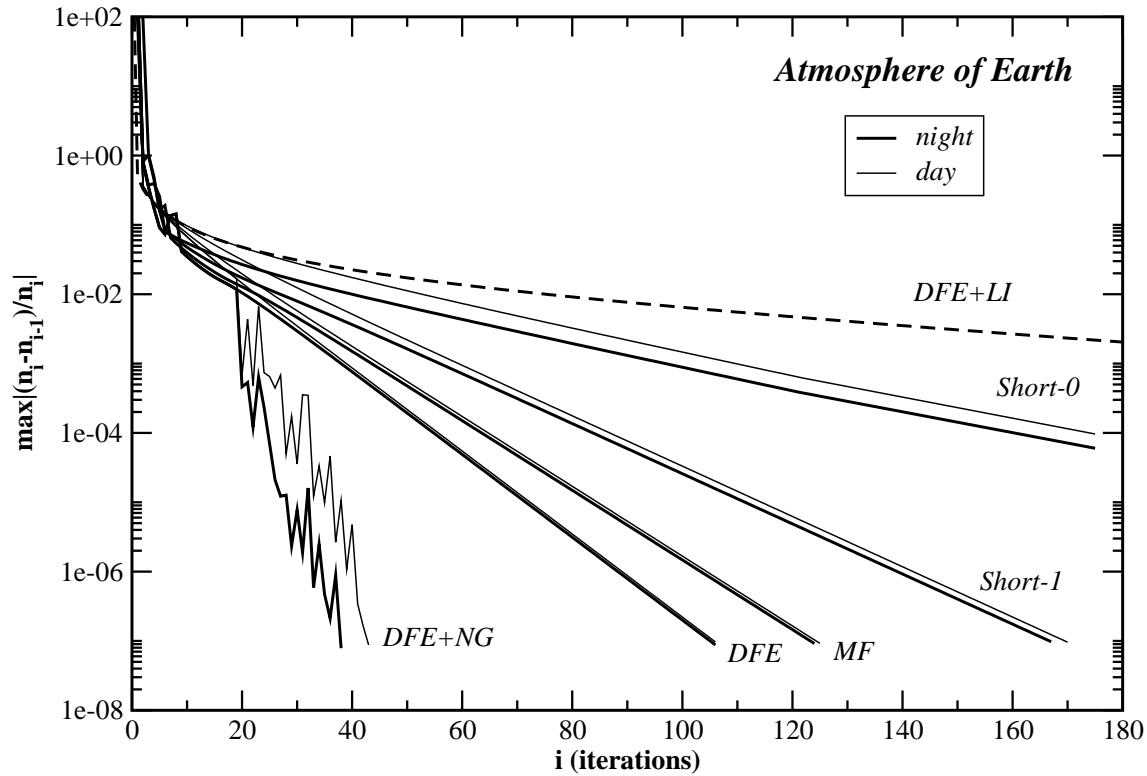


Fig. 4.5 Convergence plots for the CO₂ problem in the Earth's atmosphere for day and night conditions. Labels on the curves refer to various iteration schemes (see text for details).

Taking into account for each method of solving the RTE both time performance and the convergence rate we obtained for the total time the following relation:

$$T_{DFE}^{total} < T_{Short}^{total} < T_{Feautrier}^{total} < T_{Long}^{total}. \quad (4.2)$$

The dashed curve in Fig. 4.2 (p. 26) marked as “DFE+LI” demonstrate the convergence of lambda iterations (LI) for the daytime problem. This is obviously the slowest process among those studied, notwithstanding that we apply here the “decoupling” approach instead of “straightforward iterations” used by *Wintersteiner et al.* (219) who solved by lambda iterations similar CO₂ problem in the Earth's atmosphere.

The problems considered here include most important radiative and collisional process which govern non-LTE in CO₂ in both atmospheres. The solution of an extended non-LTE model in CO₂ in both atmospheres, which includes about 300 vibrational levels and about 800 bands, using the “DFE+NG” algorithm converged in the same way as the calculations discussed above.

We applied our code also to the solution of the non-LTE CO₂ problem in the Venusian atmosphere above the cloud layer and obtained the convergence rates very close to those for Martian atmosphere. The optical depth of this problem in Venusian atmosphere exceeds that for Martian atmosphere by a factor of 100. This could cause significantly slower convergence, however the higher pressure (about 200 mb at the upper cloud boundary) of Venusian atmosphere increases the impact of collisions and restores convergence making it comparable to that for the Martian atmosphere.

The results described above were obtained neglecting line overlapping. However, the code developed in framework of this study allows explicit treatment of line overlapping, both within each band and between bands of different species. None of the other codes available in planetary

studies have this capability. This is possible primarily because of the high efficiency and the flexible nature of the ALI procedure which easily deals with the additional non-linearities introduced by the overlapping lines. This is a major advance in the ability to treat more realistic models, in addition of being able to deal with a very large number of transitions and levels.

We utilize in our code “preconditioning within the same transition only” as described by *Rybicki and Hummer* (181; 182)). This approach leaves the form of the SEE unchanged. It is designed to handle the case when lines do not overlap or the overlap is relatively “weak” i.e. the cores of some lines overlap, while for the remainder at most only wing overlap occurs. The latter is typical for the non-LTE layers in planetary atmospheres. In this case all neighboring lines whose opacity exceeds certain threshold (usually about $10^{-15} - 10^{-14}$ of the opacity in the center of treated line) are taken into account. In order to accurately calculate their contributions along the entire line profile including the far wings (up to 300 Doppler halfwidths) we integrate on a very fine frequency grid with 10 points for each Doppler halfwidth.

It is obvious that accounting for overlapping significantly increases the computing time required for each iteration. We, therefore, tested the convergence in this case only for the most efficient process “DFE+NG”. The calculations showed that for both atmospheres considered overlapping caused moderate increase of total number of iterations by about 20–30%.

The code studied here can solve the non-LTE problem for a number of molecules and atoms in the atmospheres of Earth (CO_2 , O_3 , H_2O , N_2O , CH_4 , CO , NO , N_2 , O_2 , O , OH) and Mars (CO_2 , CO , N_2 , O_2 , O), which can emit in the infra-red spectral region and interact by inter-molecular collisional energy exchange and by line overlapping. We run the code with the “DFE+NG” algorithm for both atmospheres in order to find simultaneously populations of vibrational levels of all molecules. Since the $4.3 \mu\text{m}$ CO_2 fundamental band is the most optically thick one among all infra-red bands in both atmospheres it was not surprising that we observed convergence rates very similar to those discussed above for pure CO_2 problems.

4.3 ALI-ARMS, MCM and ARC codes

A computer code based on the ALI approach described in Section 3.4 (p. 14) was developed in framework of this study. Its capacity and performance by the solution of various problems was described in previous sections (Section G (p. 115) for its technical description). In recent applications the code was called ALI-ARMS (for “Accelerated Lambda Iteration for Atmospheric Radiation and Molecular Spectra”).

We now compare the ALI-ARMS with two other codes² used currently to solve non-LTE band problems in planetary atmospheres, namely those of *López-Puertas et al.*(109) and of *Wintersteiner et al.*(219). The first is a matrix inversion technique and the other uses lambda iteration. The main implications of this section are also relevant to other algorithms of both types which appear in the literature on atmospheric radiation (see the above-mentioned papers for references). We concentrate only on the algorithms and their convergence features. The various approximations used in other studies were discussed by *Kutepov et al.*(100) using results of a very elaborate CO_2 non-LTE calculations with 328 vibrational levels of 7 isotopes in the Earth’s atmosphere.

Groups at the Instituto de Astrofísica de Andalucía in Granada and the University of Oxford have applied the Curtis-matrix (see *Curtis and Goody* (34)) technique for the multilevel case (see *López-Puertas et al.*(109)).³ They also used the Curtis-Godson approximation, replaced the exact angle integration by the diffusion approximation, simplified the band model by grouping the lines with respect to their intensities, used the “narrow band” approximation (all lines in the band have a common source function) and ignored the conservation equations, assuming the populations of

²The preliminary version of the ALI code described here which is suitable for treatment of the non-LTE only in CO_2 is used currently at the Department of Atmospheric science of the University of St. Petersburg, Russia. Its performance corresponds to that described in Section 4.1 (p. 19)

³Unfortunately, the very short subsection of this paper devoted to the multilevel model (and referred to in all other publications of these authors) provides little information, outlining only a special case in which the number of bands equals the number of vibrational levels.

the ground molecular levels to be equal to their total number densities. The technique was applied to a number of non-LTE problems in the Earth's atmosphere (see *López-Puertas et al.*(109; 110; 112; 113; 114; 115; 116), *Edwards et al.*(43; 44) and *Rinsland et al.*(172)).

Later, certain simplifications were dropped, such as the diffusivity approximation, and the technique was called Modified Curtis-Matrix method (MCM). A crucial test of this method was provided by the solution of the CO₂ non-LTE problem in the Martian atmosphere (see *López-Valverde* (207; 208)). The scientists give little information about computational features. They were, however, unable to solve the entire system of equations (similar to that given by Eq. 3.8, (p. 12)), even for quite modest numbers of vibrational levels $L \simeq 100$ and grid points $D=45$. The entire system was broken into four fragments corresponding to four groups of levels and solved iteratively.

The code (named ARC for "Atmospheric Radiance Code") was used for the CO₂ non-LTE problem in the Earth's atmosphere by *Wintersteiner et al.*(219), *Dodd et al.*(37), *Nebel et al.*(153) and *Ratkowski et al.*(168). This scheme is labeled in the previous section as LI. *Wintersteiner et al.*(219) discussed at length the algorithm and its computational features. Their discussion in Section 5.1 refers to separate runs for single bands. This suggests that the "equivalent two-level atom" approach was used. The authors reported only the convergence for the level 01101 of the main isotope, which agrees with our results for the LI scheme ($i \simeq 25$ for coupled by $V - V$ energy exchange MARC of 10^{-4}), but give no information about the convergence for the 00011 level, which, as we have shown, exhibits the slowest convergence rate ($i \simeq 500$ for MARC of 10^{-4}) in this problem.

Wintersteiner et al.(219) searched for some procedure to accelerate the iteration process, which would not have been necessary if the total scheme converged as fast as the population of the 01101 level. The "acceleration" procedure they mention is not intended to reduce the number of iterations, but is aimed at reducing the time per iteration. This is achieved by using a matrix representation of the lambda operators for all bands (in our notation the matrices Λ_{IV} , see Eq. 3.9, (p. 12)) obtained at one iteration for a number of subsequent iterations. The time, therefore, is saved at the expense of a significant increase in computer storage: B matrices of the $D \times D$ -dimension are stored, where B is the number of bands treated which, for their elaborate molecular model, is presumably large (unfortunately the value of B is not given).

A comparison with identical input data of the MCM and ARC codes, developed by the Granada-Oxford group and in Phillips laboratory, respectively, was given by *López-Puertas et al.*(116). The results were in fairly good quantitative agreement.

We note that both of these algorithms in their current versions have a number of common features. Leaving apart several approximations used in both techniques we will concentrate on a few basic features.

Both the ARC and MCM techniques use the integral equation approach since they use the analytical form of the RTE $\bar{J} = \Lambda[S]$. The matrix representation of Λ is generated by an analytical integration of the kernel function over a set of layers in the atmosphere in which S is represented by a set of step-function in altitude. This is a very inflexible and time consuming way of computing the matrix elements in contrast to ALI algorithm, which uses a fast numerical solution of the RTE (see Section 2.1 (p. 3)).

The ARC-algorithm incorporates iteration as a basic element. Moreover, the MCM-technique now appears not to depend solely on matrix inversion and requires at least a few iterations (see Section 3.2 (p. 11)). In the application of this technique to CO₂ in the atmosphere of Mars described by *López-Valverde and López-Puertas* (207) additional iterations related to the procedure of level grouping were required. If the solution requires a large number of iterations it may be computationally more expensive than direct inversion of a large matrix. This is true especially for slowly converging lambda iterations. If in addition large amounts of intermediate data for the Λ matrices are stored, from the point of view of the computer resources, lambda iteration may have little or no advantage in comparison with direct matrix inversion. *Wintersteiner et al.*(219) have perhaps found themselves in a similar situation when, in treating large number of bands and calculating the matrices $\bar{\Lambda}$, they have been forced to store these matrices and to renew them every few iteration steps.

5. Applications of ALI-ARMS: non-LTE retrievals of the atmospheric parameters from CRISTA-1 and CRISTA-2 radiance data

The Cryogenic Infrared Spectrometers and Telescopes for the Atmosphere (CRISTA) is a limb scanning experiment that measured the thermal emissions of trace gases in the 4 - 71 μm spectral region with high spatial resolution (see *Offermann et al.*(158), *Riese et al.*(171) and *Grossmann et al.*(70)). The instrument was designed in order to resolve dynamical structures with small horizontal and vertical scales in the 15–150 km altitude region of the atmosphere. The CRISTA instrument was mounted on the ASTRO-SPAS platform which is released from the Shuttle and operates at a distance of 20 - 100 km behind the Shuttle. For improved horizontal resolution CRISTA used three telescopes that sense the atmosphere simultaneously at angles 18° apart. To achieve high measuring speed and, consequently, high spatial resolution along the track, the detectors and the optics of the instrument were cooled by cryogenic helium. The incoming limb radiance is analyzed by four Ebert-Fastie grating spectrometers: SL for Left, SCL for Central Longwave, SCS for Central Shortwave and SR for Right, respectively.

CRISTA-1 was launched in November 1994 as a part of the STS-66 shuttle mission and measured more than 1000000 limb radiance spectra in a number of different measurement modes. CRISTA-2 was launched in August 1997 as part of the STS-85 mission. In comparison to CRISTA-1 the wavelength coverage was increased by using extended spectral channels, the latitude coverage was extended to 72°S – 72°N vs. 58°S – 64°N and detectors with higher radiometric sensitivity were used, aimed at measuring temperature, CO_2 , CO and NO number densities. During CRISTA-2 more spectra were measured in the mesosphere and thermosphere modes.

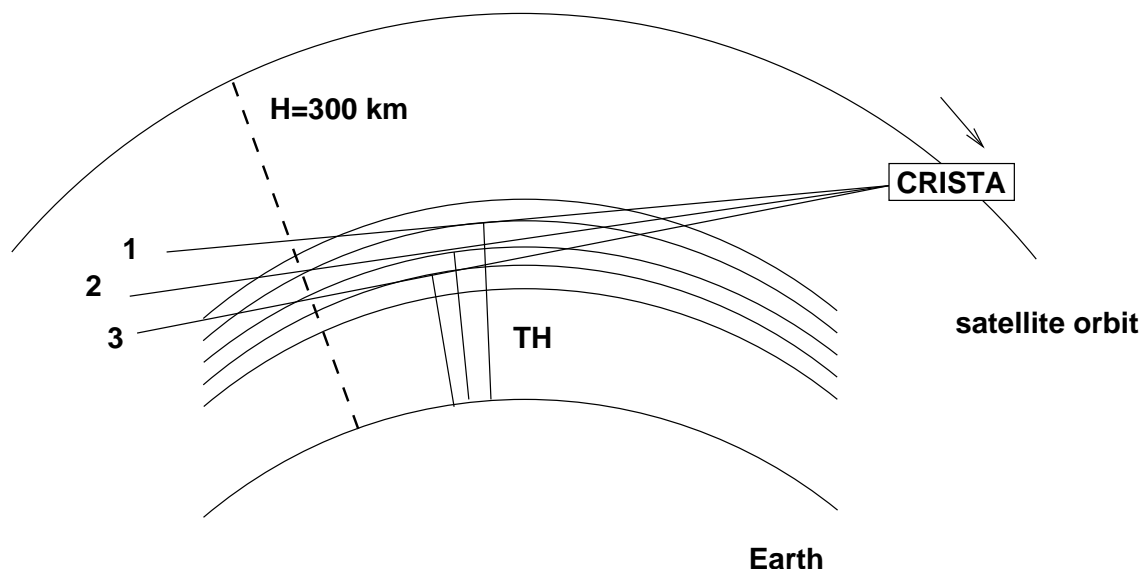


Fig. 5.1 The geometry of limb scanning (CRISTA flight parameters used)

Fig. 5.1 (p. 29) shows the details of limb scanning by CRISTA telescopes. The satellite flew at an orbit with an altitude of about 300km and measured the spectra at tangent heights (TH) with the vertical resolution in the order of 2–3km, in downward (1 \rightarrow 2 \rightarrow 3) direction.

The CRISTA wavelength range is covered by 26 (CRISTA-1) or 29 (CRISTA-2) spectral channels

Detector	Trace gases	Wavelength range (μm)
SL 1/E	CH ₄ , N ₂ O, N ₂ O ₅	7.5 - 8.6/ 9.72
SL 3/E	O ₃	8.91 - 10.22/ 11.322
SL 4/E	HNO ₃ , F-12	10.43 - 11.78/ 12.882
SL 5/E	T, O ₃ , F-11, HNO ₃ , ClONO ₂ , (CCl ₄)	11.55 - 12.88/ 13.982
SL 6/E	H ₂ O, NO ₂	6.07 - 6.73/ 7.282
SL 8/E	T, p	12.79 - 14.1/ 15.22
SCS 1/E	CH ₄ , N ₂ O, N ₂ O ₅	7.5 - 8.6/ 9.72
SCS 2/E	CO ₂ , CO, O ₃	4.18 - 4.81/ 5.362
SCS 3/E	O ₃	8.91 - 10.22/ 11.322
SCS 4/E	NO, H ₂ O	4.92 - 5.58/ 6.132
SCS 5/E	HNO ₃ , F-12	10.43 - 11.78/ 12.882
SCS 6/E	T, O ₃ , F-11, HNO ₃ , ClONO ₂ , (CCl ₄)	11.55 - 12.88/ 13.982
SCS 7/E	H ₂ O, NO ₂	6.07 - 6.73/ 7.282
SCS 8/E	T, p	12.79 - 14.1/ 15.22
SR 1/E	CH ₄ , N ₂ O, N ₂ O ₅	7.5 - 8.6/ 9.72
SR 3/E	O ₃	8.91 - 10.22/ 11.322
SR 4/E	NO, H ₂ O	4.92 - 5.58/ 6.132
SR 5/E	HNO ₃ , F-12	10.43 - 11.78/ 12.882
SR 6/E	T, O ₃ , F-11, HNO ₃ , ClONO ₂ , (CCl ₄)	11.55 - 12.88/ 13.982
SR 7/E	H ₂ O, NO ₂	6.07 - 6.73/ 7.282
SR 8/E	T, p	12.79 - 14.1/ 15.22
SCL1	O ₃	9.29 - 10.30
SCL2	T, p	14.431 - 15.58
SCL3	O(³ P _J), HF, H ₂ O	59.0 - 65.0
SCL6	O(³ P _J), HF, H ₂ O	60.1 - 66.1
SCL4	N ₂ O, CO ₂	16.211 - 17.42
SCL5	H ₂ O, HCl	65.0 - 70.91

Tab. 5.1 Spectral channels of CRISTA-1 and -2. The /E denotes the CRISTA-2 extended channels.

given in Tab. 5.1 (p. 30). The radiative transfer calculations, required to retrieve atmospheric temperatures and trace gas mixing ratios, are very extensive due to the large wavelength and altitude ranges of the measurements. Therefore, the quality of the obtained data depends on the accuracy of these calculations.

For the LTE retrieval the “onion peeling” scheme was used. The radiative transfer code was based on the BANDPAK library (Marshall *et al.*(134)). This approach utilizes transmissivity tables (see Gordley and Russell (65) that were generated by means of the LINEPAK algorithms (Gordley *et al.*(66)). The results of the LTE temperature and trace gas number density retrievals were published by a number of authors and were used to test 3D chemical-dynamical model predictions.

The retrieval under non-LTE conditions in the middle and upper atmosphere is more complex and is discussed in next sections.

5.1 CRISTA-1 and -2 spectral channels with non-LTE emissions

The channels with CO₂ and O₃ emissions that were used for the retrieval of the number densities of these two trace gases are given in Tab. 5.2 (p. 31). Other spectral channels affected by non-LTE and measured by CRISTA, including nitric oxide at 5.3 μm and water vapour at 6.3 μm , will not be discussed.

A spectrum measured by CRISTA in the SCL2 channel around 80 km is given in Fig. 5.2 (p. 31). This channel covers the ν_2 fundamental and hot 15 μm bands of various CO₂ isotopic species and partially the ν_2 14 μm O₃ bands. In the upper mesosphere and lower thermosphere one

Name	Spectral window(cm^{-1})	Resolution $\lambda/\Delta\lambda$	Step (cm^{-1})	Most important non-LTE bands
SCS2	2079-2392	415	1.4	$4.3 \mu\text{m CO}_2$, $4.7 \mu\text{m CO}$, $4.8 \mu\text{m O}_3$
SCS3	978-1120	391	0.67	$9.6 \mu\text{m O}_3$, $9.43 \mu\text{m CO}_2$
SCS8	709- 782	625	0.3	$13.9 \mu\text{m CO}_2$
SCL2	632- 697	486	0.25	$15 \mu\text{m CO}_2$
SCS8E	661- 721	625	0.25	CRISTA-2, $15 \mu\text{m CO}_2$

Tab. 5.2 CRISTA-1 and -2 spectral channels with the non-LTE emissions.

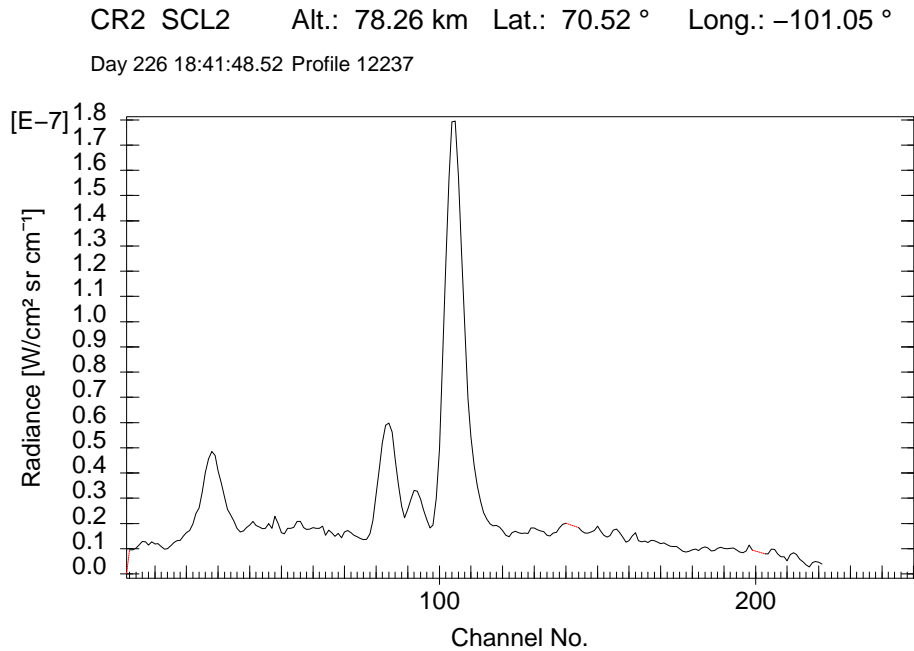


Fig. 5.2 The measured limb spectra in the SCL2 CRISTA channel

can neglect the contribution of ozone to the spectral intensity, since it exhibits low vibrational population. Fig. 5.3 (p. 32) shows that at the altitude of 80 km the spectra are mainly composed of the CO_2 (626) $01101 \rightarrow 00001$ fundamental band at 667.38 cm^{-1} ($14.98 \mu\text{m}$) the CO_2 (628) $01101 \rightarrow 00001$ fundamental band at 662.37 cm^{-1} ($15.10 \mu\text{m}$), the CO_2 (636) $01101 \rightarrow 00001$ fundamental band at 648.48 cm^{-1} ($15.42 \mu\text{m}$), the CO_2 (627) $01101 \rightarrow 00001$ fundamental band at 664.73 cm^{-1} ($15.04 \mu\text{m}$), and CO_2 (626,636) $02201 \rightarrow 00001$ first hot bands. At 100km only the fundamental bands of the CO_2 (626,636,628) are above the noise level and at 120km the only visible feature is the Q-branch (selection rule $\Delta j = 0$) of the CO_2 (626) fundamental band.

The CO_2 vibrational levels 01101 and 02201 do not deviate from LTE up to approximately 75–85 km. Therefore, in this altitude region the SCL2 emissions were used for pressure and temperature retrieval under LTE conditions, assuming a constant CO_2 volume mixing ratio. The results of the retrieval for CRISTA-1 were published by *Riese et al.*(171). As it is shown in Appendix H.1 (p. 119) at higher altitudes the populations deviate from the LTE. The main factor that controls that process is the collisional $V - T$ process with $\text{O}(^3P_j)$.

Therefore, if the number densities of CO_2 and $\text{O}(^3P_j)$ are known then the temperature can be retrieved under non-LTE conditions. Also, if the temperature is obtained using a validated different technique (from UV or microwave measurements, method of falling spheres, lidar measurements) one can validate the $\text{O}(^3P_j)$ number density or the rate constant of the $\text{CO}_2(\nu_2) + \text{O}(^3P_j)$ reaction,

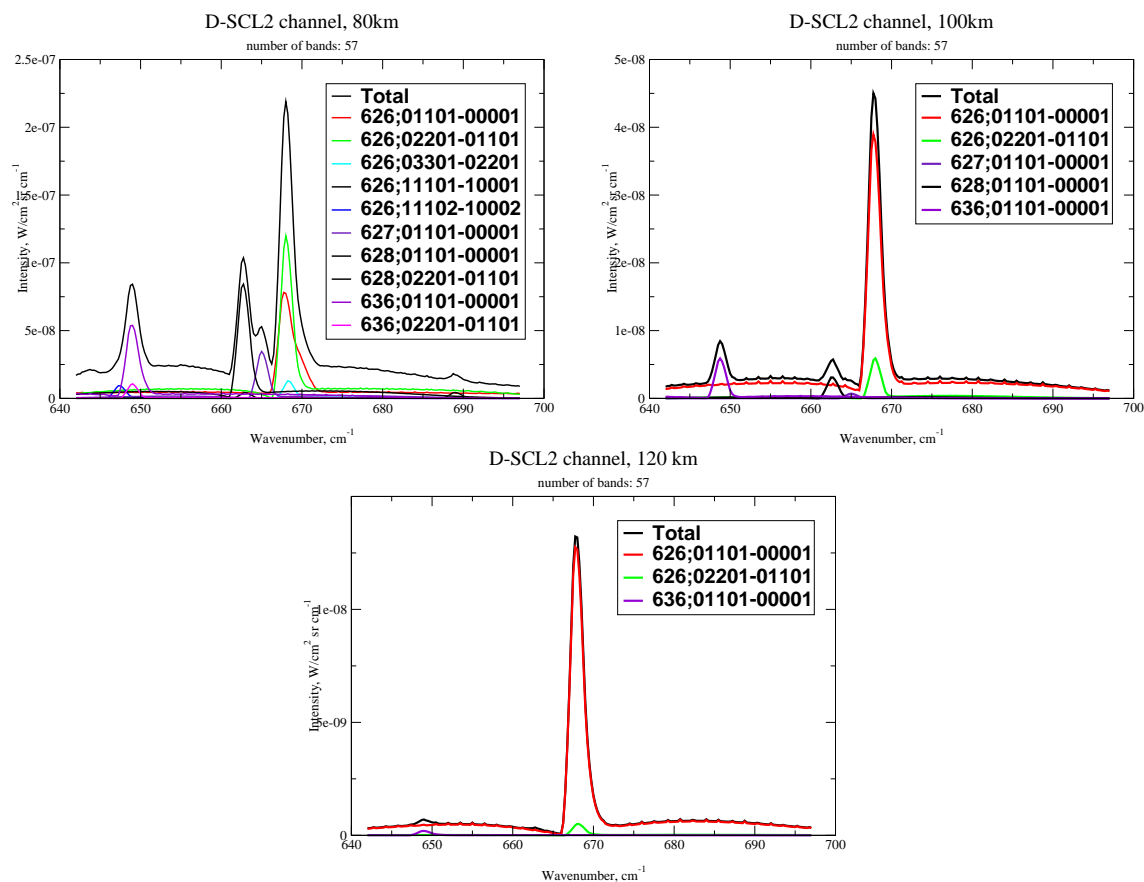


Fig. 5.3 The simulated spectra in the SCL2 CRISTA channel at different tangent heights

as it was done by *Vollmann and Grossmann* (211).

The spectra in SCS8E/SL8E/SR8E channels were measured only during the CRISTA-2 flight. These channels cover part of the SCL2 channel (only CO₂ (626) 01101 → 00001 fundamental band is measured) and the spectra were obtained by the shortwave (SCS/SL/SR) instead of the longwave (SCL) detectors. The radiance data was used for temperature retrieval in the same way as for the SCL2.

In the SCS8 mesospheric spectra (see Fig. 5.4 (p. 33) and Fig. 5.5 (p. 34)) one can easily identify the Q-branch of CO₂ (626) 12.6 μm band (Appendix B.2 (p. 72)). This signal is used for the temperature retrieval together with the main SCL2 channel, because everything written above about SCL2 can be applied here too.

Another channel of interest is SCS2, with the measured spectra given in Fig. 5.6 (p. 39). The major contributors to spectral intensity are the CO₂ 4.3 μm bands of various isotopic species, the 4.7 μm CO fundamental and first hot band and the 4.8 μm O₃ bands. For the daytime conditions the ozone signal is very weak above 60km due to the low O₃ number density (see Fig. F.2c (p. 110)). Opposite to that, the CO signal begins to increase starting from this altitude due to the increase in CO number density. During nighttime the ozone signal increases, because the nighttime O₃ VMR is up to about an order of magnitude higher than for daytime. At the same time the CO and CO₂ signals strongly decrease, because the emitting vibrational levels are not pumped by the absorption of the solar radiation anymore (see Appendix H.1 (p. 119)). Since the spectral signatures of O₃, CO and CO₂ do not overlap, it is possible to analyze them independently. One can see from Fig. 5.7 (p. 40) and Fig. 5.8 (p. 40) that many CO₂ 4.3 μm transitions provide significant contribution to the signal both for daytime and nighttime conditions. Detailed analysis shows that at daytime

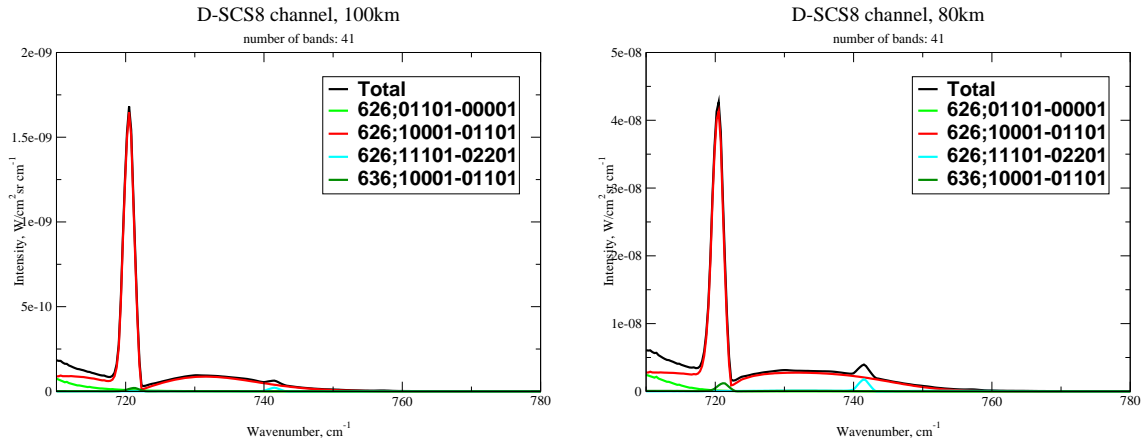


Fig. 5.4 The simulated spectra in the SCS8 CRISTA channel at different tangent heights (daytime)

1. for tangent heights above 110 km the fundamental band CO₂ (626) 00001→00000 dominates the signal,
2. in the tangent height region 60-95 km the sum of second hot bands CO₂ (626) 10011→10001, 10012→10002 and 02211→02201 contribute most strongly to the signal,
3. for the tangent heights below 65 km a number of weaker bands provides non-negligible contribution, among them the third hot bands of main isotope and second hot bands of the isotope CO₂ (636),
4. the remaining bands of main isotope CO₂ (626) as well as those of the minor isotopes have negligible contribution to the signal throughout the considered tangent height region.

The last spectral channel to be considered is SCS3. The experimental spectra measured by CRISTA is given in Fig. 5.9 (p. 41). The signal in the SCS3 channel in the mesosphere at nighttime (Fig. 5.10 (p. 42)) is completely dominated by the O₃ fundamental ν_3 9.6 μm band. The ozone hot 9.6 μm bands (see Appendix B.3 (p. 73)), located in the long wavelength part of the channel contribute less than 5% to the total integrated intensity. Another minor contribution is due to the O₃ fundamental ν_1 band. For daytime conditions (Fig. 5.11 (p. 42)) the situation for this channel is different. First, the photodissociation of ozone by UV solar radiation decreases the O₃ number density and therefore the signal by an order of magnitude. Second, due to the daytime enhancement in CO₂ (626) 00011 vibrational level population the CO₂ (626) 10 μm laser bands (Appendix B.2 (p. 72)) 00011 → 10001 and 00011 → 10002 provide up to 25% to the total radiance.

Below 60km both for the daytime and nighttime the major part of the limb radiance comes from fundamental vibrational levels of ozone that have LTE populations. It makes the non-LTE modeling unnecessary.

5.2 Method of retrieval

The majority of the methods used for the inversion of the infrared radiation data for the limb viewing geometry are based on the assumption of LTE (*Gille and Russell* (62), *Barnet* (14)). Therefore, the temperature and trace gas densities they yield usually are adequate in the altitude range up to 75–80 km. Accounting for the non-LTE effects complicates significantly the inversion of the measurements. The *forward fit* retrieval approach applied in this dissertation for the inversion of the limb radiance data is described below.

One starts with an *initial* atmospheric model, i.e. with model values of pressure, temperature and number densities of the gases. If the assumption of LTE is valid, the populations of molecular

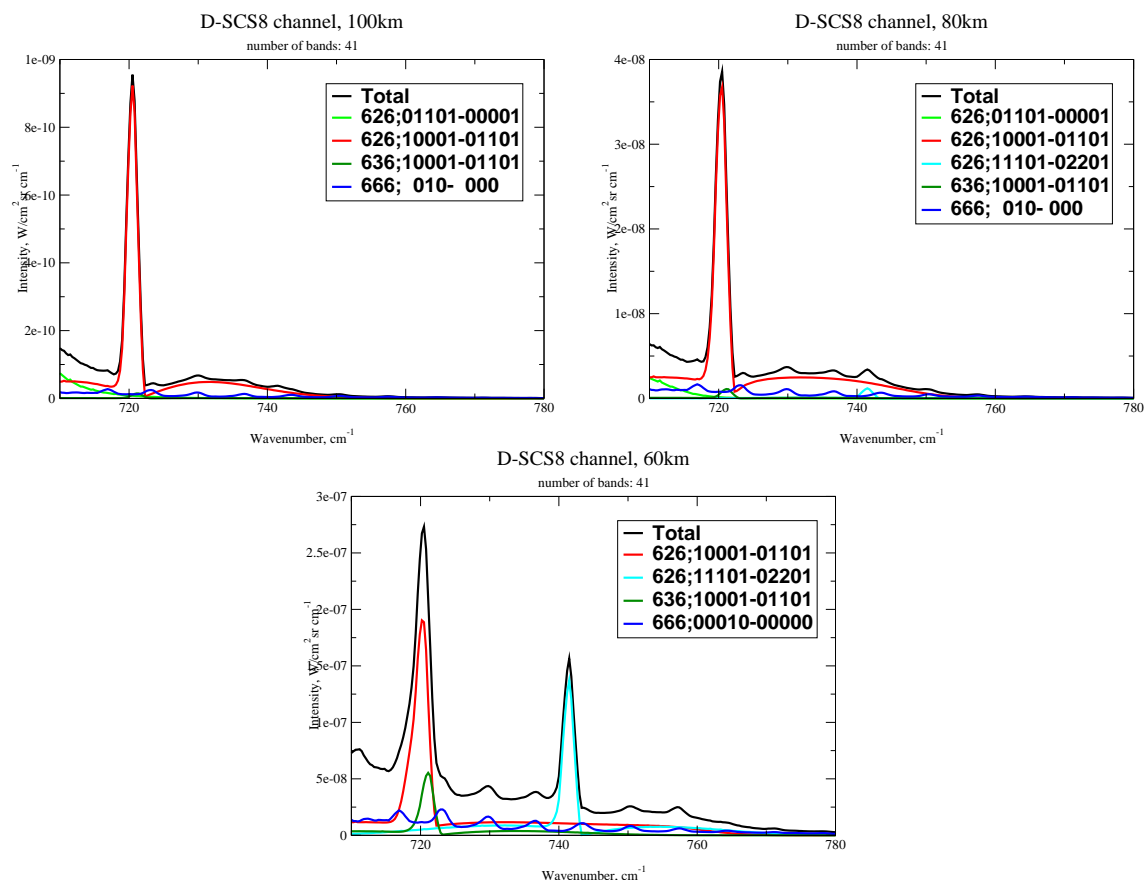


Fig. 5.5 The simulated spectra in the SCS8 CRISTA channel at different tangent heights (nighttime)

and atomic energy levels are given by the Boltzmann law (see Section 2.3 (p. 5)). Otherwise, the non-LTE populations are calculated for the given atmospheric model. After the populations are obtained, the monochromatic limb radiances are calculated and convolved with the spectral instrument function. The resulting *simulated* spectra are compared with the measured *experimental* spectra, and the corrections to the *initial* atmospheric model are applied, resulting in a *corrected* atmospheric model. This process is repeated until the difference between *simulated* and *measured* spectra satisfies some chosen criteria. With this technique the atmospheric parameters are corrected simultaneously on the whole set of tangent heights (and therefore in all atmospheric layers) and a complete new iteration is performed. Such an approach is appropriate and well founded, when the relative populations of energy levels strongly depend on the changes in the atmospheric model (for example, the temperature retrieval).

To increase the signal to noise ratio (S/N), which substantially decreases in the upper atmosphere, the individual measured spectra were integrated over the frequency. The convolved simulated spectra are integrated in the same way, and the retrieval procedure uses the integrated intensities for calculating the corrections to the atmospheric model. The fitting of spectra can still be compared, however only as a way of the retrieval validation.

The computer code ALI-ARMS used in this dissertation implements the *forward fit* technique and the differential DFE radiative transfer algorithm (see Appendix D.4.2 (p. 103)). The trace gas number densities retrieved with ALI-ARMS are compared with those obtained by using the Wuppertal non-LTE limb code “LIRA-II”. The latter utilizes the integral approach to solve the equation of radiative transfer (MLC in Appendix D.3.1 (p. 101)) and the “onion peeling” technique. The results of CO₂ and O₃ number density retrieval show very good agreement between these two different methods.

5.3 Non-LTE retrieval of CO₂ densities

Tab. 5.2 (p. 31) identifies two spectral channels with CO₂ spectral signatures in the upper mesosphere and lower thermosphere, namely SCS2 and SCL2. A sensitivity study was performed to decide which channel to use for the retrieval of CO₂ number density.

The CO₂ volume mixing ratio profiles used in this study are given in Fig. 5.12 (p. 43). The reference profile (thick black solid curve) corresponds to that used by *Shved et al.*(188) and by *Fomichev et al.*(56) (see the latter paper for the details of its derivation). It is close to the profile used by *Nebel et al.*(153), which is based on the same experimental data (see *Wintersteiner et al.*(219)). This profile was additionally rescaled from the constant value of 330 ppmv for altitudes lower than 85 km to 360 ppmv. Two profiles in Fig. 5.12 (p. 43) are labeled as “ATMOS-mean” and “ATMOS-min”. The former was obtained by averaging the complete envelope of Atmospheric Trace Molecule Spectroscopy (ATMOS) data for March-April 1992 (*Gunson et al.*(72)), whereas the latter gives the lower boundary of this envelope. These two profiles were selected for the tests as they represent the maximum deviation from the reference one.

The pressure and temperature data taken from the CRISTA LTE retrieval below the altitude of 80 km were combined with the MSISE-90 climatology for the same day and time, and the resulting model was used for all calculated signals. One can see from Fig. 5.13 (p. 43) that down to tangent heights of about 75 km the simulated signal at a given tangent height exhibits high sensitivity to the input CO₂ number density. This reflects the fact that the 4.3 μm transitions which dominate the signal in this height region remain optically thin: above 95 km it is the CO₂ (626) fundamental band transition, below this altitude these are CO₂ (626) second hot transitions (see Appendix H.1 (p. 119)). One may also see in Fig. 5.13 (p. 43) that both reference profile and the “ATMOS-mean” profile produce signals which are significantly higher than the measured one, although the “ATMOS-mean” CO₂ volume mixing ratio is much lower than the reference one below 90 km. Only the “ATMOS-min” distribution which has significantly lower values in the altitude region 70–130 km produces a signal which is lower than the experimental one for tangent heights between 80 and 100 km. However it is still higher than the latter outside of this region.

The variation of other model parameters confirmed that at daytime the asymmetric stretch vibrational mode (ν_3) of CO₂ is excited above 110 km predominantly by absorption of the solar photons. The emitted radiation in the 4.3 μm band from an atmospheric volume is primarily a function of the local solar zenith angle, intensity of the incoming infrared solar radiation and the CO₂ number densities. Therefore, one can use the signal in the SCS2 channel for the CO₂ number density retrieval.

The retrieved CO₂ volume mixing ratios for three selected CRISTA-1 profiles are shown in Fig. 5.14 (p. 44). Compared to the reference profile in Fig. 5.12 (p. 43), they provide significantly decreased CO₂ volume mixing ratio in the altitude regions of 75–90 and 105–125 km. *López-Puertas et al.*(120) found that a similar decrease of the CO₂ number density in the altitude region 70–100 km allowed better fitting of the daytime wideband channel radiances measured by Improved Stratospheric and Mesospheric Sounder (ISAMS) on the Upper Atmospheric Research Satellite (UARS).

CO₂ number densities obtained from CRISTA-1 data were used later for the calibration of CRISTA-2 radiances in the SCS2 channel. The profiles retrieved using a “forward fit” were compared with the data produced by “onion peeling” method. The excellent agreement made it possible to process all daytime CRISTA-1 and CRISTA-2 spectra using the “onion peeling” technique, which requires less computer time. The global CO₂ number density maps for further use by atmospheric models and other analyses were published by *Kaufmann et al.*(87).

The reduced CO₂ number density in the upper mesosphere and lower thermosphere has a very important geophysical impact. It requires reconsideration of the current models of turbulent mixing and critical reevaluation of the energy budget of this atmospheric region, since CO₂ is the main cooling source (see Appendix H.1 (p. 119)).

5.4 Non-LTE retrieval of O₃ densities

Ozone in the mesopause region is the key substance that controls the atmospheric oxygen and hydrogen chemistry at this altitudes and acts as an important UV absorber and IR cooler. Therefore, it is very important to be able to measure its number density both at daytime and nighttime. CRISTA is very well suited for this task, and there are two possible ways to retrieve ozone number densities from its limb spectral data:

1. to use the 9.6 μm emission from the fundamental ν_3 band 001–000 in the SCS3 channel,
2. to use the 4.8 μm emission from the $\nu_1 + \nu_3$ band 101–000 in the SCS2 channel.

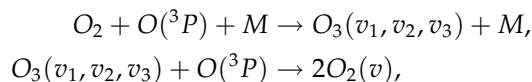
Both approaches have their strong and weak sides, but the first way is the preferred one for two following reasons:

1. the signal and S/N ratio are higher for SCS3,
2. the collisional kinetics is better understood for the levels with lower vibrational energy.

Since the ozone spectra overlap with the 9.4 μm CO₂ laser band 00011–10002 in the SCS3 channel, the latter must be modeled simultaneously with the 9.6 μm O₃ bands. The same applies to the 4.7 μm CO 1–0 fundamental band in the SCS2 channel.

The sensitivity study to the variations of atmospheric input model parameters as well as to the variations of non-LTE model parameters was made for the SCS3 channel. It has shown, that down to the altitude of 70–65 km the signal is affected by non-LTE, and

1. strongly depends on the chemical-vibrational reactions of ozone production and loss (see Appendix C.4 (p. 95))



2. depends weakly on the temperature,
3. does not depend on the absorption of the solar radiation in the infrared bands,
4. does not depend on the variation of $V - V$ energy exchange rates with N₂ and O₂ (at nighttime).

The major difference in the kinetic models described in Appendix B.3 (p. 73), namely the models of Manuilova and the Simple Single Model (SSM) model of Mlynczak is due to the way they account for chemical processes with atomic oxygen. Therefore, depending on the used model of collisional kinetics, the retrieved ozone number densities can differ by a factor of 2 above 80km, as can be seen in Fig. 5.15 (p. 45). At the same time the differences between the O₃ profiles, retrieved using different models of Manuilova is about 5%. The influence of the temperature on the retrieved O₃, simulated by the reduction of mesospheric temperature by 20K above 80 km at polar latitudes (see Lübkens (122)) was also considered in this study. It has resulted in a 10% lower retrieved ozone number volume mixing ratio. Both datasets for reference and reduced temperature profile are plotted in Fig. 5.15 (p. 45).

The results of the ozone number density retrieval have been compared with the measurements made by the Millimeter wave Atmospheric Sounder (MAS) and are given in Fig. 5.16 (p. 45). The MAS experiment measured the emission from the O₃ pure rotational bands, and therefore its data are not affected by the non-LTE. The validation with MAS was possible since it was a simultaneous measurement of ozone by the instrument flying on the same Space Shuttle as CRISTA.

The ozone profiles presented in Fig. 5.16 (p. 45) show good agreement between the results of these two experiments.

Kaufmann et al. (88) has published the results of the O₃ number density retrieval, the comparison with ozone measurements by High Resolution Doppler Imager (HRDI) on UARS and simulations with the NCAR ROSE CTM. See the latter paper for the detailed discussion of the vertical and horizontal distribution of O₃ number densities in the upper mesosphere and lower thermosphere.

5.5 Non-LTE retrieval of temperature

The algorithm described in Section 5.2 (p. 33) for the retrieval of temperature in the mesosphere and lower thermosphere was applied to CRISTA-1 and CRISTA-2 limb measurements in the SCL2 channel.

Three parameters are necessary to process the data: (1) the CO₂ number density or volume mixing ratio, (2) the O(³P_J) number density and (3) the rate constant of CO₂ V – T quenching by O(³P_J). If they are known, temperature is the only unknown parameter. Let us consider these parameters more closely. Through its flight geometry CRISTA-1 allows global coverage at daytime, while CRISTA-2 daytime scans are limited mainly to the northern hemisphere. To derive the nighttime temperatures a reference average daytime CO₂ number density profile was used and the atomic oxygen O(³P_J) number densities were taken from the GRAM-95 model. For daytime the CO₂ and O(³P_J) number densities are retrieved from CRISTA measurements: the former directly from the SCS2 channel (Section 5.3 (p. 35)) and the latter indirectly through the O₃ from SCS3 channel (Section 5.4 (p. 36)), since it is assumed that O₃ and O(³P_J) are in photochemical equilibrium.

The rate constant of the CO₂ (ν₂) + O(³P_J) collisional deactivation at thermospheric temperatures was taken from *Sharma and Wintersteiner* (184) and lies at the upper boundary of the published values (see Appendix C.2.2 (p. 84) for details).

The altitude profiles of zonally averaged temperatures retrieved for CRISTA-1 and CRISTA-2 are shown in Fig. 5.17 (p. 46) and the respective altitude-latitude cross-sections are given in Fig. 5.18 (p. 47). From these figures one can see that during the CRISTA-1 flight (November 1994) the upper mesosphere was warm (above 180 K) and the mesopause lies at altitude around 100 km for all latitudes. At high southern latitudes the mesopause lies below 85 km. For CRISTA-2 (August 1997) the situation is similar: while the mesopause lies around 100 km between 72°S and 55°N it sharply drops to 85 km at higher northern latitudes. This behaviour is called “two-level mesopause”. It was recently observed by *She and von Zahn* (185) and the theoretical explanation is found in modeling results of *Berger and von Zahn* (18). Under polar summer conditions the mesopause was not only found at a lower altitude, but its temperature was as low as 120 K for some CRISTA-2 altitude scans. However, such values are not the absolute minimum that can be reached. *Lübken* (122) reported even lower values for July, which are based on his rocket and lidar soundings.

While the retrieved averaged temperatures are in a good agreement with the climatological models, the following differences are of particular interest:

1. At high northern latitudes in summer the mesopause temperatures are lower than the predictions of both MSISE-90 and GRAM-95 models.
2. The temperatures in the thermosphere for both CRISTA-1 and CRISTA-2 flights are in a good agreement with the MSISE-90 predictions, which are significantly warmer than those from GRAM-95.

In the vicinity of the high latitude summer mesopause, where the deviation from LTE happens at lower altitudes than usual, a good agreement is found with the climatology of *Lübken* (122), based on the rocket measurements with the falling spheres.

Further data processing will increase the spatial density of the available retrieved data and allow to investigate not only latitudinal but also the longitudinal temperature variations and wave

activity in the mesosphere and lower thermosphere.

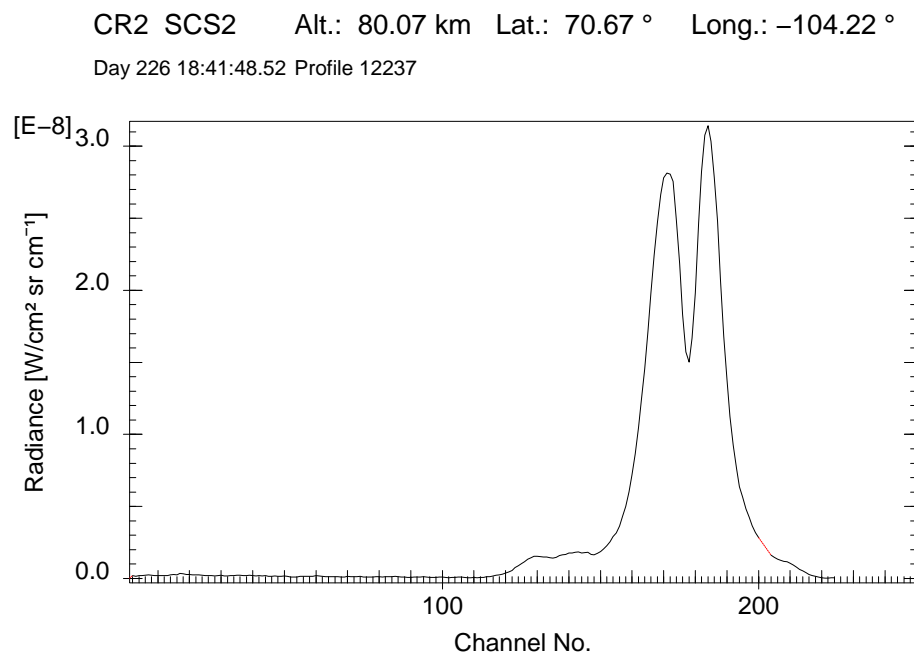
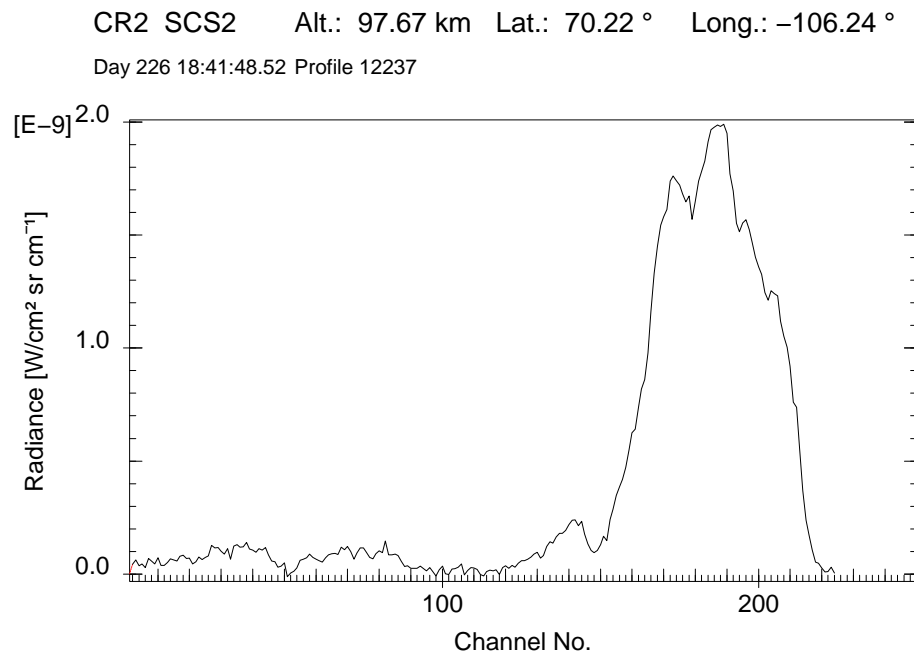


Fig. 5.6 The measured daytime limb spectra in the SCS2 CRISTA channel at different tangent heights

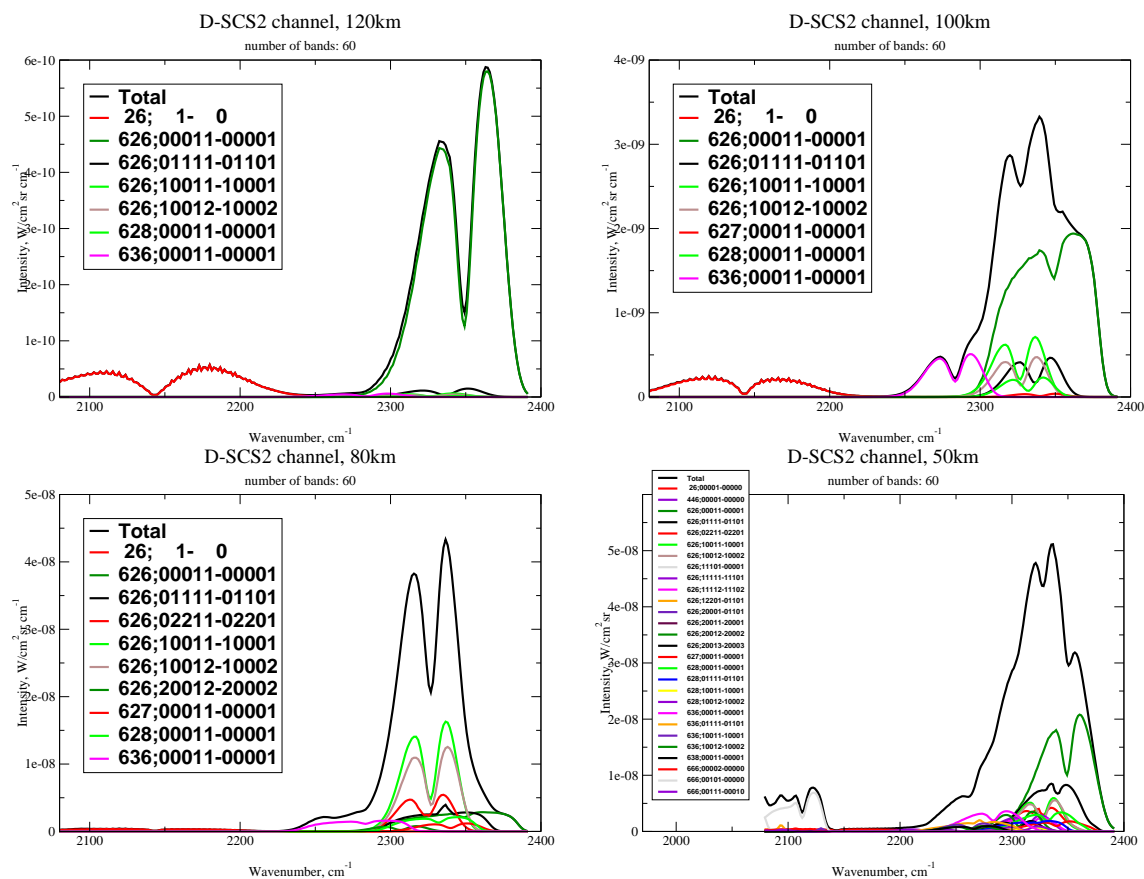


Fig. 5.7 The simulated spectra in the SCS2 CRISTA channel at different tangent heights (daytime)

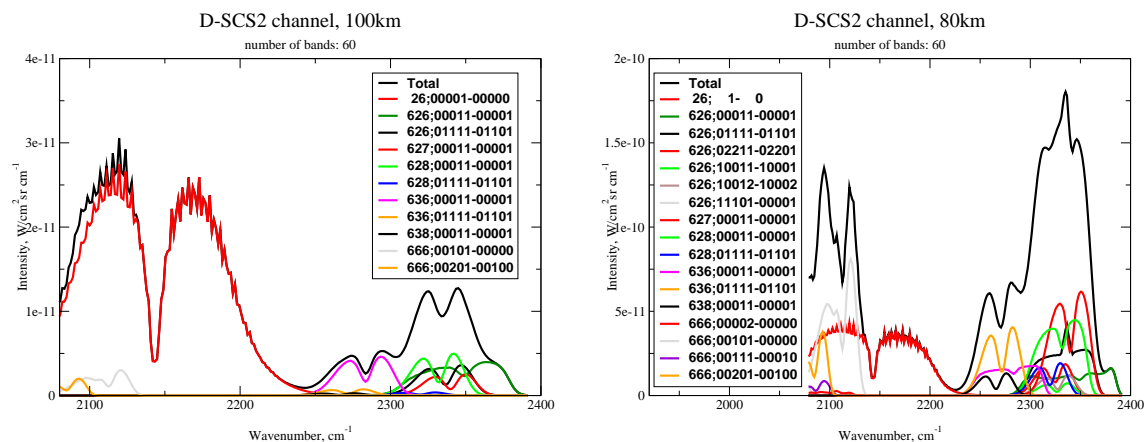
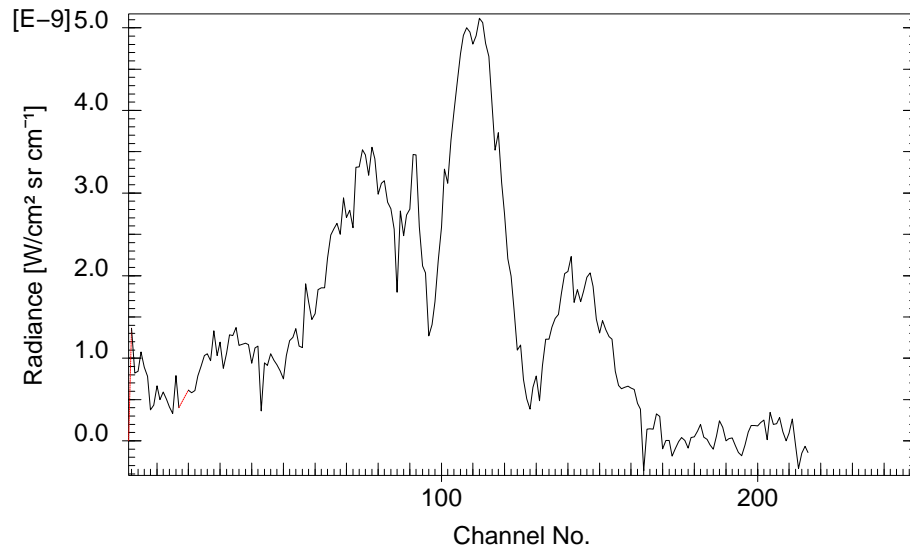


Fig. 5.8 The simulated spectra in the SCS2 CRISTA channel at different tangent heights (nighttime)

CR2 SCS3 Alt.: 77.86 km Lat.: 70.73 ° Long.: -104.12 °

Day 226 18:41:48.52 Profile 12237



CR2 SCS3 Alt.: 86.68 km Lat.: -70.24 ° Long.: 65.56 °

Day 226 19:27: 3.99 Profile 12280

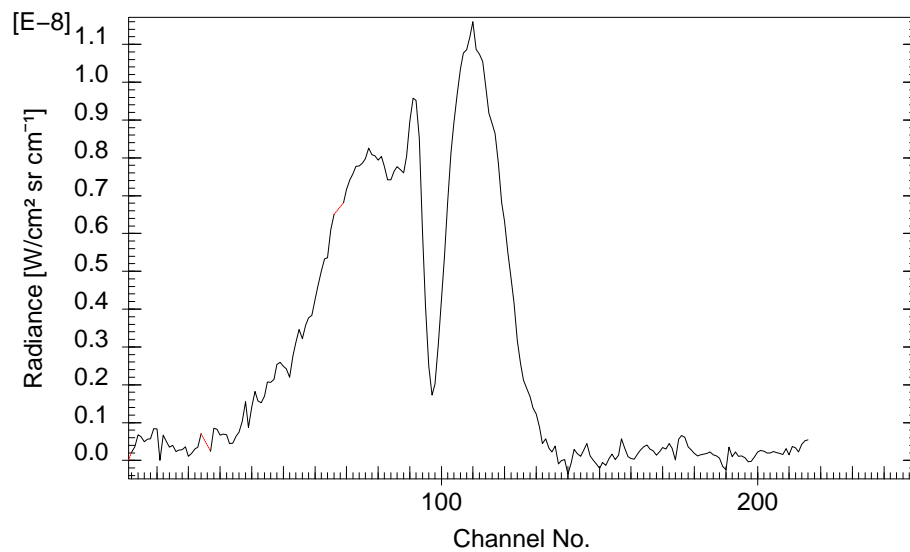


Fig. 5.9 The measured limb spectra in the SCS3 CRISTA channel (day/night)

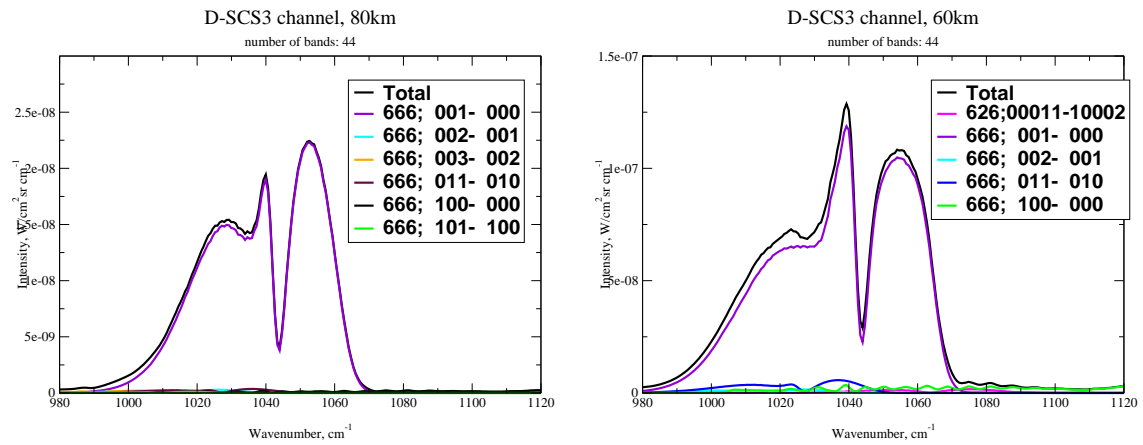


Fig. 5.10 The simulated spectra in the SCS3 CRISTA channel at different tangent heights (nighttime)

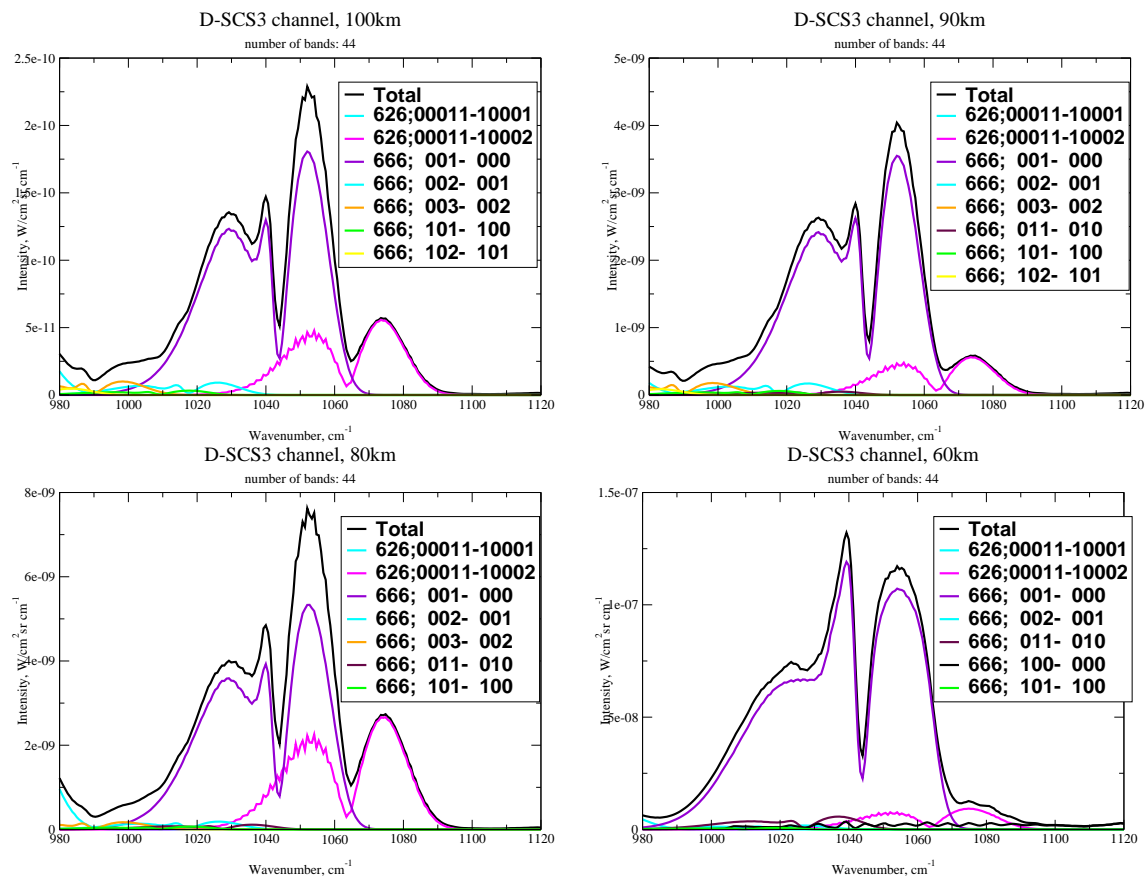


Fig. 5.11 The simulated spectra in the SCS3 CRISTA channel at different tangent heights (daytime)

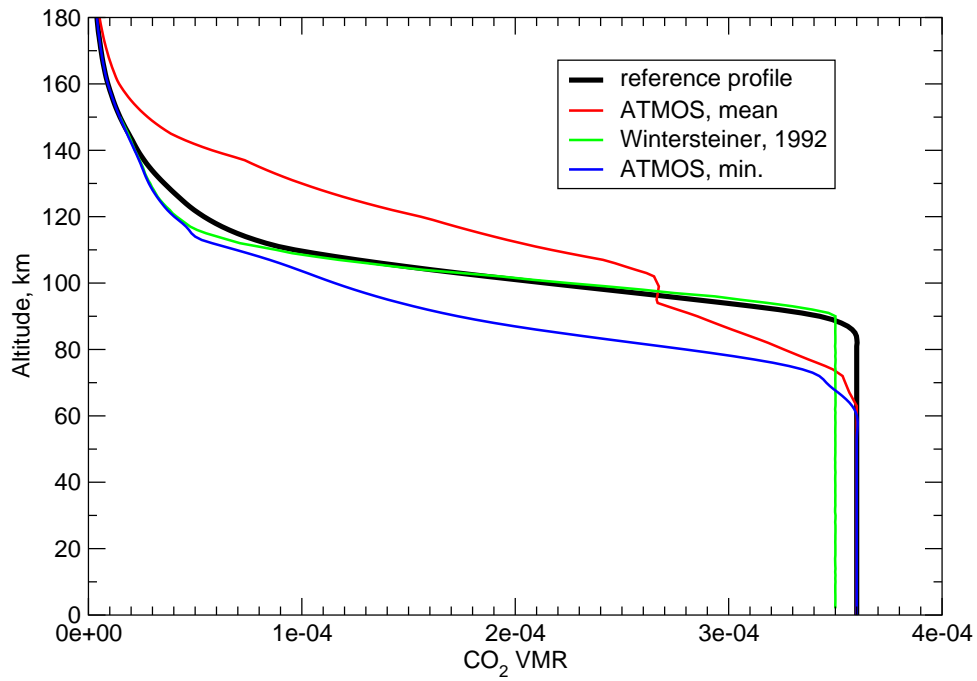


Fig. 5.12 CO₂ volume mixing ratios.

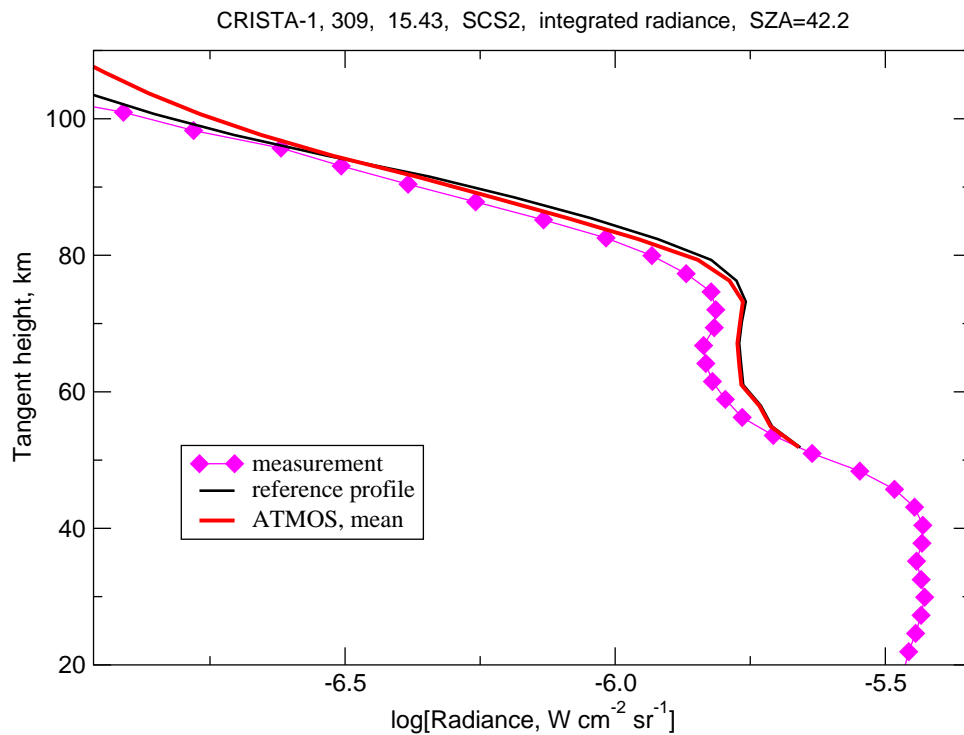


Fig. 5.13 Integrated limb radiances in the SCS2 channel for selected CO₂ profiles

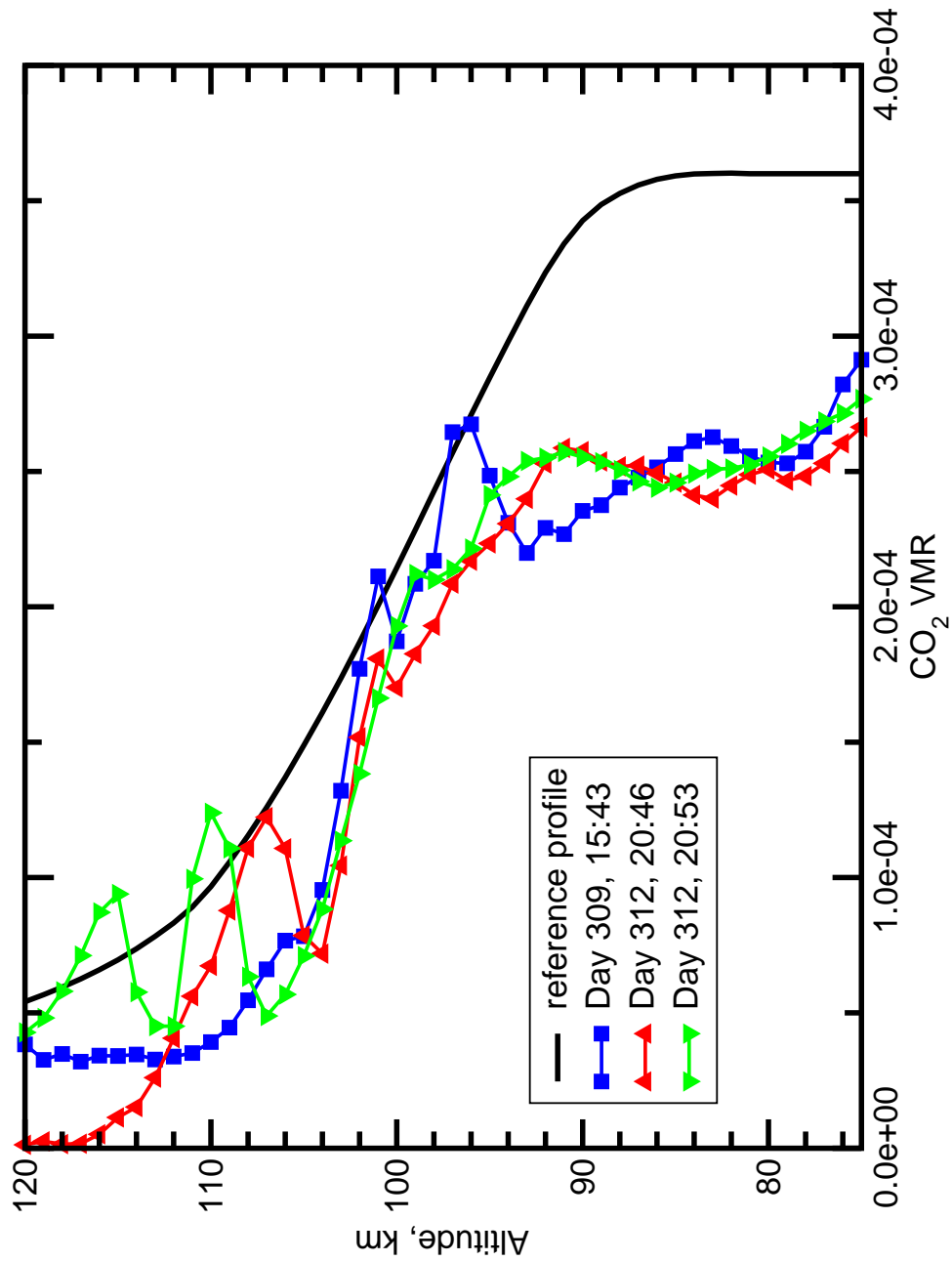


Fig. 5.14 Retrieved CO₂ VMR for selected CRISTA-1 profiles.

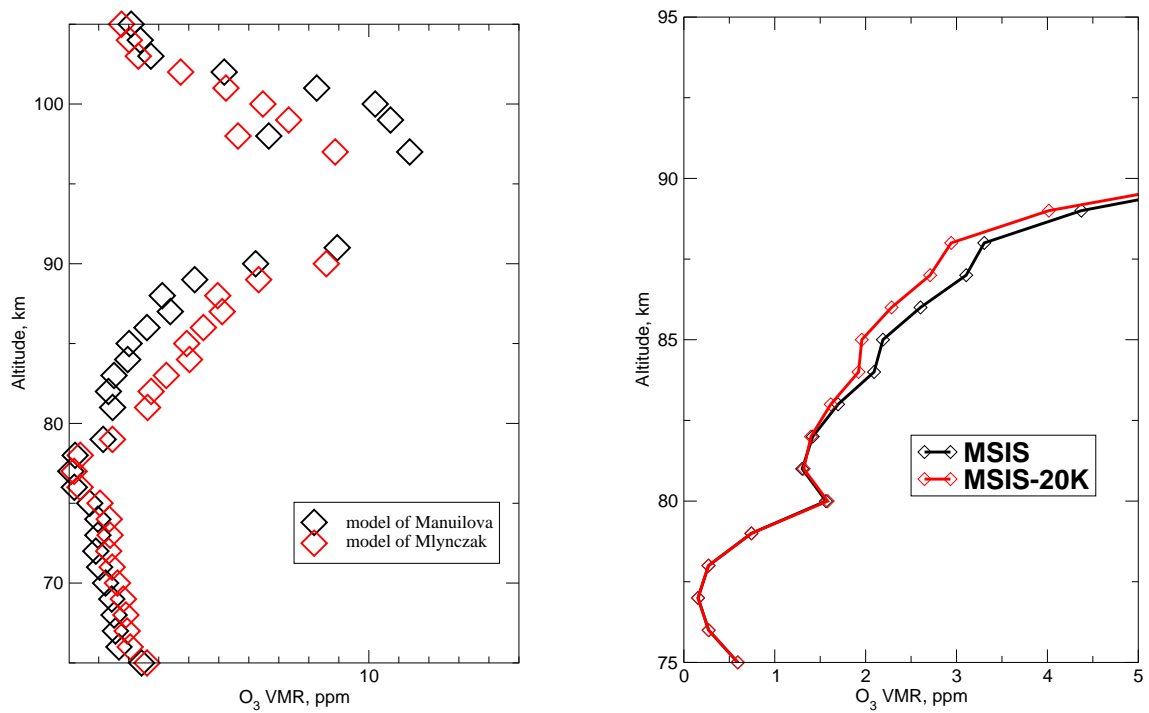


Fig. 5.15 Effects of the reduction of temperature in the mesosphere and different kinetic models used for the ozone number density retrieval

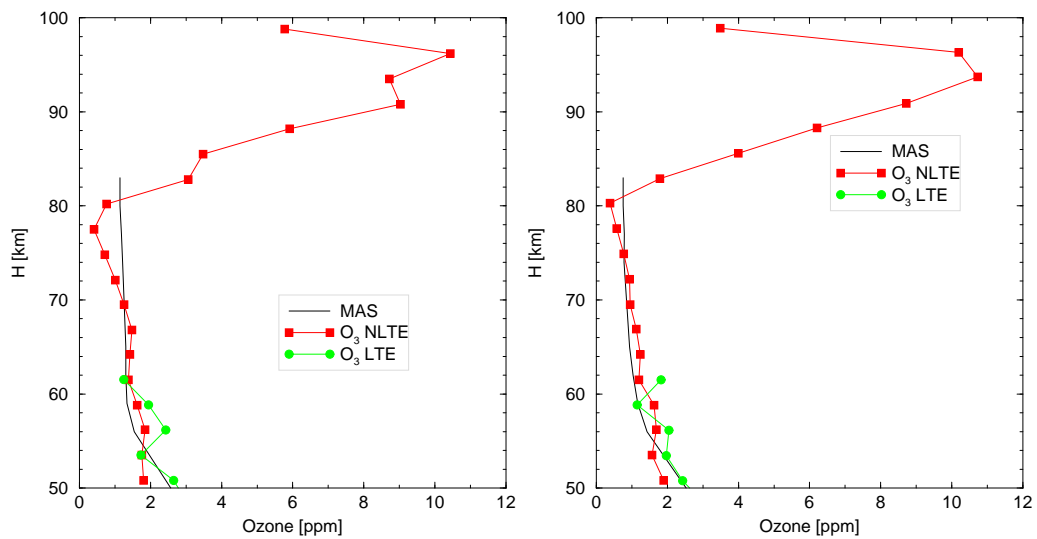
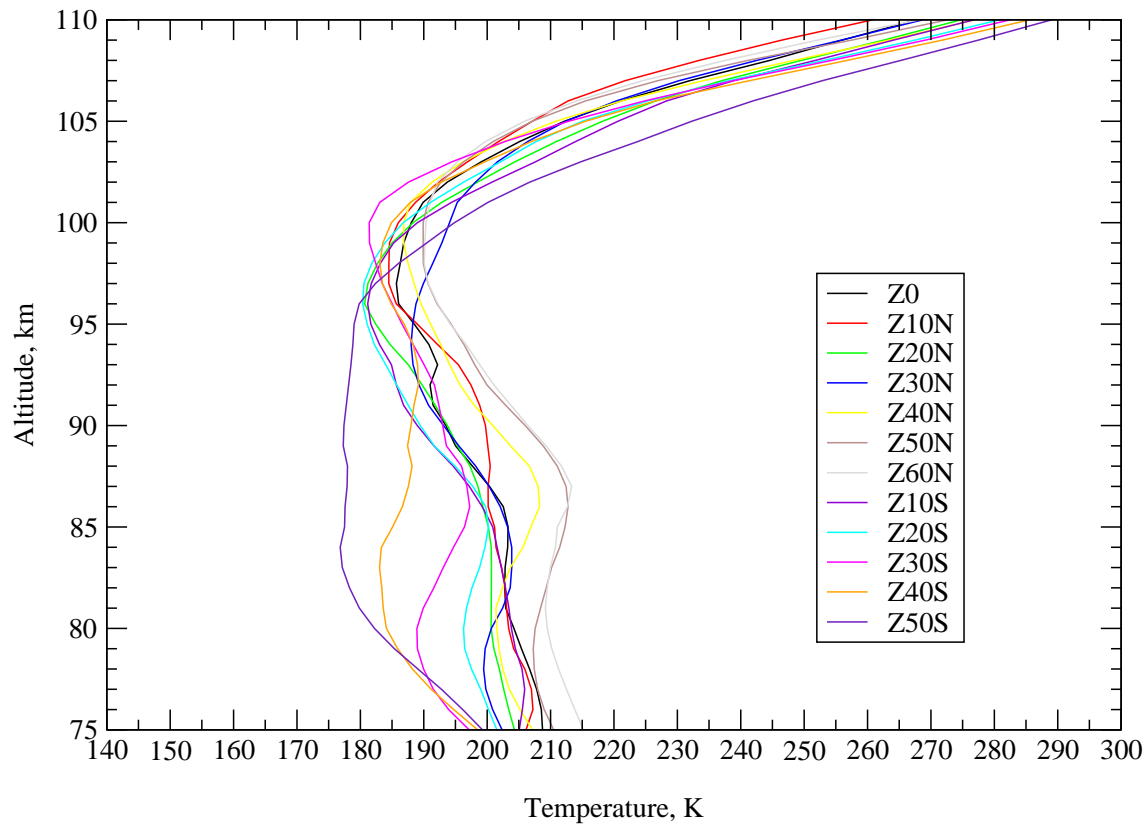


Fig. 5.16 The profiles of retrieved non-LTE O₃ VMR, the LTE retrieved O₃ VMR and the MAS measurement

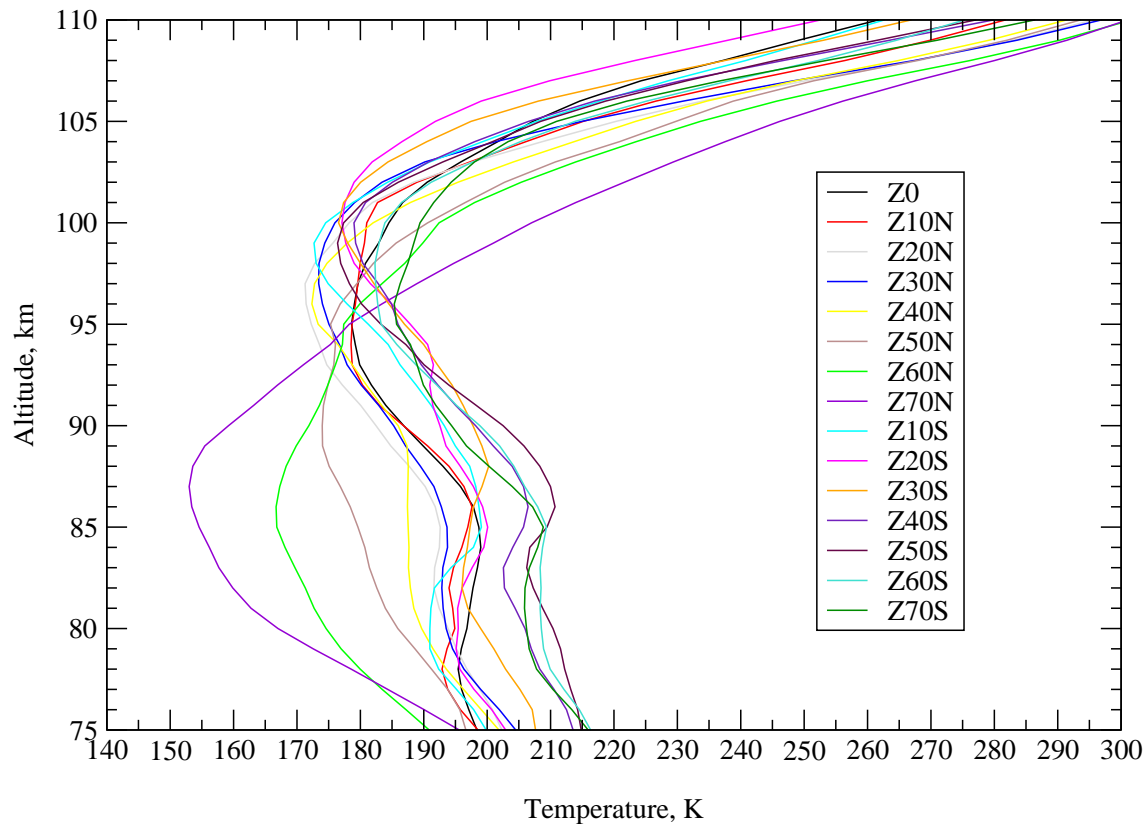
CRISTA-1, zonal averages

High Altitude scans



CRISTA-2, zonal averages

Extended scans



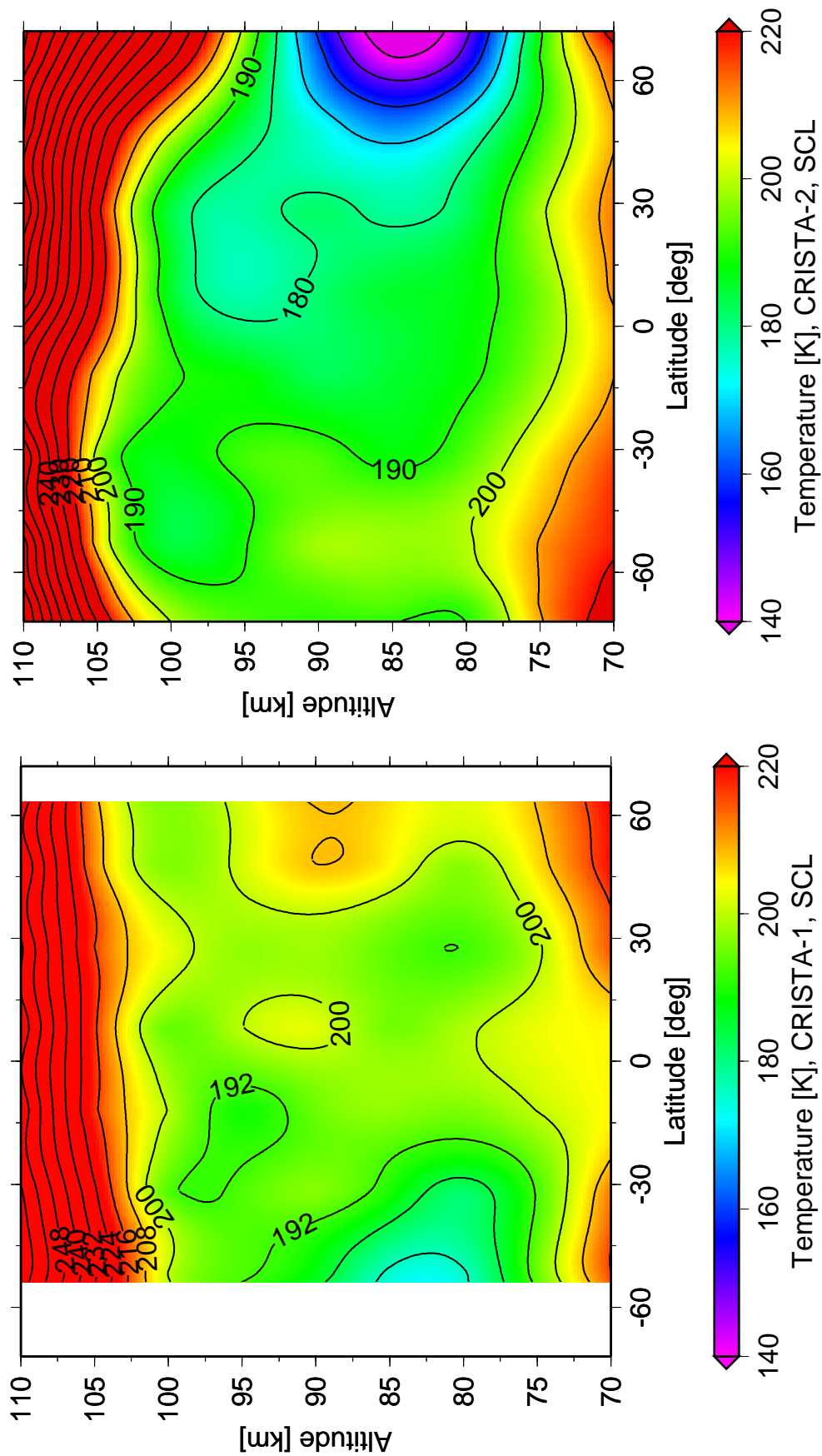


Fig. 5.18 The zonal temperature cross-section (bottom: CRISTA-1, top: CRISTA-2).

6. Applications of ALI-ARMS: analysis of the TES/MGS observations of the Martian atmosphere

Mars Global Surveyor (MGS) launched on 7 November 1996 was successfully put into an eccentric orbit around Mars on 11 September 1997. After completion of the aerobraking phase of the mission, MGS began the mapping phase in a sun-synchronous, polar circular orbit. During this phase, MGS instruments perform the measurements of the Mars surface and atmosphere.

The Thermal Emission Spectrometer (TES) on MGS is a Michelson interferometer covering the spectral range $200\text{-}1650\text{ cm}^{-1}$ (see *Christensen et al.*(30)). A rotating pointing mirror allows limb scans of the atmosphere from the surface to altitudes about 120 km.

Betz (19) and *Betz et al.*(20) first reported non-thermal $10\text{ }\mu\text{m}$ CO_2 emission in the atmospheres of Mars and Venus. *Deming and Mumma* (35) created a theoretical model for the 9.4 and $10.4\text{ }\mu\text{m}$ bands and made the observations of these bands in the Mars and Venus atmospheres. *López-Valverde et al.*(207; 208) have developed a more detailed non-LTE model, including a large number of CO_2 bands. However these authors were using several approximations in radiative transfer calculations that were discussed in Section 4 (p. 19).

To model the populations of the vibrational states with ALI-ARMS the CO_2 and N_2 volume mixing ratios were taken from *López-Valverde et al.*(207) and are given in Appendix F.2 (p. 111). The temperature altitude profiles up to 65 km were derived under LTE assumption from TES CO_2 $15\text{ }\mu\text{m}$ limb radiances using k -correlated approach (*Conrath et al.*(33)). The retrieval results for 24.01.2000 are shown in Fig. 6.3 (p. 50) together with the daytime and nighttime surface temperatures. The temperature profiles retrieved by TES were extended above 65 km by smooth linking with model temperature profiles of *Rodrigo et al.*(175).

The vibrational temperatures of CO_2 (626) are provided in Fig. 6.2 (p. 49) and Fig. 6.1 (p. 49) for nighttime and daytime respectively. It can be seen that the CO_2 (626) 01101, 02201 and 03301 vibrational levels and therefore the $15\text{ }\mu\text{m}$ limb radiation stemming from them are thermalized up to about 100 km. Above this altitude the diurnal variation in the populations of these levels is small. These figures also demonstrate the strong diurnal change in the populations of CO_2 (626) 00011 vibrational level, from which the major part of $10\text{ }\mu\text{m}$ emissions originate.

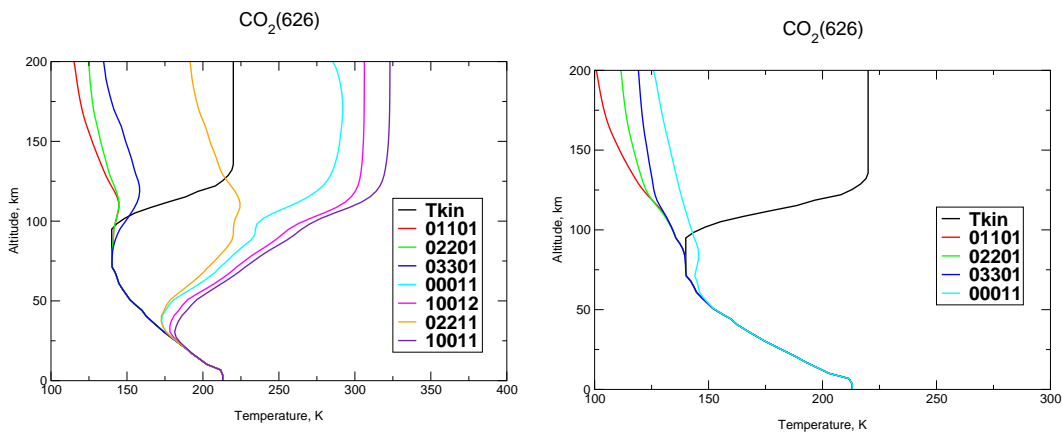


Fig. 6.1 The vibrational temperatures for CO_2 (626) levels (daytime). **Fig. 6.2** The vibrational temperatures for CO_2 (626) levels (nighttime).

The $10\text{ }\mu\text{m}$ emission is generally visible in the TES spectrum over $\approx \pm 60^\circ$ of latitude North and

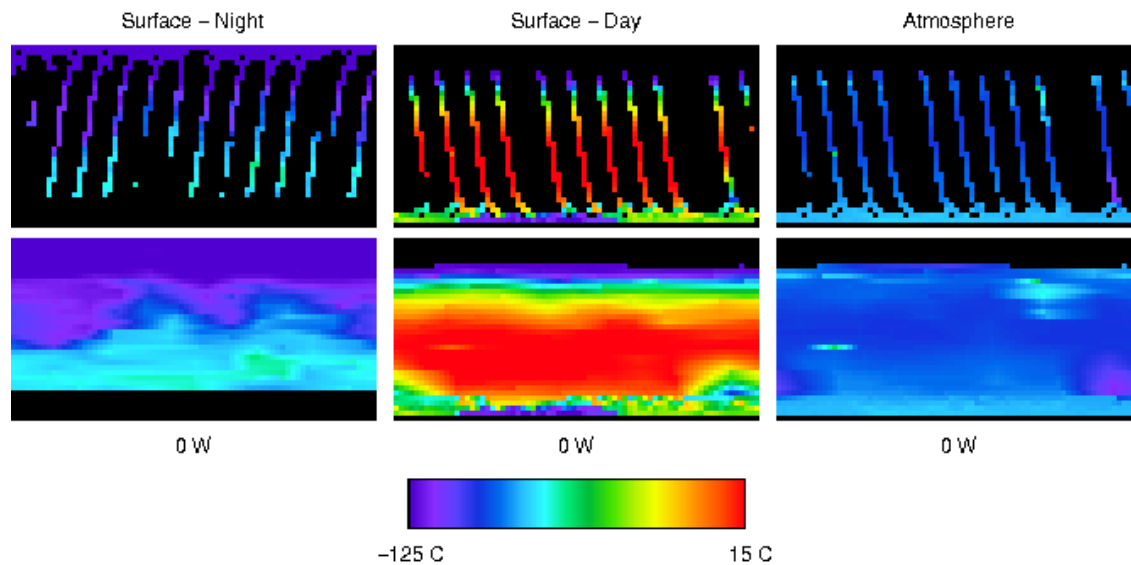


Fig. 6.3 The temperatures in Mars atmosphere and on its surface, measured by MGS/TES.

South of this point in each of the four seasons. *Maguire et al.*(126) have made the ALI-ARMS simulations of $10\ \mu\text{m}$ emission to account for the global, seasonal, diurnal dependence of this emission between 40 and 120 km and compared them to the observed averaged limb radiances. Fig. 6.4 (p. 51) provides the measured $10\ \mu\text{m}$ integrated intensities, which are represented by the background colour. The simulated values are given in the same picture by contour lines. The modeling showed that the ratio of non-LTE to LTE radiances in the TES spectrum reaches a maximum of more than 200 at 70 km altitude, decreasing to 20 within a few scale heights at higher and lower altitudes. It was shown that the centroid of the excited daytime (2 p.m.) region always follows the subsolar latitude. Excitation is absent at night (2 a.m.) except during summer solstice conditions when the summer polar region is illuminated throughout the day. In addition, band intensities are considerably stronger in the ($260 < L_s < 280$) southern summer/northern-winter season than in the corresponding northern-summer/southern-winter ($104 < L_s < 124$) season, due to the eccentricity of the martian orbit, which results in 40% more solar flux in the former season than in the latter. Here L_s is the heliocentric longitude as seen from Mars, and $L_s=0$ is the northern vernal equinox.

The comparison between measured and modelled limb radiances in $10\ \mu\text{m}$ bands, provided in Fig. 6.4 (p. 51), shows good quantitative agreement that confirms the high quality of non-LTE modeling with ALI-ARMS. Therefore, the application of ALI-ARMS retrieval algorithm is planned in the near future for the derivation of temperature under non-LTE conditions from the TES $15\ \mu\text{m}$ emissions.

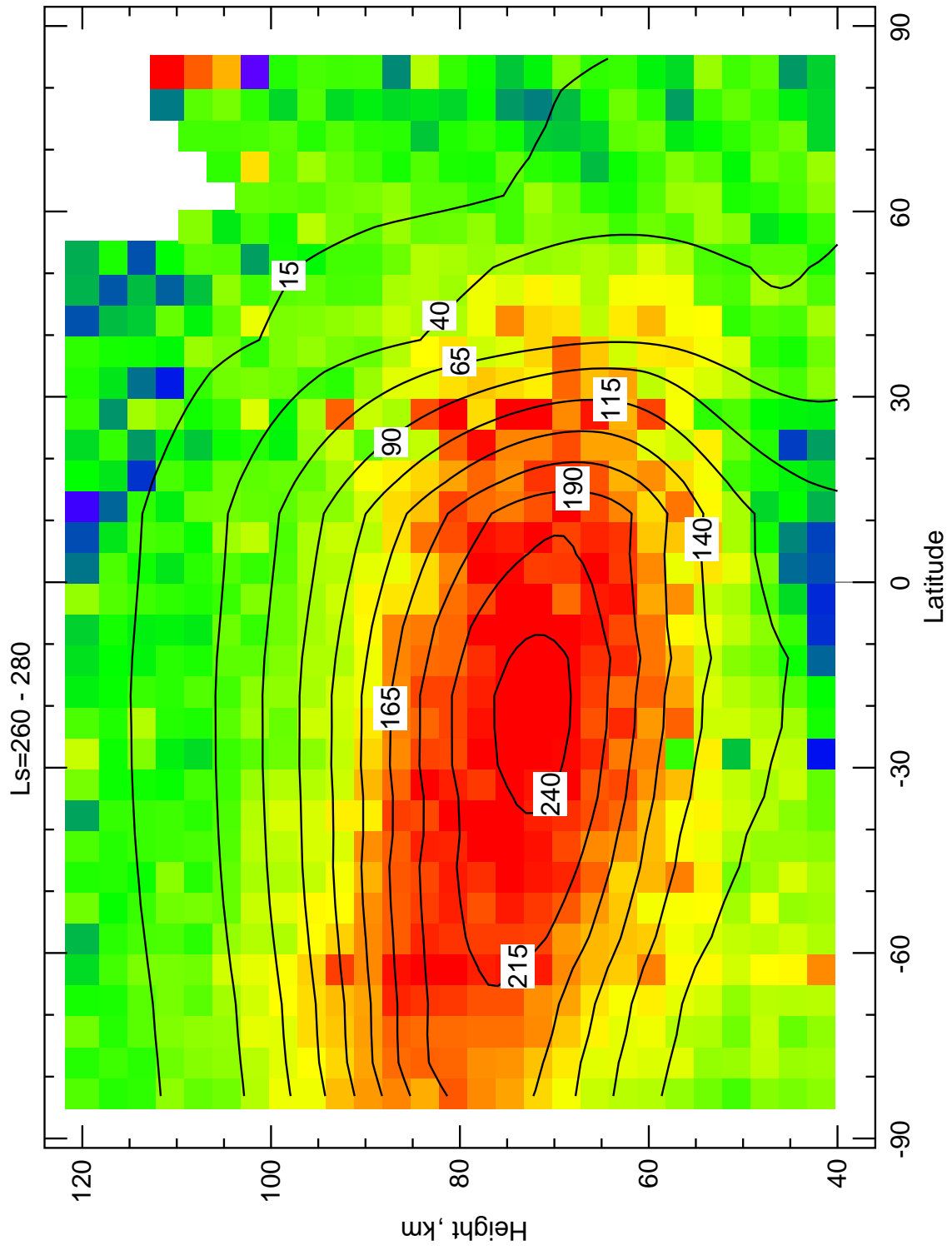


Fig. 6.4 Global distribution of the emissions in CO₂ 10 μm laser band: modelled (contour lines) and measured by MGS/TES. The figure is taken from Maguire et al. (126).

7. Applications of ALI-ARMS: vibration-rotational non-LTE in CO₂ in the Earth atmosphere

Rotational non-LTE have been demonstrated by the observation of pure rotational emission in OH, NO and CO in the Earth's upper mesosphere/lower thermosphere by a number of satellite and Earth-based experiments. The theoretical studies of this effect were done by *Kutepov et al.* (99) for CO and later by *Funke and López-Puertas* (57) for NO. The breakdown of rotational LTE in the Earth atmosphere for CO₂ was investigated with ALI-ARMS code and the results of this study are discussed below.

The analysis of the rotational distribution functions $W_v(j)$, introduced in Section 2.3 (p. 5) for the considered vibrational levels shows that for the ground level CO₂ (00001), rotational LTE is valid throughout the atmosphere both for day and night conditions. This results from the relatively low degree of vibrational excitation of CO₂ when the majority of molecules remains in the ground state and therefore have enough time to be rotationally thermalized. The same is also true for the CO₂ (01101) first excited vibrational level, due to its low vibrational energy. However, the rotational distribution functions for the CO₂ (00011) level that are given in Fig. 7.1 (p. 55), show that for the molecules in the first ν_3 excited vibrational state in the upper atmosphere rotational LTE is broken above certain altitude.

At nighttime three sources determine the population of CO₂ (00011) in the upper atmosphere, namely the absorption of the upwelling radiation from the stratosphere, the absorption of atmospheric radiation and the excitation by the $V - T$ and $V - V$ collisions. At the altitudes of 180 and 150 km the $R - T$ processes are rather inefficient and cause only minor transformations of these sources. As a result the rotational non-LTE distribution $W_v(j)$ exhibits significant departures from the rotational LTE distribution. Its well developed primary maximum is related to the maximum of the source of radiative excitation by absorption of radiation from the lower boundary. The secondary maximum at these altitudes for $j = 80 - 90$ can be explained by the relatively small optical thickness of these lines in comparison with those at the LTE maximum. The upwelling radiation coming from the lower atmospheric layers in these thinner lines causes their higher population in comparison with the lower j . At 100 km the nighttime radiative excitation by absorption of atmospheric radiation from the troposphere and the stratosphere prevails over all other excitation sources. The rotational structure of this source is very close to the LTE distribution. As a result, the CO₂ (00011) level appears to be completely thermalized and has the LTE rotational distribution.

Comparing the daytime distribution functions with those for the nighttime conditions one can conclude that the absorption of the solar radiation from the rotationally thermalized vibrational ground state CO₂ (00001) significantly dominates the initial excitation for all j . Thus the rotationally thermalized fraction of the CO₂ (00011) molecules increases. This weakens the effects of rotational non-LTE: if at 180 and 150 km the rotational non-LTE distribution still differs from the equilibrium one, then already at the altitude of 120 km one may observe only minor differences between the two distributions. At daytime the CO₂ (00011) level may be considered as completely thermalized already below 140 km.

In order to estimate the effect of the rotational non-LTE on the spectral distribution of the limb radiances the monochromatic limb radiances in each individual line were integrated over its frequency profile and the resulting values were assigned to the corresponding line center frequencies. The spectra are also presented for the complete rotational LTE.

Due to the nonequilibrium distribution of the rotational sublevels of the CO₂ (00011) vibrational level, the limb radiances at corresponding tangent heights look very different from rotational LTE radiances (see Fig. 7.2 (p. 56)). One can see that even for the tangent heights, where the LTE distribution function is restored due to increased probability of collisions (for example, 80 km), the contribution of the higher atmospheric layers with nonequilibrium rotational distribution is

57. Applications of ALI-ARMS: vibration-rotational non-LTE in CO₂ in the Earth atmosphere

still significant.

For the daytime conditions the rotational non-LTE effects in limb spectra are weaker, reflecting a much stronger degree of thermalization of CO₂ (00011) molecules. Although they are visible in spectra at tangent heights of 140 and 120 km, they completely vanish at 90 km.

It was shown in Fig.7.2 (p.56) that the spectral distributions of line radiances for the tangent heights above 120 km closely reproduce the nonequilibrium rotational distributions of emitting molecules at the tangent point. On the other hand, above 140 km the $R - T$ processes are rather inefficient and the nonequilibrium rotational distribution closely follows that of the total source of excitation. Therefore, if one derives the rotational distribution from spectral limb measurements, one also obtains a good estimate of the source of excitation. If adequate information on the atmospheric temperature profile and the volume mixing ratios is available, one could model the radiative components of the total source. In such a way one can extract the contribution of the collisional sources of excitation and make certain conclusions about the collisional relaxation rates.

This analysis shows that the retrieval of temperature from the limb spectra in the 4.3 μm spectral region for both CO₂ and CO at nighttime will be seriously distorted at the altitudes above 110 km as a result of the breakdown of rotational LTE.

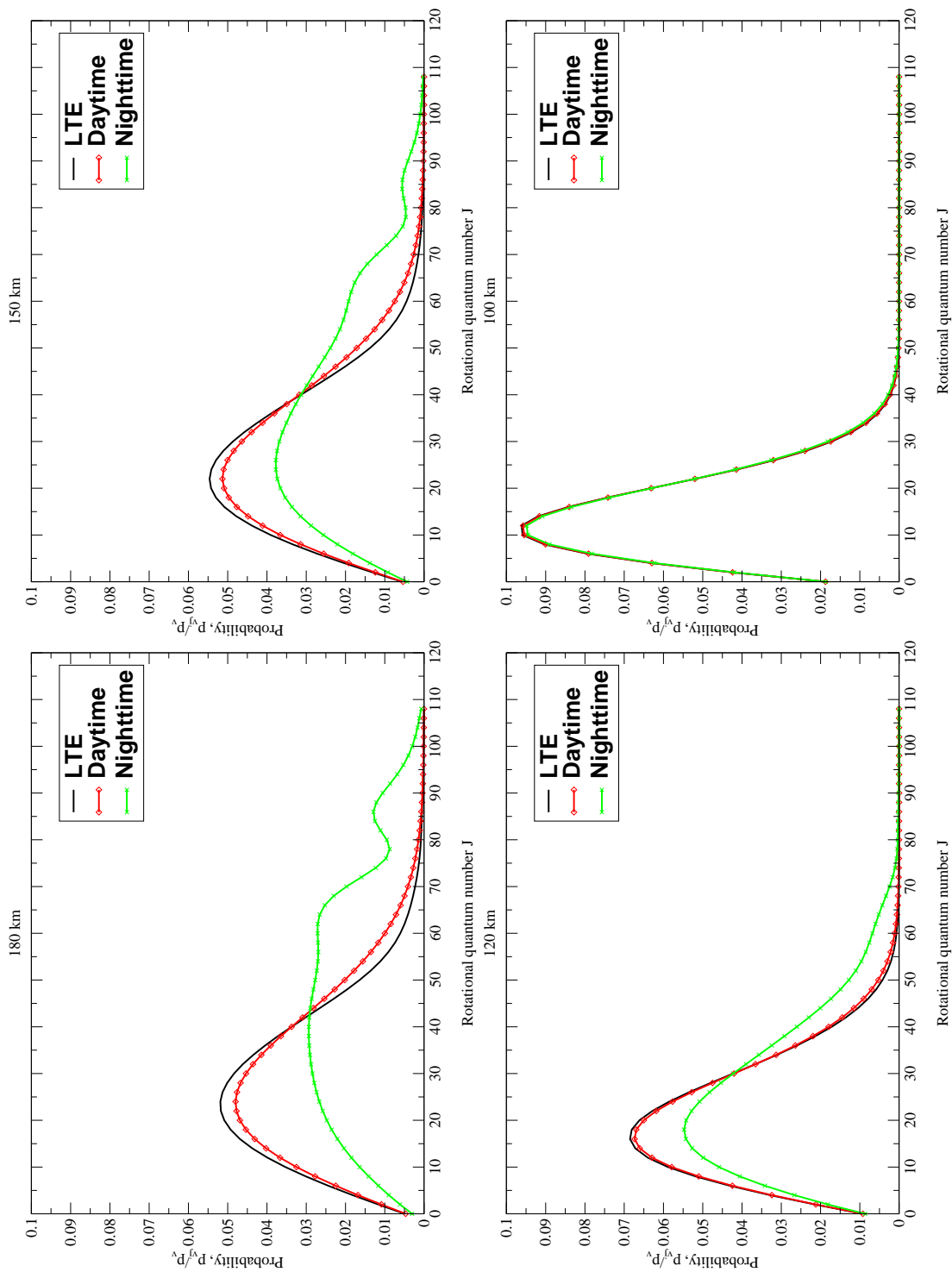


Fig. 7.1 The rotational distribution functions for the vibrational level 00011 of CO₂ (626) at different altitudes

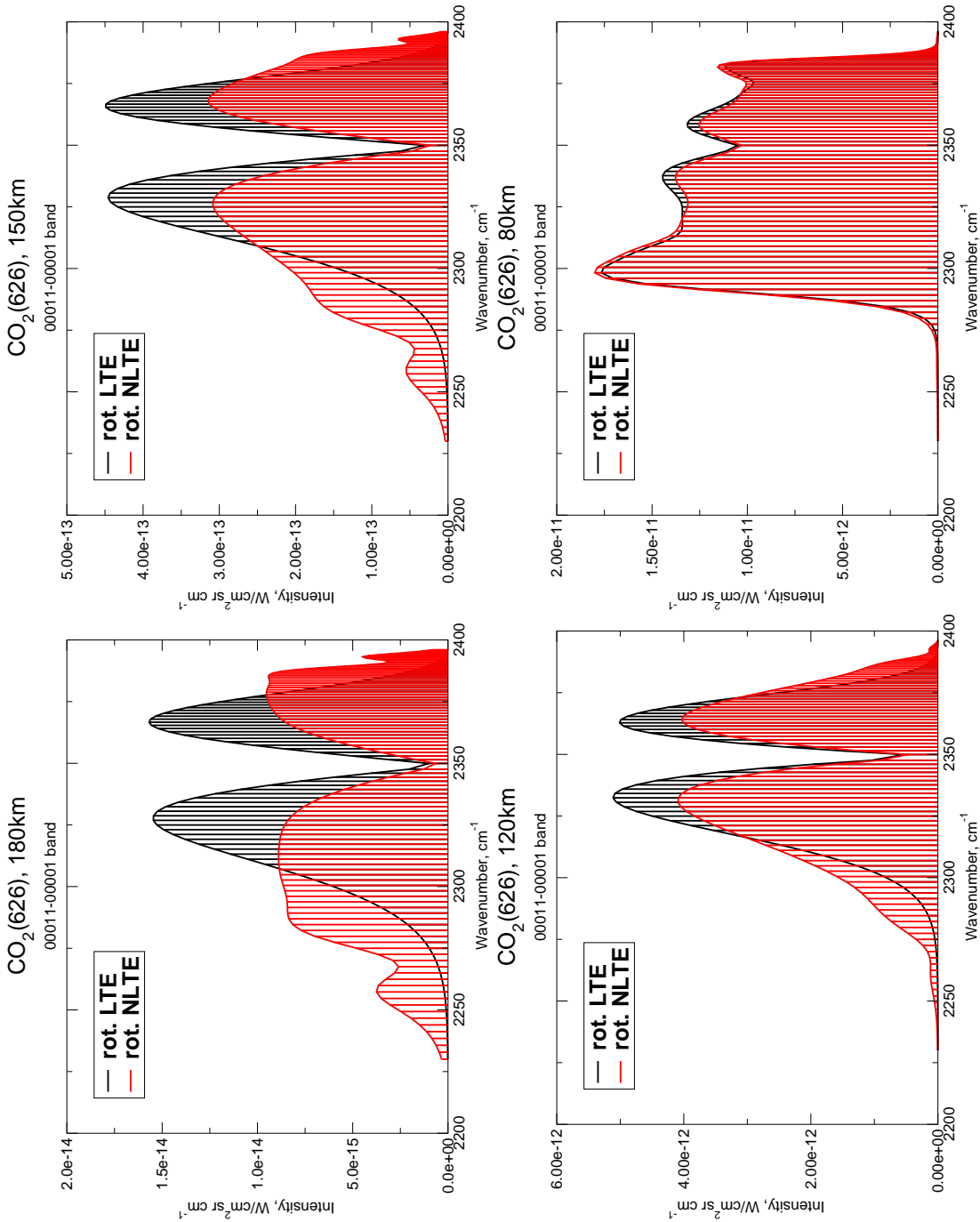


Fig. 7.2 The nighttime limb radiances for the CO₂ (626) 00011 → 00001 band at different tangent heights. Effects of the rotational LTE breakdown.

8. Conclusions

The computer code package ALI-ARMS compiled in framework of this study allows non-LTE treatment of arbitrary number of molecules interacting by collisionally induced exchange of energy and by the band overlaps. None of the other codes available in planetary studies have this capability. This is possible primarily because of the high efficiency and the flexible nature of the ALI approach adopted from the stellar astrophysics which easily deals with the nonlinearities introduced by collisions and by the overlapping lines. This is a major advance in the ability to treat more realistic models, in addition of being able to deal with a very large number of transitions and levels.

The ALI-ARMS is a line-by-line code for the general multilevel and multimolecular rovibrational non-LTE problem. It is free from many approximations used in MCM (matrix) and ARC (conventional lambda iteration) techniques and is far superior to both of them in minimizing computer time and storage and in converging much more rapidly; moreover, the convergence rate was insensitive to the initial population estimates and to a wide range of variation in the model input parameters.

The current ALI-ARMS code version is suitable for simultaneous self-consistent solution of the non-LTE problem for a number of molecules and atoms in the atmospheres of Earth (CO_2 , O_3 , H_2O , N_2O , CH_4 , CO , NO , N_2 , O_2 , O , OH) and Mars (CO_2 , CO , N_2 , O_2 , O), which emit in the infrared spectral region and interact by intermolecular collisional energy exchange and by line overlapping. It was successfully applied to the non-LTE diagnostics of the infrared limb radiance data obtained in the CRISTA experiments on the Earth's orbit and in the Martian orbit TES/MGS.

In the case of the CRISTA experiment first detailed distributions of the temperature, CO_2 , CO and O_3 concentrations in the upper mesosphere and lower thermosphere were obtained, which include but not limited to

- the experimental evidence of significantly decreased CO_2 volume mixing ratio in the altitude regions of 75–90 and 105–125 km,
- the first space observation of the “two-level” structure of the Earth's mesopause which was recently discovered in the lidar and rocket experiments.

These results provide an important contribution to the study of the mesosphere, which is considered today to be the tracer of the global climate changes.

In the case of the Martian atmosphere the ALI-ARMS modeling of the daytime $10\ \mu\text{m}$ CO_2 emission provided excellent agreement with the latitude–altitude–seasonal variation of this emission observed by the TES/MGS instrument.

All these results allow the conclusion that ALI-ARMS code is a powerful non-LTE diagnostics tool which can be used for the infrared limb radiance data interpretation of the currently operational NASA SABER (for “Sounding of the Atmosphere using Broadband Emission Radiometry”) and ESA MIPAS (for “Michelson Interferometer for Passive Atmospheric Sounding”) Earth's atmosphere experiments. In the latter case the first study of the rotational non-LTE effects on the limb radiance distribution in the CO_2 $4.3\ \mu\text{m}$ fundamental and hot bands, which is presented in the Chapter 7 can be of particular importance due to the high spectral resolution of the MIPAS instrument.

9. Appendixes

A. Using spectral line databases for non-LTE studies

To apply the theory described in Section 2.1 (p. 3) to the actual calculations, one needs a database of the molecular vibrational levels, rovibrational levels and rovibrational lines with their spectroscopic parameters. The two currently available and most advanced databases are the HITRAN family (HITRAN-2000 and HITEMP) and GEISA.

The HITRAN-2000 database (*Rothman et al.*(177; 179)) is a long-running project started by the Air Force Cambridge Research Laboratories (AFCLR) in the late 1960's in response to the need for detailed knowledge of the infrared properties of the atmosphere. The HITRAN compilation, and its analogous database HITEMP (high-temperature spectroscopic absorption parameters), are now being developed at the Atomic and Molecular Physics Division, Harvard-Smithsonian Center for Astrophysics. The HITEMP database (see *Esplin and Hoke* (48)) provides extended information with very low intensity cutoff for H₂O, CO₂ and CO. Because of that, much more line data is included for weak wings of the vibrational bands and more weak bands that are not in HITRAN-2000 are included. That makes possible very detailed studies for the instruments with high spectral resolution.

The GEISA-97 spectral database is similar to HITRAN, but developed in Europe. GEISA-97 contains line parameters for 42 molecules (96 isotopic species) with 1,346,266 entries between 0 and 22,656 cm⁻¹. The data format is different from HITRAN, therefore it was not used in this dissertation.

A.1 Using HITRAN for non-LTE applications

HITRAN provides the wavenumber $\nu_{ll'}$, the LTE linestrength at 296K $s_{ll'}^*(296)$, the Lorentzian halfwidth at 296K $\gamma_{ll'}(296)$ in cm⁻¹/atm, and the lower state energy $E_{l'}$ in cm⁻¹ of each rovibrational transition.

Unfortunately, the HITRAN database does not provide the sets of rovibrational levels. To accomplish this task, a special program was written, which extracts this data by averaging the combined sets of energies for the lower state $E_{l'}$ and for the upper state $E_l = E_{l'} + \nu_{ll'}$ for H₂O, CO₂, O₃, N₂O, CO, O₂, NO, OH, N₂ and other molecules.

The HITRAN-96 database additionally provides the following information about the 36 molecules: isotopic abundances, molar masses, and the values of the total partition sum at 296K $Q^*(296)$ (see Tab. A.1 (p. 69)).

In the text below the following terms and units would be used:

$A_{ll'}$ - in s⁻¹,

$s_{ll'}^*(296)$ - in cm/molec (taken from HITRAN),

$\nu_{ll'}$ - in cm⁻¹,

$E_{l'}$ - the energy of the lower rovibrational level,

$g_{l'}$ - the degeneracy of the lower rovibrational level,

g_l - the degeneracy of the upper rovibrational level,

α^{iso} - isotopic abundance,

$Q^*(296)$ - total partition sum at 296K. (see Tab. A.1 (p. 69)).

The linestrength $s_{ll'}$ is the integral from line opacity per unit number density

$$s_{ll'} = \frac{1}{N^\alpha} \int_0^{+\infty} \chi_{ll'}(\nu, z) d\nu. \quad (\text{A.1})$$

Taking into account the Eq. 2.3, (p. 3) we get

$$\begin{aligned} s_{ll'} &= \frac{1}{N^\alpha} \int_0^{+\infty} \frac{h\nu_{ll'}}{4\pi} (n_{l'}(z)B_{l'l} - n_l(z)B_{ll'}) \varphi_{ll'}(\nu, z) d\nu = \\ &= \frac{h\nu_{ll'}}{4\pi} (W_{l'}(z)B_{l'l} - W_l(z)B_{ll'}) \frac{1}{\alpha^{\text{iso}}}. \end{aligned} \quad (\text{A.2})$$

It was shown in Section 2.4.1 (p. 7), that in the case of rotational LTE the probability W_l can be represented as a multiple of vibrational probability W_v and rotational probability $W_v^*(j)$ ($l \equiv vj$)

$$W_l = W_{vj} = W_v w_v^*(j). \quad (\text{A.3})$$

Using the definition from Eq. A.40, (p. 67) we get

$$\begin{aligned} W_l = W_{vj} &= W_v \frac{g_v(j)}{Q_v^*(T)} \exp\left(-\frac{E_{j,v}}{kT}\right) = \frac{g_v}{g_0} \frac{Q_v^*(T)}{Q_0^*(T)} \exp\left(-\frac{E_v}{kT_v}\right) \frac{g_v(j)}{Q_v^*(T)} \exp\left(-\frac{E_{j,v}}{kT}\right) W_0 = \\ &= \frac{g_v}{g_0} \frac{g_v(j)}{Q_0^*(T)} \exp\left(-\frac{E_v}{kT_v}\right) \exp\left(-\frac{E_{j,v}}{kT}\right) W_0. \end{aligned} \quad (\text{A.4})$$

As a result, the LTE linestrength at 296K $s_{ll'}^*(296)$ has the form

$$\begin{aligned} s_{ll'}^*(296) &= \frac{h\nu_{ll'}}{4\pi} (W_{l'}^*(296)B_{l'l} - W_l^*(296)B_{ll'}) \frac{1}{\alpha^{\text{iso}}} = \\ &= \frac{1}{8\pi c \nu_{ll'}^2} \frac{A_{ll'} g_j}{Q_{ll'}^*(296)} \exp\left(-\frac{E_{v'j'}}{k \cdot 296}\right) \left(1 - \exp\left(-\frac{h\nu_{ll'}}{k \cdot 296}\right)\right) \frac{1}{\alpha^{\text{iso}}}. \end{aligned} \quad (\text{A.5})$$

The ratio $s_{vj,v'j'}(T)/s_{vj,v'j'}^*(296)$ can be represented as

$$\begin{aligned} \frac{s_{ll'}(T)}{s_{ll'}^*(296)} &= \frac{g_v(j)W_{v'j'} - g_{v'}(j')W_{vj}}{g_v(j)W_{v'j'}^*(296) - g_{v'}(j')W_{vj}^*(296)} = \\ &= \frac{W_0}{W_0^*(296)} \frac{Q_0^*(296)}{Q_0^*(T)} \frac{\exp\left(-\frac{E_{v'j'}}{kT_{v'}}\right) \exp\left(-\frac{E_{j,v'}}{kT}\right) - \exp\left(-\frac{E_v}{kT_v}\right) \exp\left(-\frac{E_{j,v}}{kT}\right)}{\exp\left(-\frac{E_{v'j'}}{k \cdot 296}\right) - \exp\left(-\frac{E_{vj}}{k \cdot 296}\right)}, \end{aligned} \quad (\text{A.6})$$

or, using $Q_0^*(296) = g_0 W_0^*(296) Q^*(296)$ (Eq. 2.26, (p. 7) with $E_v = 0$) as

$$\frac{s_{ll'}(T)}{s_{ll'}^*(296)} = W_0 \frac{Q^*(296)}{Q_0^*(T)} \frac{\exp\left(-\frac{E_{v'j'}}{kT_{v'}}\right) \exp\left(-\frac{E_{j,v'}}{kT}\right) - \exp\left(-\frac{E_v}{kT_v}\right) \exp\left(-\frac{E_{j,v}}{kT}\right)}{\exp\left(-\frac{E_{v'j'}}{k \cdot 296}\right) - \exp\left(-\frac{E_{vj}}{k \cdot 296}\right)}. \quad (\text{A.7})$$

Substituting $Q_0^*(296)/Q_0^*(T) \approx (296/T)^m$, $Q(T) = Q_0(T)Q_{\text{vib}}(T)$ in Eq. A.6, (p. 62) the approximate formula for scaling linestrengths can be written (see also *Vollmann* (210))

$$\frac{s_{ll'}(T)}{s_{ll'}^*(296)} = \frac{Q_{\text{vib}}^*(T)}{Q_{\text{vib}}^*(296)} \left(\frac{296}{T}\right)^m \frac{\exp\left(-\frac{E_{v'j'}}{kT_{v'}}\right) \exp\left(-\frac{E_{j,v'}}{kT}\right) - \exp\left(-\frac{E_v}{kT_v}\right) \exp\left(-\frac{E_{j,v}}{kT}\right)}{\exp\left(-\frac{E_{v'j'}}{k \cdot 296}\right) - \exp\left(-\frac{E_{vj}}{k \cdot 296}\right)}. \quad (\text{A.8})$$

Nevertheless, the accurate formula Eq. A.7, (p. 62) requires the knowledge of the ground vibrational state probability W_0 in addition to the vibrational temperatures. That fact makes the usage of

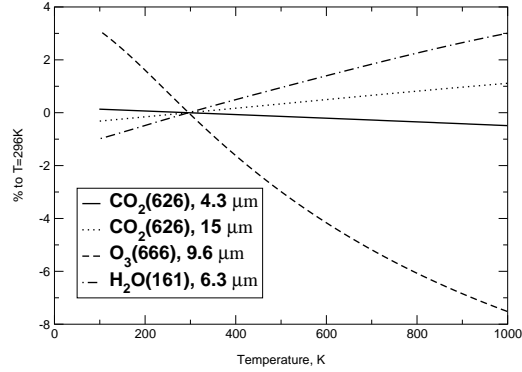


Fig. A.1 Dependence of Einstein coefficient of spontaneous emission for the vibrational band on temperature (in case of rotational LTE).

vibrational temperatures questionable in comparison with direct calculation by the formula given in Eq. A.2, (p. 62).

The HITRAN database does not provide the Einstein coefficient of spontaneous emission A_{ij} , so it should be calculated either from transition moment squared ($|\mathbf{R}_{ij}|^2$) or LTE linestrength $s_{ij}^*(296)$ both given in HITRAN (see *Gamache et al.*(61)). From Eq. A.5, (p. 62) it follows that

$$A_{ij} = \frac{64\pi^4}{3h} \nu_{ij}^3 \cdot \frac{g_j}{g_i} |\mathbf{R}_{ij}|^2 \cdot 10^{-36}, \quad (\text{A.9})$$

and

$$A_{ij} = s_{ij}^*(296) \cdot 8\pi c \nu_{ij}^2 \frac{\exp\left(\frac{E_j}{k \cdot 296}\right)}{1 - \exp\left(-\frac{h\nu_{ij}}{k \cdot 296}\right)} \cdot \frac{1}{g_i} \cdot Q^*(296) \cdot \alpha^{\text{iso}}. \quad (\text{A.10})$$

The Einstein coefficient of stimulated emission B_{ij} and absorption B_{ji} can be obtained from A_{ij} using the standard expressions.

The total partition sum for each molecule (see Eq. 2.21, (p. 6)) and the rotational partition sum for each vibrational level (see Eq. 2.27, (p. 7)) can be directly calculated for each required temperature if the information about rovibrational levels (energy and degeneracy for the given set of quantum numbers) is available (see *Gamache et al.*(60)). This data can then be stored for later processing.

The vibrational partition sum is usually used by the conventional radiative transfer algorithms for scaling the LTE linestrengths. If necessary, it is possible to calculate the vibrational partition sum by direct summation knowing the energies and degeneracies of vibrational levels. The reader should have already noticed, that $Q_{\text{vib}}(T)$ is used in the algorithm presented in Section 2.1 (p. 3).

The Eq. 2.36, (p. 8) in Section 2.4.1 (p. 7) defined the Einstein coefficient $A_{vv'}(T)$ for the vibrational band in case of rotational LTE as

$$A_{vv'}(T) = \sum_{jj' \in vv'} \frac{g_j}{Q_v^*(T)} \exp\left(-\frac{E_{j,v}}{kT}\right) A_{vj,v'j'}. \quad (\text{A.11})$$

Effectively, $A_{vv'}$ is an average of individual $A_{vj,v'j'}$ with the rotational weights of the upper state (which are dependent on T), so the resulting $A_{vv'}$ is also dependent on T . It should be noted that this dependence is not very strong for the temperatures found in the Earth or Mars atmospheres, which can be seen from Fig. A.1 (p. 63) for 6.3 μm H_2O , 4.3 μm CO_2 , 15 μm CO_2 and 9.6 μm O_3 fundamental bands.

A.1.1 Line profiles and frequency quadrature scheme

In the upper atmosphere the line profile can be with high accuracy described by the Doppler shape function

$$\varphi_{ll'}^D(\nu) = \frac{1}{\sqrt{\pi}\Delta\nu_D} \exp\left[-\frac{(\nu - \nu_{ll'})^2}{(\Delta\nu_D)^2}\right]. \quad (\text{A.12})$$

The Doppler halfwidth $\Delta\nu_D$ for the line centered at $\nu_{ll'}$ is given by

$$\Delta\nu_D = \nu_{ll'} \sqrt{\frac{2kT}{m^\alpha c^2}}, \quad (\text{A.13})$$

where

m^α is the mass of the molecule M^α .

In the lower atmosphere the line profile is better described by the Lorentz shape function

$$\varphi_{ll'}^L(\nu) = \frac{1}{\pi} \frac{\Delta\nu_L}{(\nu - \nu_{ll'})^2 + (\Delta\nu_L)^2}. \quad (\text{A.14})$$

The HITRAN includes the two following Lorentz parameters: $\gamma_{ll'}(296)$ and n , so the Lorentz (air-broadened) halfwidth $\Delta\nu_L$ is given by the following expression

$$\Delta\nu_L = \gamma_{ll'}(296) p \left(\frac{296}{T}\right)^n, \quad (\text{A.15})$$

where

$\gamma_{ll'}(296)$ - Lorentz halfwidth at $T = 296\text{K}$, $p_0 = 1$ bar,

n - coefficient of temperature dependence,

p - pressure in *bar*.

Convolving Doppler and Lorentz line shapes we come to the Voigt line shape function $\varphi_{ll'}^V(\nu)$. Defining dimensionless frequency x as the offset from the line center in Doppler halfwidths and the parameter a as the ratio of the Lorentz halfwidth $\Delta\nu_L$ to the Doppler halfwidth $\Delta\nu_D$

$$x = \frac{\nu - \nu_{ll'}}{\Delta\nu_D}, \quad a = \frac{\Delta\nu_L}{\Delta\nu_D}, \quad (\text{A.16})$$

the Voigt line shape function is given by

$$\varphi_{ll'}^V(\nu) = \frac{1}{\Delta\nu_D} U(x, a). \quad (\text{A.17})$$

Here $U(x, a)$ is the Voigt probability density function

$$U(x, a) = \frac{a}{\pi\sqrt{\pi}} \int_{-\infty}^{+\infty} \frac{e^{-t^2}}{(x-t)^2 + a^2} dt. \quad (\text{A.18})$$

The same probability formalism can be applied to the Doppler (Gauss distribution $\Phi(x)$) and Lorentz (Cauchy distribution $K(x, a)$) line shapes

$$\Phi(x) = \frac{1}{\sqrt{\pi}} \exp(-x^2) \quad (\text{A.19})$$

$$K(x, a) = \frac{1}{\pi} \frac{a}{x^2 + a^2}, \quad (\text{A.20})$$

so that

$$\varphi_{ll'}^D(\nu) = \frac{1}{\Delta\nu_D} \Phi(x), \quad (\text{A.21})$$

$$\varphi_{ll'}^L(\nu) = \frac{1}{\Delta\nu_D} K(x, a). \quad (\text{A.22})$$

The fast algorithm for the calculation of the Voigt function was developed by *Humlicek* (81). The more accurate implementation is given by *Wells* (213).

For integration over frequency the following quadrature scheme was suggested by *Hummer* (82) and implemented in the MALI code (see *Rybicki and Hummer* (181; 182)). The algorithm is also used in the ALI-ARMS code used in this dissertation.

We want to apply the quadrature scheme for Voigt profiles under the condition where the Doppler and Lorentz widths can change with depth. It is known that the uniformly spaced grid with equal weights ("trapezoidal rule") works very well for Doppler profiles, so it seems reasonable to use such a grid for the Doppler core of the profile. Such a grid would presumably also work for the Lorentz wings, but would be inefficient owing to the large bandwidth required. Thus it is necessary to alter the grid outside the Doppler core to increase the spacing for larger frequencies.

Since $\varphi(x) = U(x, a) \approx 1/x^2$ for $x \gg 1$ the wing integral can be written

$$\int_{x^*}^{+\infty} I(x)\varphi(x)dx \approx \int_{x^*}^{+\infty} I(x)\frac{1}{x^2}dx = \int_0^{1/x^*} I(1/y)dy, \quad (\text{A.23})$$

where $y = 1/x$.

Instead of making a sharp distinction between core and wing frequencies at $x = x^*$, we can introduce an analytic transformation that roughly accomplishes the same thing, namely,

$$x = x^* \tan\left(\frac{\pi y}{2}\right). \quad (\text{A.24})$$

For $x \ll x^*$ this gives a linear relation between x and y while for $x \gg x^*$ we find $x \approx \frac{1}{1-y}$, as desired. The distinction between $1 - y$ here and y is of no importance, being only a linear change of scale. Now

$$\int_0^{+\infty} I(x)\varphi(x)dx = \int_0^1 I\left(x^* \tan\left(\frac{\pi y}{2}\right)\right)\varphi\left(x^* \tan\left(\frac{\pi y}{2}\right)\right)\frac{\pi x^*}{2} \sec^2\left(\frac{\pi y}{2}\right)dy. \quad (\text{A.25})$$

Note that as $x \rightarrow +\infty$, $y \rightarrow 1$ and the quantity

$$\varphi\left(x^* \tan\left(\frac{\pi y}{2}\right)\right)\frac{\pi x^*}{2} \sec^2\left(\frac{\pi y}{2}\right) \rightarrow \frac{a}{2x^*}, \quad (\text{A.26})$$

that is, it remains bounded. Let us define the points and weights of the quadrature scheme so that

$$\begin{aligned} \int_0^{+\infty} F(x)dx &= \int_0^1 F\left(x^* \tan\left(\frac{\pi y}{2}\right)\right)\frac{\pi x^*}{2} \sec^2\left(\frac{\pi y}{2}\right)dy = \\ &= \sum_{i=0}^{NF-1} \frac{\pi x^*}{2} \sec^2\left(\frac{\pi y_i}{2}\right)F\left(x^* \tan\left(\frac{\pi y_i}{2}\right)\right) = \sum_{i=0}^{NF-1} w_i F_i. \end{aligned} \quad (\text{A.27})$$

The y_i and b_i given by the trapezoidal rule with offset grid are

$$\begin{aligned} y_i &= (i - \frac{1}{2})/NF, \\ b_i &= 1/NF. \end{aligned} \quad (\text{A.28})$$

This formulas Eq. A.27, (p. 65) and Eq. A.28, (p. 65) is also known as Gauss-Chebyshev quadrature scheme.

Since the integrand will not, in general, vanish near $y = 1$ ($x = +\infty$) we should use end corrections to the formula near $y = 1$. For cubic accuracy we note the formulas

$$\begin{aligned} y_i &= (i - \frac{1}{2})/NF \\ b_i &= 1/NF, \quad i = 0, \dots, NF - 5 \\ b_{NF-4} &= (375/384)/NF \\ b_{NF-3} &= (427/384)/NF \\ b_{NF-2} &= (309/384)/NF \\ b_{NF-1} &= (425/384)/NF. \end{aligned} \quad (\text{A.29})$$

The proof of this statement is outside the scope of the dissertation.

The above quadrature scheme has the disadvantage of a fixed ratio of number of points in core and wing, namely, equal numbers in $y \leq 1/2$ or $x \leq x^*$. Since there are cases where the core dominates, we would like to be able to vary this ratio, making it approach an equal spacing within x^* as one limit. One way to do this is to define a parameter α , $0 \leq \alpha \leq 1$ and let

$$x = x^* \left(\alpha^2 \tan\left(\frac{\pi y}{2}\right) + (1 - \alpha^2)y \right). \quad (\text{A.30})$$

In this case we still take Eq. A.29, (p. 66) to define the y -quadrature, but now

$$\begin{aligned} x_i &= x^* \left(\alpha^2 \tan\left(\frac{\pi y_i}{2}\right) + (1 - \alpha^2)y_i \right), \\ w_i &= b_i x^* \left(\alpha^2 \frac{\pi}{2} \sec^2\left(\frac{\pi y_i}{2}\right) + (1 - \alpha^2) \right). \end{aligned} \quad (\text{A.31})$$

When $\alpha = 0$ this formula reduces to an equally spaced grid in x from 0 to x^* , while for $\alpha = 1$ it gives scheme Eq. A.27, (p. 65). To determine the relation of the number of wing points NW vs. core points NC as a function of α , we first note that the ratio $NW/NC = (1 - y_c)/y_c$ where y_c is the value of y such that $x = x^*$, that is,

$$\alpha^2 \tan\left(\frac{\pi y_c}{2}\right) + (1 - \alpha^2)y_c = 1. \quad (\text{A.32})$$

For the limiting cases $\alpha = 0$ and $\alpha = 1$ we see

$$\frac{NW}{NC} = \begin{cases} 0, & \text{for } \alpha = 0, \\ 1, & \text{for } \alpha = 1. \end{cases} \quad (\text{A.33})$$

To find the intermediate behaviour let us look at the core where $\alpha \ll 1$, so we expect $y_c = 1 - \epsilon$, where $\epsilon \ll 1$. Then Eq. A.32, (p. 66) becomes

$$\begin{aligned} \alpha^2 \cot\left(\frac{\pi \epsilon}{2}\right) + (1 - \alpha^2)(1 - \epsilon) &= 1 \\ \epsilon &= \alpha^2 \left(\cot\left(\frac{\pi \epsilon}{2}\right) - 1 + \epsilon \right) \approx \alpha^2 \frac{2}{\pi \epsilon} \\ \frac{NW}{NC} &\approx \epsilon \approx \sqrt{\frac{2}{\pi}} \alpha \approx 0.8\alpha. \end{aligned} \quad (\text{A.34})$$

Thus as a rough approximation we may take

$$\frac{NW}{NC} = \alpha, \quad (\text{A.35})$$

which is consistent with Eq. A.33, (p. 66) and not too inconsistent with Eq. A.34, (p. 66). Since the distinction between ‘‘wing’’ and ‘‘core’’ is somewhat fuzzy, this formula should be perfectly satisfactory. A question of some interest is the value of the maximum frequency x_{NF-1} which corresponds to $y_{NF-1} = 1 - \frac{1}{2NF}$. Thus

$$x_{NF-1} = x^* \left[\alpha^2 \cot\left(\frac{\pi}{4NF}\right) + (1 - \alpha^2) \left(1 - \frac{1}{2NF}\right) \right]. \quad (\text{A.36})$$

For $\alpha = 1$

$$x_{NF-1} \approx x^* \frac{4}{\pi} NF. \quad (\text{A.37})$$

For $\alpha = 0$

$$x_{NF-1} \approx x^*. \quad (\text{A.38})$$

A good rough approximation for arbitrary α is

$$x_{NF-1} \approx x^*(NF \cdot \alpha^2 + 1). \quad (\text{A.39})$$

We should note that the frequency interval beyond x_{NF-1} is still estimated by the quadrature formula, basically by extrapolating $I(x)$ as a polynomial in $1/x$, so one should not be concerned if the mean intensity has not yet reached its asymptotic value at $x = x_{NF-1}$, as long as it has reached its asymptotic form as a polynomial in $1/x$.

A.2 Definitions of vibrational temperature

The solution of the SEE (Eq. 2.1, (p. 3)) gives us the populations of the vibrational and/or rovibrational states.

Using the expression for vibrational temperature given in Eq. 2.32, (p. 7), in the case of vibrational non-LTE, the vibrational temperature is given by

$$T_v = \frac{E_v}{k \log \left(\frac{g_v n_0}{g_0 n_v} \cdot \frac{Q_v^*(T)}{Q_0^*(T)} \right)}. \quad (\text{A.40})$$

The usual definition of the vibrational temperature T_v as

$$T_v = \frac{E_v}{k \log \left(\frac{g_v n_0}{g_0 n_v} \right)}, \quad (\text{A.41})$$

equals to the one given above, only if the rotational partition sums of vibrational levels are considered to be equal to the rotational partition sum of the ground state.

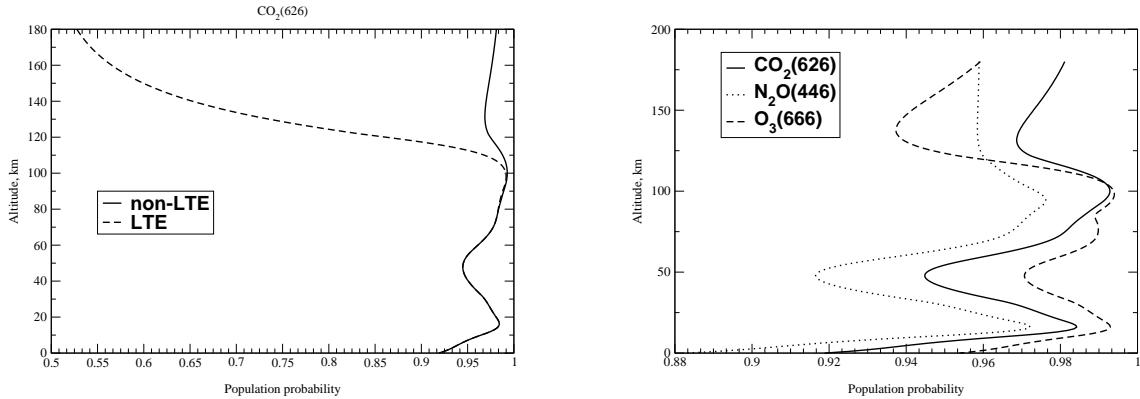


Fig. A.2 The populations of the ground vibrational state

Ignoring the dependence of the vibrational temperature on the temperature through the ratio of $Q_v^*(T)/Q_0^*(T)$ is a widely used approximation in atmospheric science (see López-Puertas *et al.*(120)).

Another common approximation is the assumption that the population of the ground state in Eq. A.41, (p. 67) equals the total number density of the molecule. It can introduce an error of a several percent, depending on the molecule under consideration, which can be easily seen from Fig. A.2 (p. 67): for N_2O molecule more than 9% of molecules can leave the ground state in the Earth atmosphere.

Index	Isotope	Short name	Abundance	$Q^*(296K)$	g_j	Molar mass	$\Delta H_0(298K)$
1		H ₂ O					
1	1	161	.997317e+00	.174626e+03	1	18.010565	-241.826
1	2	181	.199983e-02	.176141e+03	1	20.014811	-241.826
1	3	171	.371884e-03	.105306e+04	6	19.014780	-241.826
1	4	162	.310693e-03	.865122e+03	6	19.016740	-241.826
2		CO ₂					
2	1	626	.984204e+00	.286219e+03	1	43.989830	-393.51
2	2	636	.110574e-01	.576928e+03	2	44.993185	-393.51
2	3	628	.394707e-02	.607978e+03	1	45.994076	-393.51
2	4	627	.733989e-03	.354389e+04	6	44.994045	-393.51
2	5	638	.443446e-04	.123528e+04	2	46.997431	-393.51
2	6	637	.824623e-05	.714432e+04	12	45.997400	-393.51
2	7	828	.395734e-05	.323407e+03	1	47.998322	-393.51
2	8	728	.147180e-05	.376700e+04	6	46.998291	-393.51
3		O ₃					
3	1	666	.992901e+00	.348186e+04	1	47.984745	142.7
3	2	668	.398194e-02	.746207e+04	1	49.988991	142.7
3	3	686	.199097e-02	.364563e+04	1	49.988991	142.7
3	4	667	.740475e-03	.430647e+05	6	48.988960	142.7
3	5	676	.370237e-03	.212791e+05	6	48.988960	142.7
4		N ₂ O					
4	1	446	.990333e+00	.499183e+04	9	44.001062	82.05
4	2	456	.364093e-02	.334938e+04	6	44.998096	82.05
4	3	546	.364093e-02	.344940e+04	6	44.998096	82.05
4	4	448	.198582e-02	.526595e+04	9	46.005308	82.05
4	5	447	.369280e-03	.307008e+05	54	45.005278	82.05
5		CO					
5	1	26	.986544e+00	.107428e+03	1	27.994915	-110.53
5	2	36	.110836e-01	.224704e+03	2	28.998270	-110.53
5	3	28	.197822e-02	.112781e+03	1	29.999161	-110.53
5	4	27	.367867e-03	.661209e+03	6	28.999130	-110.53
5	5	38	.222250e-04	.236447e+03	2	31.002516	-110.53
5	6	37	.413292e-05	.138071e+04	12	30.002485	-110.53
7		O ₂					
7	1	66	.995262e+00	.215726e+03	1	31.989830	0.0
7	2	68	.399141e-02	.452188e+03	1	33.994076	0.0
7	3	67	.742235e-03	.263998e+04	6	32.994045	0.0
22		N ₂					
22	1	44	.992687e+00	.467136e+03	1	28.006147	0.0
34		O(³ P _J)					
34	1	6	.997628e+00	.672173e+01	1	15.994915	249.18

Tab. A.1 Molecular parameters (source - HITRAN-2000)

B. Electronic-vibrational-rotational levels and bands of molecules used in this study

From the point of view of molecular spectroscopy the molecules that are discussed in this dissertation belong to two major groups: linear molecules CO_2 , N_2O , CO , NO , O_2 , N_2 , OH and asymmetric top molecules H_2O , O_3 .

The molecules will be referred to by the number of nuclei forming the molecule modulo 10. The carbon dioxide molecule isotopic specie $^{16}\text{O}^{12}\text{C}^{16}\text{O}$ is then called CO_2 (626) or simply 626. This nomenclature is sometimes ambiguous, for example, $^{16}\text{O}^{12}\text{C}^{16}\text{O}$ and $^{16}\text{O}^{12}\text{S}^{16}\text{O}$ will have the same designation 626, but for the molecules presented in this dissertation, no such “overlapping” occurs.

The detailed discussion of molecular parameters relevant for non-LTE modeling is presented below.

B.1 H_2O

Water vapour H_2O is an asymmetric top molecule (see *Herzberg (77)*). The vibrational level v of H_2O molecule is described by quantum numbers v_1 (symmetric stretching mode), v_2 (bending mode), v_3 (asymmetric stretching mode), so $v = v_1v_2v_3$. The diagram showing the set of 14 lower excited vibrational states is presented in Fig. B.1 (p. 72). The values of the vibrational energies (in cm^{-1}) are given in Tab. B.2 (p. 72).

The vibrational-rotational state of H_2O is defined by 3 vibrational and 3 rotational quantum numbers: $(v_1, v_2, v_3, j, K_a, K_c)$.

Rotational quantum numbers j, K_a and K_c follow the rule

$$\begin{aligned} K_a &\leq j, \\ K_c &\leq j, \\ K_a + K_c &= \begin{cases} j \\ j + 1, \end{cases} \end{aligned} \quad (\text{B.1})$$

for each nonnegative integer j .

For the asymmetric H_2O isotopes (which have nonidentical H nuclei, for example, H_2O (162)), the rotational degeneracy factor is given by the usual expression

$$g_v(j) = 2j + 1. \quad (\text{B.2})$$

For the symmetric H_2O isotopes (which have identical H nuclei, i.e. 161, 171, 181) the rotational degeneracy factor has to be multiplied by factor 3, depending on the relationship between K_a and K_c quantum numbers

$$g_v(j) = \begin{cases} 3 \cdot (2j + 1), & \text{if } K_a - K_c \bmod 2 \neq 0, \\ 2j + 1, & \text{if } K_a - K_c \bmod 2 = 0. \end{cases} \quad (\text{B.3})$$

The HITRAN-96 spectroscopic database provides 85 vibrational bands for 72 vibrational levels of H_2O (161). The presented model with 14 vibrational levels includes 22 of these bands from 1.38 μm to 6.60 μm .

The fundamental and hot ν_2 bands (6.3 μm) and fundamental ν_1 and ν_3 bands (2.7 μm) are shown in Fig. B.1 (p. 72).

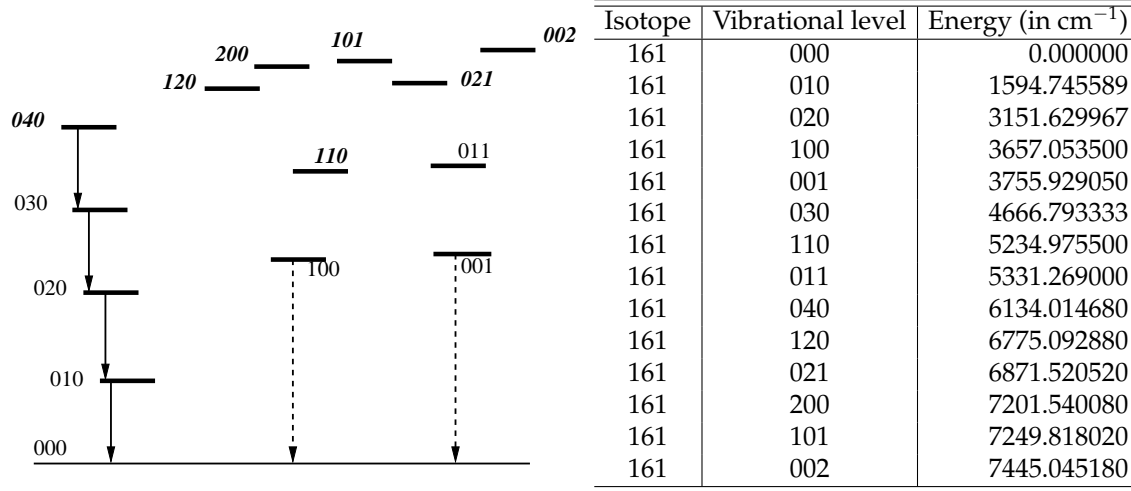


Fig. B.1 The vibrational levels and most important 6.3 μm (solid lines) and 2.7 μm (dashed lines) bands of H_2O

Fig. B.2 Energies of H_2O vibrational levels, cm^{-1}

B.2 CO_2

The CO_2 is a linear triatomic molecule which has the structure O–C–O and can be symmetric or asymmetric depending on whether the O nuclei are identical. The vibrational level of symmetric CO_2 isotopic species (626,636,828,727,828) is described by four quantum numbers- $v_1 v_2^l v_3$, attributed to the v_1 stretching mode, v_2 bending mode, angular momentum l and v_3 stretching mode, respectively. For asymmetric CO_2 isotopic species (627,637,628,638) the fifth quantum number s must be added to account for l -doubling (see *Herzberg (77)* for details).

Since the v_1 and $2v_2$ states are very close in their energies, that leads to *accidental degeneration*, also known as Fermi resonance (see *Fermi (51)*). The families of levels with the same values of

$$n = 2v_1 + v_2, \quad (\text{B.4})$$

which are in Fermi resonance were used by *Shved et al.(188)* in the description of collisional $V - T$ and $V - V$ selection rules. This nomenclature also makes the radiative selection rules more compact and will be used below, namely, instead of using the $(v_1 v_2^l v_3)$ notation for vibrational levels, we will be using $(n^l v_3, m)$. Here n is given by Eq. B.4, (p. 72), l and v_3 are the same and m enumerates the levels in Fermi-family. The AFGL notation $(v_1 v_2^l v_3 m)$ used by the HITRAN database can be easily converted to the Shved's $(n^l v_3, m)$ notation, using the Eq. B.4, (p. 72).

Shved et al.(188) described very detailed CO_2 model with 321 vibrational levels of 7 isotopic species, which is shown in Fig. B.3 (p. 78). Comparing the results with the reduced model of 60 levels for 5 isotopes in Fig. B.4 (p. 79) *Ogibalov et al.(160)* have found the latter reasonably accurate for the vibrational populations.

The energies of the CO_2 vibrational-rotational levels E_{vj} can be calculated using effective spectroscopic constants as

$$E_{vj} = G_v + B_v j(j+1) - D_v [j(j+1)]^2 + H_v [j(j+1)]^3. \quad (\text{B.5})$$

where the spectroscopic constants G_v , B_v , D_v and H_v for the vibrational states were taken from *Rothman et al.(178; 179)*.

The rotational degeneracy factor is given by the usual expression

$$g_v(j) = 2j + 1. \quad (\text{B.6})$$

The radiative transitions that satisfy the selection rule

$$n^l v_3 \rightarrow (n-1)^l v_3,$$

are called 15 μm bands. The strongest of them is the 01101 \rightarrow 00001 band of CO₂ (626), which is centered at 667.38 cm^{-1} (14.9 μm). The hot transitions 10001 \rightarrow 01101 (13.9 μm) and 10002 \rightarrow 01101 (16.2 μm), belonging to the 15 μm bands, are also of the interest in this dissertation. The hot transition 03301 \rightarrow 10002 is called 12.6 μm band.

The 10 μm bands that are described by the selection rule

$$n^l v_3 \rightarrow (n + 2)^l (v_3 - 1),$$

and are often also referred to as “laser bands” (see also Appendix D.5 (p. 104)). As it was discussed in Appendix D.5 (p. 104) the solution of the radiative transfer equation for these bands can be very challenging task, if one uses “conventional” methods.

The 4.3 μm bands, which are v_3 transitions, are described by the selection rule

$$n^l v_3 \rightarrow n^l (v_3 - 1).$$

The fundamental 4.3 μm band 00011 \rightarrow 00001 of CO₂ (626) is one of the most optically thick in the planetary atmospheres: the optical depth in the strongest lines reaches several million in the Earth atmosphere and some tens of millions in the Mars atmosphere.

The 2.7 μm and 2.0 μm bands are described by the selection rules

$$n^l v_3 \rightarrow (n - 2)^l (v_3 - 1)$$

and

$$n^l v_3 \rightarrow (n - 4)^l (v_3 - 1),$$

respectively.

B.3 O₃

Manuilova et al. (132) have suggested the model where 23 lower vibrational states of the O₃ molecule were considered. It was used as a “standard” model in this dissertation. The special attention in comparison with other models was paid to the quenching and chemical loss processes of the ozone vibrational states in nonelastic collisions with atomic oxygen.

The models of *Koutoulaki* (92), which has 245 vibrational levels (see Fig. B.5 (p. 80)) and two models by *Mlynczak and Drayson* (143; 144) (14 and 62 levels) are also described below.

Ozone, like H₂O, is an asymmetric top molecule and even the O₃ (666) isotopic specie composed of identical O nuclei is asymmetric. Therefore, the vibrational level v of O₃ molecule is described by three quantum numbers v_1 (symmetric stretching mode), v_2 (bending mode), v_3 (asymmetric stretching mode), so $v = v_1 v_2 v_3$. The diagram showing the set of 23 lower excited vibrational states can be found in Fig. B.6 (p. 80). The states whose energies are close and which have equal values of $v_1 + v_3$ and the same v_2 , have been grouped in Fig. B.6 (p. 80) and are represented by roman numbers. Group VI is an exception, because along with the four states 003, 102, 201, 300 it includes also states 031 and 130 whose energies are close to the energies of the four lower states. This grouping was introduced to simplify the comparisons with the model of *Manuilova and Shved* (129), and serves only the demonstration purposes.

Fig. B.5 (p. 80) gives the extended diagram of the O₃ vibrational levels (taken from *Koutoulaki* (92)). The energies of the lower 23 vibrational levels were taken from *Manuilova et al.* (132). For the higher levels, where possible, the measured values of energy were used. The remaining levels were calculated using the formula of *Barbe et al.* (13)

$$E_v = E_{v_1 v_2 v_3} = \sum_{i=1}^3 \omega_i (v_i + \frac{1}{2}) + \sum_{i=1}^3 \sum_{j=1}^i x_{ij} (v_i + \frac{1}{2}) (v_j + \frac{1}{2}), \quad (\text{B.7})$$

Isotope	Vibrational level	Energy (in cm^{-1})
666	000	0.000000
666	010	700.931092
666	001	1042.912937
666	100	1103.137037
666	020	1399.272825
666	011	1726.522500
666	110	1796.261925
666	002	2057.890967
666	030	2095.000000
666	101	2110.784200
666	200	2201.155250
666	021	2408.756188
666	120	2486.576650
666	012	2726.106633
666	111	2786.060567
666	040	2788.000000
666	210	2886.178000
666	003	3046.087900
666	102	3083.702867
666	031	3086.000000
666	130	3171.000000
666	201	3186.409700
666	300	3289.930100

Tab. B.1 Energies of O_3 vibrational levels

with the modifications suggested by *Koutoulaki* (92). The details concerning ω_i and x_{ij} could be found in *Koutoulaki* (92). The values of the vibrational energies (in cm^{-1}) are given in Tab. B.1 (p.74).

The vibrational levels included in models published by *Mlynczak and Drayson* (143; 144) are described in Appendix C.4 (p. 95).

The vibrational-rotational state of ozone is represented by 6 quantum numbers: $(v_1, v_2, v_3, j, K_a, K_c)$. j, K_a and K_c follow the rule (*Flaud and Bacis* (55))

$$\begin{aligned}
 K_a &\leq j \\
 K_c &\leq j \\
 K_a + K_c &= \begin{cases} j \\ j + 1, \end{cases}
 \end{aligned}
 \tag{B.8}$$

for each nonnegative integer j . The rotational degeneracy factor is always by the usual expression

$$g_v(j) = 2j + 1. \tag{B.9}$$

The strongest atmospheric infrared O_3 bands are located around 9.6 (ν_3 and ν_1), 4.8 (mainly $\nu_3 + \nu_1$) and 14.3 (ν_2) μm and are shown in Fig. B.7 (p. 81).

The following ν_1 and ν_2 transitions, which are not present in the HITRAN-96 database, were added to the model: 201-101, 300-200; 031-030, 031-021, 130-030, 130-120; 012-002, 111-101, 210-200; 030-020, 040-030,

For these transitions the Einstein coefficients of spontaneous emission for vibrational transitions $A_{v'v}$ have been estimated in accordance with the harmonic oscillator model as a multiples of the

values $A_{vv'}$ of the fundamental transitions 010–000,100–000

$$A_{(v_1,v_2,v_3)\rightarrow(v_1-1,v_2,v_3)} = v_1 A_{100\rightarrow000}, \quad A_{(v_1,v_2,v_3)\rightarrow(v_1,v_2-1,v_3)} = v_2 A_{010\rightarrow000}, \quad (\text{B.10})$$

or by an anharmonic oscillator scaling law for the ν_3 mode

$$A_{v,v-1} = v A_{001,000} \left(\frac{E_v - E_{v-1}}{\nu_{001,000}} \right)^3, \quad (\text{B.11})$$

as suggested by *Rawlins et al.*(170).

B.4 N₂O

The N₂O is a linear triatomic molecule which has the form O–N–N and therefore is asymmetric, even if the N nuclei are identical. This is the same type of the molecule as the asymmetric CO₂ isotopic species. The vibrational level of N₂O isotopic species is defined by quantum numbers $v_1 v_2' v_3$. The fifth quantum number s must be added to account for l -doubling (see *Herzberg* (77) for details). The four vibrational quantum numbers $v_1 v_2' v_3$ correspond respectively to the ν_1 stretching mode, ν_2 bending mode, angular momentum l , and ν_3 stretching mode. The set of 16 vibrational populations is shown in Fig. B.8 (p. 81) and the numerical values (in cm⁻¹) are given in Tab. B.9 (p. 81).

B.5 CO

CO is a linear molecule and its vibrational levels are nearly equally spaced in energy. For this study three lower levels $v = 0, 1, 2$ of main isotope CO (26) were included, like in similar models by *López-Puertas et al.*(115) and *Kutepov et al.*(99). The energy levels are shown in Fig. B.10 (p. 75).

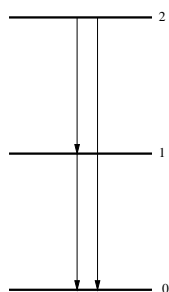


Fig. B.10 The vibrational levels and bands of CO

Isotope	Vibrational level	Energy (in cm ⁻¹)
26	0	0.0000
26	1	2143.2713
26	2	4260.0621

Fig. B.11 Energies of CO vibrational levels, cm⁻¹

The energies of the rovibrational levels were obtained from the HITRAN-2000 spectroscopic database, using the program described in Appendix A (p. 61). The rotational degeneracy factor is given by the usual expression

$$g_v(j) = 2j + 1. \quad (\text{B.12})$$

The fundamental 1 – 0 and first hot 2 – 1 4.6 μm bands and the 2 – 0 2.3 μm band that were taken into account in this study are shown in Fig. B.10 (p. 75).

B.6 O₂

Three electronic states of O₂ are included in the model: the ground state O₂(X³Σ_g⁻), the first excited state O₂(a¹Δ_g) and the second excited state O₂(b¹Σ_g⁺). Their energies are given in Tab. B.2 (p.76).

	O ₂ (X ³ Σ _g ⁻)	O ₂ (a ¹ Δ _g)	O ₂ (b ¹ Σ _g ⁺)
E _e	0.0000	7882.4238	13120.9

Tab. B.2 Energies of O₂ electronic states. The values are in cm⁻¹.

For calculating the vibrational energies of O₂ excited levels the following expression was used (Svanberg *et al.*(199))

$$\begin{aligned} \tilde{E}(v) &= \omega_e(v + \frac{1}{2}) + \omega_e x_e(v + \frac{1}{2})^2 + \omega_e y_e(v + \frac{1}{2})^3 + \omega_e z_e(v + \frac{1}{2})^4 + \\ &\quad + \omega_e a_e(v + \frac{1}{2})^5 + \omega_e b_e(v + \frac{1}{2})^6, \\ E_v &= \tilde{E}(v) - \tilde{E}(0). \end{aligned} \tag{B.13}$$

The constants used in the expression Eq. B.13, (p. 76) are given in Tab. B.3 (p. 76).

	O ₂ (X ³ Σ _g ⁻)	O ₂ (a ¹ Δ _g)	O ₂ (b ¹ Σ _g ⁺)
ω _e	1580.39	1509.0	1432.687
ω _e x _e	-12.212	-12	-13.95
ω _e y _e	7.54 × 10 ⁻²	0	-1.075 × 10 ⁻²
ω _e z _e	-4.09 × 10 ⁻³	0	0
ω _e a _e	1.30 × 10 ⁻⁴	0	0
ω _e b _e	-2.21 × 10 ⁻⁶	0	0

Tab. B.3 Constants used for the calculation of vibrational energies of O₂. The values are taken from *Laher and Gilmore* (105) and *Herzberg* (77).

The energies of the rotational sublevels were calculated using the formula given by *Herzberg* (77) for diatomic molecules

$$\begin{aligned} E_{j,v} &= B_v j(j+1) - D_v j^2(j+1)^2, \\ B_v &= B_e - \alpha_e(v + \frac{1}{2}), \\ D_v &= D_e - \beta_e(v + \frac{1}{2}). \end{aligned} \tag{B.14}$$

The constants used in the equation Eq. B.14, (p. 76) are given in Tab. B.4 (p. 77).

	$O_2(X^3\Sigma_g^-)$	$O_2(a^1\Delta_g)$	$O_2(b^1\Sigma_g^+)$
B_e	1.44566	1.4264	1.40041
α_e	1.579×10^{-2}	1.71×10^{-2}	1.817×10^{-2}
D_e	4.95×10^{-6}	0	0
β_e	8.00×10^{-8}	0	0
K	1,3,5,...	2,3,4,...	0,2,4,...
J	$K - 1, K, K + 1$	K	K

Tab. B.4 Constants used for calculation of rotational energies of O₂. The values are taken from *Herzberg (77)* in cm⁻¹.

The ground electronic state $O_2(X^3\Sigma_g^-)$ is a triplet, while the $O_2(a^1\Delta_g)$ and $O_2(b^1\Sigma_g^+)$ are singlets. One should also keep in mind that for $O_2(X^3\Sigma_g^-)$ the rotational levels with even K are forbidden, and for $O_2(b^1\Sigma_g^+)$ - the odd levels. The summary is given in Tab. B.4 (p. 77).

B.7 N₂

For calculating the vibrational energies of N₂ excited levels the following expression was used in this dissertation

$$\begin{aligned} \tilde{E}(v) &= \omega_e(v + \frac{1}{2}) + \omega_e x_e(v + \frac{1}{2})^2, \\ E_v &= \tilde{E}(v) - \tilde{E}(0). \end{aligned} \quad (\text{B.15})$$

The constants used in the expression Eq. B.15, (p. 77) are given in Tab. B.5 (p. 77).

ω_e	2329.91	<i>Herzberg (77)</i>
$\omega_e x_e$	-14.456	

Tab. B.5 Constants used for the calculation of vibrational energies of N₂. The energies are in cm⁻¹

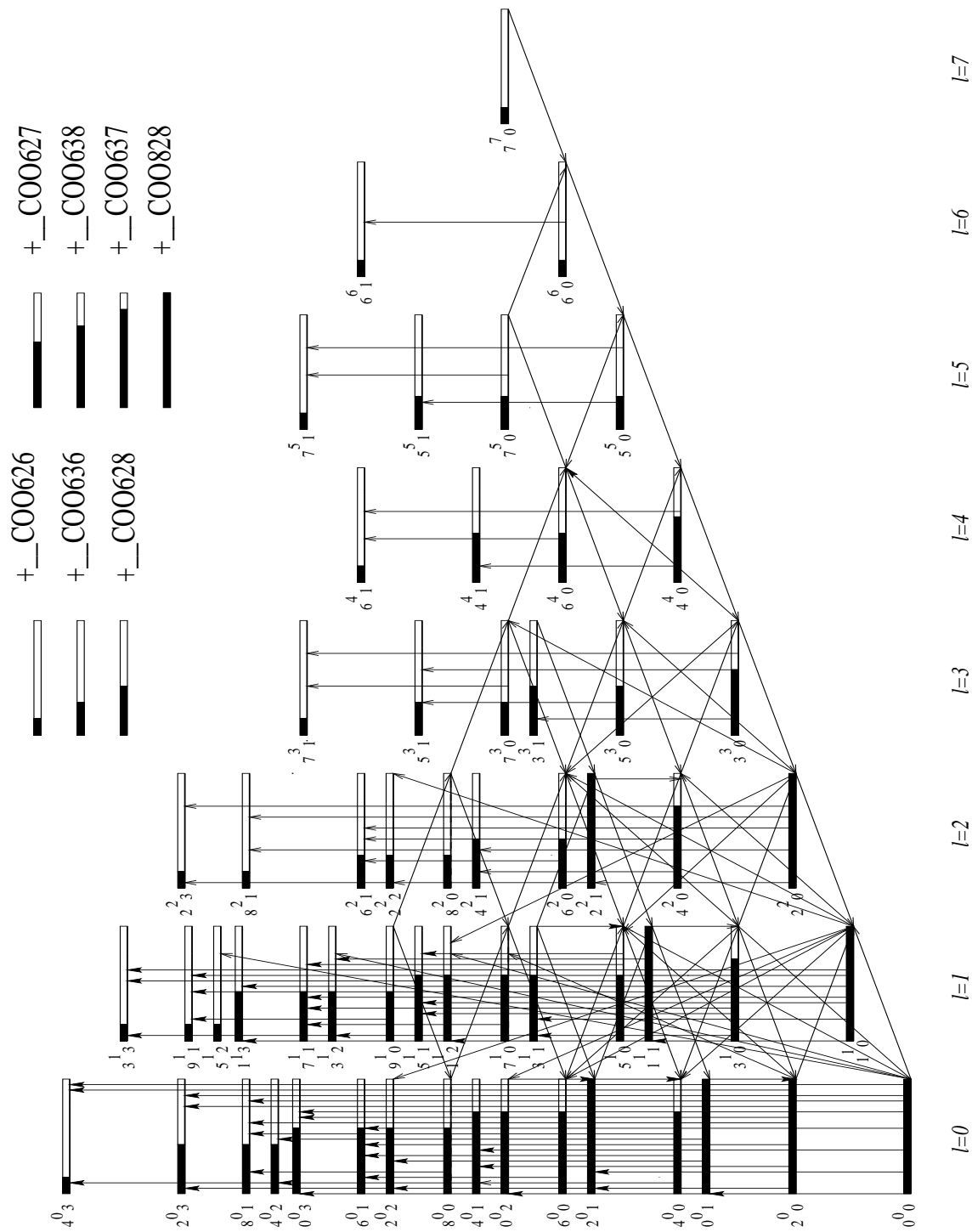
The energies of the rotational sublevels were calculated using the formula given by *Herzberg (77)* for diatomic molecules (rigid rotator)

$$E_{j,v} = B_v j(j+1). \quad (\text{B.16})$$

The constants used the in expression Eq. B.16, (p. 77) are given in Tab. B.6 (p. 77).

B_v	1.44566	<i>Herzberg (77)</i>
-------	---------	----------------------

Tab. B.6 Constants used for calculation of rotational energies of N₂. The values are in cm⁻¹

Fig. B.3 The vibrational levels of CO₂ (extended model).

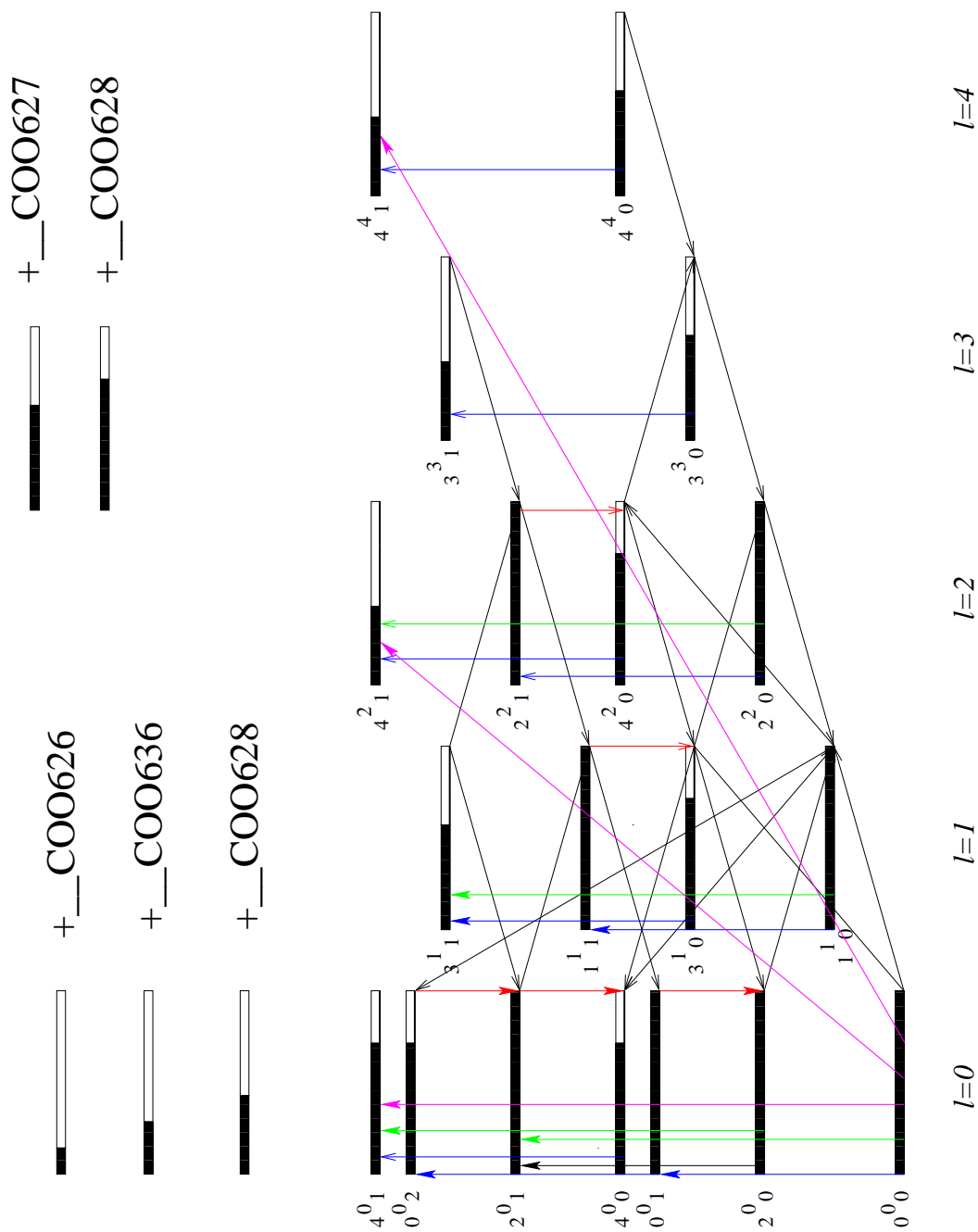


Fig. B.4 Vibrational bands of CO₂ : black - 15 μ m , red - 10 μ m , blue - 4.3 μ m , magenta - 2.0 μ m .

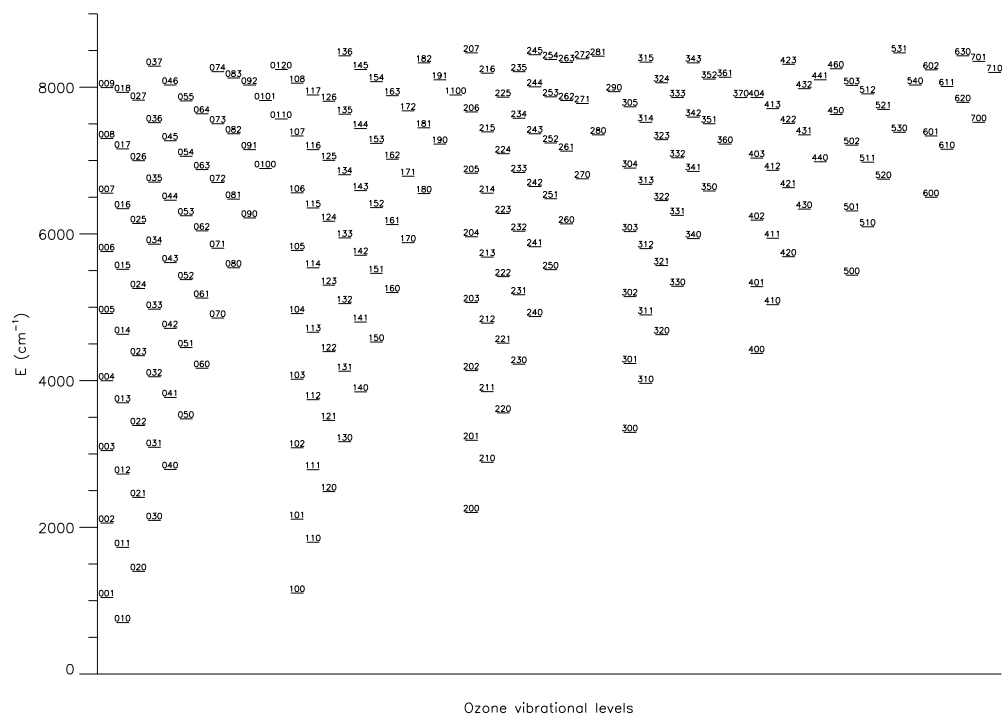


Fig. B.5 The vibrational levels of O_3 (taken from *Koutoulaki (92)*).

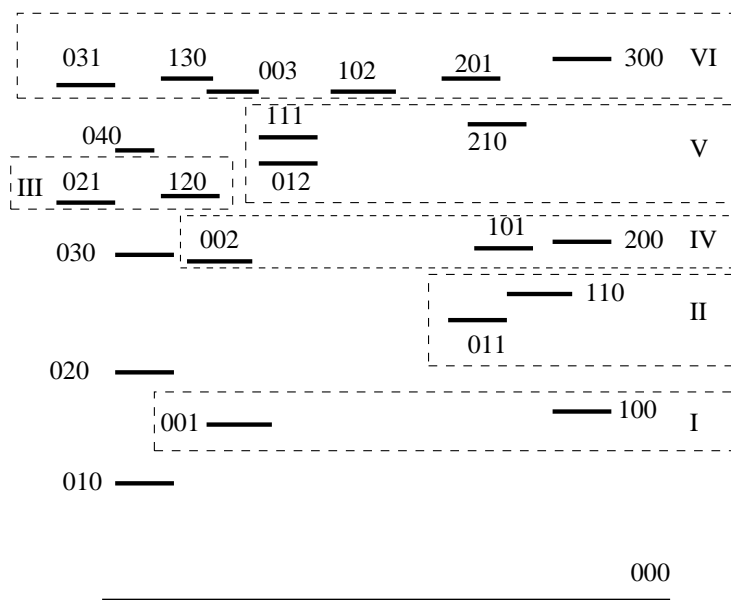


Fig. B.6 The vibrational levels of O_3 included in the model of *Manuilova et al.(132)*.

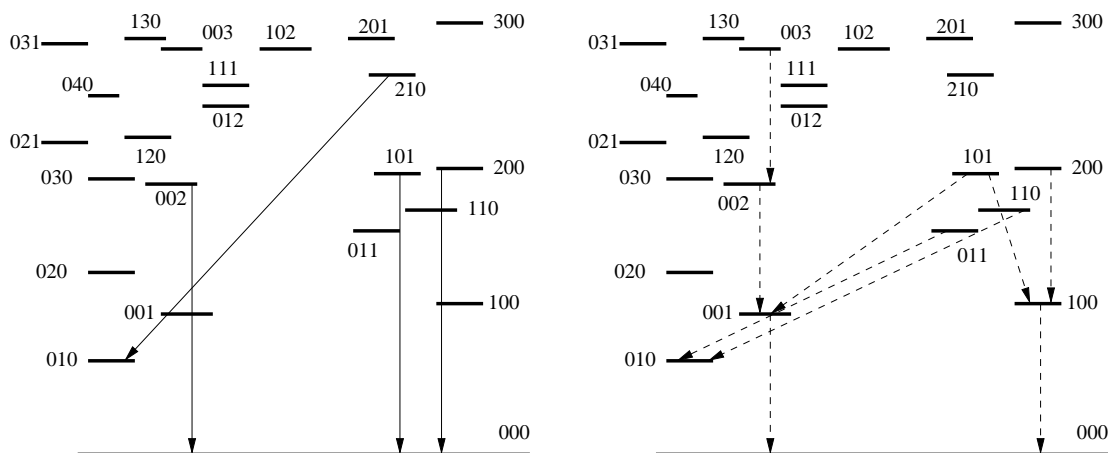


Fig. B.7 Most important 4.8 μm (left) and 9.6 μm (right) bands of O₃

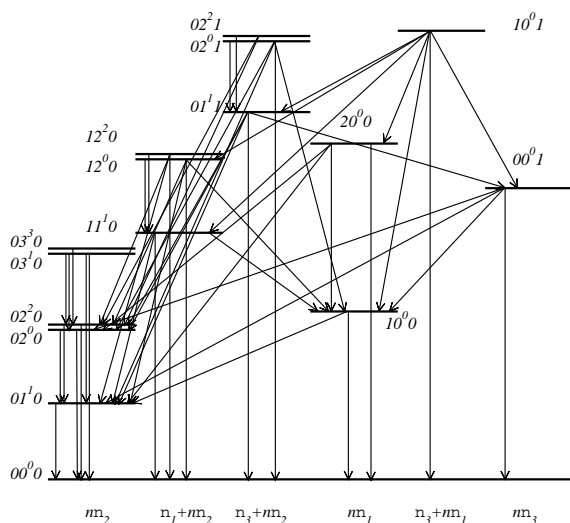


Fig. B.8 The vibrational levels and bands of N₂O .

Isotope	Vibrational level	Energy (in cm ⁻¹)
446	00 ⁰ 0	0.000000
446	01 ¹ 0	588.767800
446	02 ⁰ 0	1168.132314
446	02 ² 0	1177.744600
446	10 ⁰ 0	1284.904040
446	03 ¹ 0	1749.058000
446	03 ³ 0	1766.900000
446	11 ¹ 0	1880.268000
446	00 ⁰ 1	2223.756700
446	12 ⁰ 0	2461.996400
446	12 ² 0	2474.785000
446	20 ⁰ 0	2563.339400
446	01 ¹ 1	2789.292600
446	02 ⁰ 1	3363.976620
446	02 ² 1	3373.138000
446	10 ⁰ 1	3480.819139

Fig. B.9 Energies of N₂O vibrational levels

C. Collisional rates

C.1 $R - T$ collisional processes

C.1.1 Rate coefficients for the CO_2 $R - T$ energy exchange

The rotational relaxation of CO_2 in collisions with other molecular species remains poorly explored both in experiment and theory. Therefore, in order to obtain the required $R - T$ rate constants $k_{vj,vj'}$, it was necessary to model these quantities. Following *Kutepov et al.*(99), the model of $k_{vj,vj'}$ is based on two assumptions:

1. The change in angular momentum is more important for the $R - T$ transitions than the change in energy (*Steinfeld et al.*(195)). That leads to the following expression for $k_{vj,vj'}$

$$k_{vj,vj'} = k_{jj'} = k_j^0 [\Delta j (\Delta j + 1)]^{-a}, \quad \Delta j = j - j', \quad j > j'. \quad (\text{C.1})$$

The value of a was taken equal 0.85. For $j < j'$, $k_{jj'}$ is calculated from the detailed balance relation (see Eq. 2.12, (p. 4)).

2. The total rate constant k^{R-T} for the rotational relaxation of level j

$$k^{R-T} = \sum_{j' \neq j} k_{jj'}, \quad (\text{C.2})$$

is related to the Lorentz halfwidths $\Delta\nu_L$ of rovibrational line, originating from level j , (see *Pack et al.*(163)), namely

$$\Delta\nu_L = \gamma(296) \frac{p}{p_0} \left(\frac{296}{T} \right)^n = \frac{1}{2\pi c} \frac{p}{kT} k^{R-T}. \quad (\text{C.3})$$

Therefore

$$k^{R-T} = \frac{2\pi c k T}{p_0} \gamma(296) \left(\frac{296}{T} \right)^n, \quad (\text{C.4})$$

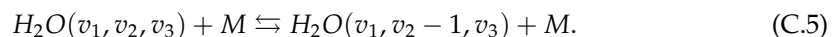
where $\gamma(296)$ is the Lorentz halfwidth at 296K and normal pressure (1 bar). This approach was used by *Kutepov et al.*(99) for their study of rotational non-LTE for CO. The similar study was performed for NO by *Funke and López-Puertas* (57), who also used a different model for $R - T$ relaxation. As it is shown by *Funke* (58; 59) these two approaches did not have any significant influence on the resulting rotational distribution. So, the approach of *Kutepov et al.*(99) described above was used in this work. See Section 7 (p. 53) for the rotational distribution functions for CO_2 (626) 00011 level in the Earth's atmosphere.

C.2 $V - T$ collisional processes

C.2.1 $V - T$ collisional transitions in H_2O

López-Puertas et al.(117) has included the following $V - T$ processes in his model, which are given in generalized form here together with their rate constants:

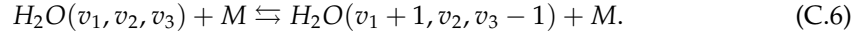
1. ν_2 transitions



M	Collisional rate constant (cm^3s^{-1})	Reference
N_2	$k^{V-T} = v_2 \cdot 4.1 \times 10^{-14} (T/300)^{1/2}$	<i>Bass et al.</i> (16)
O_2	$k^{V-T} = v_2 \cdot 4.1 \times 10^{-14} (T/300)^{1/2}$	
$\text{O}(^3P_J)$	$k^{V-T} = 1.0 \times 10^{-12} (T/300)^{1/2}$	<i>López-Puertas et al.</i> (117)

Tab. C.1 $V - T$ rate constants for H_2O ν_2 transitions.

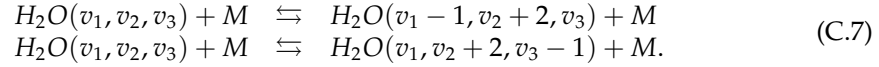
2. $\nu_1 \leftrightarrow \nu_3$ exchange



M	Collisional rate constant (cm^3s^{-1})	Reference
N_2	$k^{V-T} = 1.2 \times 10^{-11} \sqrt{T}$	<i>López-Puertas et al.</i> (117)
O_2	$k^{V-T} = 1.1 \times 10^{-11} \sqrt{T}$	

Tab. C.2 $V - T$ rate constants for H_2O $\nu_1 \leftrightarrow \nu_3$ exchange.

3. $\nu_1, \nu_3 \leftrightarrow 2\nu_2$ transitions



M	Collisional rate constant (cm^3s^{-1})	Reference
N_2	$k^{V-T} = 4.6 \times 10^{-13} (T/300)^{1/2}$	<i>Finzi et al.</i> (53)
O_2	$k^{V-T} = 3.3 \times 10^{-13} (T/300)^{1/2}$	
$\text{O}(^3P_J)$	$k^{V-T} = 3.0 \times 10^{-12} (T/300)^{1/2}$	<i>Zittel and Masturzo et al.</i> (222)

Tab. C.3 $V - T$ rate constants for H_2O $\nu_1, \nu_3 \leftrightarrow 2\nu_2$ exchange.

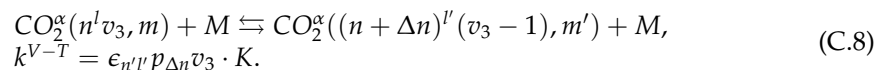
C.2.2 $V - T$ collisional transitions in CO_2

There are two modern kinetic models, namely that of *López-Puertas et al.*(120) and that of *Shved et al.*(188), which are described below.

The kinetic model of *López-Puertas* was first presented in *López-Puertas et al.*(109; 110) and then extended and improved in *López-Puertas et al.*(120). The values of the rate constants and the groups of the transitions of this model are very close to those used by *Shved et al.*(188). The main differences lie in the used scaling rules and branching ratios for $\nu_3 \rightarrow \nu_2$ processes. Therefore the model of *Shved et al.*(188) will be described together with its differences to *López-Puertas et al.*(120). The *Shved's* model was extended in this work by including the $V - T$ processes with CO_2 as a collisional partners and the $V - V$ processes with CO , to make it applicable both to the atmospheres of Earth and Mars. For this extension the set of the rate constants of *López-Valverde et al.*(207; 208) was used.

All the $V - T$ transitions in this model are divided in four groups:

1. Splitting a ν_3 -quantum into ν_2 -quanta



M	Collisional rate constant (cm^3s^{-1})	Reference
$\text{CO}_2, \Delta n = 2, 3$	$K = 7.3 \times 10^{-14} \exp(-850.3/T + 86523/T^2)$ $p_2 = 0.18, p_3 = 0.82$	<i>Bauer et al.</i> (17), <i>Lepoutre et al.</i> (106)
$\text{N}_2, \Delta n = 1, 2, 3$	$K = 4.3 \times 10^{-16} \exp(7.0 \times 10^{-3}T)$ $T \leq 190$ $p_1 = 0$ $p_2 = 0$ $p_3 = 1$ $190 < T \leq 250$ $p_1 = 0$ $p_2 = \frac{T-190}{60}$ $p_3 = \frac{250-T}{60}$ $250 < T \leq 350$ $p_1 = \frac{T-250}{100}$ $p_2 = \frac{350-T}{100}$ $p_3 = 0$ $T > 350$ $p_1 = 1$ $p_2 = 0$ $p_3 = 0$	<i>Shved et al.</i> (188)
$\text{O}_2, \Delta n = 2, 3$	$K = 1.2 \times 10^{-15} \exp(2.2 \times 10^{-3}T + 7.0 \times 10^{-6}T^2)$ $p_2 = \frac{1}{2}, p_3 = \frac{1}{2}$	<i>Shved et al.</i> (188)
$\text{CO}, \Delta n = 3$	$K = 1.7 \times 10^{-14} \exp(-448.3/T + 53636/T^2)$ $p_3 = 1$	<i>Starr and Hancock</i> (193)
$\text{O}(^3P_J), \Delta n = 2, 3$	$K = 2.0 \times 10^{-13} (T/300)^{1/2}$ $T \leq 190$ $p_2 = 0.1$ $p_3 = 0.9$ $190 < T \leq 250$ $p_2 = \frac{T-190}{75} + 0.1$ $p_3 = \frac{190-T}{75} + 0.9$ $T > 250$ $p_2 = 0.9$ $p_3 = 0.1$	<i>Buchwald and Wolga</i> (24) <i>López-Valverde et al.</i> (207; 208)

Tab. C.4 Rate constants for the $V - T$ processes, which lead to splitting of the v_3 quantum of CO_2 molecules.

M	Collisional rate constant (cm^3s^{-1})	Reference
CO_2	$K = \begin{cases} 7.3 \times 10^{-14} \exp(-850.3/T + 86523/T^2), & \text{if } T \geq 175 \\ 3.3 \times 10^{-15}, & \text{if } T < 175 \end{cases}$	<i>Lunt et al.</i> (123)
N_2	$K = 5.5 \times 10^{-17} \sqrt{T} + 6.7 \times 10^{-10} \exp(-83.8T^{-1/3})$	<i>Shved et al.</i> (188)
O_2	$K = 1.0 \times 10^{-15} \exp(23.37 - 230.9T^{-1/3} + 564.0T^{-2/3})$	<i>Shved et al.</i> (188)
CO	$K = \begin{cases} 2.1 \times 10^{-12} \exp(-2659/T + 223052/T^2), & \text{if } T \geq 175 \\ 7.6 \times 10^{-16}, & \text{if } T < 175 \end{cases}$	<i>Lunt et al.</i> (123)
$\text{O}(^3P_J)$	$K = 3.0 \times 10^{-12} (300/T)^{1/2},$ $K = 3.5 \times 10^{-13} \cdot \sqrt{T} + 2.32 \times 10^{-9} \cdot \exp(-76.75/T^{1/3})$	<i>López-Puertas et al.</i> (114) <i>Sharma and Wintersteiner</i> (184)

Tab. C.5 $V - T$ rate constants for CO_2 v_2 quenching.

The constants K for this group for different collisional partners and Δn are given in Tab. C.4 (p. 85).

2. v_2 -mode quenching

$$\text{CO}_2^\alpha(n^l v_3, m) + M \rightleftharpoons \text{CO}_2^\alpha((n-1)^l v_3, m) + M, \quad |l - l'| = 1 \quad (\text{C.9})$$

$$k^{V-T} = \begin{cases} 4 \frac{\mathbf{R}(n^l 0, m \rightarrow (n-1)^l 0, m')^2}{\mathbf{R}(02201 \rightarrow 01101)^2} \cdot K, & \text{for } M \neq \text{O}(^3P) \\ \frac{\mathbf{R}(n^l 0, m \rightarrow (n-1)^l 0, m')^2}{\mathbf{R}(01101 \rightarrow 00001)^2} \cdot K, & \text{for } M = \text{O}(^3P). \end{cases}$$

The constants K for this group are given in Tab. C.5 (p. 85).

3. v_3 -mode quenching by $\text{O}(^3P_J)$:

$$\text{CO}_2^\alpha(n^l v_3, m) + \text{O}(^3P) \rightleftharpoons \text{CO}_2^\alpha(n^l (v_3 - 1), m') + \text{O}(^3P). \quad (\text{C.10})$$

The rate constant for this group is $k^{V-T} = \epsilon_{nl} v_3 \cdot 1.15 \times 10^{-14} \sqrt{T}$, was taken from *Nebel et al.*(153).

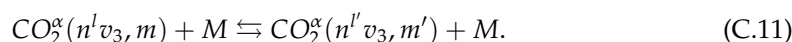
M	Collisional rate constant (cm ³ s ⁻¹)	Reference
CO ₂	$k^{V-T} = g_{l'} \cdot 5.76 \times 10^{-12} \exp(-1.312 \times 10^{-2} \Delta E)$	<i>López-Valverde et al.</i> (207; 208)
N ₂ , O ₂ , CO, O(³ P _J)	$k^{V-T} = g_{l'} 5.76 \cdot \times 10^{-13} \exp(-1.312 \times 10^{-2} \Delta E)$ $\Delta E = E_v - E_{v'} , \text{cm}^{-1}$	<i>Shved et al.</i> (188)

Tab. C.6 $V - T$ rate constants for CO₂ transitions inside the n -family.

	$l = 0$	$l \neq 0$
$n = 2k$	$\epsilon_{nl} = \frac{1}{(k+1)^2}$	$\epsilon_{nl} = \frac{2}{(k+1)^2}$
$n = 2k + 1$		$\epsilon_{nl} = \frac{2}{(k+1)(k+2)}$

Tab. C.7 Branching ratios ϵ_{nl} for CO₂ v_3 splitting.

4. Transitions between the states of the n -family



The rate constants for this group are given in Tab. C.6 (p. 86).

The expressions for the branching ratios ϵ_{nl} where not given by *Shved et al.*(188). The correct expressions for these ratios are derived below.

Each Fermi group $n^l v_3$ includes $\frac{n-l}{2} + 1$ vibrational levels. Therefore, the number of splitting channels $1/\epsilon_{nl}$ is:

for $n = 2k, \quad l = 0, 2, 4, \dots, n = 2k, \quad l_1 = n/2 = 0, 1, 2, \dots, k$

$$\begin{aligned} \frac{1}{\epsilon_{nl}} &= \left(\frac{n}{2} + 1\right) + 2 \sum_{l_1=1}^k ((k+1) - l_1) = (k+1) + 2k(k+1) - 2 \sum_{l_1=1}^k l_1 = \\ &= k+1 + k(k+1) = (k+1)^2, \end{aligned} \quad (\text{C.12})$$

and for $n = 2k + 1, \quad l = 1, 3, 5, \dots, n = 2k + 1, \quad l_1 = (l-1)/2$

$$\begin{aligned} \frac{1}{\epsilon_{nl}} &= 2 \sum_{l_1=0}^k \left(\frac{n-l}{2} + 1\right) = 2 \sum_{l_1=0}^k \left(\frac{2k+1 - (2l_1+1)}{2} + 1\right) = 2 \sum_{l_1=0}^k (k+1 - l_1) = \\ &= 2(k+1) + 2k(k+1) - 2 \frac{k(k+1)}{2} = 2(k+1) + k(k+1) = (k+1)(k+2). \end{aligned} \quad (\text{C.13})$$

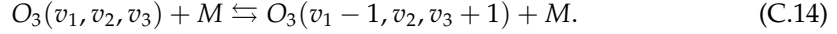
Taking into account the vibrational degeneracy factor 2 for groups with $l \neq 0$, we get the values of branching ratios ϵ_{nl} (see Tab. C.7 (p. 86)).

C.2.3 $V - T$ collisional transitions in O₃

There are two different methods of considering the $V - T$ kinetics of O₃ molecules: energy gap (EG) models, which use a single expression for the rate constants for most or all transitions, and the more detailed models trying to use the available experimental data for each measured rate and scaling techniques for the rest.

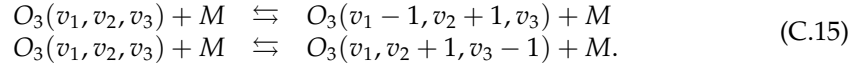
C.2.3.1 Kinetic model of Manuilova

The model of Manuilova (*Manuilova and Shved (129)* and *Manuilova et al.(132)*) is an example of the non-EG model. In kinetics of the O_3 vibrational states the following groups of inelastic collisions were taken into account (the corresponding rate coefficients are given in the tables below):

1. $\nu_1 \leftrightarrow \nu_3$ transitions

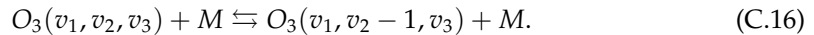
M	Collisional rate constant (cm^3s^{-1})	Reference
N_2	$k^{V-T} = (v_1 + v_3) \cdot 1.18 \times 10^{-11} (300/T)^{0.8}$	<i>Doyennette et al.(40)</i>
O_2	$k^{V-T} = (v_1 + v_3) \cdot 0.97 \times 10^{-11} (300/T)^{0.7}$	
$O(^3P_J)$	see Appendix C.4.2 (p. 96)	<i>West et al.(215; 216)</i>

Tab. C.8 $V - T$ rate constants for O_3 $\nu_1 \leftrightarrow \nu_3$ transitions.

2. $\nu_1 \leftrightarrow \nu_2$ and $\nu_3 \leftrightarrow \nu_2$ transitions

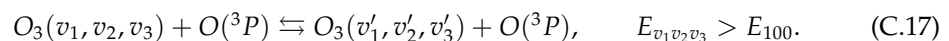
M	Collisional rate constant (cm^3s^{-1})	Reference
N_2	$k^{V-T} = (v_2 + 1)(v_1 + v_3) \cdot 0.5 \times 10^{-13} \sqrt{T} \exp(-22.8/T^{1/3})$	<i>Menard et al.(136)</i>
O_2	$k^{V-T} = (v_2 + 1)(v_1 + v_3) \cdot 1.2 \times 10^{-13} \sqrt{T} \exp(-26.8/T^{1/3})$	
$O(^3P_J)$	see Appendix C.4.2 (p. 96)	<i>West et al.(215; 216)</i>

Tab. C.9 $V - T$ rate constants for O_3 $\nu_1 \leftrightarrow \nu_2$ and $\nu_3 \leftrightarrow \nu_2$ transitions.

3. ν_2 transitions

M	Collisional rate constant (cm^3s^{-1})	Reference
N_2	$k^{V-T} = v_2 \cdot 59 \times 10^{-13} \sqrt{T} \exp(-53.8/T^{1/3})$	<i>Menard et al.(136)</i>
O_2	$k^{V-T} = v_2 \cdot 7 \times 10^{-13} \sqrt{T} \exp(-40.0/T^{1/3})$	
$O(^3P_J)$	see Appendix C.4.2 (p. 96)	<i>West et al.(215; 216)</i>

Tab. C.10 $V - T$ rate constants for O_3 ν_2 transitions.

4. Transition to the closest (by energy) state by $O(^3P_J)$ quenching (only for MODEL 2, see Appendix C.4.2 (p. 96))

M	Collisional rate constant (cm^3s^{-1})	Reference
$\text{O}(^3P_j)$	$k^{V-T} = 1.0 \times 10^{-10}$	<i>Manuilova et al.(132)</i>

Tab. C.11 $V - T$ rate constants for O_3 $\text{O}(^3P_j)$ quenching.

The recent experiments of *Menard-Bourcin et al.(137)* show good agreement with this kinetic scheme: it was confirmed that the harmonic oscillator rule gives values of rate constants for processes Eq. C.15, (p. 87) and Eq. C.16, (p. 87) which are within the experiment uncertainty of 30%.

C.2.3.2 Kinetic models of Mlynczak

Mlynczak and Drayson (143; 144) and other authors (see *Fichet et al.(52)*, *Vollmann* (210)) have used two kinetic models:

1. Energy Gap (EG) model.

The authors consider 62 vibrational levels (up to $v = 203$ with $E = 5058\text{cm}^{-1}$). Collisional $V - T$ rate constants use a single expression for all transitions

$$k_{vv'}^{V-T} = 10^{-12} \times \exp\left(-\frac{\Delta E}{200}\right) \text{cm}^3\text{s}^{-1},$$

where the energy difference between upper and lower state $\Delta E = E_v - E_{v'}$ is given in cm^{-1} .

2. Simple Single Mode (SSM) model.

The 14 vibrational levels (010) , $(00v_3)$, $v_3 = 0, \dots, 7$ and $(10v_3)$, $v_3 = 1, 2, 3, 4$ were included in the model.

C.2.3.3 Kinetic model of Koutoulaki

This model is an extension of the EG model of *Mlynczak and Drayson* (143). The available measurements of the collisional constants with N_2 and O_2 as a partner are fitted with a singular expression

$$k_{vv'}^{V-T} = A\sqrt{T} \exp(-B(E_v - E_{v'})^{\frac{2}{3}} T^{-\frac{1}{3}}), \quad (\text{C.18})$$

where the constants A and B are given in Tab. C.12 (p. 88). This represents the approach known as the Landau-Teller elementary theory of the vibrational energy transfer.

Parameters	A	B
Minimal	2.24×10^{-13}	0.62
Default	6.10×10^{-13}	0.58
Maximal	2.73×10^{-12}	0.64

Tab. C.12 Parameters A and B used by *Koutoulaki* (92).

It was suggested that this formula applies to all other possible collisional transitions, excluding six transitions in Tab. C.13 (p. 89), for which the averaged experimental values are used.

Upper state	Lower state	Collisional rate constant (cm^3s^{-1})
010	000	3.02×10^{-14}
100	010	3.77×10^{-14}
001	010	3.77×10^{-14}
100	000	3.09×10^{-15}
001	000	3.09×10^{-15}
100	001	1.07×10^{-11}

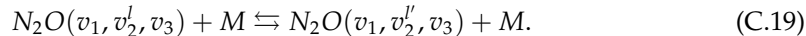
Tab. C.13 Averaged collisional rates used by *Koutoulaki* (92)

The rate constants for the collisions with atomic oxygen are higher than those for N_2 and O_2 . Because of the small number of experimental measurements of these transitions, *Koutoulaki* (92) decided to introduce only one “representative” transition $001 \rightarrow 000$ with the rate constant $k_{\text{O}(^3P)}^{V-T} = 1.05 \times 10^{-11}$, based on the measurements of *West et al.*(215; 216).

C.2.4 $V - T$ collisional transitions in N_2O

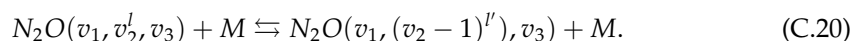
The following collisional processes for calculating the population of the N_2O vibrational states were included

1. $V - T$ process changing only the angular momentum l



It was supposed that this process is infinitely fast. This approximation is justified, since the energy gap between the states is small ($9\text{-}18 \text{ cm}^{-1}$). *Kutepov and Shved* (96) and *Wintersteiner et al.*(219) show that the approximation of the infinitely fast $V - T$ energy exchange may be used even for the 50 cm^{-1} gap.

2. ν_2 -mode quenching



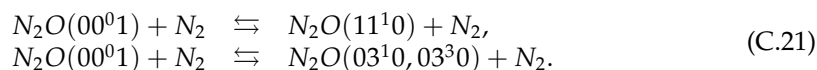
It was assumed that these vibrational transitions obey the selection rule $|l - l'| = 1$, following *Shved and Gusev* (187). The measurements of the rate constant for the $01^10 - 00^00$ transition were made for $T > 300\text{K}$ (see *Zuev* (227)). This value was rescaled to lower temperature and taken equal to $k^{V-T} = 0.87 \times 10^{-14} \text{ cm}^3\text{s}^{-1}$. As a result, the following rate constants were used:

Transitions	Rate constant (cm^3s^{-1})
$03^10 - 02^20$	$k^{V-T} = 0.87 \times 10^{-14}$
$11^10 - 10^00$	
$01^11 - 00^01$	

Tab. C.14 $V - T$ processes for N_2O ν_2 bending mode.

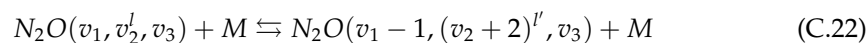
3. Splitting ν_3 -quantum into ν_2 -quanta.

This process occurs through two pathways (see *Zuev* (226))



Siddles et al.(190) have measured the total rate constant of the splitting for $T = 150 - 295\text{K}$. The value $4.3 \times 10^{-15} \text{ cm}^3\text{s}^{-1}$ at 200K was taken for this group.

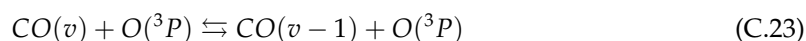
4. Exchange between the ν_1 and ν_2 modes



The energy defect for the processes Eq.C.22, (p.90) is in the $88 - 132 \text{ cm}^{-1}$ range. *Kung* (94) estimated the rate constant for the $N_2O(10^00) - N_2$ quenching as being equal to $1.0 \times 10^{-13} \text{ cm}^3\text{s}^{-1}$ at room temperature. This value is also taken at 200K. The equal probability of the ν_1 quantum energy transfer to each of two ν_2 states was assumed. Taking into account the degeneracy of the final state, the rate constants for all other processes Eq.C.22, (p.90) were scaled from the value given above.

C.2.5 $V - T$ collisional transitions in CO

López-Puertas et al.(115) have shown that the CO quenching process by $O(^3P_J)$



is the most important $V - T$ process for the formation of the non-LTE CO populations.

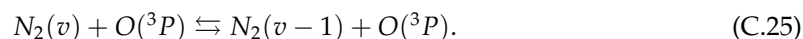
The measurements of this rate constant for different temperatures were reported by *Lewittes et al.*(108). Fitting the data by the Landau-Teller exponential law and using the harmonic oscillator scaling rule, *Kutepov et al.*(99) give the value

$$k^{V-T} = v \cdot 1.12 \times 10^{-13} T \exp(-44.3T^{-1/3}), \quad (\text{C.24})$$

where v is the number of CO vibrational quanta.

C.2.6 $V - T$ collisional transitions in N_2

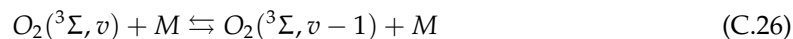
The most important $V - T$ process is the $N_2(v)$ quenching by $O(^3P_J)$



The rate constant for the process involving $N_2(1)$ was taken equal to $2.45 \times 10^{-22} T^{2.87}$, and is the same as used by *López-Puertas et al.*(109), *Nebel et al.*(153) and *Shved et al.*(188). The value for $v > 1$ was rescaled using the harmonic oscillator rule.

C.2.7 $V - T$ collisional transitions in O_2

$O_2(^3\Sigma, v)$ quenching



is the most important $V - T$ process.

The rate constants for different collisional partners are given in Tab.C.15 (p.90).

M	Collisional rate constant (cm^3s^{-1})	Reference
N_2, O_2	$k^{V-T} = 1.364 \times 10^{-12} T \exp(-137.93/T^{1/3})$	<i>Shved et al.</i> (188)
$O(^3P_J)$	$k^{V-T} = 1.3 \times 10^{-12} (T/300)$	<i>López-Puertas et al.</i> (117)

Tab. C.15 $V - T$ rate constants for $O_2(^3\Sigma, v)$ quenching.

C.3 $V - V$ collisional processes

The short description is presented below for the $V - V$ energy exchange processes that are included in the current model (in generalized form). The most important ones are shown in Fig. C.1 (p. 91).

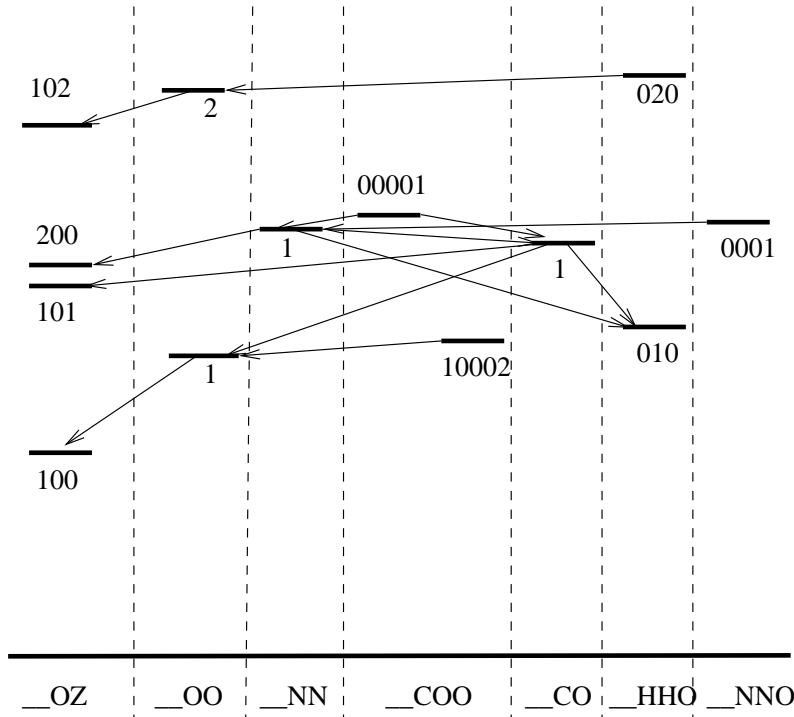
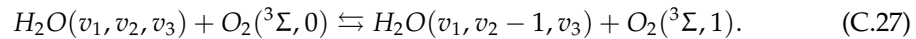


Fig. C.1 Most important $V - V$ processes.

- H_2O and O_2 .

The ν_2 -mode exchange with O_2 -vibration

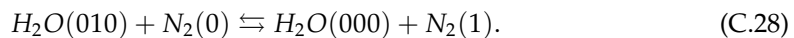


López-Puertas *et al.*(117) suggested the value

$$k^{V-V} = v_2 \cdot (1.0 \times 10^{-12} - 1.0 \times 10^{-11}).$$

- H_2O and N_2 .

The ν_2 -mode exchange with N_2 -vibration



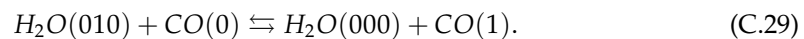
The rate constant

$$k^{V-V} = 1.2 \times 10^{-14} (T/300)^{1/2}$$

was published by Whitson and McNeal (217).

- H_2O and CO

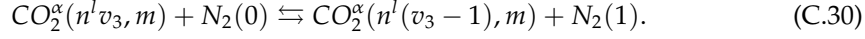
The ν_2 -mode exchange with CO -vibration



The rate constant was measured by Stephenson and Mosburg (196).

– CO₂ and N₂ .

The ν_3 -mode exchange with N₂ -vibration

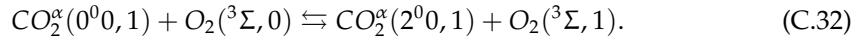


Shved et al.(188) used the rate constant

$$k^{V-V} = v_3 \cdot 8.91 \times 10^{-12} / \sqrt{T}. \quad (C.31)$$

– CO₂ and O₂ .

ν_1 -quantum exchange

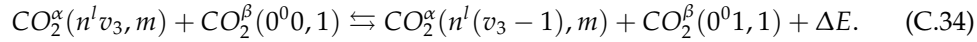


Shved et al.(188) used the following value for the rate constant

$$k^{V-V} = 5.7 \times 10^{-15} \sqrt{T} \left[2.2 - 1.3 \exp\left(-\frac{315}{T}\right) \right] \exp\left(-\frac{56.7}{\sqrt{T}}\right). \quad (C.33)$$

– CO₂ and CO₂ .

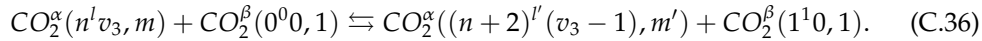
1. ν_3 -mode exchange between the CO₂ isotopes



Shved et al.(186) suggested the value

$$k^{V-V} = \begin{cases} v_3 \cdot 6.8 \times 10^{-12} T^{1/2}, & \text{if } \Delta E \leq 42 \text{cm}^{-1} \\ v_3 \cdot 3.6 \times 10^{-11} T^{1/2} \exp(-\Delta E/26.3), & \text{if } \Delta E > 42 \text{cm}^{-1}. \end{cases} \quad (C.35)$$

2. Splitting ν_3 into ν_2 -quanta

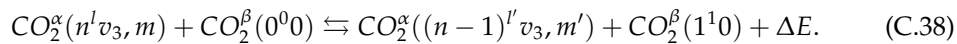


Using the measurements of *Lepoutre et al.*(106), values suggested by *López-Valverde et al.*(207) and the scaling procedure proposed by *Shved et al.*(188) , the following expressions for the rate constants are suggested

$$k^{V-V} = \begin{cases} \epsilon_{nl} v_3 \cdot 3.6 \times 10^{-13} \exp(-1660/T + 176948/T^2), & \text{if } T > 175 \\ \epsilon_{nl} v_3 \cdot 8.8 \times 10^{-15}, & \text{if } T \leq 175. \end{cases} \quad (C.37)$$

See Appendix B.2 (p. 72) for the definition and numerical value of branching ratio ϵ_{nl} .

3. ν_2 -quantum exchange between the CO₂ isotopes



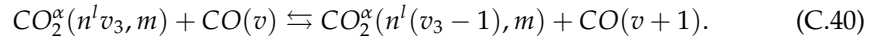
Shved et al.(188) used the rate constant

$$k^{V-V} = \begin{cases} \frac{1}{g_l} \cdot 9.4 \times 10^{-11} \exp(-0.024|\Delta E|) \frac{\mathbf{R}(n^l 0, m \rightarrow (n-1)^l 0, m')^2}{\mathbf{R}(02201 \rightarrow 01101)^2}, & \text{if } \Delta E > 0 \\ \frac{1}{g_l} \cdot 9.4 \times 10^{-11} \exp(-0.029|\Delta E|) \frac{\mathbf{R}(n^l 0, m \rightarrow (n-1)^l 0, m')^2}{\mathbf{R}(02201 \rightarrow 01101)^2}, & \text{if } \Delta E < 0, \end{cases} \quad (C.39)$$

where \mathbf{R}^2 is the squared moment of the considered ν_2 transition.

– CO₂ and CO .

1. ν_3 -mode exchange with CO -vibration

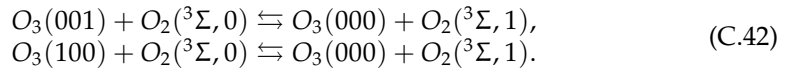


Fitting the experimental data by *Starr and Hancock* (193) with the Landau-Teller exponential law and applying the harmonic oscillator scaling rule the following expression was derived for the rate constant

$$k^{V-V} = v_3(v + 1) \cdot 1.6 \times 10^{-12} \exp(-1169/T + 77601/T^2). \quad (C.41)$$

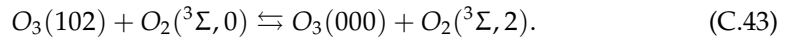
- O_3 and O_2 .

1. ν_1 -mode and ν_3 -mode exchange with O_2 -vibration



The value of the rate constant for these processes $k^{V-V} = 1.0 \times 10^{-16} \text{ cm}^3\text{s}^{-1}$ was taken from *Parker and Ritke* (165).

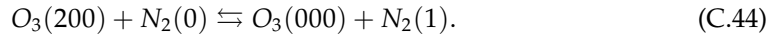
2. Near-resonant process



The rate constant value for this transition was estimated by *Rawlins et al.*(170), as $k^{V-V} = 1.0 \times 10^{-11} \text{ cm}^3\text{s}^{-1}$.

- O_3 and N_2 .

$2\nu_1$ exchange with N_2 -vibration



The value of the rate constant for this process, $k^{V-V} = 2.3 \times 10^{-14} \text{ cm}^3\text{s}^{-1}$ was reported by *Robertshaw and Smith* (173).

- O_3 and CO .

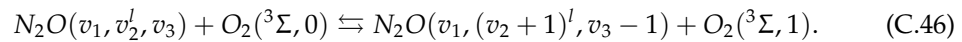
$\nu_1 + \nu_3$ exchange with CO -vibration



The rate constants were measured by *Harding et al.*(75).

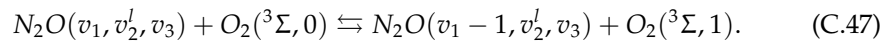
- N_2O and O_2 .

1. Splitting a ν_3 -quantum by collisions with O_2

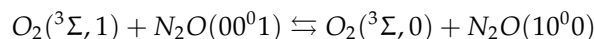


Siddles et al.(190) have measured the rate constant of N_2O (00^01) splitting at $T = 150 - 295\text{K}$. In agreement with these measurements it was taken equal to $7.0 \times 10^{-15} \text{ cm}^3\text{s}^{-1}$ at 200K.

2. Energy exchange between the ν_1 stretch mode and O_2 -vibration



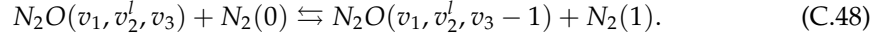
There are measurements of the rate constant for the process



for $T > 380\text{K}$ only (see *Zuev* (227)). Extrapolating these measurements to lower temperatures and taking the rate constant of the process (Eq. C.47, (p. 93)) for the N_2O (00^01) quenching, we get $k^{V-V} = 1.3 \times 10^{-15} \text{ cm}^3\text{s}^{-1}$ at 200K. The same value was also used for other transitions of this type.

- N₂O and N₂

The energy exchange between the ν_3 -mode and N₂ -vibration



Gueguen et al.(71) have measured the rate constant of the process Eq.C.48, (p.94) for the N₂O (00⁰1) quenching for $T = 150 - 1200\text{K}$. *Shved and Gusev* (187) suggested the value $k^{V-V} = 1.1 \times 10^{-13} \text{cm}^3 \text{s}^{-1}$ for 200K. This value was used for all other transitions in this group.

- CO and N₂ .

Energy exchange between CO and N₂ -vibration

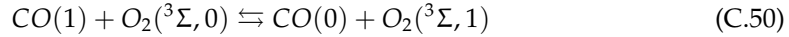


Allen and Simpson (3) have measured the rate constant of this process for different values of temperature. Fitting the data using the Landau-Teller exponential law, *Kutepov et al.*(99) gives the value of this constant

$$k^{V-V} = 3.42 \times 10^{-10} \exp(-54.7T^{-1/3}).$$

- CO and O₂ .

Energy exchange



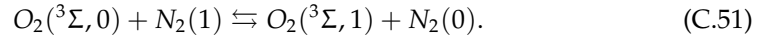
The rate constant measured by *Doyennette et al.*(39)

$$k^{V-V} = 9.79 \times 10^{-17} \exp(8.02 \times 10^{-3}(T - 300) - 2.05 \times 10^{-5}(T - 300)^2)$$

was used for this process. This expression was suggested by *López-Puertas et al.*(115).

- O₂ and N₂ .

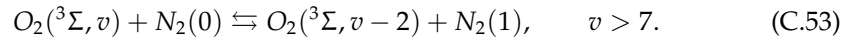
1. The process for $v = 1$



The rate constant was measured for the temperature range $T = 125-295 \text{K}$ by *Maricq et al.*(133)

$$k^{V-V} = 4.43 \times 10^{-17} T \exp\left(-\frac{49.32}{T^{1/3}}\right). \quad (C.52)$$

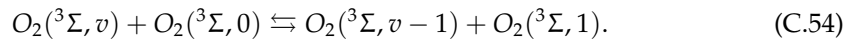
2. The process for higher v



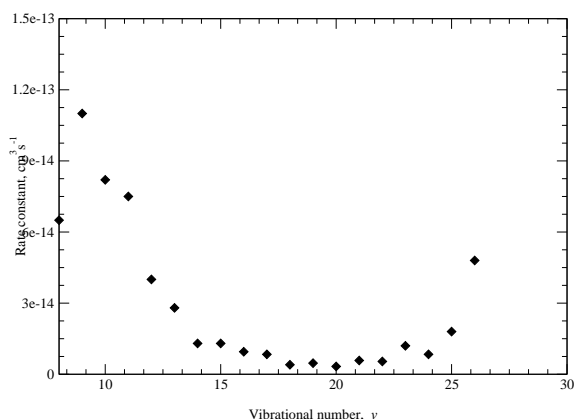
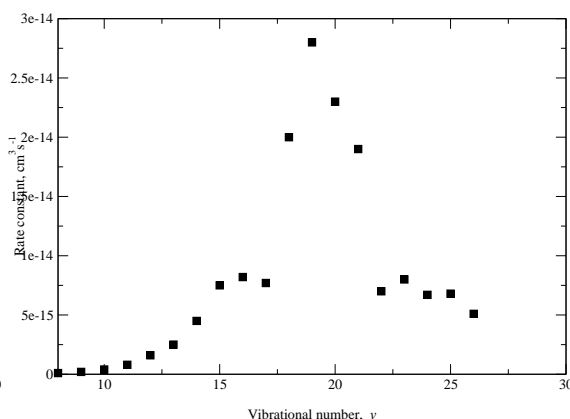
The rate constants for different v were taken from *Slanger* (191), *Park and Slanger* (164), *Klatt et al.*(90) and *Billing and Kolesnik* (21) and are given in Fig. C.3 (p.95).

- O₂ and O₂ .

Energy exchange

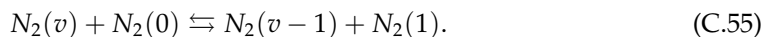


The rate constants for different v are given in Fig. C.2 (p.95).

Fig. C.2 Rate constants for $O_2(v) + O_2(0)$ process.Fig. C.3 V – V rate constants for $O_2(v) + N_2(0)$ process.

– N_2 and N_2 .

Energy exchange



The rate constants for different v suggested by *Pravilov* (166) are given in Tab. C.16 (p. 95).

v	T=200K	T=300K
2	7.0	7.5
3	7.3	8.4
4	7.5	9.3
5	6.1	8.1
6	5.4	7.6
7	4.1	6.2

Tab. C.16 Rate constants for $N_2(v) + N_2(0)$ process

The linear extrapolation is used for all temperature values.

C.4 C – V processes

C.4.1 Production of ozone: recombination reaction

For a quiet atmosphere, the most important non-thermal source of vibrationally excited ozone is the recombination reaction



The rate constants of recombination Eq. C.56, (p. 95) for $M=O_2$ and N_2 provided by *Hippler et al.*(78) are given in Tab. C.17 (p. 96). The value of the rate constant for atomic oxygen $O(^3P_j)$ was taken from *Steinfeld et al.*(194).

Rate constant (in $\text{cm}^6 \text{s}^{-1}$)	Collisional partner M
$6.9 \times 10^{-34} \cdot \left(\frac{T}{300}\right)^{-1.25}$	O_2
$5.5 \times 10^{-34} \cdot \left(\frac{T}{300}\right)^{-2.6}$	N_2
$2.15 \times 10^{-34} \cdot \exp\left(\frac{345}{T}\right)$	$\text{O}(^3P_J)$

Tab. C.17 Rate constants of O_3 chemical production

Three models are suggested for the vibrational excitation distribution of the ozone molecules produced in the recombination reaction:

1. The method of *Joens et al.*(85).

The author assumed that the ozone is formed at the vibrational levels with highest energy and then is relaxed by the collisions and spontaneous emission.

Following this theory, *Manuilova et al.*(132) suggested that the initially populated state is one of the six states from group VI in Fig. B.6 (p. 80) (namely O_3 (003)) and the vibrational LTE is assumed between the states of group VI (6 levels: 003, 102, 201, 300, 031 and 130). *Mlynczak and Drayson* (143; 144) (EG model) put the produced ozone in 8 levels (311, 005, 240, 104, 033, 132, 410, 203) with equal probability $w_{p_v} = 0.125$. *Koutoulaki* (92) has considered in one of the models, that all excited molecules are formed at the level with highest vibrational energy.

2. The method of *Rawlins* (169).

It is assumed that the nascent distribution in the v_3 manifold is decreasing gradually with the increase of v_3 , with the probability given by an expression Eq. C.57, (p. 96)

$$w_{p_{v_3}} = \frac{\left(1 - \frac{E_{v_3}}{E}\right)^{\frac{3}{2}}}{\sum_v \left(1 - \frac{E_{v_3}}{E}\right)^{\frac{3}{2}}}, \quad (\text{C.57})$$

where E is the dissociation energy of O_3 (8468 cm^{-1}).

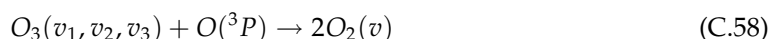
Such distribution was used by *Mlynczak and Drayson* (143; 144) (SSM model) and by *Koutoulaki* (92) ("zero surprisal" distribution).

3. Any of the O_3 (v_1, v_2, v_3) levels can be produced with equal probability.

This approach was used by *Koutoulaki* (92) in her model with 245 vibrational levels.

C.4.2 Chemical deactivation of ozone by $\text{O}(^3P_J)$

The modeling of the O_3 (v_1, v_2, v_3) deactivation by collisions with atomic oxygen accounts for the chemical reaction



with the rate constant $k_{\text{O}}^{\text{chem}}(v_1, v_2, v_3)$. The model of *Manuilova et al.*(132) is the only one among the published, which accounts for these processes.

West et al.(216) estimated the upper limit of $k_{\text{O}}^{\text{chem}}(100,001)$ as $4.5 \times 10^{-12} \text{ cm}^3\text{s}^{-1}$, and this value does not exceed 30 percent of the whole rate constant of O_3 (v_1, v_2, v_3) quenching by collisions with $\text{O}(^3P_J)$.

The direct measurements of $k_{\text{O}}^{V-T}(v_1, v_2, v_3)$ and $k_{\text{O}}^{\text{chem}}(v_1, v_2, v_3)$ exist only for three lower states 010, 001, 100. For all other states one has to use a scaling rule. Using the results of *West et al.*(215; 216) and *Rawlins et al.*(170), the following 2 models of $\text{O}_3(v_1, v_2, v_3)$ deactivation by collisions with $\text{O}(^3P_J)$ based on *Manuilova et al.*(132) were suggested:

1. MODEL 1 suggests the maximal contribution of reaction Eq. C.58, (p. 96) to the deactivation of $\text{O}_3(v_1, v_2, v_3)$.

The rate constant $k_{\text{O}}^{\text{chem}}(v_1, v_2, v_3)$ is derived from the measurements of *West et al.*(215; 216) and defined as

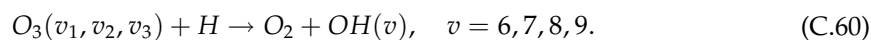
$$k_{\text{O}}^{\text{chem}}(v_1, v_2, v_3) = \begin{cases} 1.5 \times 10^{-11}, & \text{if } E_{v_1 v_2 v_3} \leq 2100 \text{cm}^{-1} \\ 5/7 E_{v_1 v_2 v_3} \cdot 10^{-14} \text{cm}^3 \text{s}^{-1}, & \text{if } E_{v_1 v_2 v_3} > 2100 \text{cm}^{-1}. \end{cases} \quad (\text{C.59})$$

These values are also in a good agreement with the lower limits of $k_{\text{O}}^{\text{chem}}(00v_3)$ for $v_3 = 2-5$ reported by *Rawlins et al.*(170).

2. MODEL 2 (“model 3” in *Manuilova et al.*(132)) supposes the minimal contribution of the reaction Eq. C.58, (p. 96) to the $\text{O}_3(v_1, v_2, v_3)$ deactivation but adds the $V - T$ energy exchange with the nearest (by energy) vibrational state for all collisional partners (see Appendix C.2.3.1 (p. 87)).

C.4.3 Destruction of ozone by reactions with other minor chemical species

Mlynczak and Drayson (143; 144) have shown that at nighttime the reaction with atomic hydroxyl Eq. C.60, (p. 97) is the second (after O) important process of ozone loss and the production of vibrationally excited OH in the lower thermosphere and upper mesosphere



DeMore et al.(36) give the following value for the rate constant of this process

$$k_{\text{H}}^{\text{chem}}(v_1, v_2, v_3) = 1.4 \times 10^{-10} \exp(-470/T). \quad (\text{C.61})$$

C.4.4 Chemical excitation of O_2

The vibrationally excited $\text{O}_2(^3\Sigma, v)$ is created in the chemical reaction of ozone and atomic oxygen



The values of rate constants for this reaction at $T = 200$ K for different v and based on experimental measurements and theoretical predictions were taken from *Balakrishnan et al.*(11) and are plotted in Fig. C.4 (p. 98).

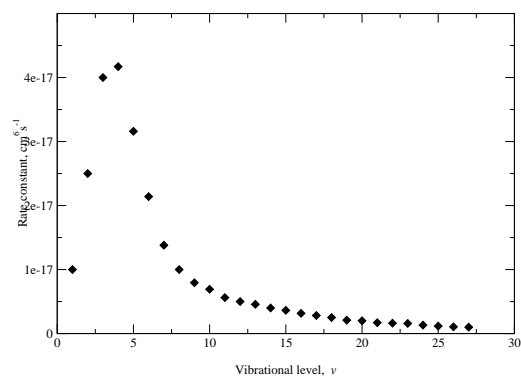


Fig. C.4 Chemical production rate constant of $O_2(^3\Sigma, v)$ from O_3

D. Solution of the radiative transfer equation (RTE)

To deal with the solution of the RTE in plane-parallel atmosphere, the atmospheric radiation at any point in the atmosphere is splitted into two parts: the radiation coming in the atmosphere from outer space direction $I_{\mu\nu}^-$, which is called "incoming radiation", and the radiation emitted from the direction of the planetary surface (or upper boundary of clouds) $I_{\mu\nu}^+$, which is called "outgoing radiation".

For the intensity of incoming radiation $I_{\mu\nu}^-(z)$

$$I_{\mu\nu}^-(z) = I_{\mu\nu}(z), \quad \mu = \cos(\theta_{\text{in}}) < 0,$$

and the intensity of outgoing radiation $I_{\mu\nu}^+(z)$

$$I_{\mu\nu}^+(z) = I_{\mu\nu}(z), \quad \mu = \cos(\theta_{\text{out}}) > 0,$$

the boundary conditions will be

$$I_{\mu\nu}^-(0) = 0, \quad I_{\mu\nu}^+(D) = I^{\text{surface}}(\mu, \nu). \quad (\text{D.1})$$

Taking into consideration the definitions of $I_{\mu\nu}^+$, $I_{\mu\nu}^-$, and using their symmetric average $u_{\mu\nu}(z)$ (see also Appendix D.4.1 (p. 102))

$$u_{\mu\nu} = \frac{I_{\mu\nu}^+(z) + I_{\mu\nu}^-(z)}{2}, \quad (\text{D.2})$$

the Eq. 2.8, (p. 4) can be rewritten as

$$\bar{J}_{l\nu}(z) = \int_0^1 \left(\int_0^{+\infty} u_{\mu\nu}(z) \varphi_{l\nu}(\nu, z) d\nu \right) d\mu. \quad (\text{D.3})$$

If both $\chi_\nu(z)$ and $\eta_\nu(z)$ are known, then the RTE (Eq. 2.2, (p. 3)) is a nonhomogenous linear differential equation, for which the formal solution can be written as

$$I_{\mu\nu}(z) = I_{\mu\nu}(z_0) \exp\left(-\frac{1}{\mu} \int_{z_0}^z \chi_\nu(z') dz'\right) + \int_{z_0}^z \eta_\nu(z') \exp\left(-\frac{1}{\mu} \int_z^{z'} \chi_\nu(z'') dz''\right) dz'. \quad (\text{D.4})$$

It should be noted that from the point of view of the computer time consumption, the simple numerical quadrature Eq.D.4, (p. 99) will be very inefficient, because it requires to calculate a lot of exponentials. That was the reason for the development of several numerical methods, that minimize the number of calculated exponentials or even avoid them at all.

In general, all the methods can be divided into two groups:

- integral methods, based on the formal solution of the transfer equation Eq. D.4, (p. 99),
- differential methods.

The differential methods can be of two kinds:

- based on the first order form of the transfer equation (DFE method of *Castor et al.*(26))
- based on the second order form of the transfer equation (Feautrier method of *Feautrier* (50)).

All these methods are described below, but first the optical depth and lambda operator need to be defined.

D.1 Optical depth

To simplify the form of the RTE (Eq. D.4, (p. 99)), the “optical depth” is defined. If the opacity $\chi_\nu(z)$ is positive along the ray, then the integral

$$\tau_{\mu\nu}(z) = -\frac{1}{\mu} \int_z^{+\infty} \chi_\nu(z') dz' \quad (\text{D.5})$$

is a monotonously increasing function. If $\chi_\nu(z)$ is negative in some altitude regions (the stimulated emission term in Eq. 2.3, (p. 3) is higher than the absorption term and there is no substantial overlapping with other lines to compensate for that difference), then we have a situation of an infrared Amplification by Stimulated Emission of Radiation, or natural infrared laser. This specific situation requires special treating, which will be presented in Appendix D.5 (p. 104). The infrared natural laser effect in the planetary atmospheres was observed by *Mumma et al.* (1952) in the CO₂ bands around 10 μm and studied by many authors. The theoretical estimations showed that the laser effect can also potentially happen for 9.6 μm O₃ hot bands and H₂O 6.3 μm hot bands in the Earth atmosphere, though there is no experimental confirmation of that so far.

The integral in Eq. D.5, (p. 100) is called “optical depth”. Using optical depth the nonlaser RTE (Eq. 2.2, (p. 3)) can be rewritten in the following form

$$\frac{dI_{\mu\nu}(z)}{d\tau_{\mu\nu}} = -I_{\mu\nu}(z) + S_\nu(z), \quad (\text{D.6})$$

where S_ν is the source function, introduced in Eq. 2.6, (p. 4).

D.2 Lambda and psi operators

The monochromatic lambda operator $\Lambda_{\mu\nu}$ along the ray with direction μ is defined by the formal solution of the RTE (Eq. D.6, (p. 100)) as

$$I_{\mu\nu} = \Lambda_{\mu\nu} S_\nu. \quad (\text{D.7})$$

If one assumes that the atmosphere consists of D layers enumerated from 0 to $D - 1$, then the lambda operator from Eq. D.7, (p. 100) has the following matrix representation

$$\begin{pmatrix} I_0 \\ I_1 \\ \vdots \\ I_{D-1} \end{pmatrix} = \begin{pmatrix} \Lambda_{0,0} & \Lambda_{0,1} & \dots & \Lambda_{0,D-1} \\ \Lambda_{1,0} & \Lambda_{1,1} & \dots & \Lambda_{1,D-1} \\ \vdots & \vdots & \dots & \vdots \\ \Lambda_{D-1,0} & \Lambda_{D-1,1} & \dots & \Lambda_{D-1,D-1} \end{pmatrix} \begin{pmatrix} S_0 \\ S_1 \\ \vdots \\ S_{D-1} \end{pmatrix}. \quad (\text{D.8})$$

The monochromatic psi operator $\Psi_{\mu\nu}$ along the ray with direction μ defined as

$$I_{\mu\nu} = \Psi_{\mu\nu} \eta_{\mu\nu} \quad (\text{D.9})$$

will have similar matrix representation. One should notice that the psi operator is linear in level populations, which simplifies its application by accelerated methods of the form described in Section 3.4 (p. 14) in comparison with the lambda operator. Specifically, the preconditioning strategy becomes more straightforward and natural.

The local (diagonal) approximate operator Λ^* has the form

$$\Lambda^* = \begin{pmatrix} \Lambda_{0,0} & 0 & \dots & 0 \\ 0 & \Lambda_{1,1} & \dots & 0 \\ \vdots & \vdots & \dots & \vdots \\ 0 & 0 & \dots & \Lambda_{D-1,D-1} \end{pmatrix}. \quad (\text{D.10})$$

The ALI method that was described in Section 3.4 (p. 14), in its discrete form needs to be able to calculate the vector of intensities I_d and the vector (the diagonal of the matrix) of lambda matrix $\Lambda_{d,d}$ on the depth grid $d = 0, \dots, D - 1$. Obviously, they are connected with each other in a simple way: the $\Lambda_{d,d}$ is the term multiplied by S_d in the expression for I_d at each grid point $d = 0, \dots, D - 1$.

Later in this chapter we will see how the different methods reach this goal.

D.3 Integral methods

D.3.1 Method of long characteristics (MLC)

Using the definition of optical depth Eq. D.5, (p. 100) the formal solution of the radiative transfer equation Eq. D.4, (p. 99) ($\tau < \tau_0$) transforms to

$$I(\tau) = I(\tau_0)e^{-(\tau_0-\tau)} + \int_{\tau}^{\tau_0} S(t)e^{\tau-t} dt. \quad (\text{D.11})$$

Accounting for the intensities of an incoming radiation I^- and outgoing radiation I^+ , we get

$$\begin{aligned} I^+(\tau) &= I^+(D)e^{-(D-\tau)} + \int_{\tau}^D S(t)e^{\tau-t} dt, \\ I^-(\tau) &= I^-(0)e^{-\tau} + \int_0^{\tau} S(t)e^{\tau-t} dt. \end{aligned} \quad (\text{D.12})$$

Integrating $I^{\pm}(\tau)$ over the solid angle, and using the calculated value of $\bar{J}(\tau)$ one can easily implement the ‘‘lambda iteration’’ method (see Section 3.1 (p. 11)). The name MLC comes from the necessity to integrate over the whole line of sight.

D.3.2 Method of short characteristics (MSC)

Using the formal solution given by Eq. D.12, (p. 101) only for the slab between τ_d and τ_{d+1} (for the intensity of outgoing radiation $I^+(\tau)$) and between τ_d and τ_{d-1} (for the intensity of incoming radiation $I^-(\tau)$) (instead of $(0, \tau)$ and (τ, D) for MLC) we get

$$\begin{aligned} I^+(\tau_d) &= I^+(\tau_{d+1})e^{-\Delta\tau_d} + \int_{\tau_d}^{\tau_{d+1}} S(t)e^{\tau_d-t} dt = I^+(\tau_{d+1})e^{-\Delta\tau_d} + \Delta I_d^+, \\ I^-(\tau_d) &= I^-(\tau_{d-1})e^{-\Delta\tau_{d-1}} + \int_{\tau_{d-1}}^{\tau_d} S(t)e^{\tau_{d-1}-t} dt = I^-(\tau_{d-1})e^{-\Delta\tau_{d-1}} + \Delta I_d^-, \end{aligned} \quad (\text{D.13})$$

where

$$\Delta\tau_d = \tau_{d+1} - \tau_d, \quad d = 0, \dots, ND - 1.$$

If the source function $S(t)$ is the linear function of t inside the slabs (τ_{d-1}, τ_d)

$$S(t) = S(\tau_d) \frac{t - \tau_{d-1}}{\tau_d - \tau_{d-1}} + S(\tau_{d-1}) \frac{\tau_d - t}{\tau_d - \tau_{d-1}}, \quad (\text{D.14})$$

and (τ_d, τ_{d+1})

$$S(t) = S(\tau_{d+1}) \frac{t - \tau_d}{\tau_{d+1} - \tau_d} + S(\tau_d) \frac{\tau_{d+1} - t}{\tau_{d+1} - \tau_d}, \quad (\text{D.15})$$

then substituting these equations in Eq. D.13, (p. 101) and then integrating over t , we get

$$\begin{aligned} I^+(\tau_d) &= I^+(\tau_{d+1})e^{-\Delta\tau_d} + S(\tau_d) \left(1 - \frac{1-e^{-\Delta\tau_d}}{\Delta\tau_d}\right) + S(\tau_{d+1}) \left(\frac{1-e^{-\Delta\tau_d}}{\Delta\tau_d} - e^{-\Delta\tau_d}\right), \\ I^-(\tau_d) &= I^-(\tau_{d-1})e^{-\Delta\tau_{d-1}} + S(\tau_d) \left(1 - \frac{1-e^{-\Delta\tau_{d-1}}}{\Delta\tau_{d-1}}\right) + S(\tau_{d-1}) \left(\frac{1-e^{-\Delta\tau_{d-1}}}{\Delta\tau_{d-1}} - e^{-\Delta\tau_{d-1}}\right). \end{aligned} \quad (\text{D.16})$$

From Eq. D.16, (p. 101) we can easily write the expressions for the diagonal elements of the lambda matrix $\Lambda_{d,d}$ (see Appendix D.2 (p. 100) and Section 3.4 (p. 14)) for using them in the ALI algorithm:

$$\begin{aligned}\Lambda_{d,d} &= \frac{\lambda^+(\tau_d) + \lambda^-(\tau_d)}{2}, \quad \text{where} \\ \lambda^+(\tau_d) &= 1 - \frac{1 - e^{-\Delta\tau_d}}{\Delta\tau_d}, \\ \lambda^-(\tau_d) &= 1 - \frac{1 - e^{-\Delta\tau_{d-1}}}{\Delta\tau_{d-1}}.\end{aligned}\tag{D.17}$$

Olson and Kunasz (162) suggested using the parabolic interpolation in $S(t)$. In that case the ΔI_d^\pm in Eq. D.13, (p. 101) is given by

$$\Delta I_d^\pm = \alpha_d^\pm S(\tau_{d-1}) + \beta_d^\pm S(\tau_d) + \gamma_d^\pm S(\tau_{d+1}).\tag{D.18}$$

It can be shown that the factors α_d^\pm , β_d^\pm and γ_d^\pm are given by

$$\begin{aligned}\alpha_d^- &= e_{0d} + \frac{e_{2d} - (\Delta\tau_d + 2\Delta\tau_{d-1})e_{1d}}{\Delta\tau_{d-1}(\Delta\tau_d + \Delta\tau_{d-1})}, \\ \beta_d^- &= \frac{(\Delta\tau_d + \Delta\tau_{d-1})e_{1d} - e_{2d}}{\Delta\tau_{d-1}\Delta\tau_d}, \\ \gamma_d^- &= \frac{e_{2d} - \Delta\tau_d e_{1d}}{\Delta\tau_d(\Delta\tau_d + \Delta\tau_{d-1})}, \\ \alpha_d^+ &= \frac{e_{2d+1} - \Delta\tau_d e_{1d+1}}{\Delta\tau_{d-1}(\Delta\tau_d + \Delta\tau_{d-1})}, \\ \beta_d^+ &= \frac{(\Delta\tau_d + \Delta\tau_{d-1})e_{1d+1} - e_{2d+1}}{\Delta\tau_{d-1}\Delta\tau_d}, \\ \gamma_d^+ &= e_{0d+1} + \frac{e_{2d+1} - (\Delta\tau_{d-1} + 2\Delta\tau_d)e_{1d+1}}{\Delta\tau_d(\Delta\tau_d + \Delta\tau_{d-1})},\end{aligned}\tag{D.19}$$

where

$$\begin{aligned}e_{0d} &= 1 - \exp(-\Delta\tau_{d-1}) \\ e_{1d} &= \Delta\tau_{d-1} - e_{0d} \\ e_{2d} &= (\Delta\tau_{d-1})^2 - 2e_{1d}.\end{aligned}\tag{D.20}$$

The diagonal elements $\Lambda_{d,d}$ are calculated as the halfsums of β_d^- and β_d^+ .

D.4 Differential methods

D.4.1 Feautrier method

The symmetric average of the intensities of incoming and outgoing radiation $u_{\mu\nu}(z)$ was defined in Section 2.1 (p. 3) (see Eq. D.2, (p. 99)). One can also define the antisymmetric average $v_{\mu\nu}(z)$

$$v_{\mu\nu}(z) = \frac{I_{\mu\nu}^+(z) - I_{\mu\nu}^-(z)}{2}.\tag{D.21}$$

Using $u_{\mu\nu}(z)$ and $v_{\mu\nu}(z)$, and the independence of source function S_ν on angle μ , the pair of first order radiative transfer equations for I^+ and I^- can be replaced by one second order differential equation (see *Mihalas* (139))

$$\frac{d^2 u_{\mu\nu}}{d\tau_{\mu\nu}^2} = u_{\mu\nu}(z) - S_\nu,\tag{D.22}$$

with the boundary conditions

$$\left. \frac{du_{\mu\nu}}{d\tau_{\mu\nu}} \right|_{\tau=0} = u_{\mu\nu}(0) - I^-(0), \quad \left. \frac{du_{\mu\nu}}{d\tau_{\mu\nu}} \right|_{\tau=\tau_{D-1}} = I^+(z_{D-1}) - u_{\mu\nu}(z_{D-1}). \quad (\text{D.23})$$

After discretization on the optical depth grid, the Eq. D.22, (p. 102) is written as

$$-A_d u_{d-1} + B_d u_d - C_d u_{d+1} = S_d, \quad d = 1, \dots, D-2, \quad (\text{D.24})$$

where

$$\begin{aligned} A_d &= \frac{1}{\Delta\tau_{d-1}\Delta\tau_d}, \\ C_d &= \frac{1}{\Delta\tau_{d+1}\Delta\tau_d}, \\ B_d &= 1 + A_d + C_d. \end{aligned} \quad (\text{D.25})$$

The boundary conditions for it will be

$$\begin{aligned} B_0 &= 1 + \frac{2}{\Delta\tau_1} + \frac{2}{(\Delta\tau_1)^2} ; & B_{D-1} &= 1 + \frac{2}{\Delta\tau_{D-2}} + \frac{2}{(\Delta\tau_{D-2})^2} \\ C_0 &= \frac{2}{(\Delta\tau_1)^2} ; & A_{D-1} &= \frac{2}{(\Delta\tau_{D-2})^2}. \end{aligned} \quad (\text{D.26})$$

This tridiagonal set of equations is easily solved by the Gaussian elimination, consisting of a forward-backward recursive sweep. There are two variants of this procedure: original Feautrier elimination scheme, and improved Rybicki-Hummer elimination scheme (for both see *Rybicki and Hummer* (181; 182)).

As it will be shown below in Appendix D.6 (p. 105), the DFE method has the same accuracy as Feautrier method, while requiring less computing time. Another disadvantage of Feautrier method is that being applied to the laser lines, it produces erroneous results (negative monochromatic intensities) and has high sensitivity to singularities in the source function.

D.4.2 Discontinuous finite element (DFE) method

This method was first described by *Castor et al.* (26) in the astrophysical context and used by *Hu-bený and Lanz* (79) for stellar atmosphere modeling within their TLUSTY code.

One assumes in this method that both the source function $S(\tau)$ and intensity $I(\tau)$ are linear functions of τ in an interval (τ_d, τ_{d+1})

$$\begin{aligned} S(\tau) &= S(\tau_d) \frac{\tau - \tau_{d-1}}{\tau_d - \tau_{d-1}} + S(\tau_{d-1}) \frac{\tau_d - \tau}{\tau_d - \tau_{d-1}}, \\ I(\tau) &= I_d^p \frac{\tau_{d+1} - \tau}{\tau_{d+1} - \tau_d} + I_{d+1}^m \frac{\tau - \tau_d}{\tau_{d+1} - \tau_d}. \end{aligned} \quad (\text{D.27})$$

If $I_d^p = I_d^m$ then $I(\tau)$ is continuous function of τ . The DFE method allows that $I_d^p \neq I_d^m$, so the step discontinuities appear at boundaries τ_d . The derivative $\frac{dI}{d\tau}$ is thus given by an expression

$$\frac{dI}{d\tau} = \frac{I_{d+1}^m - I_d^p}{\tau_{d+1} - \tau_d} + (I_d^p - I_d^m) \delta(\tau - \tau_d) + (I_{d+1}^p - I_{d+1}^m) \delta(\tau - \tau_{d+1}). \quad (\text{D.28})$$

Substituting all these expressions in the RTE Eq. D.6, (p. 100), multiplying them first by $(\tau_{d+1} - \tau)/\Delta\tau_d$, then by $(\tau - \tau_d)/\Delta\tau_d$ and integrating over τ , we get the following equations

$$\begin{aligned} \frac{I_{d+1}^m + I_d^p - 2I_d^m}{\Delta\tau_d} &= \frac{2}{3}(S_d - I_d^p) + \frac{1}{3}(S_{d+1} - I_{d+1}^m), \\ \frac{I_{d+1}^m - I_d^p}{\Delta\tau_d} &= \frac{1}{3}(S_d - I_d^p) + \frac{2}{3}(S_{d+1} - I_{d+1}^m). \end{aligned} \quad (\text{D.29})$$

Castor et al.(26) have found that one can replace the Eq. D.29, (p. 103) by

$$\begin{aligned}\frac{I_{d+1}^m + I_d^p - 2I_d^m}{\Delta\tau_d} &= S_d - I_d^p, \\ \frac{I_{d+1}^m - I_d^p}{\Delta\tau_d} &= S_{d+1} - I_{d+1}^m.\end{aligned}\quad (\text{D.30})$$

The Eq. D.30, (p. 104) leads to the same final solution of non-LTE problem as Eq. D.29, (p. 103), but proved to have better numerical robustness (see *Castor et al.*(26) for details). Solving the system Eq. D.30, (p. 104) we get linear recurrence relations for I_d^p and I_d^m

$$\begin{aligned}I_{d+1}^m &= \frac{S_d + \Delta\tau_d(1 + \Delta\tau_d)S_{d+1}}{1 + (1 + \Delta\tau_d)^2}, \\ I_d^p &= (1 + \Delta\tau_d)I_{d+1}^m - \Delta\tau_d S_{d+1},\end{aligned}\quad (\text{D.31})$$

with the boundary conditions

$$I_0^m = 0, \quad I_{D-1}^m = I_{D-1}.\quad (\text{D.32})$$

The intensity at τ_d is then a linear combination of “discontinuous” intensities I_d^p and I_d^m

$$I_d = I_d^m \frac{\Delta\tau_d}{\Delta\tau_d + \Delta\tau_{d-1}} + I_d^p \frac{\Delta\tau_{d-1}}{\Delta\tau_d + \Delta\tau_{d-1}}.\quad (\text{D.33})$$

The “discontinuous” diagonal elements λ_d^p and λ_d^m are given by

$$\begin{aligned}\lambda_{d+1}^m &= \frac{1 + \Delta\tau_d}{1 + (1 + \Delta\tau_d)^2} \Delta\tau_d, \\ \lambda_d^p &= \frac{1 + \Delta\tau_d}{1 + (1 + \Delta\tau_d)^2} (\Delta\tau_d + 2\lambda_d^m),\end{aligned}\quad (\text{D.34})$$

with the boundary condition

$$\lambda_0^m = 0.\quad (\text{D.35})$$

Finally, the diagonal element λ_d is the linear combination of “discontinuous” diagonal elements λ_d^p and λ_d^m

$$\lambda_d = \lambda_d^m \frac{\Delta\tau_d}{\Delta\tau_d + \Delta\tau_{d-1}} + \lambda_d^p \frac{\Delta\tau_{d-1}}{\Delta\tau_d + \Delta\tau_{d-1}}.\quad (\text{D.36})$$

Applying the described method to both incoming intensity I_d^- and outgoing intensity I_d^+ , and finding the symmetric averages for I_d^+ and I_d^- , λ_d^+ and λ_d^- (given by Eq. D.34, (p. 104)) we get \bar{J}_d from Eq. D.2, (p. 99) and $\Lambda_{d,d}$

$$\Lambda_{d,d} = \frac{\lambda_d^+ + \lambda_d^-}{2}.\quad (\text{D.37})$$

D.5 Treating laser bands

If the gas is in LTE, then both the line source functions $S_{l\nu}(z)$ introduced in Section 2.1 (p. 3) (and equal to Planck function, see Eq. 2.16, (p. 5)) and line opacity coefficients $\chi_{l\nu}(\nu, z)$ are positive and the infrared laser condition can not happen. Under non-LTE, the stimulated emission term $n_l(z)B_{l\nu}$ can be equal or even higher than the absorption term $n_{l'}(z)B_{l\nu}$. That leads to $\chi_{l\nu}(\nu, z) < 0$ and singularity in $S_{l\nu}(z)$. So this is strictly a non-LTE effect, which can be caused by the absorption of the external (in our case, solar) radiation and/or chemical (or any other kind of external) pumping of upper states, which causes their overpopulation relative to the levels with lower

energy. If the radiative transitions exist, the reemission of this absorbed radiation in a very narrow frequency range happens with (possibly) huge amplification. For the CO₂ “laser bands” (for definition, see Appendix B.2 (p. 72)) in the Martian atmosphere this effect was observed and described by *Mumma et al.*(152). The modeling of this effect was done by *Deming and Mumma* (35) and others. Unfortunately, the authors did not account for the radiative transfer in the laser bands themselves. This is not surprising, because the traditional methods, using “source function” and “optical depth” do not work in such situation. The scientists facing this problem (see *Mlynczak et al.*(148)) simply suggest to ignore this effect.

The suggested modification of the DFE method described in Appendix D.4.2 (p. 103) and working only in terms of emissivity and opacity, produces a stable working method for the negative optical depth increments $\Delta\tau_d > -1$.

Replacing $\Delta\tau_d$ and S_d in Eq. D.30, (p. 104) by $\chi_d\Delta h_d$ and η_d/χ_d respectively, where Δh_d is the path length increment, we rewrite it in the following form

$$\begin{aligned} I_{d+1}^m + I_d^p - 2I_d^m &= \eta_d\Delta h_d - I_d^p\Delta\tau_d, \\ I_{d+1}^m - I_d^p &= \eta_{d+1}\Delta h_d - I_{d+1}^m\Delta\tau_d, \end{aligned} \quad (\text{D.38})$$

which has no singularity when $\chi(z) = 0$ (see Fig. D.1 (p. 106)) and transforms to the following recurrence relations

$$\begin{aligned} I_{d+1}^m &= \frac{1}{1 + (1 + \Delta\tau_d)^2} \left(\Delta h_d\eta_d + \Delta h_d(1 + \Delta\tau_d)\eta_{d+1} \right), \\ I_d^p &= \frac{1}{1 + (1 + \Delta\tau_d)^2} \left(2(1 + \Delta\tau_d)I_d^m + \Delta h_d(1 + \Delta\tau_d)\eta_d - \Delta h_d\eta_{d+1} \right). \end{aligned} \quad (\text{D.39})$$

The intensity at z_d will be a linear combination of “discontinuous” intensities I_d^p and I_d^m

$$I_d = I_d^m \frac{\Delta h_d}{\Delta h_d + \Delta h_{d-1}} + I_d^p \frac{\Delta h_{d-1}}{\Delta h_d + \Delta h_{d-1}}. \quad (\text{D.40})$$

These equations do not use the source function, which is singular at the altitudes where the line opacity is equal to zero (see Fig. D.1 (p. 106)), and causes numerical instability in “traditional” methods. Instead, they include the emissivity coefficient $\eta(z)$, which is positive both for laser and non-laser lines.

The same approach can be applied to the non-laser lines too, but is not practical because of additional memory overhead in comparison with the original DFE method.

D.6 Comparison of the methods

To decide which of the three presented methods (short characteristics, DFE and Feautrier) is the best, the test run was made using each of them to calculate the integrated intensity $\bar{J}_{ll'}$ for one line. The number of depth points was fixed at $ND = 61$, the number of angle integration points $NA = 4$ (Gauss quadrature), the frequency integration was made with $NF = 32$ using the method described in Appendix A.1.1 (p. 65). The functions were implemented in C programming language, making them portable, also there was no attempt to hand-optimize the assembler output of the compiler. One should also keep in mind the following facts:

- The DFE method and the Feautrier method are second order accurate on the boundaries, the short characteristics method is not.
- Because of the small values of ND, NA and NF the memory bandwidth and amount does not play any significant role: the code and data reside in I- and D-cache on RISC processors and in first level cache on Intel processors respectively.

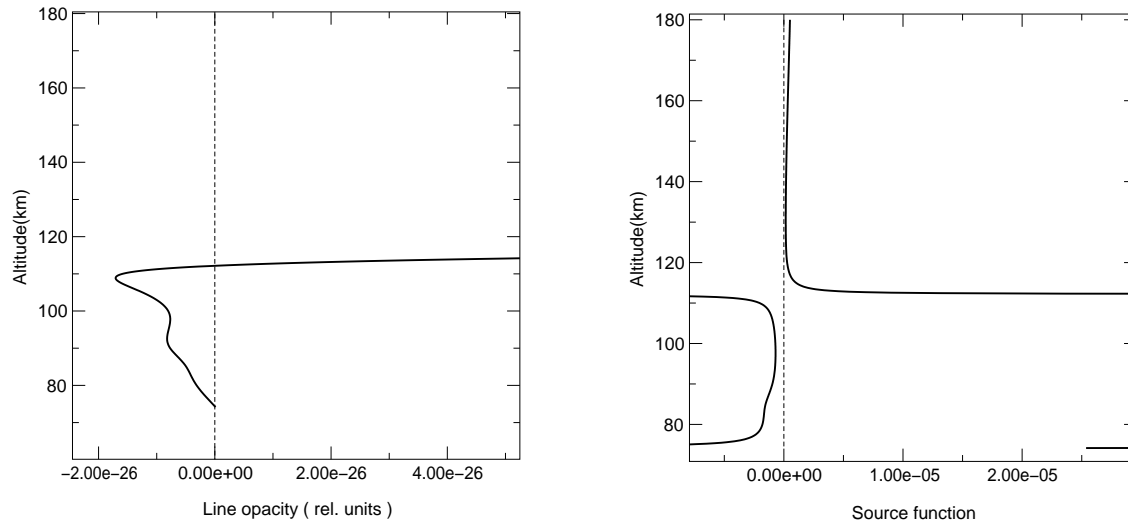


Fig. D.1 Line opacity and source function for laser line from CO₂ (626) 00011 → 10002 10.4 μm band

- The DFE method and Feautrier method use only arithmetic operations, while short characteristics method uses exponent function, which is calculated with hardware support on one processors and without it on the others.

The run timings on Intel PII-400 processor are given in Tab. D.1 (p. 106)

DFE method	Feautrier method	Method of short characteristics
7.87	11.88	10.92

Tab. D.1 Time (in ms) required to find the integrated line intensity \bar{J}_{ll} .

The results can be summarized as follows:

1. It should be noted, that although the “short characteristics” method runs faster than the Feautrie method in this test, it is very unstable, when applied to very optically thick lines (for example, for CO₂ (626) 00011 → 00001 4.3 μm fundamental band), so actually requires much finer optical depth grid to get correct result and is therefore slower.
2. The DFE method and the Feautrier method are quite comparable with each other, but DFE requires 20% less raw processor time and less memory for local data.
3. There is no alternative to modified DFE method for calculating radiative transfer in the lines with negative opacity (laser lines, see Appendix D.5 (p. 104)).

So, among these three described methods, the Discontinuous Finite Element (DFE) method is the clear winner. All the results presented in this dissertation were obtained using it.

E. Numerical acceleration techniques

The convergence of the iterative refinement schemes is often slow, so usually some form of acceleration is used to enhance it. *Rybicki and Hummer* (182) described their variant of a powerful acceleration procedure proposed by *Ng* (154). This is a purely numerical procedure and is not to be confused with the much improved convergence due to the ALI technique, which it supplements. The Ng algorithm predicts the solution using results obtained at previous iterations but differs from acceleration methods which extrapolate in iteration number.

The Ng technique and similar Orthomin technique used by *Klein et al.*(91) are described below. It is assumed that after the $m - 1$ th iterations we decide to take the sets of populations for previous K steps and build from them the “accelerated” set of the populations according to some minimization criteria.

E.1 Ng acceleration

The method was first introduced by *Ng* (154). In this method it is supposed that the vector of populations at m th iteration p_m is a result of the linear transformation of the vector at $m - 1$ th iteration p_{m-1} with an operator F

$$p_m = F(p_{m-1}). \quad (\text{E.1})$$

We are looking for such linear combination z_{m-1} of populations p_{m-i} with normalized weights x_i

$$\begin{aligned} z_{m-1} &= \sum_{i=1}^K x_i p_{m-i}, \\ \sum_{i=1}^K x_i &= 1, \end{aligned} \quad (\text{E.2})$$

that minimizes $\|F(z_{m-1}) - z_{m-1}\|$. Of course, vector x depends on the chosen norm. Substituting Eq. E.2, (p. 107) in Eq. E.1, (p. 107) and using the linearity of F we get

$$\begin{aligned} &\|F(z_{m-1}) - z_{m-1}\| = \\ &= \|F(x_1 p_{m-1}) + F(x_2 p_{m-2}) + \dots + F(x_K p_{m-K}) - (x_1 p_{m-1} + x_2 p_{m-2} + \dots + x_K p_{m-K})\| = \\ &= \|x_1 (p_m - p_{m-1}) + x_2 (p_{m-1} - p_{m-2}) + \dots + x_K (p_{m-K+1} - p_{m-K})\| \rightarrow \min \end{aligned} \quad (\text{E.3})$$

If one defines the vectors $d_i = p_i - p_{i-1}$, $i = m, m - 1, \dots, m - K + 1$, the problem can be reformulated in the following way

$$\begin{aligned} &\|x_1 d_1 + x_2 d_2 + \dots + x_K d_K\| \rightarrow \min \\ &\sum_{i=1}^K x_i = 1. \end{aligned} \quad (\text{E.4})$$

Defining the Lagrange function

$$\mathbb{L} = (x_1 d_1 + x_2 d_2 + \dots + x_K d_K)^2 + 2\lambda(x_1 + x_2 + \dots + x_K - 1), \quad (\text{E.5})$$

and equating its partial derivatives $\frac{\partial \mathbb{L}}{\partial x}$ and $\frac{\partial \mathbb{L}}{\partial \lambda}$ to zero, we get the following linear system $((d_i, d_j))$

is the scalar product of d_i and d_j)

$$\begin{pmatrix} (d_1, d_1) & (d_1, d_2) & \dots & (d_1, d_{K-1}) & 1 \\ (d_2, d_1) & (d_2, d_2) & \dots & (d_2, d_{K-1}) & 1 \\ \dots & \dots & \dots & \dots & \dots \\ (d_{K-1}, d_1) & (d_{K-1}, d_2) & \dots & (d_{K-1}, d_{K-1}) & 1 \\ 1 & 1 & \dots & 1 & 0 \end{pmatrix} \times \begin{pmatrix} x_1 \\ x_2 \\ \vdots \\ x_{K-1} \\ \lambda \end{pmatrix} = \begin{pmatrix} 0 \\ 0 \\ \vdots \\ 0 \\ 1 \end{pmatrix}. \quad (\text{E.6})$$

The vector z_{m-1} of the normalized populations for each molecule M^α will be taken as the set of “accelerated” populations for this molecule. Note, that the fact of the normalization of x_i makes possible to satisfy the particle conservation law.

Several L^2 -type scalar products were tested by *Olson et al.*(161) and *Klein et al.*(91) as the vector norm to be minimized. It was suggested that the weighted L^2 scalar product

$$(p_i, p_j) = \sum_{k=0}^{NF-1} \sum_{d=0}^{ND-1} \frac{1}{\omega_{dk}^2} p_{ik} p_{jk} \quad (\text{E.7})$$

with carefully selected weights delivers the most robust solution of this problem.

E.2 Orthomin acceleration

This method was first introduced by *Vinsome* (209). The idea is very close to the Ng method described above: namely, after m th iteration we are searching for such vector of weights x_i that minimizes the difference between the p_m and the linear combination of $p_{m-1}, p_{m-2}, \dots, p_{m-K}$. The vector z_m composed with these weights for each molecule M^α will be taken as the set of the “accelerated” populations for this molecule. So, if the Ng method is trying to optimize the norm of *first difference of populations* between the iterative steps, the Orthomin method optimizes, operating on the populations itself. Again, the individual weighting factors x_i are normalized too, to satisfy the particle conservation law:

$$\begin{aligned} & \|x_1 p_{m-1} + x_2 p_{m-2} + \dots + x_K p_{m-K} - p_m\| \rightarrow \min, \\ & \sum_{i=1}^K x_i = 1. \end{aligned} \quad (\text{E.8})$$

The name of this method comes from the well known fact, that the linear combination of p_{m-1}, \dots, p_{m-K} , which provides this minimum, must be orthogonal to p_m .

Defining the Lagrange function

$$\mathbb{L} = (x_1 p_{m-1} + x_2 p_{m-2} + \dots + x_K p_{m-K} - p_m)^2 + 2\lambda(x_1 + x_2 + \dots + x_K - 1), \quad (\text{E.9})$$

and equating its partial derivatives $\frac{\partial \mathbb{L}}{\partial x}$ and $\frac{\partial \mathbb{L}}{\partial \lambda}$ to zero, we get the following linear system ((p_i, p_j) is the scalar product of p_i and p_j)

$$\begin{pmatrix} (p_{m-1}, p_{m-1}) & (p_{m-1}, p_{m-2}) & \dots & (p_{m-1}, p_{m-K}) & 1 \\ (p_{m-2}, p_{m-1}) & (p_{m-2}, p_{m-2}) & \dots & (p_{m-2}, p_{m-K}) & 1 \\ \dots & \dots & \dots & \dots & \dots \\ (p_{m-K}, p_{m-1}) & (p_{m-K}, p_{m-2}) & \dots & (p_{m-K}, p_{m-K}) & 1 \\ 1 & 1 & \dots & 1 & 0 \end{pmatrix} \times \begin{pmatrix} x_1 \\ x_2 \\ \vdots \\ x_K \\ \lambda \end{pmatrix} = \begin{pmatrix} (p_{m-1}, p_m) \\ (p_{m-2}, p_m) \\ \vdots \\ (p_{m-K}, p_m) \\ 1 \end{pmatrix}. \quad (\text{E.10})$$

The solution of this linear system delivers us the set of x_i , which allows to compute the “accelerated” z_m .

F. Atmospheric models used in this study

F.1 Earth atmosphere

Two Earth's atmospheric models were used for the modeling, namely the MSISE-90 and the GRAM-99.

The MSISE-90 model (see *Hedin et al.*(76)) describes the temperature and number densities of He, $O(^3P_1)$, N_2 , O_2 , Ar, H and N in Earth's atmosphere from the ground to the thermospheric heights. Below 72.5 km the model is primarily based on the Middle Atmosphere Program (MAP) Handbook (see *Labitzke et al.*(103)) tabulation of the zonal average temperature and pressure by *Barnett and Corney*, which was also used for the CIRA-86. Below 20 km these data were supplemented with the information from the US National Meteorological Center (NMC). In addition, pitot tube, falling sphere, and grenade sounder rocket measurements from 1947 to 1972 were taken into consideration. Above 72.5 km MSISE-90 is essentially a revised MSIS-86 model taking into account data derived from space shuttle flights and newer incoherent scattering results.

GRAM-99 (see *Justus and Johnson* (86)) provides complete geographical and altitude coverage for each month of the year. GRAM-99 uses a specially-developed data set, also based on MAP data for 20-120 km altitudes, and NASA's 1999 version Marshall Engineering Thermosphere (MET-99) model for heights above 90 km. Fairing techniques assure smooth transition in overlap height ranges (20-27 km and 90-120 km). GRAM-99 includes 12 atmospheric constituents (H_2O , CO_2 , O_3 , N_2O , CO, CH_4 , N_2 , O_2 , O, Ar, He and H).

F.1.1 Pressure and temperature

The model calculations were made using the pressure and temperature profiles produced by MSISE-90 model (see *Hedin et al.*(76)) for selected near-equatorial profile from CRISTA-1 mission (latitude -8° , longitude -102° , solar zenith angle 42°) and is presented in Fig. F.1 (p. 109). This particular choice of the equatorial region was determined by specifics of CRISTA-1 flight trajectory, that results in the lowest SZA values and highest signal to noise ratio (S/N) in the middle and upper atmosphere. These profiles were considered equal for daytime and nighttime for the purposes of this chapter.

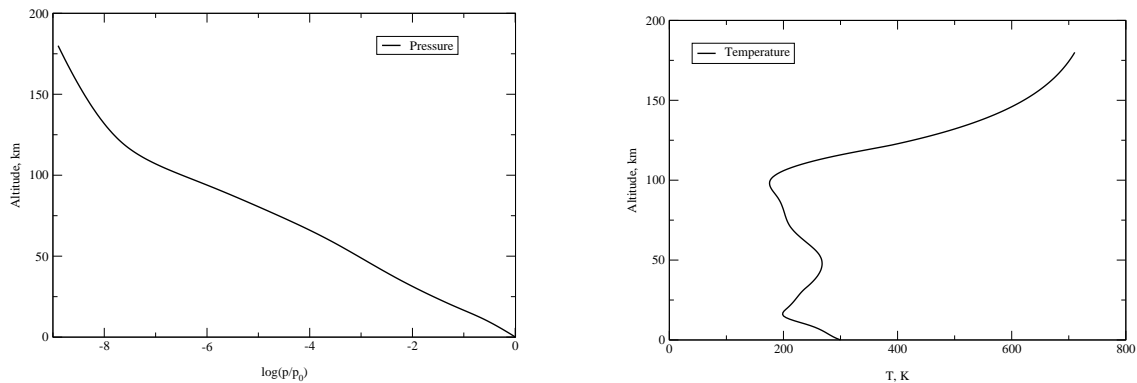


Fig. F.1 Altitude profiles of pressure and temperature, used for the Earth atmosphere modeling.

F.1.2 Volume mixing ratios

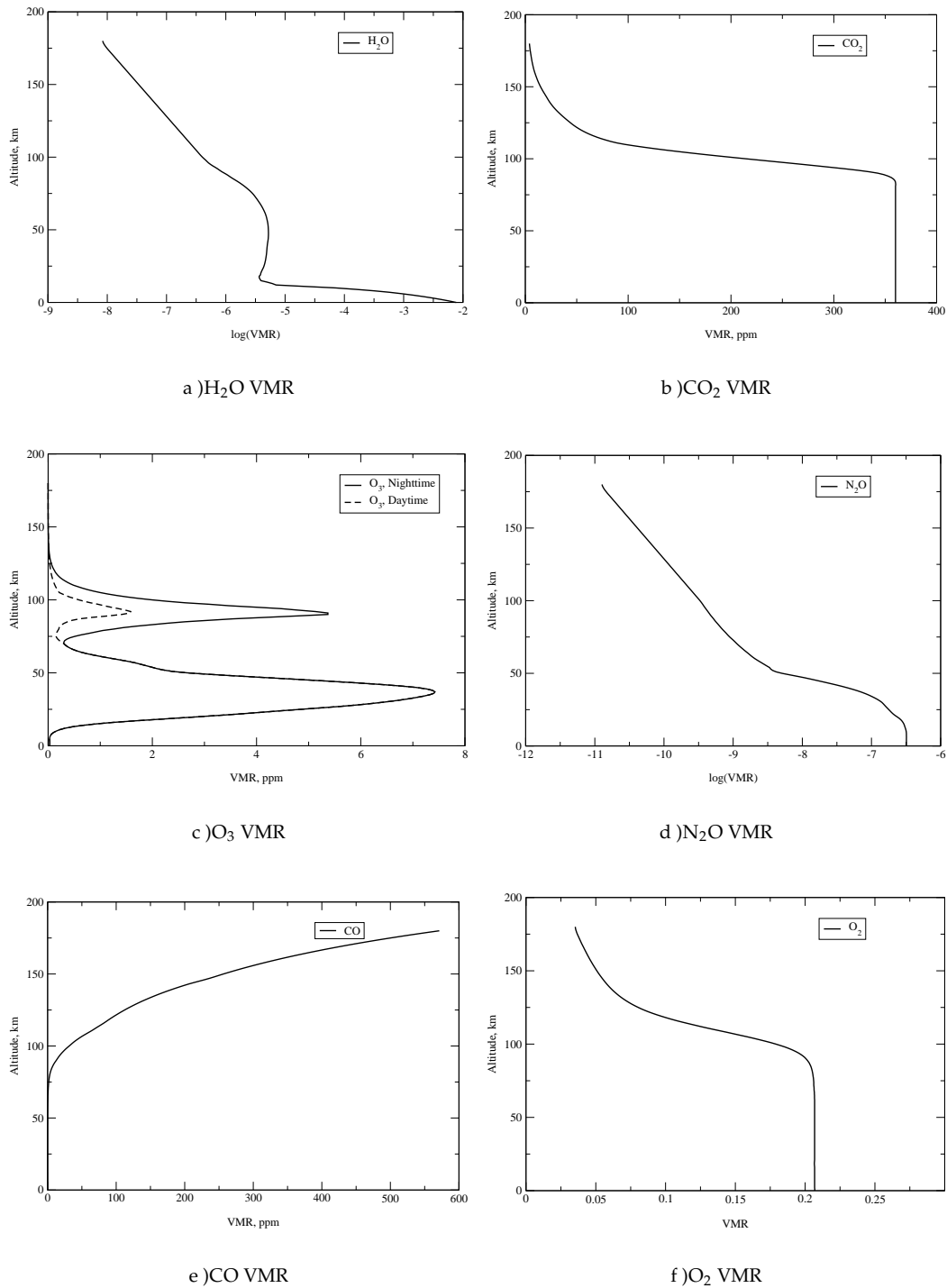


Fig. F.2 Altitude profiles of molecular VMRs used for the Earth atmosphere modeling.

Fig. F.2 (p. 110) and Fig. F.3 (p. 111) give the used volume mixing ratio data for different molecular species combined with the data from other sources: H_2O and N_2O from the U.S. Standard At-

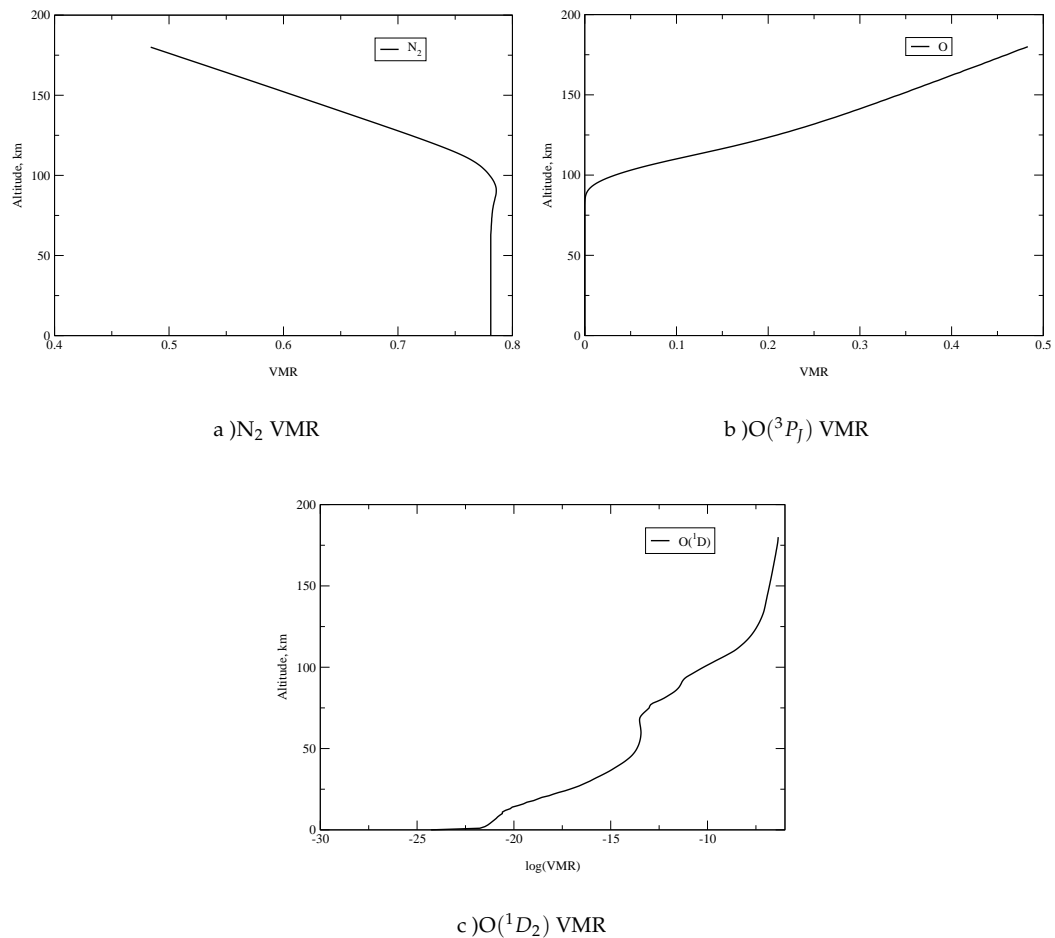


Fig. F.3 Altitude profiles of molecular VMRs used for the Earth atmosphere modeling (cont.)

mosphere (USSA) as compiled by *Anderson et al.*(6), CO_2 and $O(^1D_2)$ were taken from *Shved et al.*(188), CO was taken from *Kutepov et al.*(99).

F.2 Mars atmosphere

The Mars Global Reference Atmospheric Model (Mars-GRAM) was developed as an engineering-oriented, empirical model of the Mars atmosphere. Mars-GRAM is based on surface and atmospheric temperature data observed during the Mariner (orbiter) and Viking (orbiter and lander) missions and on surface pressure data observed by the Viking landers. At the higher altitudes (above about 120 km), Mars-GRAM was based on the model of *Stewart* (200) for the global-mean thermosphere.

Mars-GRAM provides both mean atmospheric pressure and temperature for any location (height, latitude and longitude) and time (seasonal and diurnal).

The model calculations were made using the pressure and temperature profiles delivered by Mars-GRAM model which is presented in Fig. F.4 (p. 112) and is very close to the model used by *López-Valverde et al.*(207; 208). The profiles were considered equal for daytime and nighttime.

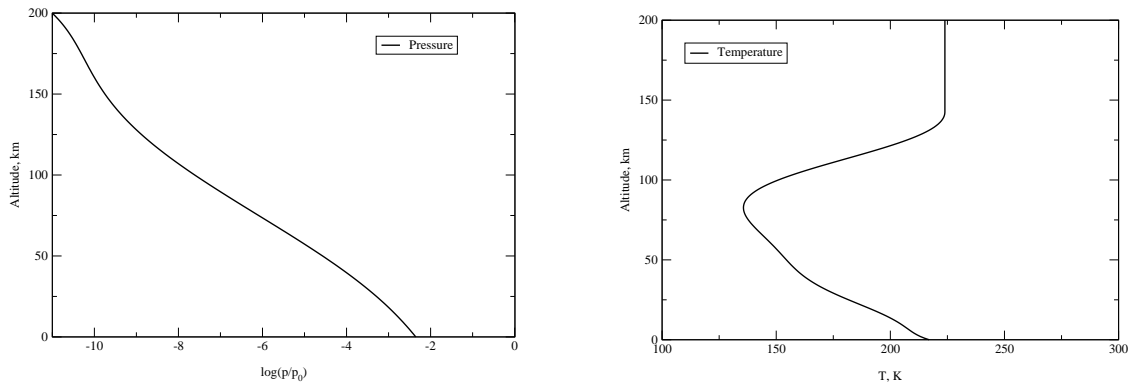


Fig. F.4 Altitude profiles of pressure and temperature, used for the modeling of Mars atmosphere.

The main component of the Martian atmosphere is carbon dioxide, while the molecular nitrogen is becoming important in the thermosphere. The VMRs of trace gases CO and $O(^3P_f)$ are given in Fig. F.7 (p. 112) and Fig. F.8 (p. 112).

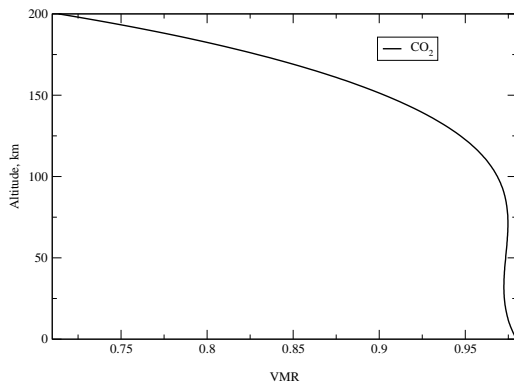


Fig. F.5 Volume mixing ratio of CO_2 in Mars atmosphere

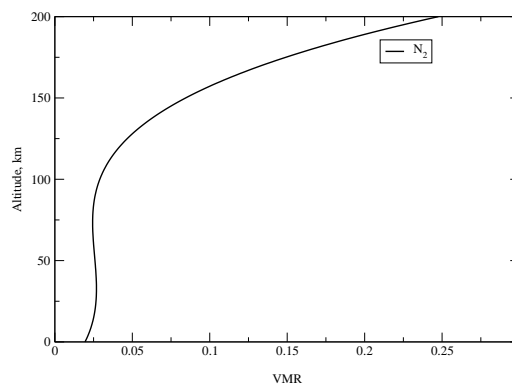


Fig. F.6 Volume mixing ratio of N_2 in Mars atmosphere.

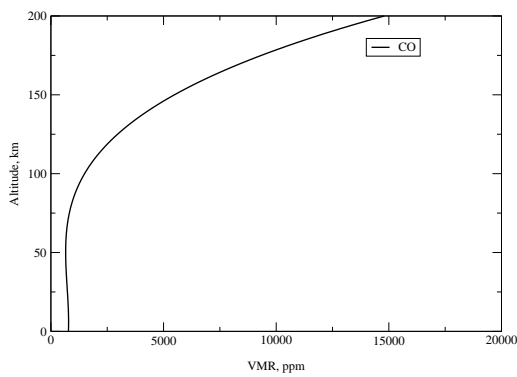


Fig. F.7 Volume mixing ratio of CO in Mars atmosphere

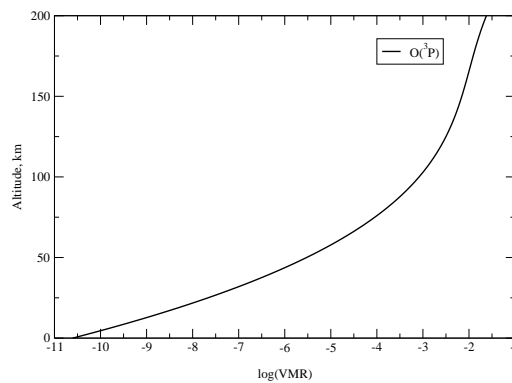


Fig. F.8 Volume mixing ratio of $O(^3P_f)$ in Mars atmosphere.

F.2.1 Mars and Earth atmospheres: the comparison

From Fig. F.5 (p. 112)-Fig. F.8 (p. 112) and Fig. F.2a (p. 110)-Fig. F.3c (p. 111) one can see that in the Earth's atmosphere the main components are N_2 , O_2 and $O(^3P_f)$, while the Mars atmosphere consists of CO_2 and N_2 . All other gases have only minor concentrations and therefore are called trace gases.

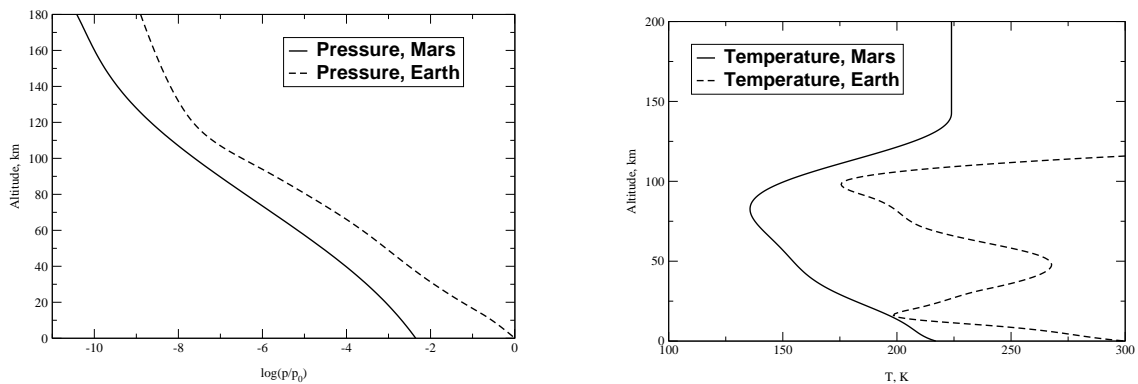


Fig. F.9 Altitude profiles of pressure and temperature, used for the Earth and Mars atmospheres

Fig. F.9 (p. 113) shows that the Martian pressure is lower than the Earth's (surface values are ≈ 6 vs. 1013 mbar) and that the typical temperature is comparable or lower. The second distinct feature of the Martian atmosphere is the absence of the warm stratopause, which is a result of missing oxygen and ozone, that warm this part of the atmosphere.

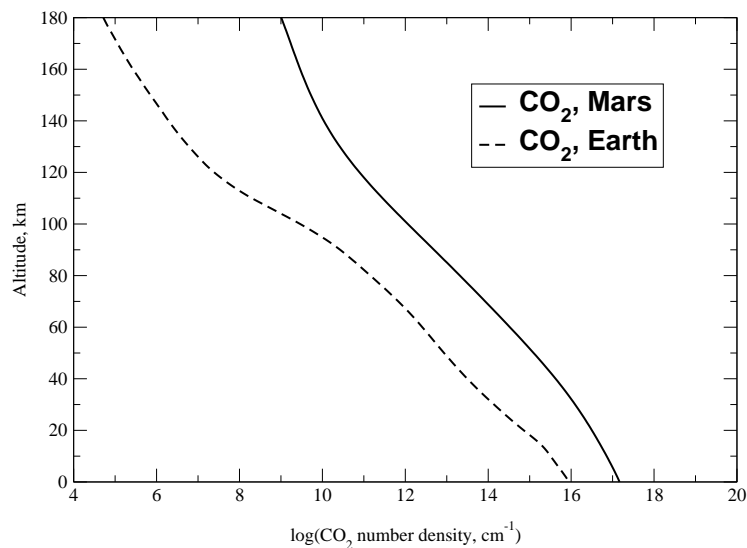


Fig. F.10 Altitude profiles of CO_2 number density in the Earth and Mars atmospheres

The differences in pressure, temperature and volume mixing ratio result in the overall higher CO_2 number density (see Fig. F.10 (p. 113)). On one hand that fact means higher optical thickness of the atmosphere, but on the other hand it increases the efficiency of collisional processes. Therefore, the detailed modeling of CO_2 non-LTE behaviour in the respective atmospheres shows substantially different results (see Appendix H.1 (p. 119) for details).

G. Current status of the code package ALI-ARMS (technical details)

Several groups solved limited number of selected and separate problems. However, the self-consistent modeling of sophisticated experiments and the reevaluation of the energy budget of the mesosphere-lower thermosphere (MLT) region required development of a new code free of limitations of other codes and easy extendable for the combined treatment of non-LTE processes and dynamics.

The ALI code developed in the Institute for Astronomy and Astrophysics of Munich University, that has included all the features described in Section 2.1 (p. 3) is called ALI-ARMS. Within its flexible framework it allowed not only the unified and consistent treatment of the non-LTE problem, but it also includes the opportunity to simulate and compare the results of the models used by other groups.

G.1 General features of the code

The ALI-ARMS is written in C programming language and can be easily run under any sane (i.e. POSIX) operating system. It has the following distinct features:

- arbitrary number of arbitrary molecules in arbitrary planetary atmospheres: the following molecules are included in ALI-ARMS code package at the time of this writing: H_2O , CO_2 , O_3 , N_2O , CO , O_2 , NO , N_2 , OH , O (CH_4 , NO_2 and HO_2 need some work),
- vibrational and rovibrational non-LTE,
- various $R - T$, $V - T$, $V - V$ and $C - V$ collisional transitions,
- various external sources of excitation,
- overlapping with passive continua (aerosol).

The specifics of the problem is determined only by the given input, which includes:

1. molecules, for which one wants to calculate the populations and the limb spectra (`molecules.data`),
2. vibrational levels which are included for each molecule (`v1.data`). It is also indicated if their sublevels are in rotational LTE or not.
3. rotational sublevels of vibrational levels (`r1.data`),
4. rovibrational lines: full radiative transfer (`vrt.data`), absorption of the solar radiation (`vrt.sun.data`) and calculation of the limb radiance (`vrt.limb.data`),
5. list of “thin” bands, where the radiative transfer equation is solved approximately (`avt.data`),
6. list of $V - T$ processes (`cvt.data`),
7. list of $V - V$ processes (`cvv.data`),
8. list of $C - V$ processes (`chv.data`),
9. list of photodissociation processes (`pho.data`),
10. atmospheric model: pressure, temperature, VMRs for gases composing the atmosphere on the altitude grid (`atmospheric.data`),

11. list of spectral channels with pointers to their parameters (`channels.data`).

For the description of the inputs see:

- spectroscopy - Appendix A (p. 61)
- molecules, vibrational and rovibrational levels - Appendix B (p. 71)
- collisional rates ($R - T$, $V - T$, $V - V$ and $C - V$): the databases of collisional reactions rates are given in Appendix C (p. 83)
- solar spectra.

The outputs include, but are not limited to:

1. the populations of energy levels (rovibrational or vibrational),
2. vibrational temperatures,
3. cooling/heating rates, (radiative, photochemical, collisional, chemical) for each transition and each molecule separately,
4. line-by-line limb radiances for prescribed spectral intervals,
5. convolved line spectra with the given instrument function,
6. finally, one can perform the pressure/temperature and/or number density retrieval, if the experimental spectra for the spectral channels is provided.

G.2 Possible future extensions

ALI-ARMS solved and gave an opportunity to solve many problems, but there is also space for improvements: 2-D and 3-D geometry, accounting for multiple scattering, opacity distribution function/correlated k -distribution (ODF/CKD) approach, etc. This is ongoing work resulting in the better and faster code.

G.3 Implemented models

The following models were compiled for the purposes of this dissertation and were used for the comparisons with the results published by other authors:

1. LP95: includes H₂O (161), O₂ (66), N₂ (44), and O(³P₁) (H₂O in the Earth atmosphere, see *López-Puertas et al.*(117), *Mlynczak et al.*(150), *Zhou et al.*(224))
2. MA97: includes H₂O (161), O₂ (66), N₂ (44), and O(³P₁) (H₂O in the Earth atmosphere, see *Manuilova* (130))
3. LP98: includes CO₂ (626), CO₂ (636), CO₂ (628), CO₂ (638), CO₂ (627), O₂ (66), N₂ (44), O, OH (CO₂ in the Earth atmosphere, see *López-Puertas et al.*(120))
4. LV98: includes CO₂ (626), CO₂ (636), CO₂ (628), CO (26) (CO₂ and CO in the Mars atmosphere, see *López-Valverde et al.*(207; 208))
5. SH97: includes N₂O (446), O₂ (66), N₂ (44) (N₂O in the Earth atmosphere, see *Shved and Gusev* (187))
6. SH98: includes CO₂ (626), CO₂ (636), CO₂ (628), CO₂ (638), CO₂ (627), O₂ (66), N₂ (44), O, OH (CO₂ in the Earth atmosphere, see *Shved et al.*(188))

7. OG98: includes CO₂ (626), CO₂ (636), CO₂ (628), CO₂ (638), CO₂ (627), O₂ (66), N₂ (44), O, OH (CO₂ in the Earth atmosphere, see *Ogibalov et al.*(160))
8. MA98_1/2/3: includes O₃ (666), O₂ (66), N₂ (66), O(³P_J) (3 models of Manuilova for O₃ in the Earth atmosphere, see *Manuilova et al.*(132))
9. KO98_1/2/3: includes O₃ (666), O₂ (66), N₂ (66), O(³P_J) (O₃ in the Earth atmosphere, see *Koutoulaki* (92))
10. ML90_1: includes O₃ (666), O₂ (66), N₂ (66), O(³P_J) (O₃ SSM model, see *Mlynczak and Drayson* (143; 144), *Vollmann* (210)) and *Zhou et al.*(223))
11. ML90_2: includes O₃ (666), O₂ (66), N₂ (66), O(³P_J) (O₃ EG model, see *Mlynczak and Drayson* (143; 144) and *Mlynczak et al.*(149))
12. KU97: includes CO (26), O₂ (66), N₂ (66), O(³P_J) (CO in the Earth atmosphere, see *Kutepov et al.*(99))
13. FU97: includes NO (46), O₂ (66), N₂ (66), O(³P_J) (NO in the Earth atmosphere, see *Funke and López-Puertas et al.*(57))
14. GU99: includes H₂O (161), CO₂ (626), CO₂ (636), CO₂ (628), CO₂ (638), CO₂ (627), CO₂ (828), CO₂ (728), O₃ (666), N₂O (446), CO (26), O₂ (66), N₂ (44), O, OH (unified non-LTE model combined from all the previous models, i.e. composed of all gases).

H. The non-LTE problems for various molecules in the Earth atmosphere solved by ALI-ARMS

In the middle and upper planetary atmospheres the excited vibration-rotational energy levels of molecules of main constituents and trace gases build the non-LTE system of levels coupled by a variety of collisional and radiative energy exchange processes. The radiative transitions between these levels lead to many infrared bands in wavelength region between 1 and 50 μm , (such as 15 μm , 10 μm and 4.3 μm bands of CO_2 , 9.6 μm bands of O_3 , 6.3 μm bands of H_2O , 4.7 μm band of CO and others) used in remote sounding and also important for the energy balance of these atmospheric layers.

The computer code ALI-ARMS was applied to the calculations of the vibrational level populations, infrared cooling rates and limb spectral radiances of the following molecules in the Earth's atmosphere: H_2O , CO_2 , O_3 , N_2O , CO , O_2 , N_2 . The calculations with ALI-ARMS yield improved values of the molecular level populations, which allow high accuracy calculations of the spectral distribution of the emitted infrared radiation for different atmospheric models. The results and the comparisons with the similar modeling performed by other research groups are presented below.

H.1 Vibrational non-LTE in CO_2

The carbon dioxide molecule is one of the most frequently and thoroughly studied molecules. In the last ten years, the observations of CO_2 emissions in several infrared bands by rocket and satellite-based instruments have inspired the development of the extensive models for CO_2 vibrational populations and limb spectra, namely *López-Puertas and Taylor* (111), *Wintersteiner et al.* (219), *Nebel et al.* (153), *López-Puertas et al.* (120) and *Shved et al.* (188).

For the nighttime conditions the 15 μm vibrational levels of all CO_2 isotopes do not deviate significantly from the LTE through the stratosphere and lower mesosphere, where the collisional $V - T$ and $V - V$ processes dominate over radiative processes, and the absorption of the solar radiation can be also neglected. In the upper mesosphere and lower thermosphere the relative value of the upwelling radiative flux absorption to the thermal collision rate becomes much more important. The collisional processes in the mesospheric region try to thermalize the level populations at the local temperatures. The radiation coming from the stratosphere affects the level populations in the mesosphere through the absorption of the upwelling radiation flux. The vibrational levels

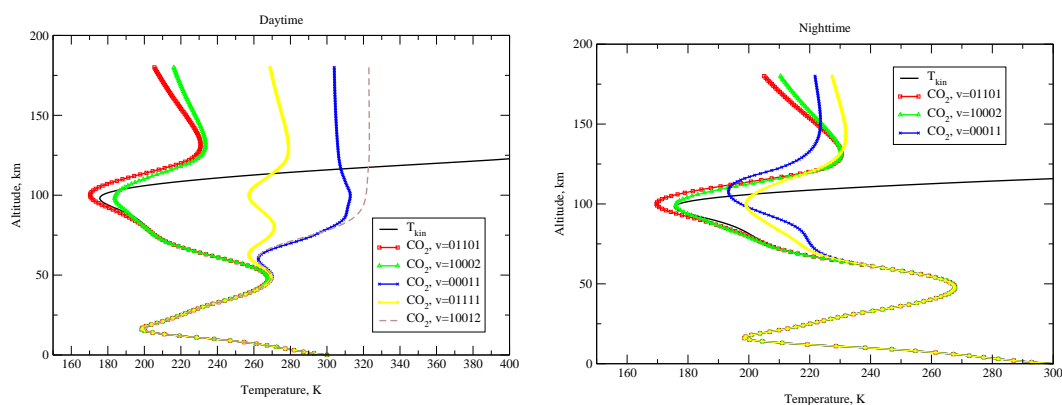


Fig. H.1 The vibrational temperatures for CO_2 (626) levels (daytime). **Fig. H.2** The vibrational temperatures for CO_2 (626) levels (nighttime).

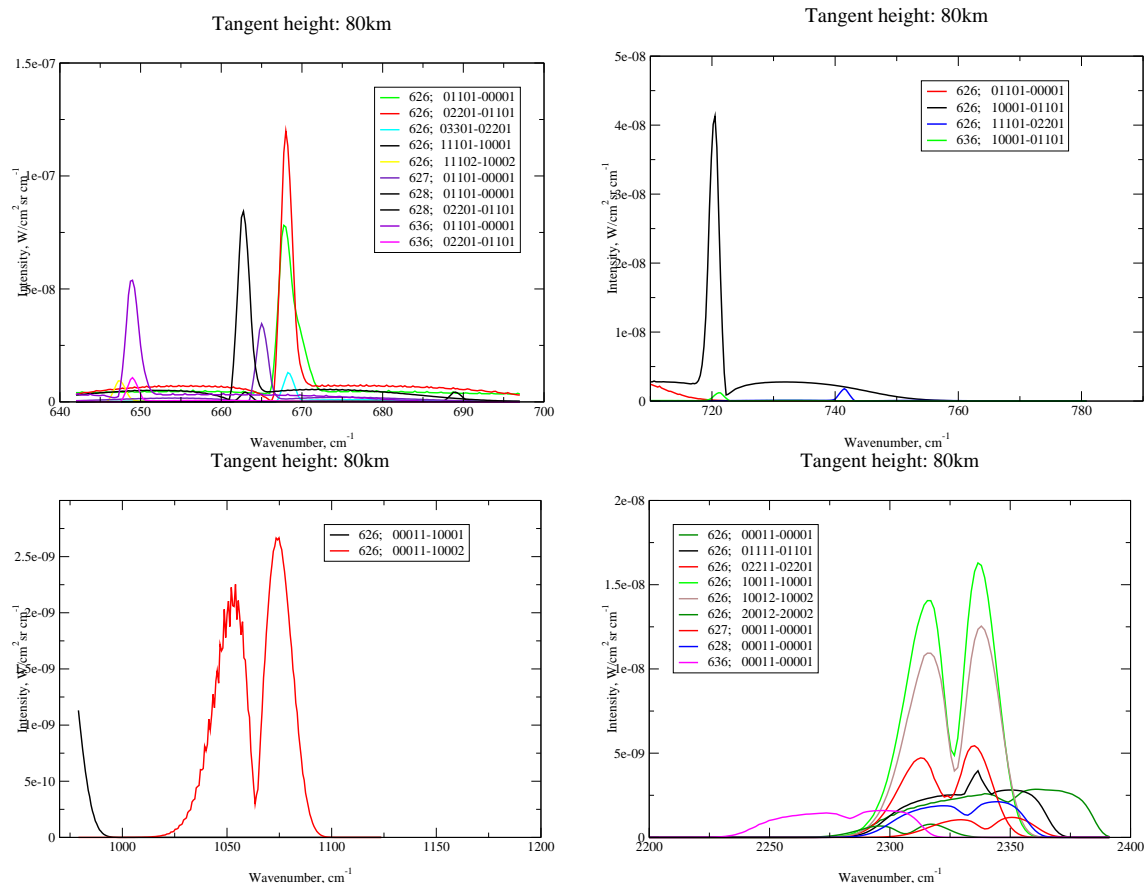


Fig. H.3 The convolved limb radiances of CO₂ 15, 12.6, 9.4, 4.3 μm bands (only daytime profiles are shown)

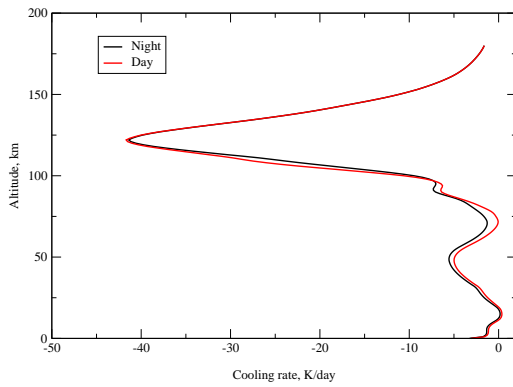
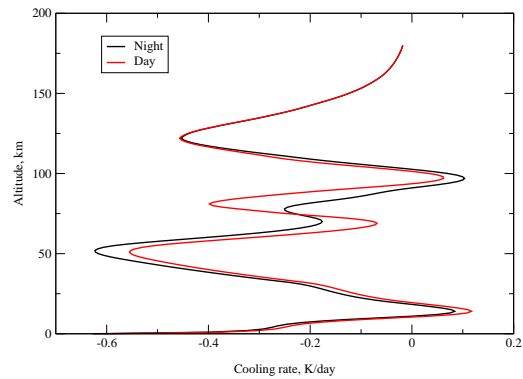
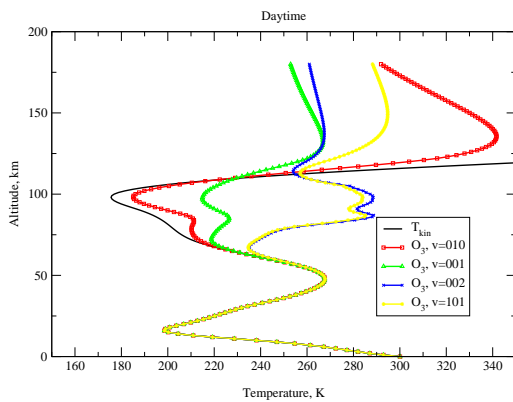
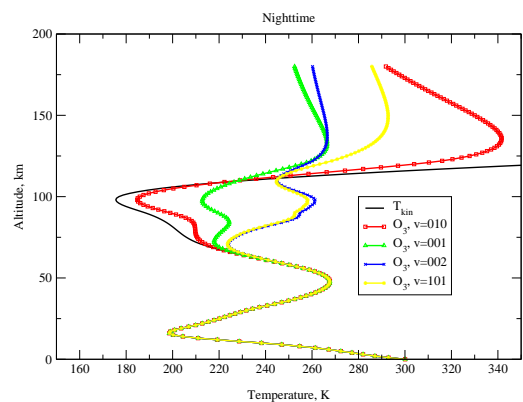
with higher energy earlier and stronger deviate from the LTE, compared to the levels with lower energy. For the daytime the 15 μm vibrational levels are also indirectly subject to the absorption of solar radiation in 2.7, 4.3 and 2.0 μm CO₂ bands. Strong solar absorption in 2.7 μm directly pumps 10011 and 10002 levels, which relax with emission of 4.3 μm quanta to 15 μm levels. The results shown in Fig. H.1 (p. 119) and Fig. H.2 (p. 119) are consistent with the latest studies reported by López-Puertas *et al.*(120), Shved *et al.*(188), and Ogibalov *et al.*(160).

The Fig. H.3 (p. 120) show the convolved limb radiances of CO₂ 15, 14.3, 10, 4.3 μm bands. They appear to be in good agreement with those described by other authors.

The 15 μm CO₂ bands dominate the radiative cooling throughout the middle atmosphere. This is one of the most important radiative mechanisms providing radiative cooling in the upper mesosphere and lower thermosphere, where the breakdown of the LTE conditions occurs. The Fig. H.4 (p. 121) shows the cooling rate by the main CO₂ (626) isotopic specie and the second most abundant CO₂ (636) isotope. The rate constant of CO₂ -O(³P_J) V - T process was taken from López-Puertas *et al.*(120)

H.2 Vibrational non-LTE in O₃

Theoretical studies of the populations of ozone vibrational states in the middle atmosphere at the conditions of LTE breakdown were made by Rawlins (169), Mlynczak and Drayson (143; 144), Manuilova and Shved (129), Fichet and Jevais *et al.*(52), Vollmann (210), Mlynczak and Zhou (149), Manuilova *et al.*(132) and Koutoulaki (92).

Fig. H.4 The cooling rates for CO₂ (626) moleculeFig. H.5 The cooling rates for CO₂ (636) moleculeFig. H.6 The vibrational temperatures for O₃ (666) levels (daytime).Fig. H.7 The vibrational temperatures for O₃ (666) levels (nighttime).

The calculations of vibrational temperatures were carried out for the daytime and nighttime reference atmospheres. The results for the selected vibrational levels are shown in Fig. H.6 (p. 121) and Fig. H.7 (p. 121). The effect of the processes Eq. C.42, (p. 93) and Eq. C.44, (p. 93) of the intermolecular $V - V$ exchange between the states of O₃ (200,001 and 100) and N₂ (1), O₂ (1) on the populations of the states 200,001 and 100 is negligibly small. The solar radiation absorption affects the populations of the states far less than the recombination reaction Eq. C.56, (p. 95). The vibrational temperatures for the models 1 and 2 (see Appendix B.3 (p. 73)) of the deactivation of O₃ ($v_1 > 1, v_2 > 1, v_3 > 1$) states with energies higher than 2100 cm⁻¹ by collisions with atomic oxygen are nearly the same. The differences start to be detectable only above 80 km and are less than 1%. The effects of the quenching of O₃ ($v_1 > 1, v_2 > 1, v_3 > 1$) result in higher vibrational populations for the majority of levels. This is that one should expect, since in this case the quenching is smaller and the energy of the levels with higher energy is then transferred to the lower levels mainly by the $V - T$ processes.

As it is expected from the O₃ collisional scheme, the O₃ vibrational temperatures are very strongly affected by the number density of O(³P_J). This atmospheric constituent has very variable abundance; large changes in the O₃ vibrational populations are therefore expected. As a rule, higher O(³P_J) results in higher vibrational temperatures. The quenching rate is also higher for the more abundant O(³P_J) but its effect is much smaller than the change in the chemical production. The variations can reach 100K for the 111 state, if the O(³P_J) number density changes by the order of magnitude.

Usually, the vibrational levels with higher energy have higher vibrational temperatures, particularly at daytime. That is an effect of the nascent distribution of the recombination reaction, which

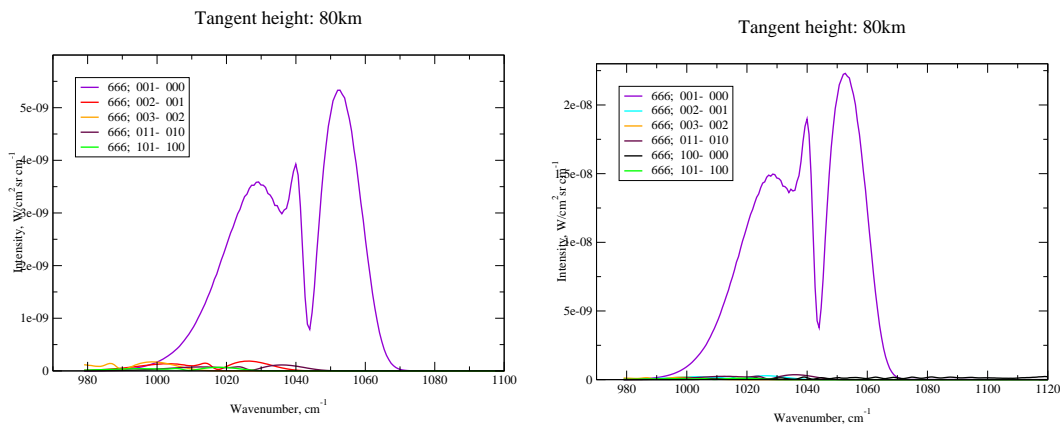


Fig. H.8 The convolved limb radiances of O₃ 9.6 μm bands (daytime) Fig. H.9 The convolved limb radiances of O₃ 9.6 μm bands (nighttime)

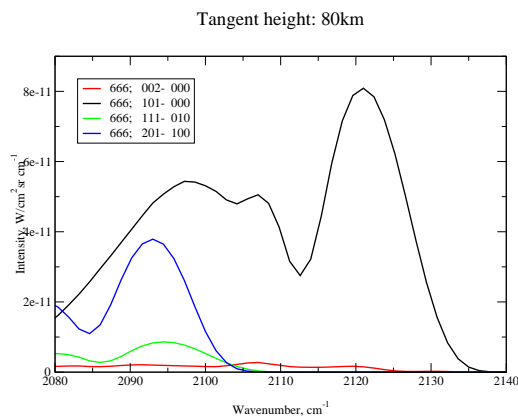


Fig. H.10 The convolved limb radiances of O₃ 4.8 μm bands (nighttime)

initially populates these higher energy levels. One can see that populations of some of these levels deviate from the LTE even at the stratospheric altitudes, and the lower the energy of the level is, the higher the level starts deviating from the LTE. It is also noticeable that the vibrational temperatures are higher at daytime. Unlike CO₂, this is not a direct consequence of the absorption of the solar radiation, but caused by higher O(³P_J) number density, which plays a major role in recombination reaction. In fact, the O₃ level populations depart from the LTE at night only above 70-75 km, where the presence of O(³P_J) starts being significant in the O₃ kinetics.

The limb radiance calculations have been performed for both daytime and nighttime reference models. The results are shown in Fig. H.8 (p. 122) and Fig. H.10 (p. 122). In general, the results have good agreement with the calculations published by *Manuilova and Shved* (129). More detailed discussion can be found in Section 5.4 (p. 36).

The role of the 9.6 μm O₃ bands in the energetics of the upper mesosphere is significant because of the contribution these bands deliver at the mesopause, where non-LTE plays an important role. *Mlynczak* (145) has shown that the conversion of chemical energy (mainly produced in ozone recombination reaction) and infrared radiation to kinetic energy by processes involving ozone is a significant source of heat near the mesopause, and the heating may exceed 6 K/day. However, accurate calculation of this effect required knowledge of not very well known parameters, such as efficiency of the excitation of the vibrational states of the O₃ molecule in the recombination reaction and rates of the kinetic processes in a vibrationally excited O₃ molecule. At the altitudes of the second ozone maximum the contribution of the hot bands exceeds the contribution of the

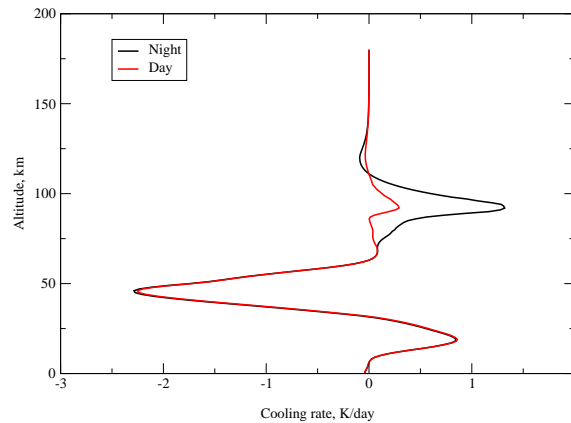


Fig. H.11 The cooling rate for O₃ molecule

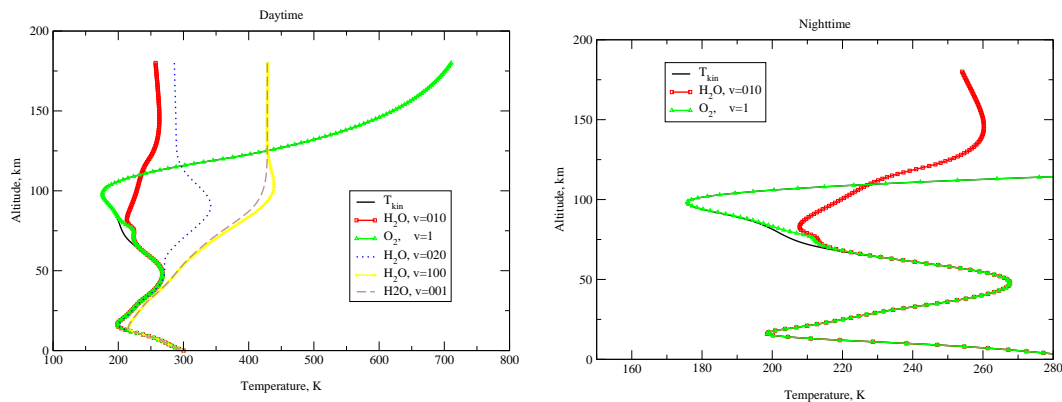


Fig. H.12 The vibrational temperatures for H₂O (161) levels (daytime). Fig. H.13 The vibrational temperatures for H₂O (161) levels (nighttime).

fundamental bands (the transformation of chemical energy results in additional cooling by hot bands). Therefore, the accurate calculation of the infrared cooling required the detailed model not limited to the fundamental bands. The results of this modeling are shown in Fig. H.11 (p. 123) and confirm the results reported by *Mlynczak* (145).

H.3 Vibrational non-LTE in H₂O

Theoretical models for the populations of the water vapour vibrational states in the middle Earth atmosphere at the conditions of the LTE breakdown were performed in recent years by *Manuilova and Shved* (128), *Sharma and Wintersteiner* (183), *Kerridge and Remsberg* (89), *Toumi* (203) and *López-Puertas et al.* (117). The model presented below is the generalization of *López-Puertas et al.* (117). It includes more vibrational levels (14 instead of 7), more $V - T$ and $V - V$ transitions with different set of rate constants compiled by *Manuilova* (130), and accounts for all rovibrational lines included in the HITRAN-2000 line database both for the radiative transfer and the absorption of solar radiation.

The Fig. H.13 (p. 123) and Fig. H.12 (p. 123) show the vibrational temperatures of the H₂O levels for nighttime and daytime respectively. Under the nighttime conditions the $V - V$ exchange between H₂O and O₂ dominates the production of both vibrationally excited molecules up to about 80 km. Therefore, all other processes affecting one of them will also affect the other. Below 60 km the coupled H₂O (010) - O₂ (1) group is held in LTE by the thermal collisions with N₂ and O₂.

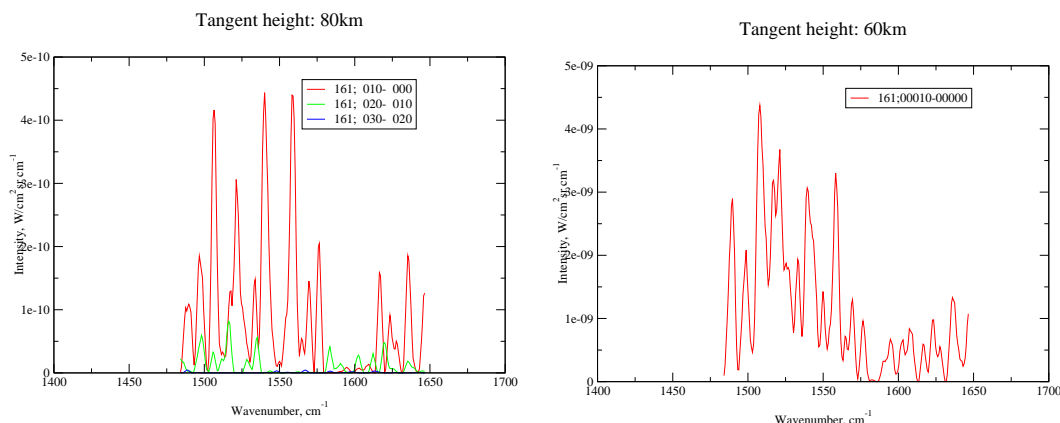


Fig. H.14 Daytime convolved limb radiances of 6.3 μm **Fig. H.15** Nighttime convolved limb radiances of 6.3 μm H_2O bands.

Above 80 km the radiative absorption in the 6.3 μm band dominates over the thermal collisional excitation populating H_2O (010) and increases the populations of both H_2O (010) and O_2 (1). Above 110 km the efficiency of collisional quenching is very small in comparison with spontaneous emission and thus the vibrational temperature becomes lower than the kinetic temperature. The vibrational temperatures of H_2O (020) and H_2O (001) levels are mainly controlled by the absorption of the upwelling radiation, resulting in larger populations at altitudes where the thermal collisions lose their importance. During daytime the populations of H_2O (020) and H_2O (001) vibrational levels strongly increase in comparison with their nighttime values, as a consequence of the absorption of the solar radiation by H_2O 2.7 μm bands and its collisional relaxation. The daytime population of H_2O (010) is slightly higher partly because of direct absorption of solar radiation and collisional relaxation from 2.7 μm levels. The potential enhancement from the $V - V$ processes with N_2 (1) proved to be less important. The additional daytime excitation of H_2O (010) through the $V - V$ coupling with O_2 (1), which appears to be more excited at daytime, is also very important.

As can be seen from the Fig. H.15 (p. 124), during the nighttime only the emission from the fundamental ν_2 band 010-000 should be taken into consideration, while for the daytime conditions (Fig. H.15 (p. 124)) one should also account for the contribution of the first ν_2 hot band 020-010.

Combined cooling rate by the H_2O vibrational and rotational bands is only about 5% of the total infrared cooling in the middle atmosphere and is mostly produced by the rotational 000-000 band (see *Zhu et al.*(225)). Given that the rotational bands are always in LTE, the non-LTE modeling is not required to calculate the cooling rate. Nevertheless, to make the picture complete, Fig. H.16 (p. 125) provides with the contribution of vibrational-rotational bands of H_2O to the total infrared cooling rate.

H.4 Vibrational non-LTE in N_2O

There are only two publications dealing with the non-LTE modeling for N_2O : *Gordiets et al.*(64) estimated the non-equilibrium N_2O emission of the 4.5, 7.8 and 17 μm bands in the thermosphere. *Shved and Gusev* (187) calculated the vibrational populations in the stratosphere and mesosphere, but have used the approximation of the optically thin atmosphere. Such treatment was chosen due to the small volume mixing ratio of N_2O (see *Brasseur and Solomon* (23)).

The modeling with ALI-ARMS provides the vibrational temperatures shown in Fig. H.17 (p. 125) and Fig. H.18 (p. 125). The N_2O nighttime heights of the transition to non-LTE decrease with vibrational energy from about 70 km for the (01¹0) state to about 55 km for the states excited in the ν_3 mode. For daytime, the vibrational temperatures of the (00⁰1) state and of the higher N_2O states far exceed those for nighttime. For the N_2O (02⁰1, 02²1, 10⁰1) states the daytime non-LTE layer

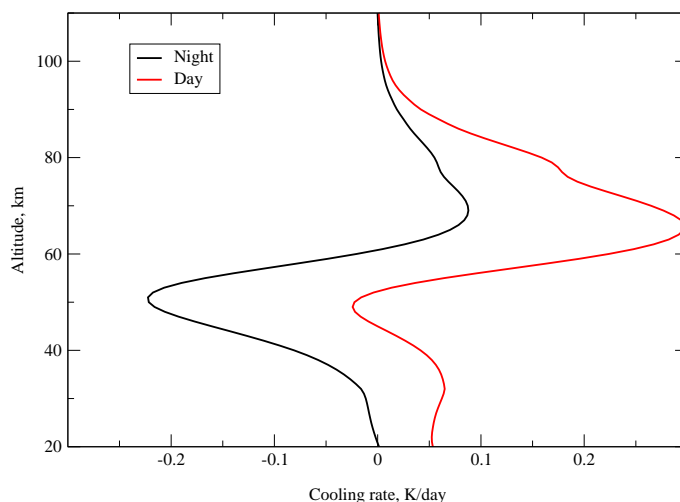


Fig. H.16 The cooling rate for H₂O molecule

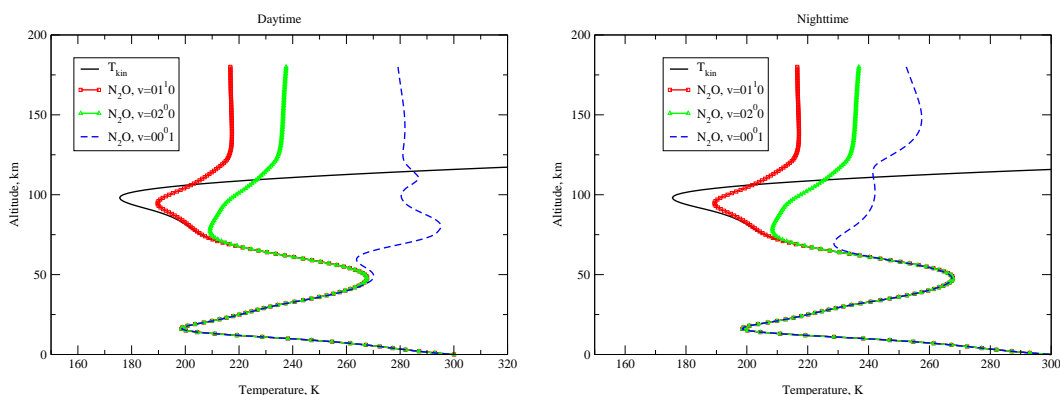


Fig. H.17 The vibrational temperatures for N₂O (446) levels (daytime). Fig. H.18 The vibrational temperatures for N₂O (446) levels (nighttime).

extends through the entire stratosphere. The $V - V$ energy exchange with N₂ and O₂ is very important in the mesosphere for populating the N₂O states.

The higher radiative deexcitation rate for a vibrational state causes the breakdown of the LTE at lower heights for the given state, when all other rates are the same. The N₂O radiative deexcitation rates of the states belonging to the different vibrational modes differ by an order of magnitude or more (for example, $A_{01^1_0,00^0_0} = 0.15 \text{ s}^{-1}$, $A_{10^0_0,00^0_0} = 12 \text{ s}^{-1}$, $A_{00^0_1,00^0_0} = 210 \text{ s}^{-1}$). The nighttime heights of the transition to non-LTE are about 70 km for the (01¹₀) state, about 60 km for the states excited in the ν_1 mode, and about 55 km for the states excited in the ν_3 mode.

The daytime vibrational temperature increases in comparison with nighttime both due to the absorption of the solar radiation in the N₂O rovibrational bands and the $V - V$ energy transfer from the N₂ (1) state producing much higher daytime populations than at nighttime. The vibrational temperature increase is significant for the (00⁰₁) state and the higher states. For the (02⁰₁, 02²₁) and especially the (10⁰₁) state, the daytime non-LTE layer extends throughout the stratosphere. The smallest daytime increase of vibrational temperature is obtained for the states excited only in the ν_2 mode. It is about 1.5K and 1K for the states (03¹₀, 03³₀) and (02⁰₀, 02²₀), respectively, and is negligible for the N₂O (01¹₀).

The processes of the $V - V$ energy exchange between the ν_3 mode and the N₂-vibration are very important in populating the states excited in the ν_3 mode. Ignoring them would extend the non-

LTE layer for these state over the entire stratosphere even at nighttime. The daytime mesospheric maximum of vibrational temperature for the states excited in the ν_3 mode comes also from these processes. That shows that the N_2O state populations are highly sensitive to the N_2 (1) non-LTE population in the mesosphere.

The N_2 (1) population, however, is controlled mainly by the interaction between CO_2 and N_2 vibrational states.

The $V - V$ energy exchange between the ν_1 mode and O_2 -vibration contributes negligibly to populating the N_2O states (even for the (10^00) state), if the rate constants specified in Appendix C (p. 83) are used. However, *Zuev et al.*(227) noted that the measured value of the rate constant for this process depends strongly on the kinetic model of the vibrational states. One should expect that the rate constants of the processes will be revised when more accurate experiments will be available.

The calculations show that for nighttime, the vibrational temperatures of the states $(02^00, 02^20)$, $(03^10, 03^30)$, $(12^00, 12^20)$, and $(02^01, 02^21)$ are close to the vibrational temperatures of the (10^00) , (11^10) , (20^00) , and (10^01) states, respectively. This is caused by the intramolecular $V - V$ energy exchange between the ν_1 and ν_2 modes, which tends to equalize T_v of these states. This $V - V$ exchange causes the closeness of the heights of the transition to non-LTE for the states $(02^00, 02^20)$ and $(03^10, 03^30)$ with those for the (10^00) and (11^10) states, respectively. The different solar pumping of the states involved in the $V - V$ exchange can result in significant daytime increase of the vibrational temperature gap between these states, even leading to such strong differences of the T_v -profiles as have been found for the $(02^01, 02^21)$ and (10^01) states. The increase of the rate constant will result in even greater closeness of the T_v for the states mentioned above.

There are no measurements of the rate constants for the collisional quenching of the N_2O vibrational states by $\text{O}(^3P_f)$. One can expect that these quenching rates are significantly higher than those for collisions with N_2 and O_2 , similar to the collisional quenching of the CO_2 vibrational states (e.g. *Shved et al.*(188)). Since the $\text{O}(^3P_f)$ mixing ratio increases strongly above 80 km, one would expect that the vibrational temperatures of the N_2O states will be different from T_v obtained here, starting from this height. As in the case of the CO_2 state populations, taking into account the collisional quenching by $\text{O}(^3P_f)$ must shift the T_v of the N_2O states toward the kinetic temperature T .

The results of the calculations of the vibrational state populations can be summarized as follows: at nighttime the transition to non-LTE occurs near 70 km for the (01^10) state, near 60 km for the states excited both in the ν_2 mode more than one-fold and in the ν_1 mode, and near 55 km for the states excited in the ν_3 mode. In the daytime the vibrational temperatures increase significantly in comparison with nighttime for the (00^01) state and the higher states. For the (02^01) , (02^21) , and (10^01) states the daytime non-LTE layer extends throughout the entire stratosphere. The mesospheric population of the N_2O states excited in the ν_3 mode depends on the N_2 (1) population which mainly is determined by interaction with CO_2 . Other external production mechanisms mentioned in the literature, like electron/proton pumping were not included in the current model because of their high uncertainty, and therefore are not discussed here.

H.5 Vibrational non-LTE in CO

The non-LTE radiative transfer models for the vibrational populations of CO were published by *López-Puertas et al.*(115) for the purposes of the carbon monoxide retrievals from the infrared limb emissions measured by Improved Stratospheric and Mesospheric Sounder (ISAMS) on the Upper Atmospheric Research Satellite (UARS) and by *Kutepov et al.*(99) for the Michelson Interferometer for Passive Atmospheric Sounding (MIPAS) on the european ENVISAT-1 (see *Endemann and Fischer*(47)). *Kutepov et al.*(99) have also discussed the possible effects of breakdown of rotational LTE on the measured limb radiances.

The vibrational temperatures of CO levels are shown in Fig. H.19 (p. 127) and Fig. H.20 (p. 127) for

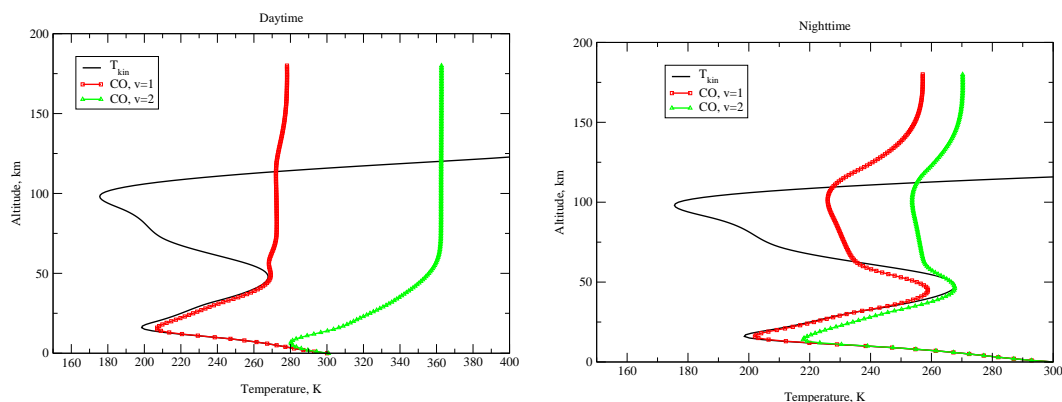


Fig. H.19 The vibrational temperatures for CO (26) levels (daytime). **Fig. H.20** The vibrational temperatures for CO (26) levels (nighttime).

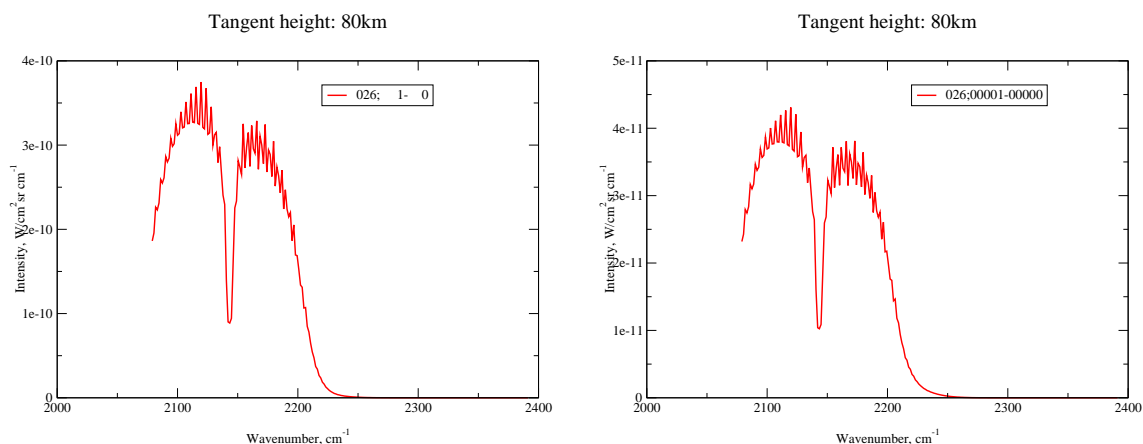


Fig. H.21 The convolved limb radiances of CO₂ 4.7 μm bands

daytime and nighttime conditions. They are in good agreement with the values of *López-Puertas et al.*(115) and *Kutepov et al.*(99). During daytime the vibrational temperature T_2 above 50 km is about 100 K higher than T_1 as result of strong pumping of CO($v = 2$) by the absorption of the solar radiation in the 2.3 μm band. The solar pumping also keeps CO ($v = 2$) in vibrational non-LTE down to the altitude of 5 km, while at night it is thermalized just below the stratopause. At night T_2 is up to 30 K higher than T_1 above the stratopause, showing that the absorption of the 4.7 μm upwelling radiation in the hot 2–1 band contributes stronger to the excitation of CO($v = 2$) in these layers than the absorption in the 1–0 fundamental band to the excitation of CO($v = 1$).

The daytime limb spectra Fig. H.21 (p. 127) is also in good agreement with *Kutepov et al.*(99). The effects of possible breakdown of rotational LTE were not considered.

The cooling rate due to CO shown in Fig. H.22 (p. 128) is increasing with the altitude, but is nevertheless negligible in comparison with the cooling by NO, O and CO₂.

H.6 Vibrational non-LTE in O₂

The molecular oxygen molecule in ground electronic state $O_2(X^3\Sigma_g^-)$ does not have any significant infrared bands, however due to its high volume mixing ratio in the Earth's atmosphere appears to be one of the most important collisional partners in $V - T$ and $V - V$ processes with optically active molecules as the big reservoir of vibrational energy.

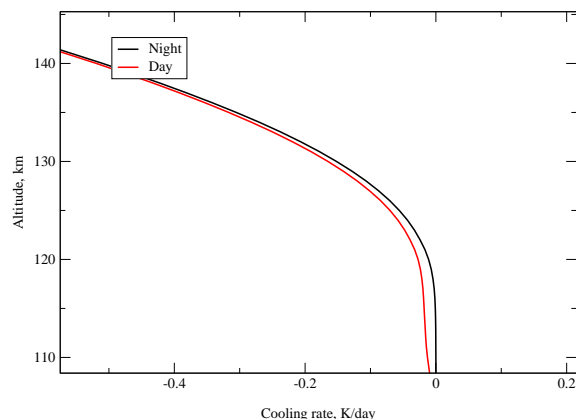


Fig. H.22 The cooling rate for CO molecule

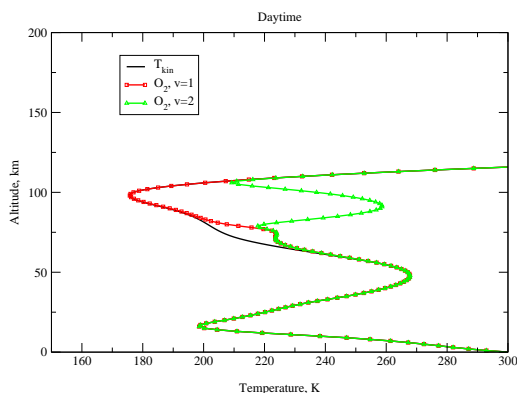


Fig. H.23 The vibrational temperatures for O_2 (66) levels (daytime).

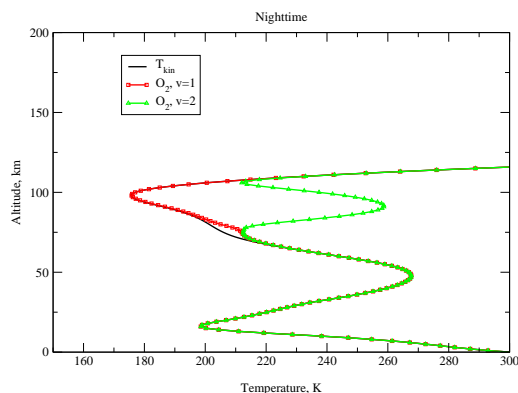


Fig. H.24 The vibrational temperatures for O_2 (66) levels (nighttime).

Therefore, all radiative terms in SEE (see Eq. 2.1, (p.3)) for the $O_2(X^3\Sigma_g^-)$ molecule disappear. The vibrational populations of $O_2(X^3\Sigma_g^-)$ are controlled by the $V - T$ collisional processes, the $V - V$ collisional processes with other molecules and by the production of the vibrationally excited $O_2(X^3\Sigma_g^-)$ mainly by the photodissociation of ozone. While the $V - T$ processes (the most strong is the collisional quenching by $O(^3P_j)$) try to keep O_2 in the LTE, the strong $V - V$ coupling with the $H_2O(010)$ vibrational level causes the $O_2(1)$ deviation from the LTE in the mesosphere and lower thermosphere for both daytime and nighttime conditions (see Fig. H.23 (p. 128) and Fig. H.24 (p. 128)). The $O_2(1)$ population is higher during the daytime, partly because of the photodissociation of ozone by the UV solar radiation. Another important factor is the absorption of the solar radiation by H_2O and subsequent energy transfer from $H_2O(010)$ to $O_2(1)$.

These mechanisms were published and discussed by *Manuilova and Shved* (128), *López-Puertas et al.*(109; 110; 117), *Zhou et al.*(224) and other authors, and found their confirmation in the presented model.

H.7 Vibrational non-LTE in N_2

Like $O_2(X^3\Sigma_g^-)$, the molecular nitrogen molecule does not have any significant infrared bands, however due to its high volume mixing ratio in the Earth atmosphere appears to be the most important collisional partner in the $V - T$ and $V - V$ processes with optically active molecules as the big reservoir of vibrational quanta.

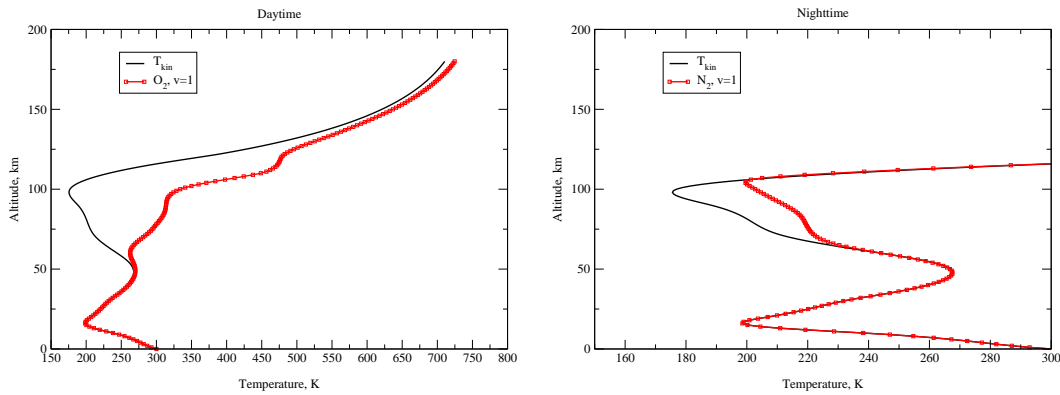


Fig. H.25 The vibrational temperatures for N₂ (44) levels (daytime). **Fig. H.26** The vibrational temperatures for N₂ (44) levels (nighttime).

It was already mentioned that the N₂ molecule only has very weak collisionally induced infrared spectra, so all the radiative terms in the SEE (see Eq. 2.1, (p. 3)), disappear. That means that the vibrational populations of N₂ are controlled by the $V - T$ collisional processes, $V - V$ collisional processes with other molecules and by the production of vibrationally excited N₂ by external processes. While the $V - T$ processes (the most strong from them is the collisional quenching by O(³P₁)) try to keep N₂ in the LTE, the strong $V - V$ coupling with CO₂ (00011) vibrational level of multiple isotopes cause the N₂ (1) deviation from the LTE in the mesosphere and lower thermosphere for both daytime and nighttime conditions. At nighttime, the pumping of N₂ (1) by the $V - V$ exchange with OH (v) causes additional increase in N₂ (1) population.

For the daytime conditions, the $E - V$ exchange of N₂ (v) states ($v \leq 7$) with O(¹D₂) becomes a substantial factor forming the N₂ (1) population in the mesosphere and thermosphere (see Fig. H.25 (p. 129)). This process influences the populations of CO₂ (00011) too, as was discussed in Appendix H.1 (p. 119). See López-Puertas *et al.*(110; 111; 120) and Shved *et al.*(186; 188) for the detailed discussion of this topic.

Acknowledgements

This work would be impossible without Rolf-Peter Kudritzki, who has not only scientifically supervised it, but during the five years of my stay at the Institute for Astronomy and Astrophysics of Munich University always found time and good will to help the development of accurate non-LTE methods for the planetary atmospheres in numerous ways.

The years spent in discussions and very fruitful joint work with Alex Kutepov, my scientific adviser, made an immense contribution to the success of this work. It is not a big exaggeration that every word and every formula in this dissertation was X-rayed by his pencil.

I owe a debt of gratitude to S. L. Nosov, who showed me a proper way to do the scientific research. With Rada O. Manuilova I began my work in the wonderful world of the O_3 non-LTE modeling in 1993 and have never regretted it.

I am also grateful to K. -U. Großmann and D. Offermann from Bergische Universität-Gesamthochschule Wuppertal, who have designed and managed the CRISTA experiment. Due to the efforts of CRISTA team it became possible for the university project to obtain high quality global maps of temperature and trace gas number densities in the Earth's atmosphere, that stretch from the troposphere to the "edge of space".

The work on this dissertation was supported in frame of the grants Ku474/18-2 and -3 from the Deutsche Forschungsgemeinschaft (DFG), research stipend of the Deutscher Akademischer Austauschdienst (DAAD), research stipend of Max Planck Society, and the "Non-LTE Diagnostik der infraroten CRISTA-Horizontspektren" project (Kennzeichen 50 OE 9701 9), supported by Deutsche Agentur für Raumangelegenheiten (DARA/DLR) in 1997-2000.

Lebenslauf

Persönliche Daten

Oleg Goussev

Tel.: (089) 2180-6009

E-Mail: oleg@usm.uni-muenchen.de

Geb. am 19. 08. 1970 in St. Petersburg, Rußland

Schulbildung

09/1977–06/1984 Grundschule und Gymnasium Nr.157 in St. Petersburg

09/1984–06/1987 Gymnasium Nr.30 in St. Petersburg

Studium

09/1987–06/1992 Universität St. Petersburg, Fakultät für angewandte Mathematik; Student

09/1992–11/1994 Universität St. Petersburg, Fakultät für angewandte Mathematik; Doktorand

10/1995–07/1996 Universität Munchen, Fakultät für Mathematik; Student

10/1998–03/1999 Max-Planck-Institut für Astronomie, Garching bei München; Stipendiat

10/1999–07/2000 Universität München, Fakultät für Physik; Doktorand

Berufserfahrung

04/1997–05/2000 Institut für Astronomie und Astrophysik der Universität München; wissenschaftlicher Mitarbeiter der Universitäts-Sternwarte

seit 06/2000 Bergische Universität-Gesamthochschule Wuppertal; wissenschaftlicher Mitarbeiter der Arbeitsgruppe Weltraumforschung, Fachbereich 8 - Physik, Experimentalphysik

München, 25. November 2002

Bibliography

- [1] Abramowitz, M., and A. Stegun, Pocketbook of mathematical functions, Verlag Harri Deutsch, (1984).
- [2] Adams, M. L., Discontinuous finite-element transport solutions in the thick diffusion limit in Cartesian geometry, *Proceedings of the International Topical Meeting on Advances in Mathematics, Computations and Reactor Physics*, Pittsburgh, Pennsylvania, The American Nuclear Society, pp. 21.1, (1991).
- [3] Allen, D. S., and C. J. S. M. Simpson, Vibrational energy exchange between CO and the isotopes of N₂ between 300 K and 80 K, *Chem. Phys.*, **45**, 203–211, (1980).
- [4] Adler-Golden, S. M., J. Gruninger, and D. R. Smith, Derivation of atmospheric oxygen and hydrogen profiles from ozone ν_3 band emission, *J. Geophys. Res.*, **97**, 19509–19570, (1992).
- [5] Adler-Golden, S., D. R. Smith, J. Vail, A. Berk, R. Nadile, and L. Jeong, Simulations of mesospheric and thermospheric IR radiance measured in the CIRIS-1A shuttle experiment, *J. Quant. Spectrosc. Radiat. Transfer*, **61**, 1397–1410, (1999).
- [6] Anderson, G. P., S. A. Clough, F. X. Kneizys, J. H. Chetwynd, and E. P. Shettle, AFGL atmospheric constituent profiles (0-120km), *AFGL Tech. Rep., AFGL-TR-86-0110*, Air Force Geophys. Lab., Hanscom Air Force Base, Bedford, Mass, (1986).
- [7] Anderson, G. P., F. X. Kneizys, J. H. Chetwynd, J. Wang, M. L. Hoke, L. S. Rothman, L. M. Kimball, R. A. McClatchey, E. P. Shettle, S. A. Clough, W. O. Gallery, L. W. Abreu, and J. E. A. Selby, FASCO-DE/MODTRAN/LOWTRAN: Past/Present/Future, *18th Annual Review Conference on Atmospheric Transmission Models*, (1995).
- [8] Auer, L., An Hermitian method for solution of radiative transfer problems, *J. Quant. Spectrosc. Radiat. Transfer*, **16**, 931–937, (1976).
- [9] Avramides, E., and T. E. Hunter, Vibrational-vibrational and vibrational- translational/rotational processes in methane, oxygen gas-phase mixtures: Optoacoustic measurements, *Molec. Phys.*, **48**, 1331–1343, (1983).
- [10] Avrett, E. H., Source-function equality in multiplets, *Astrophys. J.*, **144**, 59–75, (1966).
- [11] Balakrishnan, N., and G. D. Billing, Quantum-classical reaction path study of the reaction $O(^3P) + O_3(^1A_1) \rightarrow 2O_2(X^3\Sigma_g^-)$, *J. Chem. Phys.*, **104**, 9482–9498, (1996).
- [12] Balakrishnan, N., A. Dalgarno, and G. D. Billing, Multiquantum vibrational transitions in O₂ ($v \geq 25$) + O₂ ($v = 0$) collisions, *Chem. Phys. Lett.*, **288**, 657–662, (1998).
- [13] Barbe, A., C. Secroun, and P. Jouve, Infrared spectra of ¹⁶O₃ and ¹⁸O₃ : Darling and Dennison resonance and anharmonic potential function of ozone, *J. Mol. Spectr.*, **49**, 171–182, (1974).
- [14] Barnet, J. J., Satellite-borne measurements of middle-atmosphere temperature, *Phil. Trans. R. Soc. London*, **A 323**, 527, (1987).
- [15] Barthol, P., *Das optische System des CRISTA-Experiments*, Doktorarbeit, WUB-DIS 94-4, Fachbereich Physik, Bergische Universität - Gesamthochschule Wuppertal, 42097 Wuppertal, Deutschland, (1994).
- [16] Bass, H. E., R. G. Keaton, and D. Williams, Vibrational and rotational relaxation in mixtures of water vapor and oxygen, *J. Acoust. Soc. Amer.*, **60**, 74–77, (1976).
- [17] Bauer, S. H., J. F. Caballero, R. Curtis, and J. R. Wiesenfeld, Vibrational relaxation rates of CO₂ (00⁰1) with various collision partners for $T < 300$ K, *J. Chem. Phys.*, **91**, 1778–1785, (1987).
- [18] Berger, U., and U. von Zahn, The two-level structure of the mesopause: A model study, *J. Geophys. Res.*, **104**, 22083–22093, (1999).
- [19] Betz, A. L., Ph.D. thesis, University of California, Berkeley, Calif., (1976).
- [20] Betz, A. L., M. A. Johnson, R. A. McLaren, and E. C. Sutton, Heterodyne detection of CO₂ emission lines and wind velocities in the atmosphere of Venus, *Astrophys. J.*, **208**, 141–144, (1976).
- [21] Billing, G. D., and R. E. Kolesnik, Vibrational relaxation of oxygen. State to state rate constants, *Chem. Phys. Lett.*, **200**, 382–386, (1992).
- [22] P. M. Borrell, and K. R. Grant, Vibrational relaxation of excited oxygen, O₂($a^1\Delta_g$), studied with a discharge flow/shock-tube technique. *J. Chem. Soc., Faraday Trans.*, **76**, 923–928, (1980).
- [23] Brasseur, G., and S. Solomon, *Aeronomy of the Middle Atmosphere: Chemistry and Physics in the Stratosphere and Mesosphere*, D. Reidel, Hingham, Mass., 452 pp., (1986).
- [24] Buchwald, M. I., and G. J. Wolga, Vibrational relaxation of CO₂ (00⁰1) by atoms, *J. Chem. Phys.*, **62**, 2828–2832, (1975).
- [25] Cannon, C. J., *The transfer of spectral line radiation*, Cambridge University Press, (1985).
- [26] Castor, J. I., P. G. Dykema, and R. I. Klein, A new scheme for multidimensional line transfer, Part II, *Astrophys. J.*, **387**, 561–571, (1992).
- [27] Chabrillat, S., and G. Kockarts, Simple parameterization of the absorption of the solar Lyman-alpha line, *Geophys. Res. Lett.*, **24**, 2659–2662, (1997).
- [28] Chandler, E. T., A. E. Gregory, R. M. Siddles, and C. J. S. M. Simpson, Vibrational energy exchange between CO ($v=1$) and ¹⁴N₂ and CO ($v=1$) and ¹⁵N₂ measured to 60K in the gas phase, *Chem. Phys. Lett.*, **78**, 236–240, (1981).
- [29] Chapman, S., and S. Green, Accuracy of the IOS approximation for highly inelastic $R - T$ collisional energy

- transfer CO -Ar, *Chem. Phys. Lett.*, **112**, 436–440, (1984).
- [30] Christensen, P. R., Thermal Emission Spectrometer experiment: The Mars Observer Mission, *J. Geophys. Res.*, **97**, 7719–7734, (1992).
- [31] Clarmann, T., “RAT: A Computational Tool for Retrieval of Atmospheric Trace Gas Profiles from Infrared Spectra,” *KfK 5423*, Forschungszentrum Karlsruhe, Germany, (1994).
- [32] Connor, B. J., D. E. Siskind, J. J. Tsou, A. Parrish, and E. E. Remsberg, Ground-based microwave observations of ozone in the upper stratosphere and mesosphere, *J. Geophys. Res.*, **99**, 16757–16770, (1994).
- [33] Conrath, B. J., J. C. Pearl, M. D. Smith, W. C. Maguire, S. Dason, M. S. Kaelberer and P. R. Christensen, Mars Global Surveyor Thermal Emission Spectrometer (TES) observations: Atmospheric temperatures during aerobraking and science phasing, *J. Geophys. Res.*, **105**, 9509–9519, (2000).
- [34] Curtis, A. R., and R. M. Goody, Thermal radiation in the upper atmosphere, *Proc. Roy. Soc. A.*, **236**, 193–206, (1956).
- [35] Deming, D., and M. J. Mumma, Modeling of the 10 μm Natural Laser Emission from the Mesospheres of Mars and Venus, *Icarus*, **55**, 356–368, (1983).
- [36] DeMore, W. B., S. P. Sander, D. M. Golden, R. F. Hampson, M. J. Kurylo, C. J. Howard, A. R. Ravishankara, C. E. Kolb, and M. J. Molina, Chemical Kinetics and Photochemical Data for Use in Stratospheric Modeling. Evaluation Number 12, (1987).
- [37] Dodd, J. A., J. R. Winick, W. A. M. Blumberg, S. J. Lipson, P. S. Armstrong, and J. R. Lowell, CIRRIS-1A observation of $^{13}\text{O}^{16}\text{C}$ and $^{12}\text{O}^{18}\text{C}$ fundamental band radiance in the upper atmosphere, *Geophys. Res. Lett.*, **20**, 2683–2686, (1993).
- [38] Dothe, H., F. von Esse, and R. D. Sharma, Rotational temperatures of infrared active species in the daytime terrestrial thermosphere, In *Abstracts, Week A, XXI General Assembly of IUGG, Boulder, Colorado, July 2–14, 1995*, MA51B–07, (1995).
- [39] Doyennette, L., G. Mastrocinque, A. Chakroun, H. Guenguén, M. Margottin-Maclou, and L. Henry, Temperature dependence of the vibrational relaxation of CO ($v = 1$) by NO, O₂, and D₂, and the self-relaxation of D₂, *J. Chem. Phys.*, **67**, 3360–3366, (1977).
- [40] Doyennette, L., C. Boursier, J. Menard, and F. Menard-Bourcin, Coriolis-assisted intermode transfers in O₃ - M gas mixtures (M=O₂ and N₂) in the temperature range 200–300 K from IR double resonance measurements, *Chem. Phys. Lett.*, **197**, 157–160, (1992).
- [41] Echle, G., H. Oelhaf, and A. Wegner, Measurements of atmospheric parameters with MIPAS, *ESA-contract 9597/91/NL/SF, final report*, ESA Publications Division, 2200 AG Noordwijk, The Netherlands, (1992).
- [42] Echle, G., H. Oelhaf, T. von Clarmann, and M. Schmidt, “Definition of Spectral Intervals for the Retrieval of Trace Gas Concentrations From MIPAS Limb Emission Spectra,” *10993/94/NL/PR*, European Space Agency, Paris, France, (1995).
- [43] Edwards, D. P., M. López-Puertas, and M. Á. López-Valverde, Non-local thermodynamic equilibrium studies of the 15 μm bands of CO₂ for atmospheric remote sensing, *J. Geophys. Res.*, **98**, 14955–14977, (1993).
- [44] Edwards, D. P., M. López-Puertas, and M. G. Mlynczak, Non-local thermodynamic equilibrium limb radiance from O₃ and CO₂ in the 9–11 μm spectral region, *J. Quant. Spectrosc. Radiat. Transfer*, **52**, 389–407, (1994).
- [45] Edwards, D. P., J. B. Kumer, M. López-Puertas, M. G. Mlynczak, A. Gopalan, J. C. Gille, and A. Roche, Non-local thermodynamic equilibrium limb radiance near 10 μm as measured by UARS CLAES, *J. Geophys. Res.*, **101**, 26577–26588, (1996).
- [46] Edwards, D. P., M. López-Puertas, and R. R. Gamache, The non-LTE correction to the vibrational component of the internal partition sum for atmospheric calculations, *J. Quant. Spectrosc. Radiat. Transfer*, **59**, 423–436, (1997).
- [47] Endemann, M., and H. Fischer, *ESA bulletin*, **76**, 47, (1994).
- [48] Esplin, M. P., and M. L. Hoke, High temperature, high resolution line position measurements of CO₂ in the 580 to 940 cm^{-1} region. *J. Quant. Spectrosc. Radiat. Transfer*, **48**, 573–580, (1992).
- [49] Farmer, C. B., and R. H. Norton, A high-resolution atlas of the infrared spectrum of the sun and the earth atmosphere from space, *NASA Ref. Publ. 1224*, Vols. 1 and 2, Office of Management (NASA), Washington, DC, (1989).
- [50] Feautrier, P., Sur la resolution numerique de léquation de transfert, *Compt. Rend. Acad. Sci. Paris*, **258**, 3189–3191, (1964).
- [51] Fermi, E., *Z. Physik*, **71**, 250, (1931).
- [52] Fichet, P., and J. R. Jevais, NLTE processes in ozone: importance of O and O₃ densities near the mesopause, *Planet. Space Sci.*, **40**, 989, (1992).
- [53] Finzi, J., F. E. Howis, V. N. Panfilov, P. Hess, and C. B. Moore, Vibrational relaxation of water vapor, *J. Chem. Phys.*, **67**, 4053–4061, (1977).
- [54] Fischer, H., MIPAS (Michelson Interferometer for Passive Atmospheric Sounding on the European Polar Platform), *ESA-proposal/MIPAS-PPF July 1988*, (1988).
- [55] Flaud, J. M., R. Bacis, The ozone molecule: infrared and microwave spectroscopy, *Spectrochimica Acta*, **54**,

3–16, (1998).

- [56] Fomichev, V. I., J.-P. Blanchet, and D. S. Turner, Matrix parameterization of the 15 μm CO₂ band cooling in the middle and upper atmosphere for variable CO₂ concentration, *J. Geophys. Res.*, **103**, 505–528, (1998).
- [57] Funke, B., and M. López-Puertas, Non-LTE vibrational, rotational and spin state distribution of NO ($v=0,1,2$) under quiescent atmospheric conditions. *J. Geophys. Res.*, in press, (1999).
- [58] Funke, B., *private communication*, (1999).
- [59] Funke, B., “Ein Modell für die Zustandsverteilung von NO bei nicht vorhandenem lokalem thermodynamischem Gleichgewicht und dessen Nutzung zur Ableitung atmosphärischer Parameter aus 5.3 μm Emissionsspektren”, PhD thesis, Institut für Meteorologie und Klimaforschung, Karlsruhe, (1999).
- [60] Gamache, R. R., R. L. Hawkins, and L. S. Rothman, Total internal partition sums in the temperature range 70–3000K: Atmospheric linear molecules, *Journal of molecular spectroscopy*, **142**, 205–219, (1990).
- [61] Gamache, R. R., and L. S. Rothman, Extension of the HITRAN database to non-LTE applications, *J. Quant. Spectrosc. Radiat. Transfer*, **48**, 519–525, (1992).
- [62] Gille, J. C., and J. M. Russell III, The limb infrared monitor of the stratosphere: experiment description, performance and results, *J. Geophys. Res.*, **89**, 5125–5140, (1984).
- [63] Goody, R. M., *Atmospheric radiation: Theoretical Basis*, Oxford University Press, Oxford, 436 pp., (1964).
- [64] Gordiets, B. F., M. N. Markov, and L. A. Saburova, Rotational relaxation and infrared emission spectrum involving vibration-rotational transitions of molecules in the upper atmosphere, *Opt. Spectrosc.*, **41**, 554–558, (1976).
- [65] Gordley, L. L., and J. M. Russell III, Rapid inversion of limb radiance data using an emissivity growth approximation, *Appl. Opt.*, **20**, 807, (1981).
- [66] Gordley, L. L., B. T. Marshall, and D. A. Chu, Linepak: Algorithms for modeling spectral transmittance and radiance, *J. Quant. Spectrosc. Radiat. Transfer*, **54**, 563–580, (1994).
- [67] Grossmann, K. U., M. Kaufmann, and K. Vollmann, The fine structure emission of thermospheric atomic oxygen, *Adv. Space Res.*, **19**, 595–598, (1997).
- [68] Grossmann, K. U., M. Kaufmann, and E. Gerstner, A global measurement of lower thermosphere atomic oxygen densities, *Geophys. Res. Lett.*, **27**, 1387–1390, (2000).
- [69] Grossmann, K. U., O. Gusev, M. Kaufmann, and A. Kutepov, Atmospheric parameters retrieved from CRISTA measurements in the upper mesosphere and lower thermosphere, *SPIE, Toulouse*, (2001).
- [70] Grossmann, K. U., D. Offermann, O. Gusev, J. Oberheide, M. Riese and R. Spang, The CRISTA-2 mission, *J. Geophys. Res.*, **10.1029/2001JD000667**, (2002).
- [71] Gueguen, H., F. Yzambart, A. Chakroun, M. Margottin-Maclou, L. Doyennette, and L. Henry, Temperature dependence of the vibration-vibration transfer rates from CO₂ and N₂O excited in the (00⁰1) vibrational level to ¹⁴N₂ and ¹⁵N₂ molecules, *Chem. Phys. Lett.*, **35**, 198–201, (1975).
- [72] Gunson, M. R., M. M. Abbas, M. C. Abrams, M. Allen, L. R. Brown, T. L. Brown, A. Y. Chang, A. Goldman, F. W. Irion, L. L. Lowes, E. Mahieu, G. L. Manney, H. A. Michelsen, M. J. Newchurch, C. P. Rinsland, R. J. Salawitch, G. P. Stiller, G. C. Toon, Y. L. Yung, and R. Zander, The Atmospheric Trace Molecule Spectroscopy (ATMOS) experiment: Deployment on the ATLAS Space Shuttle missions”, *Geophys. Res. Lett.*, **23**, 2333–2336, (1996).
- [73] Gusev, O., M. Kaufmann, and K. U. Grossmann, Kinetic temperatures in the upper mesosphere and lower thermosphere derived from CRISTA limb radiance data, *Proceedings of the 15th ESA Symposium on European Rocket and Balloon Programmes and Related Research*, Biarritz, France (ESA SP-471), 97–101, (2001).
- [74] Gusev, O., and A. A. Kutepov, Non-LTE problem for molecular gas in planetary atmospheres, *STELLAR ATMOSPHERE MODELING*, ASP Conference Series, (2002).
- [75] Harding, D. R., R. E. Weston Jr., and G. W. Flynn, Energy transfer to CO (v) in the O(¹D₂) +CO (¹ Σ_g^+) reaction, *J. Chem. Phys.*, **88**, 3590–3598, (1988).
- [76] Hedin, A. E., Extension of the MSIS thermosphere model into the middle and lower atmosphere, *J. Geophys. Res.*, **96**, 1159–1172, (1991).
- [77] Herzberg, G., *Spectra of Diatomic Molecules*, Van Nostrand Reinhold, New York, (1950).
- [78] Hippler, H., R. Rahn, and J. Troe, Temperature and pressure dependence of ozone formation rates in the range 1–1000 mbar and 90–370 K, *J. Chem. Phys.*, **93**, 6560–6569, (1990).
- [79] Hubený, I., and T. Lanz, NLTE line blanketed model atmospheres of hot stars. I. Hybrid Complete Linearization/Accelerated Lambda Iteration Method, *Astrophys. J.*, **439**, 875–904, (1995).
- [80] Hubený, I., D. Mihalas, and K. Werner, *STELLAR ATMOSPHERE MODELING*, ASP Conference Series, (2002).
- [81] Humlicek, J., Optimised computation of the Voigt and complex probability functions, *J. Quant. Spectrosc. Radiat. Transfer*, **27**, 437–444, (1982).
- [82] Hummer, D., *private communication*, (1991).
- [83] Inoue, G., and S. Tsuchiya, Vibration-vibration energy transfer of CO₂ (00⁰1) with N₂ and CO at low temperatures, *J. Phys. Soc. Jpn.*, **39**, 479–486, (1975).
- [84] Ivanov, V. V., *Transfer of radiation in spectral lines*, National Bureau of Standards., (U.S) Spec. Pub., **385**, 480pp,

- (1973).
- [85] Joens, J. A., J. B. Burkholder, and E. J. Bair, Vibrational relaxation in ozone recombination, *J. Chem. Phys.*, **76**, 5902–5916, (1982).
- [86] Justus, C. G., and D. L. Johnson, The NASA/MSFC Global Reference Atmospheric Model — 1999 Version (GRAM99), Marshall Space Flight Center, USA, (1999).
- [87] Kaufmann, M., O. A. Gusev, K. U. Grossmann, R. G. Roble, M. E. Hagan, C. Hartsough, and A. A. Kutepov, The vertical and horizontal distribution of CO₂ densities in the upper mesosphere and lower thermosphere as measured by CRISTA, *J. Geophys. Res.*, **10.1029/2001JD000704** (2002).
- [88] Kaufmann, M., O. A. Gusev, K. U. Grossmann, F. J. Martín-Torres, D. R. Marsh, and A. A. Kutepov, Satellite observations of day- and nighttime ozone in the mesosphere and lower thermosphere, *J. Geophys. Res.*, **2002JD002800R** (2002).
- [89] Kerridge, B. J., and Remsberg E. E., Evidence from the limb infrared monitor of the stratosphere for non-local thermodynamic equilibrium in the ν_2 mode of mesospheric water vapor and the ν_3 mode of stratospheric nitrogen dioxide, *J. Geophys. Res.*, **94**, 16323–16342, (1989).
- [90] Klatt, M., W. M. Smith, A. C. Symonds, R. P. Tuckett, and G. N. Ward, *J. Chem. Soc. Faraday Trans.*, **92**, 193, (1996).
- [91] Klein, P. I., P. G. Dykema, and J. I. Castor, A new scheme for multidimensional line transfer, Part I, *submitted to Astrophys. J.*, (1991).
- [92] Koutoulaki, K., Study of Ozone Non-thermal IR Emission Using ISAMS Observations, *Dissertation, University of Oxford*, (1998).
- [93] Kumer, J. B., and T. C. James, Non-LTE calculation of HCl earthlimb emission and implication for detection of HCl in the atmosphere, *Geophys. Res. Lett.*, **9**, 860–862, (1982).
- [94] Kung, R. T. V., Vibrational relaxation of the N₂O ν_1 mode by Ar, N₂, H₂O, and NO, *J. Chem. Phys.*, **63**, 5313–5317, (1975).
- [95] Kurucz, R. L., and B. Bell, Atomic Line Data, Kurucz CD-ROM No. 23. Cambridge, Mass.: Smithsonian Astrophysical Observatory, (1995).
- [96] Kutepov, A. A., and G. M. Shved, Radiative transfer in the 15 μm CO₂ band with the breakdown of local thermodynamic equilibrium in the Earth's atmosphere, *Izvestiya, Atmospheric and Oceanic Physics*, **14**, 18–30, (1978).
- [97] Kutepov, A. A., D. G. Hummer, and C. B. Moore, Rotational relaxation of the 00⁰1 level of CO₂ including radiative transfer in the 4.3 μm band of planetary atmospheres, *J. Quant. Spectrosc. Radiat. Transfer*, **34**, 101–113, (1985).
- [98] Kutepov, A. A., D. Kunze, D. G. Hummer, and G. B. Rybicki, The solution of radiative transfer problems in molecular bands without the LTE assumption by accelerated lambda iteration method, *J. Quant. Spectrosc. Radiat. Transfer*, **46**, 347–365, (1991).
- [99] Kutepov, A. A., H. Oelhaf, and H. Fischer, Non-LTE radiative transfer in the 4.7 and 4.3 μm bands of CO : vibration-rotational non-LTE and its effects on limb radiances, *J. Quant. Spectrosc. Radiat. Transfer*, **57**, 317–339, (1997).
- [100] Kutepov, A. A., O. Gusev, and V. P. Ogibalov, Solution of the non-LTE problem for molecular gas in planetary atmospheres: Superiority of accelerated lambda iteration, *J. Quant. Spectrosc. Radiat. Transfer*, **60**, 199–220, (1998).
- [101] Kylling, A., Radiation transport in cloudy and aerosol loaded atmosphere, Ph.D. thesis, University of Alaska, (1992).
- [102] Kylling, A., K. Stamnes, and S.-C. Tsay, A reliable and efficient two-stream algorithm for radiative transfer; Documentation of accuracy in realistic layered media, *Journal of Atmospheric Chemistry*, **21**, 115–150, (1995).
- [103] Labitzke, K., J. J. Barnett, and B. Edwards, Handbook MAP 16, SCOSTEP, University of Illinois, Urbana, (1985).
- [104] Lacoursière, J., S. A. Meyer, G. W. Faris, T. G. Slanger, B. R. Lewis, and S. T. Gibson, The O(¹D₂) Yield from O₂ Photodissociation near H Lyman- α (121.6 nm), *J. Chem. Phys.*, **10**, 1949–1958, (1999).
- [105] Laher, R. R., and F. R. Gilmore, Improved fits for the vibrational and rotational constants of many states of nitrogen and oxygen, *J. Chem. Phys. Ref. Data*, **20**, 685, (1991).
- [106] Lepoutre, F., G. Louis, and H. Manceau, Collisional relaxation in CO₂ between 180 K and 400 K measured by the spectrophone method, *Chem. Phys. Lett.*, **48**, 509–615, (1977).
- [107] Lewis, B. R., I. M. Vardavas, and J. H. Carver, The aeronomic dissociation of water vapor by solar H Lyman- α radiation *J. Geophys. Research*, **88**, 4935–4940, (1983).
- [108] Lewittes, M. E., C. C. Davis, and R. A. McFarlane, Vibrational deactivation of CO ($v=1$) by oxygen atoms, *J. Chem. Phys.*, **69**, 1952–1957, (1978).
- [109] López-Puertas, M., R. Rodrigo, A. Molina, and F. W. Taylor, A non-LTE radiative transfer model for infrared bands in the middle atmosphere. I. Theoretical basis and application to CO₂ 15 μm bands, *J. Atmos. Terr. Phys.*, **48**, 729–748, (1986).
- [110] López-Puertas, M., R. Rodrigo, J. J. López-Moreno, and F. W. Taylor, A non-LTE radiative transfer model

- for infrared bands in the middle atmosphere. II. CO₂ (2.7 and 4.3 μm) and water vapor (6.3 μm) bands and N₂ and O₂ vibrational levels, *J. Atmos. Terr. Phys.*, **48**, 749–764, (1986).
- [111] López-Puertas, M., and F. W. Taylor, Carbon dioxide 4.3 μm emission in the Earth's atmosphere. A comparison between NIMBUS 7 SAMS measurements and non-LTE radiative transfer calculations, *J. Geophys. Research*, **94**, 13045–13068, (1989).
- [112] López-Puertas, M., M. Á. López-Valverde, and F. W. Taylor, Studies of solar heating by CO₂ in the upper atmosphere using a non-LTE model and satellite data, *J. Atmos. Sci.*, **47**, 809–822, (1990).
- [113] López-Puertas, M., M. Á. López-Valverde, and F. W. Taylor, Vibrational temperatures and radiative cooling of the CO₂ 15 μm bands in the middle atmosphere, *Q. J. R. Meteorol. Soc.*, **118**, 499–532, (1992).
- [114] López-Puertas, M., M. Á. López-Valverde, C. P. Rinsland, and M. R. Gunson, Analysis of the upper atmosphere CO₂ (ν₂) vibrational temperatures retrieved from ATMOS/Spacelab 3 observations, *J. Geophys. Res.*, **97**, 20469–20478, (1992).
- [115] López-Puertas, M., M. Á. López-Valverde, D. P. Edwards, and F. W. Taylor, Non-local-thermodynamic-equilibrium populations of the first vibrational excited state of CO in the middle atmosphere, *J. Geophys. Res.*, **98**, 8933–8947, (1993).
- [116] López-Puertas, M., P. P. Wintersteiner, R. H. Picard, J. R. Winick, and R. D. Sharma, Comparison of line-by-line and Curtis Matrix calculations for the vibrational temperatures and radiative cooling of the CO₂ 15 μm bands in the middle and upper atmosphere, *J. Quant. Spectrosc. Radiat. Transfer*, **52**, 409–423, (1994).
- [117] López-Puertas, M., G. Zaragoza, B. J. Kerridge, and F. W. Taylor, Non-local-thermodynamic-equilibrium model for H₂O 6.3 and 2.7 μm bands in the middle atmosphere, *J. Geophys. Res.*, **5**, 9131–9147, (1995).
- [118] López-Puertas, M., G. Zaragoza, M. Á. López-Valverde, F. J. Martín-Torres, G. M. Shved, R. O. Manuilova, A. A. Kutepov, O. A. Gusev, T. von Clarmann, A. Linden, G. Stiller, A. Wegner, and J.-M. Flaud, "Evaluation of the non-LTE effects in MIPAS pressure, temperature and volume mixing ratio retrievals (Non-LTE study)", *Final Report*, ESTEC Purchase Order 151625/1995, (1996).
- [119] López-Puertas, M., G. Zaragoza, M. Á. López-Valverde, F. J. Martín-Torres, G. M. Shved, R. O. Manuilova, A. A. Kutepov, O. Gusev, T. Clarmann, A. Linden, G. Stiller, A. Wegner, H. Oelhaf, D. P. Edwards, and J.-M. Flaud, Non-local thermodynamic equilibrium limb radiances for the MIPAS instrument on Envisat-1, *J. Quant. Spectrosc. Radiat. Transfer*, **59**, 377–403, (1998).
- [120] López-Puertas, M., G. Zaragoza, M. Á. López-Valverde, and F. W. Taylor, Non local thermodynamic equilibrium (LTE) atmospheric limb emission at 4.6 μm . 1. An update of the CO₂ non-LTE radiative transfer model, *Journal of Geophysical Research*, **103**, D7, 8499–8513, (1998).
- [121] López-Puertas, M., F. W. Taylor. *Non-LTE radiative transfer in the atmosphere*, Singapore : World Scientific, (Series on atmospheric, oceanic and planetary physics ; v.3), (2001).
- [122] Lübken, F.-J., Thermal structure of the Arctic summer mesosphere, *Journal of Geophysical Research*, **104**, D8, 9135, (1999).
- [123] Lunt, S. L., C. T. Wickham-Jones, and C. J. S. M. Simpson, Rate constants for the deactivation of the 15 μm band of carbon dioxide by the collisional partners CH₃F, CO₂, N₂, Ar and Kr over the temperature range 300 to 150 K, *Chem. Phys. Lett.*, **115**, 60–64, (1985).
- [124] Mack, J. A., K. Mikulecky, and A. M. Wodtke, Resonant vibration-vibration energy transfer between highly vibrationally excited O₂ (X³Σ_g⁻, v = 15 – 26) and CO₂, N₂O, N₂, and O₃, *J. Chem. Phys.*, **105**, 4105, (1996).
- [125] Makhlof, U. B., R. H. Picard, and J. R. Winick, Photochemical-dynamical modeling of the measured response of airglow to gravity waves. 1. Basic model for OH airglow, *J. Geophys. Res.*, **100**, 11289–11311, (1995).
- [126] Maguire, W. C., J. C. Pearl, M. D. Smith, B. J. Conrath, A. A. Kutepov, M. S. Kaelberer, E. Winter, and P. R. Christensen, Observation of high altitude, CO₂ hot bands on Mars by the orbiting thermal emission Spectrometer, *J. Geophys. Res.*, **10.1029/2001JE001516** (2002).
- [127] Mantas, G. P., and H. C. Carlson, Reinterpretation of the 6300-Å airglow enhancements observed in ionosphere heating experiments based on analysis of Platteville, Colorado, data, *J. Geophys. Res.*, **101**, 195–209, (1996).
- [128] Manuilova, R. O., and G. M. Shved, The 2.7 and 6.3 μm H₂O band emissions in the middle atmosphere, *J. Atmos. Terr. Phys.*, **47**, 413–422, (1985).
- [129] Manuilova, R. O., and G. M. Shved, The 4.8 and 9.6 μm O₃ band emissions in the middle atmosphere, *J. Atmos. Terr. Phys.*, **54**, 1149–1168, (1992).
- [130] Manuilova, R. O., *private communication*, (1997).
- [131] Manuilova, R. O., *private communication*, (1998).
- [132] Manuilova, R. O., O. Gusev, A. A. Kutepov, T. von Clarmann, H. Oelhaf, G. P. Stiller, A. Werner, M. López-Puertas, F. J. Martín-Torres, G. Zaragoza, and J.-M. Flaud, Modeling of non-LTE limb spectra of IR ozone bands for the MIPAS space experiment, *J. Quant. Spectrosc. Radiat. Transfer*, **59**, 405–422, (1998).
- [133] Maricq, M. M., E. A. Gregory, and C. J. S. M. Simpson, Non-resonant V – V energy transfer between diatomic molecules at low temperatures, *Chem. Phys.*, **95**, 43–56, (1985).
- [134] Marshall, T. B., L. L. Gordley, and D. A. Chu, Bandpak: Algorithms for modeling broadband transmission

- and radiance, *J. Quant. Spectrosc. Radiat. Transfer*, **54**, 581–599, (1994).
- [135] McDade, I. C., The photochemistry of the MLT oxygen airglow emissions and the expected influences of tidal perturbations, *Advances in Space Research*, **21**, 787–794, (1998).
- [136] Menard, J., L. Doyennette, and F. Menard-Bourcin, Vibrational relaxation of ozone in O₃-O₂ and O₃-N₂ gas mixtures from infrared double-resonance measurements in the 200-300 K temperature range, *J. Chem. Phys.*, **96**, 15773–15780, (1992).
- [137] Menard-Bourcin, F., L. Doyennette, and J. Menard, Vibrational energy transfer in ozone excited into (101) state from double-resonance measurements, *J. Chem. Phys.*, **101**, 8636, (1994).
- [138] Mertens, C. J., M. G. Mlynczak, M. López-Puertas, P. P. Wintersteiner, R. H. Picard, J. R. Winick, L. L. Gordley, J. M. Russell III, Retrieval of mesospheric and lower thermospheric kinetic temperature from measurements of CO₂ 15 μm Earth limb emission under non-LTE conditions, *Geophys. Res. Lett.*, **28**, 1391–1394, (2001).
- [139] Mihalas, D., *Stellar Atmospheres*, Freeman, San Francisco, 632 pp., (1978).
- [140] Miller, S. M., J. R. Winick, and H. E. Snell, Simultaneous retrievals of middle atmospheric temperature and trace gas species volume mixing ratios from Cryogenic Infrared Radiance Instrumentation for Shuttle (CIRRI-1A), *J. Geophys. Res.*, **104**, 18697–18714, (1999).
- [141] Miller, S. M., and J. Winick, Non-LTE effects on retrieval of temperature from CO₂ laser bands using CIRRI-1A data, *J. Geophys. Res.*, **105**, 10193–10202, (2000).
- [142] Minschwaner, Absorption of Solar Radiation by O₂ : Implications for O₃ and lifetimes of N₂O, CFCl₃ and CF₂Cl₂, *J. Geophys. Res.*, **98**, 10543–10561, (1993).
- [143] Mlynczak, M. G., and S. R. Drayson, Calculation of Infrared Limb Emission by Ozone in the Terrestrial Middle Atmosphere. I. Source Functions, *J. Geophys. Res.*, **95**, 16497–16511, (1990).
- [144] Mlynczak, M. G., and S. R. Drayson, Calculation of Infrared Limb Emission by Ozone in the Terrestrial Middle Atmosphere. II. Emission Calculations, *J. Geophys. Res.*, **95**, 16513–16521, (1990).
- [145] Mlynczak, M. G., Nonlocal thermodynamic equilibrium processes in ozone: implications for the energy budget of the mesosphere and lower thermosphere, *J. Geophys. Res.*, **96**, 17217–17228, (1991).
- [146] Mlynczak, M. G., and S. Solomon, A detailed evaluation of the heating efficiency in the middle atmosphere, *J. Geophys. Res.*, **98**, 10517–10542, (1993).
- [147] Mlynczak, M. G., S. Solomon, and D. S. Zaras, An updated model for O₂(a¹Δ_g) concentrations in the mesosphere and lower thermosphere and implications for SME data, *J. Geophys. Res.*, **98**, 18639–18648, (1993).
- [148] Mlynczak, M. G., D. S. Olander, and M. López-Puertas, Rapid computation of spectrally integrated non-local thermodynamic equilibrium limb emission, *Geophys. Res. Lett.*, **99**, 25761–25772, (1994).
- [149] Mlynczak, M. G., and D. K. Zhou, Kinetic and spectroscopic requirements for the measurement of mesospheric ozone at 9.6 μm under non-LTE conditions, *Geophys. Res. Lett.*, **5**, 639–642, (1998).
- [150] Mlynczak, M. G., D. K. Zhou, M. López-Puertas, G. Zaragoza, and J. M. Russell III, Kinetic requirements for the measurement of water vapor at 6.8 μm under non-LTE conditions, *Geophys. Res. Lett.*, **26**, 63–66, (1999).
- [151] Molisch, A. F., and B. P. Oehry, Radiation trapping in atomic vapors, 510+xxvi p., Oxford University Press, Oxford, U.K., (1998).
- [152] Mumma, M. J., D. Buhl, G. Chin, D. Deming, F. Espenak, T. Kostyuk, and D. Zipoi, *Science*, **212**, 45-49, (1981).
- [153] Nebel, H., P. P. Wintersteiner, R. H. Picard, J. R. Winick, and R. Sharma, CO₂ non-local thermodynamic equilibrium radiative excitation and infrared dayglow at 4.3 μm : Application to spectral infrared rocket experimental data, *J. Geophys. Res.*, **99**, 10409–10419, (1994).
- [154] Ng, K. C., Hypernetted chain solutions for the classical one-component plasma up to $\Gamma = 7000$, *J. Chem. Phys.*, **61**, 2680–2689, (1974).
- [155] Oberheide, J. and O. A. Gusev, Observation of migrating and nonmigrating diurnal tides in the equatorial lower thermosphere, *Geophys. Res. Lett.*, **2002GL016213**, (2002).
- [156] Oberheide, J., M. E. Hagan, R. G. Roble and O. A. Gusev, A global view on tidal temperature perturbations above the mesopause: preliminary model/observation intercomparison, *submitted to Adv. Space Res.*, (2002).
- [157] Oelhaf, H., and H. Fischer, Relevance of upper atmosphere non-LTE effects to limb emission of stratospheric constituents, in *IRS'88: Current problems in atmospheric radiation*, edited by J. Lenoble and J.-P. Geleyn, pp. 460-463, Deepak, Hampton, Va, (1989).
- [158] Offermann, D., CRISTA: A Shuttle experiment for middle atmosphere small scale structures, E.V. Thrane *et al.* (editor), Coupling processes in the lower and middle atmosphere, p. 389, Kluwer Academ. Publ., Holland, (1993).
- [159] Offermann, D., K. U. Grossmann, P. Barthol, P. Knieling, M. Riese, and R. Trant, Cryogenic Infrared Spectrometers and Telescopes for the Atmosphere (CRISTA) experiment and middle atmosphere variability, *J. Geophys. Res.*, **104**, 16311–16325, (1999).

- [160] Ogibalov, V. P., A. A. Kutepov, and G. M. Shved, Non-local thermodynamic equilibrium in CO₂ in the middle atmosphere. II. Populations in the $\nu_1\nu_2$ mode manifold states, *J. Atmos. Sol. Terr. Phys.*, **60**, 315–329, (1998).
- [161] Olson, G. L., L. H. Auer, and J.-R. Buchler, *J. Quant. Spectrosc. Radiat. Transfer*, **35**, 431, (1986).
- [162] Olson, G. L., and P. B. Kunasz, Short characteristic solution of the non-LTE line transfer problem by operator perturbation. I. The one-dimensional planar slab, *J. Quant. Spectrosc. Radiat. Transfer*, **38**, 325–336, (1987).
- [163] Pack, R. T., Pressure broadening of the dipole and Raman lines of the CO₂ by He and Ar. Temperature dependence, *J. Chem. Phys.*, **70**, 3424–3433, (1979).
- [164] Park, H., and T. G. Slanger, *J. Chem. Phys.*, **100**, 187, (1994).
- [165] Parker, J. G., and D. W. Ritke, Effect of ozone on the vibrational relaxation time of oxygen, *J. Chem. Phys.*, **59**, 5725, (1973).
- [166] Pravilov, A. M., *private communication*, (1999).
- [167] Price, J. M., J. A. Mack, C. A. Rogaski, and A. M. Wodtke, Vibrational-State-Specific Self-Relaxation Rate Constant. Measurements of Highly Vibrationally Excited O₂ ($v = 19 - 28$), *J. Chem. Phys.*, **175**, 83–89, (1993).
- [168] Ratkowski, A. J., R. H. Picard, J. R. Winick, K. U. Grossmann, D. Homann, J. C. Ulwick, and A. J. Paboojian, Lower-thermospheric infrared emissions from high-latitude twilight – B. Analysis of 15 μm emission and comparison with non-LTE models, *J. Atmos. Terr. Phys.*, **56**, 1899–1914, (1994).
- [169] Rawlins, W. T., Chemistry of vibrationally excited ozone in the upper atmosphere, *J. Geophys. Res.*, **90**, 12283–12292, (1985).
- [170] Rawlins, W. T., G. E. Caledonia, R. A. Armstrong, Dynamics of vibrationally excited ozone formed by three-body recombination reaction. II. Kinetics and mechanism, *J. Chem. Phys.*, **87**, 5209, (1987).
- [171] Riese, M., R. Spang, P. Preusse, M. Ern, M. Jarisch, D. Offermann, and K. Grossmann, Cryogenic Infrared Spectrometers and Telescopes for the Atmosphere (CRISTA) data processing and atmospheric temperature and trace gas retrieval, *J. Geophys. Res.*, **104**, 16349–16367, (1999).
- [172] Rinsland, C. P., M. R. Gunson, R. Zander, and M. López-Puertas, Middle and upper atmosphere pressure-temperature profiles and the abundances of CO₂ and CO in the upper atmosphere from ATMOS/Spacelab 3 observations, *J. Geophys. Res.*, **97**, 20479–20495, (1992).
- [173] Robertshaw, J. S., and I. W. M. Smith, Vibrational energy transfer from CO ($v=1$), N₂ ($v=1$), CO₂ (00^0_1), N₂O (00^0_1) to O₃, *J. Chem. Soc. Faraday Trans.*, **76**, 1354, (1980).
- [174] Rodrigo, R., J. J. López-Moreno, M. López-Puertas, F. Moreno, and A. Molino, Neutral atmospheric composition between 60 and 220 km: A theoretical model for mid-latitudes, *Planet. Space Sci.*, **34**, 723–743, (1986).
- [175] Rodrigo, R., E. Garcia-Alvarez, M. J. Gonzalez, J. J. Lopez-Moreno, A Nonsteady One-Dimensional Theoretical Model of Mars Neutral Atmospheric Composition between 30 km and 200 km, *J. Geophys. Res.*, **95**, 14795–14810, (1990).
- [176] Rodrigo, R., M. J. López-Gonzalez, and J. J. López-Moreno, Variability of the neutral mesospheric and lower thermospheric composition in the diurnal cycle, *Planet. Space Sci.*, **39**, 803–820, (1991).
- [177] Rothman, L. S., R. R. Gamache, R. H. Tipping, C. P. Rinsland, M. A. H. Smith, D. Chris Benner, V. Malathy Devi, J.-M. Flaud, C. Camy-Peyret, A. Perrin, A. Goldman, S. T. Massie, L. R. Brown, and R. A. Toth, The HITRAN molecular database: editions of 1991 and 1992, *J. Quant. Spectrosc. Radiat. Transfer*, **48**, 469–507, (1992).
- [178] Rothman, L. S., R. R. Gamache, and R. H. Tipping, Energy levels, intensities, and linewidths of atmospheric carbon dioxide bands, *J. Quant. Spectrosc. Radiat. Transfer*, **48**, 537–566, (1992).
- [179] Rothman, L. S., C. P. Rinsland, A. Goldman, S. T. Massie, D. P. Edwards, J.-M. Flaud, A. Perrin, C. Camy-Peyret, V. Dana, J. Y. Mandin, J. Schroeder, A. Mccann, R. R. Gamache, R. B. Wattson, K. Yoshino, K. V. Chance, K. W. Jucks, L. R. Brown, V. Nemtchinov, and P. Varanasi, The HITRAN molecular spectroscopic database and Hawks (HITRAN atmospheric workstation): 1996 edition, *J. Quant. Spectrosc. Radiat. Transfer*, **60**, 665–710, (1996).
- [180] Ridolfi, M., B. Carli, M. Carlotti, T. von Clarmann, B. Dinelli, A. Dudhia, J.-M. Flaud, M. Höpfner, P. E. Morris, P. Raspollini, G. Stiller, and R. J. Wells, Optimized forward model and retrieval scheme for MIPAS near-real-time data processing, *Applied Optics*, **39**, 1323–1340, (2000).
- [181] Rybicki, G. B., and D. G. Hummer, An accelerated lambda iteration method for multilevel radiative transfer. I. Non-overlapping lines with background continuum, *Astron. Astrophys.*, **245**, 171–181, (1991).
- [182] Rybicki, G. B. and D. G. Hummer, An accelerated lambda iteration method for multilevel radiative transfer. II. Overlapping transitions with full continuum, *Astron. Astrophys.*, **262**, 209–215, (1992).
- [183] Sharma, R. D., and P. P. Wintersteiner, CO₂ component of daytime Earth limb emission at 2.7 μm , *J. Geophys. Res.*, **90**, 9789–9803, (1985).
- [184] Sharma, R. D., and P. P. Wintersteiner, Role of carbon dioxide in cooling planetary atmospheres, *Geophys. Res. Lett.*, **17**, 2201–2204, (1990).

- [185] She, C. Y., and U. von Zahn, Concept of a two-level mesopause: Support through new lidar observations, *J. Geophys. Res.*, **103**, 5855–5863, (1998).
- [186] Shved, G. M., G. I. Stepanova, and A. A. Kutepov, Transfer of 4.3 μm CO_2 radiation on departure from local thermodynamic equilibrium in the atmosphere of the Earth, *Atmos. Oceanic. Phys.*, **14**, 589–596, (1978).
- [187] Shved, G. M., and O. A. Gusev, Non-local thermodynamic equilibrium in N_2O , CH_4 and HNO_3 in the middle atmosphere, *J. Atmos. Terr. Phys.*, **60**, 2167–2176, (1997).
- [188] Shved, G. M., A. A. Kutepov, and V. P. Ogibalov, Non-local thermodynamic equilibrium in CO_2 in the middle atmosphere. I. Input data and populations of the ν_3 manifold states, *J. Atmos. Terr. Phys.*, **60**, 289–314, (1998).
- [189] Siddles, R. M., G. J. Wilson, and C. J. S. M. Simpson, The vibrational deactivation of the bending modes of CD_4 and CH_4 measured down to 90K, *Chem. Phys.*, **188**, 99–105, (1994).
- [190] Siddles, R. M., G. J. Wilson, and C. J. S. M. Simpson, The vibrational deactivation of the (00^01) mode of N_2O measured down to 150K, *Chem. Phys. Lett.*, **225**, 146–149, (1994).
- [191] Slanger, T., Studies on Highly Vibrationally-Excited O_2 , AIAA 97-2502, 32nd Thermophysics Conference, (1997).
- [192] Solomon, S., J. T. Kiehl, B. J. Kerridge, E. E. Remsberg, and J. M. Russel III, Evidence for nonlocal thermodynamic equilibrium in the ν_3 mode of mesospheric ozone, *J. Geophys. Res.*, **91**, 9865–9876, (1986).
- [193] Starr, D. F., and J. K. Hancock, Vibrational energy transfer in CO_2 - CO mixtures from 163 to 406 K, *J. Chem. Phys.*, **63**, 4730–4734, (1975).
- [194] Steinfeld, J. I., S. M. Adler-Golden, and J. W. Gallagher, Critical Survey of Data on the Spectroscopy and Kinetics of Ozone in the Mesosphere and Thermosphere, *J. Chem. Phys. Ref. Data*, **16**, 911–951, (1987).
- [195] Steinfeld, J. I., P. Ruttenberg, G. Millot, G. Fanjoux, and B. Lavorel, Scaling laws for inelastic collision processes in diatomic molecules, *J. Phys. Chem.*, **95**, 9638–9647, (1991).
- [196] Stephenson, J. C., and E. R. Mosburg Jr., Vibrational energy transfer in CO from 100 to 300 K, *J. Chem. Phys.*, **60**, 3562–3566, (1974).
- [197] Stevens, M. H., R. R. Conway, Ch. R. Englert, M. E. Summers, K. U. Grossmann, and O. A. Gusev, PMCs and water frost point in the Arctic summer mesosphere, *Geophys. Res. Lett.*, **28**, 4449–4452, (2001).
- [198] Sun, Y., and A. Dalgarno, Collisional excitation of metastable $\text{O}(^1D_2)$ atoms, *J. Chem. Phys.*, **96**, 5017–5019, (1992).
- [199] Svanberg, M., J. B. C. Pettersson, and D. Murtagh, Ozone photodissociation in the Hartley band: a statistical description of the ground state decomposition channel $\text{O}_2(X^3\Sigma_g^-) + \text{O}(^3P_J)$, *J. Chem. Phys.*, **102**, 8887–8896, (1995).
- [200] Stewart, A. I. F., Revised Time Dependent Model of the Martian Atmosphere for use in Orbit Lifetime and Sustainance Studies, *Final report JPL PO# NQ-802429*, March 26, (1987).
- [201] Thekaekara, M. P., Solar radiation measurements: technique and instrumentation, *Solar Energy*, **18**, 309–325, (1976).
- [202] Thompson, P., D. E. Cox, and J. B. Hastings, *J. Appl. Crystallogr.*, **20**, 79–83, (1987).
- [203] Toumi, R., B. J. Kerridge, and J. A. Pyle, Highly vibrationally excited oxygen as a potential source of ozone in the upper stratosphere and mesosphere, *Nature*, **351**, 217–219, (1991).
- [204] Trujillo-Bueno, J., and P. Fabiani-Bendicho, A novel iterative scheme for the very fast and accurate solution of Non-LTE radiative transfer problems, *Astrophys. J.*, **455**, 646, (1995).
- [205] Turnbull, D. N., and R. P. Lowe, New hydroxyl transition probabilities and their importance in the airglow studies *Plant. Space Sci.*, **37**, 723–738, (1989).
- [206] Unsöld, A., *Physik der Sternatmosphären*, Springer-Verlag Berlin, Heidelberg, New York, 866 pp, (1968).
- [207] López-Valverde, M. Á., and M. López-Puertas, A non-local thermodynamic equilibrium radiative transfer model for infrared emissions in the atmosphere of Mars, 1. Theoretical basis and nighttime populations of vibrational levels, *J. Geophys. Res.*, **99**, 13093–13115, (1994).
- [208] López-Valverde, M. Á., and M. López-Puertas, A non-local thermodynamic equilibrium radiative transfer model for infrared emissions in the atmosphere of Mars, 2. Daytime populations of vibrational levels, *J. Geophys. Res.*, **99**, 13117–13132, (1994).
- [209] Vinsome, P. K. W., *Proceedings of the Fourth Symposium on Reservoir Simulation*, Society of Petroleum Engineers, 149, (1976).
- [210] Vollmann, K., “Messungen und Modelirungen von Infrarotemissionen der Spurengase Kohlendioxid und Ozone unter der Bedingung des Nicht-Lokalen-Thermodynamischen-Gleichgewicht” *Measurements and modeling of infrared emissions of trace gases carbon dioxide and ozone under the condition of the non-local thermodynamic equilibrium*, PhD thesis, Bergische Universität - Gesamthochschule Wuppertal, Fachbereich 8 - Physik, (1996).
- [211] Vollmann, K., and K. U. Grossmann, Excitation of 4.3 μm CO_2 emissions by $\text{O}(^1D_2)$ during twilight, *Advances in Space Research*, **20**, 1185–1189, (1997).
- [212] Ward, W. E., Tidal mechanisms of dynamical influence on oxygen recombination airglow in the mesosphere and lower thermosphere, *Advances in Space Research*, **21**, 795–805, (1998).

- [213] Wells, R. J., Rapid approximation to the Voigt/Faddeeva function and its derivatives, *J. Quant. Spectrosc. Radiat. Transfer*, **62**, 29–48, (1999).
- [214] Werner, K., and D. Husfeld, *Astron. Astrophys.*, **148**, 417, (1985).
- [215] West, G. A., R. E. Weston Jr., and G. W. Flynn, Deactivation of vibrationally excited ozone by $O(^3P_1)$ atoms, *Chem. Phys. Lett.*, **42**, 488–493, (1976).
- [216] West, G. A., R. E. Weston Jr., and G. W. Flynn, The influence of reactant vibrational excitation on the $O(^3P_1) + O_3^*$ bimolecular reaction rate, *Chem. Phys. Lett.*, **56**, 429–433, (1978).
- [217] Whitson, M. E., and R. J. McNeal, Temperature dependence of the quenching of the vibrationally excited N_2 by NO and H_2O , *J. Chem. Phys.*, **66**, 2696–2698, (1977).
- [218] Winick, J. R., P. P. Wintersteiner, and R. H. Picard, Non-LTE emission from CO ($v=1$) in the mesosphere and lower thermosphere and its effect on remote sensing, in *Digest of Topical Meeting on Optical Remote Sensing of the Atmosphere*, **4**, 611–614, (1990).
- [219] Wintersteiner, P. P., R. H. Picard, R. D. Sharma, J. R. Winick, and R. A. Joseph, Line-by-line radiative excitation model for the non-equilibrium atmosphere: Application to CO_2 15 μm emission. *J. Geophys. Res.*, **97**, 18083–18117, (1992).
- [220] Wise, J. O., R. L. Carovillano, H. C. Carlson, R. G. Roble, S. Adler-Golden, R. M. Nadile, and M. Ahmadjian, CIRRIIS-1A global observations of 15 μm CO_2 and 5.3 μm NO limb radiance in the lower thermosphere during moderate to active geomagnetic activity, *J. Geophys. Res.*, **100**, 21357–21371, (1995).
- [221] Zachor, A. S., and R. D. Sharma, Retrieval of non-LTE vertical structure from a spectrally resolved infrared limb radiance profile, *J. Geophys. Res.*, **90**, 467–475, (1985).
- [222] Zittel, P. F., and D. E. Masturzo, Vibrational relaxation of H_2O from 295 K to 1020 K, *J. Chem. Phys.*, **90**, 977–989, (1989).
- [223] Zhou, D. K., M. G. Mlynczak, G. E. Bingham, J. O. Wise, and R. M. Nadile, CIRRIIS-1A limb spectral measurements of mesospheric 9.6 μm airglow and ozone, *Geophys. Res. Lett.*, **5**, 643–446, (1998).
- [224] Zhou, D. K., M. G. Mlynczak, G. E. López-Puertas, and G. Zaragoza, Evidence of non-LTE effects in mesospheric water vapor from spectrally-resolved emissions observed by CIRRIIS-1A, *Geophys. Res. Lett.*, **26**, 67–70, (1999).
- [225] Zhu, X., An accurate and efficient radiation algorithm for middle atmosphere model, *J. Atmos. Sci.*, **51**, 3593–3614, (1994).
- [226] Zuev, A. P., Analysis of experimental data on vibrational relaxation of N_2O , *Sov. J. Chem. Phys.*, **7**, 1516–1540, (1985).
- [227] Zuev, A. P., Shock-tube laser-schlieren measurements of $V - T$ and $V - V$ relaxation in mixtures of N_2O with N_2 and O_2 , *Sov. J. Chem. Phys.*, **4**, 2439–2450, (1989).